PRESSURE MEASUREMENTS NEAR THE TIP OF A HOVERING MODEL ROTOR BLADE AND A PRELIMINARY INVESTIGATION OF THE FLOW IN THE ROTOR WAKE

A THESIS

Presented to

The Faculty of the Division of Graduate Studies

By

T. P. Shivananda

In Partial Fulfillment

of the Requirements for the Degree

Doctor of Philosophy

in the School of Aerospace Engineering

Georgia Institute of Technology

December, 1977

PRESSURE MEASUREMENTS NEAR THE TIP OF A HOVERING MODEL ROTOR BLADE AND A PRELIMINARY INVESTIGATION OF THE FLOW IN THE ROTOR WAKE

Approved:

Howard M. McMahon, Chairman

Robin B. Gray

G. Alvin Pierce

Date approved by Chairman: 12/2/77

Dedicated to

My late father

ACKNOWLEDGMENTS

It gives me a great pleasure to express my deep gratitude to my teacher and advisor, Dr. Howard M. McMahon, and Dr. Robin B. Gray for suggesting the thesis topic and their sustained guidance throughout the course of this research program. Their ever-willingness to discuss various aspects of the investigation is sincerely appreciated.

I also thank Drs. Alvin G. Pierce, Charles F. Martin and Prof. James E. Hubbart for their careful examination of the manuscript and for their constructive comments.

My thanks are due to Dr. Craig and Dr. Sparrow for their valuable assistance during the development of the computer software needed in the research program.

Mr. John Caudell helped in solving many instrumentation problems. I am very grateful for his help. I also express my thanks to Mr. John Palfery, Mr. Dewey Ransom, and Mr. Harald Meyer for their aid in various phases of the experiments.

I appreciate the help of fellow graduate students who extended their help when needed.

The financial assistance provided by the School of Aerospace Engineering is gratefully acknowledged.

My sincere thanks go to Mrs. Peggy Weldon for an immaculate job she has done in typing this thesis.

I want to express deepest gratitude to my mother and late father who have provided encouragement throughout my education. I also want to thank my brother for his moral support.

TABLE OF CONTENTS

TABLE OF CONTENTS (Continued)

LIST OF TABLES

LIST OF ILLUSTRATIONS

LIST OF ILLUSTRATIONS (Continued)

LIST OF ILLUSTRATIONS (Continued)

LIST OF ILLUSTRATIONS (Continued)

LIST OF ILLUSTRATIONS (Continued)

NOMENCLATURE

a	surface area of the hot film
C	rotor blade chord
C_p	pressure coefficient $(p-p_a)/q$
C_T	Thrust coefficient
d	diameter of the hot film
$E_{I,II}$	bridge voltages for films I and II
q	acceleration due to gravity
h_f	convection heat transfer coefficient
I	heating current
$I_{I,II}$	heating current of film I and II
k_m	thermal conductivity of air measured at mean temperature, T_m
k	constant in expression for effective cooling velocity (Appendix C)
Nu	Nusselt number
p	pressure
p_a	ambient pressure
p_s	standard atmospheric pressure
Q	total heat transfered per unit time from one sensor
q	dynamic pressure based on local-blade element velocity; also heat transfer per unit time from one film (Appendix C)
r	local rotor blade radius
R	rotor blade tip radius
R_e	Reynolds number

$R_{e_{tip}}$	Reynolds number based on rotor blade tip velocity
R_{e_d}	Reynolds number based on diameter of hot film
$R_{I,II}$	hot film resistances, for films I and II
$R_{c_{I,II}}$	cable resistances for films I and II
$R_{M_{I,II}}$	resistances of the bridge arm adjacent film for films I and II
U	local velocity
U_s	velocity at standard condition
U_{es}	effective cooling velocity
v_∞	free-stream velocity
v_m	measured velocity
v_a	Instantaneous axial velocity
$\overline{v}_a$	mean axial velocity
v_r	instantaneous radial velocity
$\overline{v}_r$	mean radial velocity
v_t	instantaneous tangential velocity
$\overline{v}_t$	mean tangential velocity
v_o	absolute value of momentum induced velocity ($\Omega R\sqrt{C_T}/2$)
T_a	ambient temperature
T_m	mean temperature between film and air
T_f	film operating temperature
T_s	standard atmospheric temperature
x	non dimensional radius, r/R
X	chordwise distance from the blade leading edge
Y	radial distance inward from blade tip
z	axial distance from the rotor plane

ψ	blade azimuth angle
Ω	rotor angular velocity
ρ	density
ϕ	angle of yaw of the sensors

SUMMARY

The wake of a helicopter rotor in hover strongly influences the rotor aerodynamics and hence, the hovering performance of the helicopter. The aim of the present investigation is to add to the basic understanding of the rotor wake by means of pressure and velocity measurements. The experiments were carried out in the rotor test facility at Georgia Tech using a single-bladed model rotor to generate the wake. The constant chord, untwisted rotor blade has a square tip and a NACA 0012 airfoil section.

The investigation was conducted in two parts. In the first part, pressure measurements were made over the tip region of the hovering rotor blade with the aim of understanding more about the generation of the tip vortex. The second part was aimed at understanding the flow field in the near wake of the hovering rotor.

Blade-tip surface pressures were measured in detail for blade pitch angles of 0°, 6.2°, and 11.4°. These angles correspond to thrust coefficients of 0, 0.0026, and 0.0055. The pressure measurements were made at six radial stations outboard of the 94% radial location on the rotor blade. The points of vortex inception inferred from the pressure data agree well with those noted by other investigators using surface flow visualization techniques. The presence of both a primary and a secondary vortex near the rotor tip at a pitch angle of 11.4° is observed. At 0° pitch angle, the measured pressure distribution in the tip region is in good agreement with the pressure distribution obtained

from semi-infinite wing theory.

In the second part, instantaneous velocity components were measured in detail in the near-wake of the rotor at several radial and axial stations by using a hot-film vector anemometer. (The near-wake being the portion of the wake within one or two wake revolutions from the rotor.) The geometry of the vortex sheet and of the tip vortex was obtained from these velocity data, and the data were averaged to determine the mean velocity components in the wake. The experimental results show good agreement with available theory.

CHAPTER I

INTRODUCTION

The requirement that a helicopter be capable of hovering out of ground effect sometimes represents a critical design condition, and is typically used for purposes of design evaluation of the helicopter. In those instances where hovering capability is required, a 5% variation in static lift represents a change in pay load of approximately 20%, due to the low pay load to gross weight ratio (usually around 0.25) of rotary wing aircraft. Thus, the pay load penalty associated with deficiencies in rotor hover performance may be critical to the success of a given helicopter. This demonstrates the importance of improving the hover performance of a helicopter rotor and hence the need for a complete understanding of the rotor aerodynamics in the hovering condition.

The rotor aerodynamics is strongly influenced by the rotor wake. However, the rotor wake is not yet well understood. As an example, in a recent Advisory Group for Aerospace Research and Development (AGARD) technical evaluation report[1] summarizing a Fluid Dynamics Panel Specialists meeting on the aerodynamics of rotary wings, the following conclusions were noted:

"We are not able to describe in sufficient detail, much less model, the physical processes in the following:

(1) The wake of a hovering rotor in and out of ground effect;

(2) The formation of a blade tip vortex;

(3) The rolling up of the blade trailing wake."

Thus, there is a strong requirement for a better understanding of the rotor wake in hover and its effect on rotor aerodynamics in the hovering condition. The experimental work reported here is aimed at increasing the understanding of rotor wake in the hovering condition.

The rotor wake, which strongly influences the rotor aerodynamics, contains two primary features. The first is the strong tip vortex, which is generated in the tip region of the rotor blade. The second is the vortex sheet shed from the inboard sections of the blade. In this dissertation, an attempt is made to understand certain aspects of each of these flow features. The dissertation divides naturally into two parts. The first part deals with pressure measurements at the tip of a hovering single-bladed model rotor and is aimed at understanding the formation mechanics of the tip vortex. The second part is concerned with the flow in the rear wake and involves the measurement of instantaneous velocities in that region. In this work, the rear wake is defined as that portion of the wake within one or two wake revolutions from rotor.

Pressure Measurements Near the Tip

As indicated previously the operating characteristics of a rotory wing aircraft are strongly influenced by the vortex wake generated by the rotating blades. The dominant feature of this vortex wake is the helical vortices which have their origin at the tips of the rotor blades. The interaction of rotor blade with the vortex wake changes the aerodynamic loading on the blade and thus affects the rotor blade operating performance, vibration and noise characteristics. Rotor

theory has progressed to the point where a detailed knowledge of the structure of the tip vortex is needed. In the reveiw of the recent AGARD meeting on rotary wing areodynamics mentioned earlier, Ham[1] points out the need for a better understanding of the physical processes in the formation and structure of the blade tip vortex.

Furthermore, the outer elements of a rotor blade play a much more important role in providing lift than does the wing tip region of an airplane because the dynamic pressure is much higher at the blade tip than over the inboard portions of the blade. The traditional approach of using a "tip loss factor" in helicopter performance calculation needs to be made more precise. The tip losses are not simply related to the thrust coefficient as currently assumed in evaluating the tip loss factor.

Thus, there is a need for more detailed knowledge of the flow field very near the tip of a helicopter rotor blade. Therefore, the surface pressures in the tip region of a model rotor were measured in detail.

Literature Review

Qualitative information on the local flow direction near a rotor tip is available from flow visualization studies.[2] Other experiments on tip vortex abatement[3] and on blade-vortex interactions[4,5] have given some insight into the flow at the tip region but these studies have dealt either with flow visualization of the tip vortex or with the measurement of unsteady pressures for $r/R \leq 0.95$ in a forward-flight condition. There is a lack of detailed pressure data very near the rotor tip.

The generation of a tip vortex by a fixed wing has received considerable attention from several investigators.[6,7,8,9] Measurement of surface pressure distributions on a wing with square tips has shown the presence of a primary as well as a secondary vortex near the tip on the top surface of the lifting wing. Velocity distributions[8] in the trailing vortex also has shown the presence of both a primary and a secondary vortex. Some flow visualization studies have been carried out[6,7] to investigate the applicability of fixed wing results to rotating wings. It is felt[7] that the location of the tip vortex is not affected by centrifugal forces or pressure gradients on the rotor blade but remain at the same relative position as for the fixed wings.

Research Objective

It is the aim of this part of the study to provide detailed pressure distribution data very near the tip(outboard of $r/R = 0.94$) of a single-bladed model helicopter rotor in hover. This experimental data should be of considerable value in formulating theoretical models for the tip vortex. The experimental data will be examined in detail with the following goals in mind:

(1) Obtain information regarding the position and strength of the tip vortex and their dependence on the blade loading.

(2) Use the experimental data for guiding the development of theoretical analyses for flow in the tip region of a rotor.

(3) Compare the experimental data with available theoretical calculations for flow in the tip region and with other available experimental data for both rotors and fixed wings.

Velocity Measurements in the Rotor Wake

The flow field generated by a helicopter rotor is extremely complex and difficult to predict with acceptable accuracy. Validation and further improvement of theoretical predictions can best be accomplished by detailed measurements of the rotor wake structure. In the recent AGARD meeting on Aerodynamics of Rotory Wings[1] one of the conclusions was that, "Though much ingenius modelling has been done, the fact remains that the position of the all-important first spiral of vorticity cannot be predicted satisfactorily due to an apparent gap in the physical understanding." Therefore, a quantitative investigation of the velocity field in the wake of a hovering rotor should be an important contribution to the understanding of the vortex wake and hence the rotor aerodynamics.

In predicting rotor performance, some theoretical methods using a so-called prescribed wake analysis require a detailed knowledge of the geometric characteristics of the rotor wake so that the mathematical models can be formulated. Analytical rotor performance predictions, obtained using the prescribed wake analysis, are very sensitive to the wake geometry. Results of a prescribed wake analysis[10] show that the incorporation of a realistic wake geometry provides a significantly improved prediction of the rotor performance characteristics. The so-called free-wake analysis which does not incorporate any experimental data, does not give performance results that agree well with experiments.[11] This is because the analytical wake geometry that is determined in the free-wake case does not agree well with the measured wake geometry particularly in the near wake.

In most cases, the geometry of the wake vortex system near

the rotor which is used in emperical theories is determined from flow visualization techniques. These techniques are insufficient to adequately describe the vortex wake and core structure. Thus, there is a strong requirement for detailed information which is not available through flow visualization studies alone.

Literature Review

Many flow visualization studies[10,12,13,14] have given qualitative and quantitative information about rotor wakes. These smoke-flow visualization studies have resulted in the development of a generalized emeprical equation for the tip vortex and vortex sheet geometries in the near wake. Most of the information regarding the wake characteristics gathered in these tests is based upon observed phenomena rather than upon direct measurements.

Some attempts[15,16,17,18] have been made to use hot wire or hot film anemometry as a method for providing information additional to that observed through flow visualization. Boatwright[16,17] made velocity measurements in the wake of a full-scale OH-13E helicopter rotor in hover. However, none of these investigations has produced any detailed measurement of the vortex sheet shed inboard of the tip at the blade trailing edge.

Recently, several studies[19,20,21,22] have been made using laser velocimetry as a technique for mapping the rotor flow field. Biggers and Orloff[19,20] used a two-color laser velocimeter to measure the flow velocity in the wake of a helicopter rotor in a forward flight and obtained two components of both the instantaneous and time-averaged velocities. Their main objective was to obtain the velocity variation very

near the rotor blade and to study the suitability of using a laser velocimeter to measure velocity distribution in the rotor wake. None of these studies, to date, have reported detailed velocity measurements in the near wake of a rotor in the hovering condition.

Flow visualization techniques[10] using Schlieren and laser holography are also being used to investigate the characteristics of the wake. To the author's knowledge, no results using these techniques have been published to date.

Research Objectives

It is the aim of this part of the study to make detailed measurements of the instantaneous velocities in the near wake of a single-bladed model helicopter rotor in hover. The velocity data will be studied with the following goals in mind:

(1) Obtain information regarding the geometry and strength of the vortex sheet shed inboard of the rotor tip at the trailing edge;

(2) Determine the geometry of the tip vortex trail;

(3) Compare the results thus obtained and the measured mean velocity distribution in the rotor wake with results from a theoretical analysis[23] for the hovering rotor.

(4) Obtain information useful in guiding the development of theoretical analysis of the rotor wake.

The two investigations described in this dissertation require completely different experimental methods and instrumentation. Thus, the equipment, experimental procedure and results of each investigation are discussed separately after the rotor test facility is described in the next chapter.

CHAPTER II

ROTOR TEST FACILITY

The experimental investigations reported here were carried out in the rotor test facility at the Georgia Institute of Technology. A general description of the test facility along with a description of the rotor are included in this chapter.

Test Facility

The experiments were carried out in the rotor test cell shown in Figure 1. The test cell was developed as a facility for studying hovering model helicopter rotors. The test cell provided adequate protection for personnel and equipment, while the interior of the test cell was desinged to simulate free air conditions(i.e., solid boundries at infinity) for the rotor.

The cell is constructed of wood and has a safety barrier of steel and wood that extends for a distance of 2 feet on either side of the plane of rotation of the rotor. The interior dimensions of the cell are 9 x 9 x 21 feet. Flow visualization is facilitated by windows in the sidewall and in the door. The cell is divided by a honeycomb partition (Figure 2) which suppresses the turbulence in the return flow. This partition has a circular hole centered on the axis of rotation of the rotor and large enough to pass the contracted wake. A bell-mouth inlet provides for a freer and more uniform passage of the rotor wake through

this hole. Ventilation ports were cut in the walls of the test cell in order to reduce the intensity of vortices which were observed extending from the thrust side of the rotor to the walls of the cell. The final configuration of the test cell was determined after extensive flow visualization studies were conducted in order to evaluate the flow behaviour. Additional information regarding the configuration of the test cell and the flow visualization studies is given in Appendix A.

The rotor is driven by a 15 horsepower variable speed direct current motor which is controlled and protected by a speed control unit. The speed of the rotor can be varied from zero to 2000 RPM, and is measured by a tachometer which consists of a magnetic pickup and an electric counter. The magnetic pickup generates sixty pulses per one revolution of the rotor and the counter displays the speed in RPM. The speed of the rotor is varied and controlled by a potentiometer connected to the feedback unit of the motor.

Figure 3 shows the slipring assembly, d.c. motor, magnetic pick-up and shaft angle encoder, which are all supported on a heavy steel frame located next to the test cell. The drive motor and rotor shaft unit, along with the sliprings are rigidly supported on the steel frame work. A 52 channel mercury slipring assembly is connected to the rotor shaft. These sliprings transfer the signal currents between the transducers in the rotating blade and the stationary data acquisition equipment by means of a disc rotating in a pool of mercury. By using mercury sliprings, the electrical noise in the output singals was greatly reduced compared to the then available brush-contact

sliprings. According to the manufacturer, the contact resistance for this mercury slipring system in 5 milli-ohm and the rotational resistance deviation is ±0.25 milli-ohm between 0 and 600 RPM, with no resistance deviation above 600 RPM.

Rotor

Figure 4 shows the rotor used in the experiments. The rotor has a single, constant chord, untwisted blade with a square, flat tip and the following geometric characteristics:

Airfoil section . . . . NACA 0012

Blade radius . . . . 24 inches

Blade chord . . . . 5 inches

Rotor solidity 0.0663

Aspect ratio 4.8

Collective pitch, range 0 to 12 degrees.

The blade leading edge and spar are made of steel, while the trailing edge is made of alumimium. The dimensions of the rotor blade were established by the size of the test cell and the internal blade volume required for the installation of the pressure transducers. Although the model blade is not proportioned exactly like full-scale rotor blades, the data obtained in the model tests should be satisfactory for guiding the development of theoretical analyses and for comparison with the results of such analyses.

The blade is statically balanced with an appropriate counterweight. A single-bladed rotor was used in the experiments since it eliminates such complex phenomena as the interaction between a tip

vortex from one blade and the passage of a closely-following blade. The choice of only one blade also eliminates the necessity of constructing two or more exactly identical blades. Previous tests have shown that considerable care must be exercised to assure that the tip vortex strengths of multi-bladed rotors are the same, otherwise the vortices will follow different paths.

PART ONE

PRESSURE MEASUREMENTS NEAR THE TIP

CHAPTER III

EQUIPMENT AND INSTRUMENTATION

In order to make surface pressure measurements in the tip region of the rotor blade, a removable blade tip was designed and fabricated. The details of the blade tip assembly and of the instrumentation required for pressure measurements are included in this chapter. The data acquisition system is also explained herein.

Blade Tip Assembly

The removable blade tip forms the outermost 1.75" of the rotor blade and is made of magnesium. Figure 5 shows an exploded view of the blade and the tip assembly. The tip consists of two pieces of equal width which are cemented with epoxy along the chordwise interface and which are held together by bolts which run through the tip and into the blade. Before these two pieces were cemented together, matching holes of diameters ranging from 0.0625" to 0.203" were drilled into each piece. Groups of these holes were joined together by slots along the mating surface between the two pieces in order to form six cavities. Figure 6 shows a typical cavity in detail. Transducer mounting plugs are screwed into these cavities through the inboard end of the largest hole in each cavity. The plugs extend approximately 0.70" into the cavity.

Surface pressure orifices having a diameter of 0.025" were drilled from the airfoil surface into the cavities. Care was taken to see that the orifices were perpendicular to the airfoil surface.

The orifices are located in chordwise planes at the 94.0, 96.6, 98.0, 98.7, 99.1 and 99.5 percent blade radius stations. In each plane, 20 orifices are located on the upper surface, 20 on the lower surface and one at the leading edge of the airfoil. Twenty-five pressure orifices were drilled on the square, flat outboard tip. Nine of these orifices were located along the chord line, with the remaining 16 located symmetrically on lines parallel to the chordline and 0.037 chord lengths above above and below the chordline.

Paddle type subminiature pressure transducers were cemented onto a flat segment on each transducer plug. The wires from the transducers pass through a small hole in the plug and are led along slots cut in the interface between the removable tip and the blade. They then are led through an aluminum tube inside the blade to a terminal block on the rotor hub. From there the wires are led inside the rotor shaft to the sliprings, through which the signals were transfered to the stationary recording equipment.

When cutting the threads and machining the flat segments on the plugs, care was taken to make sure that when the plugs were screwed in tightly, the flats on which the transducers were mounted were perpendicular to the airfoil chordline. This was done so as to minimize the effects of inertia forces on the transducer output.

After making sure that all the orifices were open and that there were no leaks between the cavities, the two pieces making up the removable tip were epoxied together. Care was taken to make sure that this joint was leak tight. The transducers were mounted on the plugs

using RTV cement and the plugs were screwed into the cavities. Both the threads on the plugs and the lead wires passing through the access holes in the plugs were cemented with RTV cement to achieve a good seal. Finally, the entire assembly was checked for leaks and made as leak-tight as possible.

Thus, the tip assembly consists of six irregularly shaped cavities whose volume varied from 0.06 to 0.10 cubic inches. Each of these cavities contain a pressure transducer which is exposed to the airfoil surface pressure through the several orifices drilled into that cavity. During a data run, pressures were measured at six surface locations at a time. This was accomplished by leaving one orifice per cavity open and covering the remaining orifices with a leak-tight tape.

Instrumentation

Surface pressures were measured using model SA-8J-7F1 pressure gages manufactured by Sensotec, Inc. This subminiature transducer utilizes a stainless steel diaphragm(1/8" diameter) on which four active strain gages are bonded to form a wheatstone bridge configuration. This "F" type transducer is very thin(0.034") and is suitable for use inside the rotor tip. A temperature compensation network is located on one end of the transducer.

The nominal output of these gages is approximately 1 mv/psi per volt of excitation, and the manufacturer states that the sensitivity of these gages to inertia loads in a direction tangential to the diaphragm is about 0.05 mv/1000 "g". The wheatstone bridge is

temperature compensated in the sense that variations in resistance due to temperature changes are compensated. However, larger variations in temperature can cause expansion or contraction of the metal diaphragm and alter the signal output of the bridge. The temperature in the test cell was monitored, and was found to vary not more than 2-3° F over the 10 minute duration of a data run.

In order to reduce inaccuracies caused by possible changes in the sliprings resistance, the null-balancing of the transducer bridge must be accomplished in the circuit before rather than after the slip-rings. Rather than incorporating this complication into the circuit it was decided not to balance the bridges at no-load but rather to work with a zero offset in the transducer outputs. This was possible because the signal outputs due to the anticipated pressures were not large enough to saturate the amplifiers. Table 1 gives the sensitivity of the transducers used in the pressure measurements.

A kulite Model CQL-080-5 sub-miniature transducer was mounted flush with the rotor surface at the 90.6 percent radial station and 75 percent chord location, on the thrust side of the rotor. This transducer consists of a sub-miniature silicon diaphragm on which a fully active four arm wheatstone bridge has been bonded using solid state diffusion. The gage has an outside diameter of 0.08" and an output of 0.485 mv/psi per volt of excitation. Since he transducer is flush mounted it has a very good frequency response. This gage was primarily used to determine whether or not the pressures in the tip region of the rotor was steady. The output of this transducer was examined using an oscilloscope, and it was concluded that the surface pressure in the

tip region is essentially constant with time. Thus, the poor frequency response characteristics inherent in the cavity mounting of the Sensotec transducers did not affect the surface pressure measurements.

Data Acquisition System

A block diagram showing the details of the data acquisition system is shown in Figure 7. The output signals from the pressure transducers are led from the rotor hub through the mercury sliprings to Type 122 NEFF d.c. amplifiers. Since the signals from the transducers are very small (of the order of 0.5 mv), they are amplified 200 times. Care was taken to make sure that the amplifiers did not reach their saturation levels of 10 volts output. The amplified signals were periodically observed on an oscilloscope to make sure that the data being recorded did not contain excessive noise.

The amplified signals are routed through a 20 channel Monsanto Data Scanner to a Hewlett-Packard 2401C integrating didital voltmeter. The sampling period of the DVM was set at 0.1 seconds to make sure that the data were averaged over at least one revolution of the rotor blade.

Each of the amplified signals was displayed on the voltmeter and directly recorded with a Hewlett-Packard 2114B digital computer. The other parameters of the data run, such as RPM, ambient pressure Pa, ambient temparature Ta, Day, Time, Run Number and the locations of six open pressure orifices were manually input to the computer through a teletype. After each data run, the complete data were transfered from the H.P. 2114 B computer on-site to a central H.P.

2100 digital computer using the Satellite Communicative Executive (SCE) System software. The data were examined for consistency before transfer, and were stored on disc using a H.P. 7900 A Disc Drive in conjunction with the H.P. 2100 computer.

CHAPTER IV

EXPERIMENTAL PROCEDURE

Prior to the measurement of the surface pressures, the output of the transducers mounted in the cavities had to be calibrated. Since, at the operating RPM, the pressure transducers are subjected to very high inertia loads (of the order of 1000"g"s), the effect of these "g" loads on the transducer output had to be evaluated. The static calibration of the pressure transducers and evaluation of the acceleration correction due to the "g" loads are explained in this chapter. The test program and the data acquisition and reduction procedures are also described.

Static Calibration

Figure 8 shows a schematic of the equipment used for static calibration of the pressure transducers. An air-tight lucite box was installed over the end of the rotor blade and sealed off at its inboard end with an O-ring around the blade contour. The box was satisfactorily leak tight when properly positioned and tightened on the wing tip. This box was pressurized with nitrogen. The pressure inside the box was accurately measured with a Barocel capacitance transducer. This Barocel transducer was checked for accuracy by calibrating it with a dead weight tester. It was found that the Barocel used had a linear response and was accurate within 0.01 psi. All the pressure transducers in the rotor blade were subjected to the same pressure, the

level of which was varied between -2 psig to +2 psig. The corresponding output of the pressure transducers, after passing through the amplifier, were read using the integrating digital voltmeter. These signal outputs and the corresponding box pressures, were fed into the H.P. 2114B computer which was programmed to fit a least square curve to the transducer outputs. The response of the transducers was found to be linear (as indicated by the manufacturer). Sample static calibration data are plotted in Figure 9. The plots show the linearity and repeatability of the transducer outputs. It can be seen that the output of all the transducers was repeatable within 1.5 percent. With 3 volts excitation (the normal operating excitation) and before amplification the output of the transducer in cavity 6 was 1.337 mv/psi, while the transducers in other cavities had outputs in the range of 2.244 to 2.917 mv/psi. The static calibration was checked frequently during data acquisition period(about once every 2 days) to make sure that there was no shifting of the bridge resistances, which could result in a change in the sensitivity of the transducers.

Acceleration Correction

In the present application, the pressure transducers are subjected to a very high centripetal acceleration. When diaphragm-type pressure transducers are installed in an accelerating system, the resulting inertia loads on the diaphragm result in a diaphragm deflection, and hence an output signal, which is indistinguishable from that due to an applied pressure. Specifications supplied by the manufacturer of the Sensotec transducers state that the acceleration

sensitivity of the pressure gages is 1% of full scale output/1000 "g" when the inertia load is tangential to the diaphragm and 6% of full scale output/1000 "g" when the inertia load is perpendicular to the diaphragm. Thus, the output of the transducers due to a "g" load depends on the orientation of the diaphragm of the transducers with respect to the inertia force. The gages were carefully installed to ensure that the inertia loading due to blade rotation was tangential to the diaphragm of the transducers. At 1350 RPM, the inertia load due to the centripetal acceleration was about 1200 g's at the radiel location of the pressure gages. The magnitude of the "g" load transducer outputs was appreciable compared to the output signals due to pressure loading and in some cases it was of the same order as the pressure signals. Thus, to obtain correct pressure measurements, it was essential to evaluate the "g" correction accurately.

The method employed to establish the correction was to carefully seal off all of the pressure orifices and then to run the blade up to the operating RPM, and then to record the output of the pressure gages. This output of the gages is caused by the inertia loading on the diaphragm of the gages and the column of air trapped in the cavity.

The effect of the inertia loading on the column of air trapped in the cavity is to cause a pressure variation along the column(recall that the cavities have their long dimension along the radial direction). If there were no "g" loading, the pressure would be constant along the column and would be equal the ambient pressure trapped in the cavity. However, due to "g" loading at the operating RPM, the pressure in the

air column at the location of the transducer differs from Pa and hence changes the output signal of the transducer. This is termed the "air column effect" portion of the 'g' correction. The magnitude of the effect depends on the location of the transducer diaphragm in the cavity and the dimensions of the cavity. It is calculated as follows.

As a result of the centripetal acceleration ($\Omega^2 r$), the infinitesimal change in pressure over an infinitesimal radial length along the air column is $dp = \rho(\Omega^2 r)dr$. Then, the pressure difference between the inboard end of the cavity ($r = 1.875'$) and a general location ($r = r_1$) is

$$p_{r_1} - p_{r=1.875} = \int_{1.875}^{r_1} \rho\Omega^2 r dr$$

and, assuming ρ = constant,

$$p_{r_1} - p_{r=1.875'} = (\rho\Omega^2/2)(r_1^2 - 1.875^2) \qquad (1)$$

Using this equation for the pressure variation along the trapped air column in the cavity due to the inertia loading, the change (from Pa) in the pressure at the transducer diaphragm was evaluated. Since the location of the transducer diaphragm is identical in each cavity, this pressure correction is the same for all transducers, being -0.0132 psi at 1350 RPM and -0.0072 psi at 1000 RPM. Thus, the "air column effect" was calculated.

The determination of the correction for inertia loading on the diaphragm itself turned out to be more complicated. Since the volume of the cavities is very small, a small leak into or out of the closed

volume (because the cavities are not perfectly leak-tight) results in an appreciable change in pressure in the air trapped in the cavity, thus causing the output of the pressure transducer to vary with time instead of remaining at a constant value at constant RPM with all the orifices sealed. This time variation makes it difficult to establish the apparent pressure output due to the inertia loading on the transducer diaphragm. Although the removable rotor tip was carefully assembled and leak-checked at each step of assembly, it was not perfectly leak-tight. In addition, the tape covering the orifices did not make a perfect seal. This latter source of leak was corrected by first trying different types of tapes to seal the pressure orifices. All of them resulted in unacceptable leaks. The final solution was to cover the blade tip completely with strips of Scotch Brand Number 471 plastic tape (yellow marking tape) and then to paint the tape and a small adjoining portion of the blade with Spraylat Corporation's "Sign-Strip" paint. This strippable paint gives a thin leak-resistant plastic-like coating which is easily removable. While there were still some minute leaks round the plug threads and, at other places, the outputs of the transducers during "g" correction tests with this tape sealing arrangement did not vary too much at a fixed RPM. In most of the cases, after a small variation just after reaching the desired RPM, the output of the transducers attained a steady value at the fixed RPM. By plotting the variation with time of the gage outputs as the rotor was brought up to the desired RPM, held at that RPM for some time and then stopped quickly, it was possible to separate out the effect of the "g" loads

on the transducer diaphragm and air column from the effects of the leaks.

As a sample case, the data acquired during "g" correction evaluation tests for the pressure gage in cavity No. 4 is plotted in Figure 10. The transducer output with all the orifiecs sealed was measured at regular intervals of time as the rotor was brought up to the operating RPM from zero speed, maintained at the operating RPM for a few minutes, and then brought down to zero RPM. In Figure 10, the full lines show the variation in the pressure gage output as the rotor was either brought up from zero to the operating RPM or down to zero speed from the operating RPM. The dotted lines show the variation of the gage output when the rotor was running at a fixed RPM. The variations in this case are due to some minute leaks. Since the rotor was brought down to zero speed from the operating RPM in a very short time, the sudden drop in the transducer output during that time period is primarily due to the effect of the "g" loading on the diaphragm of the gage and on the air column trapped in the cavity. Figure 10 shows that this "g" effect varies with operating RPM, as would be expected. Similar behavious was observed for all of the other transducers. Using plots similar to Figure 10, the "g" effect on the diaphragm of the transducer and on air column was determined for transducers in each of the cavities.

The "g" correction evaluation tests were repeated many times, each time freshly sealing the pressure orifices to get a measure of the repeatability of the "g" corrections. Resulting "g" corrections for the diaphragm were -0.0913, -0.044, 0, -0.126, 0.064, and -0.041 psi respectively for the pressure gages in cavities 1,2,3,4,5 and 6 at 1350 RPM. These "g" corrections were added to the measured pressures

to get the corrected pressures. The "g" corrections were repeatable within ± 0.008 psi.

The pressure gradient due to inertia loading on the air columns within the cavities must also be accounted for in the measurement of the surface pressures if the open pressure orifice is at a different radial location than that of the diaphragm. Again using equation(1) for the variation in pressure in the cavity due to "g" loading and knowing the relative locations of the diaphragm and the open orifice, the difference between the pressure at the orifice and the pressure at the diaphragm may be calculated. This correction was applied to all of the measured pressures (pressure at the diaphragm) to get the pressure at the orifice location.

Figure 11 shows the uncorrected chordwise pressure distribution at a typical radial station together with the pressure distribution obtained after applying the "g" correction mentioned earlier. Also shown in Figure 11 are the relative magnitudes of the "g" corrections due to the effect of inertia loading on the diaphragm and on the air column for a typical case. This figure emphasizes the importance of evaluating the "g" corrections accurately. The corrected pressure distribution ($\gamma/R = 0.940$) in Figure 11 is relatively smooth and, as will be seen later, is in satisfactory agreement with two-dimensional theory.

Test Program

The objective of the test program was to get complete pressure distribution in the tip region of the rotor blade outboard of the 94 percent radius position at different blade collective pitch angles. In each data run, pressures at six different locations on the tip surface

were measured. At a number of the pressure orifice locations, the pressure was measured during two separate runs in order to check the repeatability of the data.

The pressure distributions were measured at pitch angles of 0°, 6.2°, and 11.4° at 1350 RPM, which corresponds to a tip Reynolds Number (based on chord) of 7.36×10^5 . At 1000 RPM which corresponds to a tip Reynolds Number of 5.44×10^5, the pressure distributions were measured at pitch angles of 0° and 6.2°.

Data Acquisition and Reduction

Before a data run, the blade tip region was completely sealed by covering it with tape and then one orifice into each cavity was opened by piercing it with a needle. Thus pressures were measured at six surface locations during each run. It should be noted that the small leaks which caused a problem in determining the "g" corrections were not as significant during the surface pressure measurements because the cavities were not sealed off. Preliminary tests with different tape orientations and thicknesses indicated that the measured pressures were not affected vy the presence of the tape.

Before taking data, the NEFF Amplifiers were calibrated. This was done by shorting the input to the amplifiers and zeroing the output at zero gain and at a gain of 200. This calibration of the amplifiers was repeated periodically during the data acquisition period. Some of the pressure transducer output signals were found to contain high frequency noise. This noise was suppressed by passing the signal through a low pass filter which filtered out all the noise at frequen-

cies higher than 10 HZ. Since the output signal due to the pressures was essentially steady, no significant signal was lost by this filtering.

Before starting a data run, the zero-drifts of the transducer outputs were established by recording 4 or 5 output readings from each of the pressure gages at 20 second intervals. An acceptable zero drift for the transducers was taken as a change over an interval of time of one minute, of less than 1% of the anticipated pressure levels.

If the zero drifts were acceptable, after recording the transducer outputs at zero RPM, the rotor was brought up to the operating RPM in less than 30 seconds and the outputs of the six pressure transducers were measured and recorded. At least 3 readings were taken for each transducer output over a time interval of one minute in order to make sure that the output of the pressure gages were stable and repeatable at a particular RPM. The rotor was then stopped in less than 20 seconds and a few zero readings were sampled at 20 second intervals to ensure that an acceptable zero drift had been maintained. For all the measurements, the integrating digital voltmeter was set to integrate over a 0.1 second time period.

The signal output of each pressure gage was determined by subtracting the initial zero reading from the first reading taken during the run at the operating RPM, and subtracting the final zero reading from the last reading taken at the operating RPM; the average of the two differences was taken to represent the signal output of the pressure gage. After correcting for the acceleration effects ("g" correction), the data were expressed in pressure coefficient form by using dynamic head

corresponding to the ambient air density and the local blade velocity.

For every set of 6 pressure orifices, pressure measurements were made first at 1350 RPM and then on the next run at 1000 RPM. Following this, the rotor tip was retaped. This process was repeated until all of the required pressure data were obtained. In the process of filling out the pressure distribution data, repeatability checks were made. Figure 12 shows the typical repeatability of the data. It is estimated that the uncertainity of the pressure coefficient presented is less than $\pm 5\%$ except for $X/C > 0.8$ where the uncertainity is less than $\pm 8\%$.

CHAPTER V

RESULTS AND DISCUSSION

The pressure distributions measured in the tip region of the rotor blade are discussed in detail in this chapter. Some of the available theortical results for the flow in the tip region of the rotor blade are compared with this experimental data. The pressure distribution data are also compared with the results of flow visualization studies[2] made very near the tip of a rotor blade, and with available experimental data for the case of flow around wing tips.

The complete pressure data taken in the course of this study are tabulated for reference in Tables 2 through 8. The data are expressed in pressure coefficent form using ambient air density and local blade velocity. The column headed Row 1, Row 2, and Row 3 under "Flat Tip" refer to the pressures measured on the flat tip of the rotor. Row 1 is located 0.0375 chord lengths above the chord line; Row 2 along the chord line; and Row 3, 0.0375 chord lengths below the chord line. The values in the tables represent an average of all the data taken at a particular location.

It was found that the pressure distribution on the tip was essentially the same (within experimental error) at 1000 RPM and 1350 RPM. Thus, only the results at 1350 RPM are discussed in detail.

Figure 13 shows the measured chordwise pressure distribution at 0° pitch angle and 1350 RPM at six different radial locations ranging from $r/R = 0.940$ to $r/R = 0.995$. Because of the symmetry

at 0° pitch angle (seen from pressure measurement made on both the upper surface and the lower surface at a few locations), detailed pressure measurement was made only on the upper surface. Figure 14 shows a comparison of the measured pressure data with theoretical solutions at r/R= 0.940 and r/R = 0.995. At the innermost section (r/R =0.940), the measured pressures agree well with conventional two-dimensional air foil theory and with the semi-infinite wing theory of Raj[24] over the first fifty percent of the chord. At the outermost station (r/R = 0.995), the agreement with the semi-infinite wing theory is good over the forward half of the surface. At both radial stations, the measured pressures are lower over the aft portion of the blade surface than those predicted by the theories. This is thought to be due to viscous effects and centrifugal pumping of the boundary layer, neither of which are taken into account in the theories. As seen in Figure 13, the suction peak on the airfoil decreases towards the tip because of a three-dimensional relief effect.

Figure 15 shows the pressure distribution on the surface of the square tip at 0° pitch angle and 1350 RPM. The data is symmetrical about the rotor chord line. A suction peak is seen close to the leading edge.

Figure 16 shows a comparison of the measured pressures with those predicted by the rotor blade-element theory of Samant[23], which takes into account of the inflow at the lifting line. The agreement is reasonable over the first sixty percent of the chord where the viscous effects neglected in the theory are small.

The chordwise pressure distribution at six radial stations at a pitch angle of 6.2° and 1350 RPM are plotted in Figure 17. An examination of this figure shows that the pressures on the lower surface increases by a very small amount with increasing radius. The suction peak on the upper surface decreases towards the tip. This is due to a three-dimensional relief effect near the tip. Outboard of r/R = 0.980 there is a second suction peak on the upper surface which is located near the trailing edge at r/R = 0.987 and which moves forward with increasing radius until it is at the 60% chord station at r/R = 0.995, the outermost radial station. This suction peak is associated with the primary tip vortex. The flow rolls up around the tip and spills over onto the upper surface because of the large pressure gradient which exists between the upper and lower surfaces at the tip. This flow from the lower surface to the upper surface results in the formation of a vortex on the top surface of the tip region. (See Figure 18, taken from Ref. 2.) Coincident with its formation, the local velocities are increased and the surface static pressures are decreased, forming a second suction peak.

Figure 19 shows constant pressure contours on the upper surface of the rotor blade at a pitch angle of 6.2° and 1350 RPM. The values shown on the contours indicate pressures (in psi) above or below ambient pressure. The isobar pattern indicates that the tip vortex is centered (i.e. has its maximum pressure effect) at about the 60% chord station at r/R = 0.995 and then moves inboard and aft. This behaviour is also shown in the movement, with r/R, of the second suction peak in the chordwise pressure distributions (Figure 17). The radial flow along

the blade tip (from regions of higher pressure to lower pressure) is inboard over approximately the first 40% of the surface, outboard from about 40% to 75%, and then inboard again. These changes in radial flow direction are due to the presence of the tip vortex on the upper surface, as is illustrated schematically in Figure 19.[2]

The pressure distributions on the surface of the square tip at 6.2° pitch angles at 1350 RPM are plotted in Figure 20. The pressure distribution along the chord line (Row 2) is very similar to the one measured at 0° pitch angle in that it also shows a suction peak near the leading edge. Along the upper row (Row 1) over the first 25% of the surface, the pressures are slightly larger than the values at the same location at 0° pitch angle. At the corresponding location along the lower row (Row 3), the pressures are lower than the values at 0° pitch angle.

The chordwise pressure distributions at six radial locations at a pitch angle of 11.4° and 1350 RPM are shown in Figure 21. Except at r/R = 0.995, the pressure distributions plotted are all on the upper surface. On the lower surface at r/R = 0.995, the pressure distribution is similar to that at the same location at 6.2° pitch angle and does not yield any new information. For this reason, pressure measurements on the upper surface of the blade were emphasized at 11.4° pitch angle.

As in the case for a 6.2° pitch angle, the effect of the primary tip vortex at a pitch angle of 11.2° is seen as a second suction peak on the upper surface at r/R=0.980 and at the three other radial locations outboard of r/R = 0.980. The pressure distributions show that the second suction

peak is located near the trailing edge at r/R = 0.980 and progressively further forward at increasing radii until it is located at the 45% chord station at r/R = 0.995. When these chordwise pressure distributions are compared with those for a pitch angle of 6.2°, it is seen that the primary vortex moves towards the blade leading edge with increasing pitch angle. It is also noticed that the effect of the primary tip vortex is measurable further inboard with increasing pitch angle. This latter observation confirms that the primary tip vortex is stronger at higher pitch angles.

Examining Figure 21 further, it is seen that at r/R = 0.995 there is a decrease in pressure aft of the second suction peak which was not present at θ=6.2°. This behavior is not observed inboard of r/R= 0.995 at θ=11.4°. It is probably associated with a small secondary vortex located very near the rotor tip and centered near the trailing edge (about 73% chord). Flow visualization studies and pressure measurements over the surface very near the tip of a fixed wing at 12° angle of attack (Refs. 6,7) have shown the presence of a secondary vortex near the trailing edge very near the tip (See Figure 22, taken from Ref. 7).

Constant pressure contours on the upper surface of the blade at θ=11.4° and 1350 RPM are shown in Figure 23. The primary vortex is seen to be centered at approximately the 45% chord station at r/R= 0.995 and moves inboard and aft as was the case at θ=6.2°. The same flow direction pattern is observed at θ=11.4° as at θ=6.2°. At θ=11.4° the radial flow on the upper surface as deduced from pressure distribution is inboard from the leading edge to about the 30% chord, outboard

from there to about the 70% chord, and then inboard again.

The chordwise pressure distributions measured at 1000 RPM and at pitch angles of 0° and 6.2° are shown in Figures 24 through 27. It is seen that the chordwise pressure distribution at 1000 RPM are almost identical to those at 1350 RPM. The chordwise locations of the suction peaks are unchanged, and only minor variations are observed in the pressure distributions. Figures 28 and 29 show a comparison of the pressure distribution taken at 1350 RPM and 1000 RPM for pitch angles of 0° and 6.2° respectively. From these figures, it is seen that the Cp values are always slightly lower at 1350 RPM than at 1000 RPM. However, the differences in Cp are very small (less than 0.06) and could be due to small errors in the pressure measurement or in the evaluation of the "g" corrections. Thus, the effect on the pressure distribution of changing the Reynolds number from 5.44×10^5 to 7.36×10^5, for $\theta=0°$ and 6.2° is seen to be very small. A larger variation of Reynolds number was not possible in the study. The lower limit on RPM was determined by the transducer sensitivity and the rotor exhibited vibration problems at an RPM much in excess of 1350.

The pressure data discussed in the preceding paragraphs were examined and the results compared with flow visualization studies (Ref. 2) made very near the tip of a rotor blade. The flow visualization technique consisted of bleeding ammonium vapour through orifices on the rotor, the surface of which was painted with diazonium salt solution. These flow visualization studies gave an indication

of the local flow direction at the surface of the blade. The results showed the presence of vortices on the upper surface of the rotor near the tip and also on the flat end of the blade. The local flow direction inferred from the pressure contours of the present study (Figure 19 and 23) agree with the flow directions at the surface observed in Ref. 2. The first point along the chord at which the radial flow near the blade tip suddenly changes direction is attributed in Ref. 2 to the inception of the tip vortex. The points of vortex inception in the pressure distributions (interpreted in the constant pressure contours as being the chordwise location at $r/R = 0.995$ where the radial pressure gradient changes sign) agree with the locations of vortex inception in Ref. 2. The flow visualization studies also indicated that the points of vortex inception move forward towards the blade leading edge with increasing pitch angle. From the measured pressure distributions at $\theta=6.2°$ and $11.4°$, the same trend is noted. At $\theta=6.2°$, the pressure data indicate vortex inception at 40% chord while the results presented in Ref. 2 show the point of vortex inception to be at about the 44% chord station. At $\theta = 11.4°$, the pressure data indicate vortex inception at the 28% chord station while flow visualization (Ref. 2) indicates the 33% chord station.

The surface pressure measurements reported here were also compared with measurements made near the tip of a fixed wing (References 6,7, 8). The wing surface pressure measurements, which were on an NACA 0015 profile, indicated the presence of a primary and secondary vortex near the tip at an angle of attack of 12°. The same phenomena were observed in the present rotor tests with an NACA 0012 profile at

a pitch angle of 11.4°. However, in the present study of the rotating blade the primary suction peak is further aft than that measured for the fixed wing. The fixed wing chordwise pressure distribution data (Refs.6,7) showed that at the outermost radial location (Y/C=0.022) the primary tip vortex was located near the 36% chord, whereas for the rotor case, at the outermost radial location(Y/C=0.024), the primary tip vortex was located at about the 45% chord station. The primary vortex extends inboard by almost the same distance (in Y/C) in both cases.

CHAPTER VI

CONCLUSIONS AND RECOMMENDATIONS

On the basis of the results obtained from the detailed surface pressure measurements in the tip region of the model rotor blade in hover, the following conclusions are drawn:

1. The surface pressure distributions indicate the presence of a primary vortex on the upper surface of the blade in the tip region.
2. At a collective pitch angle of 6.2°, the primary vortex is located above the upper surface near the trailing edge at r/R= 0.987 and progressively further forward at increasing radii until it is at r/R= 0.995 at the 60% chord station. With increasing blade pitch angle, the point of inception of the primary vortex moves toward the leading edge of the rotor blade. With increasing blade pitch angle, the peaks in the pressure distributions caused by the primary vortex spread further inboard.
3. The magnitude of the peaks in the pressure distributions increases with increasing blade pitch angle, indicating that the primary vortex is stronger at higher pitch angles.
4. At a pitch angle of 11.4°, the pressure measurements indicate the presence of a small secondary vortex on the upper surface which is located near the blade-tip and near the trailing edge (approximately 73% chord).

5. The effect of a change in Reynolds number from 7.36×10^5 to 5.44×10^5 does not significantly influence the pressure distributions near the tip, for blade pitch angles of both 0° and 6.2°.
6. The pressure contour plots will be helpful in defining the tip vortex geometry in the blade tip region where little other information is available for guiding the development of theoretical analyses.
7. The points of vortex inception inferred from the pressure data are in good agreement with those noted by other investigations using surface flow visualization techniques.
8. At 0° blade pitch angle there is good agreement between the measured pressure data and that predicted from semi-infinite wing theory (rounded tip) over the forward half of the blade surface where viscous effects, which are not considered in the theory, are small.
9. Comparing the measured pressure data with the pressure distribution on the tip surface of a fixed wing(NACA 0015 airfoil), the trend of the pressure distributions in both cases was observed to be the same.

Based upon knowledge gained in the present study, the following recommendations are made:

1. Detailed surface pressure measurements on the tip surface of a rotor blade with a rounded tip should be made. This will yield data for comparison with results from a theoretical analysis which, for simplicity, uses a body-of-revolution

tip model.

2. The same rotor blade should be tested in a wind tunnel as a fixed wing to obtain the detailed surface pressure distributions at the tip. Then, a comparison should be made to study the differences in pressure distribution on the rotor blade tip and the wing tip. This should provide insight into the applicability of fixed wing data to the problem of a rotating blade.
3. Detailed flow visualization studies should be carried out to gain more insight into the flow behaviour in the tip region of a rotor blade.
4. Detailed pressure distribution measurements should be made at a few more blade pitch angles in order to more precisely determine the effect of pitch angle on the inception point of the tip vortex.
5. Attempt should be made to model the primary and the secondary vortex in potential flow (in the tip region of a rotor blade), to see if the results from theory would be in agreement with measured pressures.

PART TWO

VELOCITY MEASUREMENTS IN THE ROTOR WAKE

CHAPTER VII

EQUIPMENT AND INSTRUMENTATION

In order to investigate the velocity distribution in the wake of a hovering blade, it is necessary to determine instantaneous velocity components at different locations in the wake. A vector anemometer system was used to measure these velocity components. An actuator system that would poisition the anemometer probe accurately was fabricated and installed in the helicopter test cell. The details regarding the vector anemometer system and the actuator are presented in this chapter, which concludes with a description of the data acquisition system.

Total Vector Anemometer System

A Thermo-System, Inc. Model 1080 total vector anemometer system was used to measure the instantaneous velocity components in the rotor wake. The anemometer system consists of a Model 1296F probe, Model 1082 control circuit, a Model 1081 regulator, and a Model 1088-3 chassis. Figure 30 shows the anemometer probe and the chassis which is a cabinet containing the internal wiring for the control circuit and the regulator. The control circuit contains the anemometer bridges, amplifiers, balance potentiameters, and output pin jacks. A schematic drawing of the probe is presented in Figure 31.[25]

The velocity-sensitive element of the anemometer probe consists of three quartz rods on each of which is mounted a split-film sensor.

The three sensors form a mutually perpendicular array with each sensor inclined at an angle of 54.73 degrees with respect to the probe axis. The platinum films are approximately 1000 angstroms thick and 0.08 inches long and are coated on the 0.2 inches long, 0.006 inch diameter cylindrical quartz rods. A thin coat of quartz over the films provides environmental protection. The platinum film on each rod consists of two segments, each segment covering approximately 180° of circumference on the rod. The orientation of the platinum segments on each rod is such that it allows the determination of the octant in which the instantaneous velocity vector is located. The heat flux distribution around the sensor is the key to the actant detection system of this split-film sensor. For any inclination of the velocity vector with respect to the sensor, the ratio of the heat flux on the downstream segment of the split film to the heat flux on the upstream segment is always less than 1. This result is made use of in the date reduction. In order to minimize support interference, the three sensors are each attached at only one end to a long, thin supporting structure. When not in use, the sensors are protected by a retractable aluminum shield.

The anemometer furnishes six simultaneous velocity-dependent voltages as outputs. These voltages allow the computation of the magnitude and direction of the instantaneous velocity vector over the complete solid angle. Calibration constants for each individual anemometer and a set of data reduction equations are supplied by the manufacturer. The published characteristics[25] of the vector anemometer system are as follows:

Frequency response:	DC to 1000 Hz
Usable velocity range:	0 to 300 ft/Sec (Air, atmospheric pressure)
Magnitude accuracy:	± 3% of Reading and ± 0.1% of full scale, 0-150 fps
Direction accuracy:	within 3° over the complete solid angle (4 Steradians)
Spatial resolution:	The three orthogonal sensors fit within a 0.3 inch diameter sphere.

Further information on the anemometer and its operation is available in Ref. 25.

Actuator

In order to make velocity measurements at various locations in the rotor wake, the anemometer probe had to be positioned rigidly and accurately at various locations in the wake, preferably while the rotor was running. This was accomplished by fabricating an actuator which could vary the axial and radial coordinates of the probe with respect to the rotor axis by remote control from outside the test cell. Figure 32 shows the actuator as installed in the test cell.

The actuator consists of a vertical tube which is mounted on two carriages. These carriages are fitted with gears and move on racks which are aligned in the axial and radial directions. The actuator is moved remotely by using flexible shafts which are connected to drive gears. Two high-turn potentiometers located on the traversing carriages and connected to the gears are used to indicate the position

of the anemometer probe by means of voltage drops across the resistance of the potentiometers. These voltage drops, which were calibrated with respect to the location of the carriages, give the position of the anemometer probe by means of a digital voltmeter readout. The error in location of the probe was less than $\pm$ 0.03 inches.

The vertical position of the anemometer probe is manually adjustable. The pitch and Yaw orientations of the anemometer probe are also manually adjustable.

Data Acquisition System

The data acquisition system for this experiment had to be capable of recording six velocity-dependent voltages from the anemometer system simultaneously. It was also decided to have the capability to record voltages at every 1 degree interval of the rotor blade azimuth position and to store the resulting large quantity of data in an easily accessible form. These requirements were met by assembling a data acquisition system consisting of a 6-channel analog-to-digital converter, a shaft angle encoder and mini-computers with disc storage capability.

A block diagram showing the details of the data acquisition system is given in Figure 3.3. The six voltage signals from the anemometer system are fed into the 6-channel analog-to-digital (A/D) converter where the signals are converted into digital form. The 8-bit A/D converter which was designed and built at the School of Aerospace Engineering, has an unavoidable quantizing error of $\pm$19.5 millivolts. The range of the A/D converter is 0-10 volts, and the conversion time

20 μ seconds. The A/D converter has a sample and hold circuit to facilitate simultaneous measurement of the six voltage outputs from the anemometer system.

The shaft angle encoder (made by Sequential Information Systems Inc.) was driven by the rotor shaft through a timing belt and rotated at the same speed as the rotor. The shaft encoder produces voltage pulses at every one degree rotation of the rotor. It also provides a voltage pulse whenever the rotor blade passes through an arbitrary zero degree azimuthal position. These pulses were fed into the A/D converter. Using these pulses, starting at the zero degree azimuth position of the rotating blade, the 6 analog voltages are recorded at predetermined increments of the rotor blade azimuth position and the digitized voltages are fed into the Hewlett-Packard 2114B mini-computer.

Because of the limited memory capacity (8K) of the H.P. 2114B mini-computer, a large quantity of data can not be stored at the test site. Accordingly, after each run the digital data for that run were transferred to a Hewlett-Packard 2100 computer using the Satellite Communicative Executive System (SCE System) software. The SCE System Software was specially designed and written to transfer, at a rapid rate, the large amount of data which was generated. Using the SCE System, the data were transferred at the rate of about 50 computer words per second, the speed being limited by the disc-drive.

The data were stored on disc using a H.P. 7900 A disc drive which was connected to the H.P. 2100 computer. Storing the data on discs gave very easy access to the large quantity of data and made data reduction much easier.

CHAPTER VIII

EXPERIMENTAL PROCEDURE

Prior to using the total vector anemometer system for measurement of instantaneous velocities in the rotor wake, the anemometer system had to be evaluated. In addition, some exploratory tests were conducted to assess the suitability of using the total vector anemometer to measure instantaneous velocities which could be varying at a rapid rate. Information regarding the evaluation of the anemometer, the calibration of the A/D converters, and the exploratory tests are given in this chapter. The test program and the data acquisition and reduction procedures are also described.

Evaluation and Calibration of the Equipment

(A) Total Vector Anemometer System

Since the anemometer system was to be used in the present study to measure instantaneous velocities in the rotor wake where the flow directions would be constantly changing, it was decided to conduct several tests in the Georgia-Tech nine-foot wind-tunnel in order to determine the accuracy of the anemometer system. Details about these wind tunnel tests and the results of the tests are given in Appendix B.

These calibration tests revealed that the accuracy of the velocity measurements made using the anemometer system is strongly dependnet

upon the orientation of the probe with respect to the main flow direction. The best accuracy was obtained when the probe shank was aligned closely to the flow direction. Only with this orientation of the probe did the measured data give results consistent with the stated accuracy of the anemometer system. At other orientations of the probe, especially when the probe shank was inclined at an angle of 30 degrees or more to the flow direction, large errors in the measured velocity directions were noted. Two sample calibration plots are shown in Figures 34 and 35.

The accuracy of the anemometer system obtained from the calibration tests was as follows

Velocity magnitude error	± 6% of reading
(Velocity range: 10 to 30 ft/sec)	
Angular error	
(a) Probe shank aligned with flow	± 6 degrees
(angle less than 30 degrees)	
(b) Probe shank at > 30° to flow	+ 15° to -20°

No definite pattern was observed in the velocity direction errors and hence no emperical correction of the measured data was feasible.

One of the objectives of the present study was to obtain information regarding the geometry and strength of the vortex sheet shed inboard of the tip at the trailing edge of the rotor blade. Because of the large angular errors encountered in the velocity measurements, no quantitative information about the strength of the vortex sheet could be obtained. Whereas, to obtain the vortex sheet location, the rapid

changes in the magnitude and direction of the velocity are more important than their exact values. Thus the angular errors in velocity measurements, mentioned above, should not affect the present results with respect to the geometry of the vortex sheet. Because of these reasons, the emphasis in the present study was mainly on measuring the geometry (location) of the vortex sheet.

In the inner wake region ($r/R < 1$) the resultant velocity vector has a large component in the axial direction. Since, during velocity measurements the probe shank was parallel to the axial direction, it was aligned close to the main flow direction. The change in velocity associated with the passage of the vortex sheet was not large and hence, it is believed that the probe shank was aligned less than 45° to the flow. Thus, the velocities measured in the inner wake region are not expected to have very large angular errors.

In the tip vortex region the change in velocity associated with the passage of tip vortex was large, and hence very large angular errors are expected in the measured velocities. Since the changes in velocity associated with tip vortex passage are large (of the order of 50 ft/sec), the location of the tip vortex could be obtained fairly accurately.

(B) Analog to Digital Converters

Six Burr-Brown, analog-to-digital converters were used to obtain a digital output from the 6 voltage outputs of the anemometer system. It was found during initial trials that the output of the A/D converters were not linearly proportional to the analog input. Therefore, all of the 6 A/D converters were calibrated by applying a known voltage to the

input and recording the corresponding digital outputs. The variations from the expected linear output of the A/D converters were larger than the unavoidable quantizing error of 19.5 milli-volts. The outputs, in fact, varied from the inputs by 0.04 to 0.30 volts. A typical non-linear output of one of the A/D converters is shown in Figure 36. This nonlinear behaviour was different for each one of the A/D converters. Since a change in voltage of 0.1 to 0.2 volts can change the velocity vector direction by 5 to 10 degrees, this non-linear behaviour of the A/D converters had to be accounted for in the data reduction by incorporating curve-fitting routines to infer the correct voltage outputs from the A/D converter outputs. The calibration curves for the A/D converters were checked frequently during the data acquisition period in order to insure that this non-linear behaviour did not vary with time.

Two of the six A/D converters showed a digital output of zero volts when the analog input was in the range 5.09 to 5.18 volts. This was due to a malfunctioning of the A/D converters which could not be corrected. The voltage outputs of the anemometer system were always greater than 3 volts. It was assumed in the data reduction that when the A/D converter indicated zero output, its actual output was 5.14 volts. This assumption can result in a maximum error of less than 5° in velocity direction.

Exploratory Tests

Before making detailed instantaneous velocity measurements in the rotor wake using the total vector anemometer system, many exploratory tests were conducted to study the flowfield in the wake of the hovering

rotor and to assess the suitability of using the total vector anemometer. Also, several trial data runs were made to determine some of the parameters required in the final detailed measurements. These exploratory tests are discusses in this section.

(A) Hot Wire Anemometer Data

According to the manufacturer of the split-film total vector anemometer, the film's characteristic small time constant gives a frequency response up to 1000 HZ for the anemometer system. However, one of the other investigators[26] who used this system states that the anemometer system has a lower frequency response. Since the vector anemometer system was to be used for measuring instantaneous velocities in the wake of the hovering rotor at 1000 RPM, it was necessary to make sure that the frequency response of the vector anemometer was adequate to record accurately the rapid changes in the wake velocities with time. For this reason, it was decided to make some velocity measurements in the rotor wake at a few locations using a hot-wire anemometer which has much higher frequency response, and to compare the fluctuations in velocity measured using the hot-wire anemometer with the fluctuations in velocity measured using the total vector anemometer system at the same locations. If the frequency response of the hot film anemometer is not adequate to measure the rapidly changing velocities, the fluctuations in velocities measured using the hot-film anemometer will be smaller than those measured using the hot-wire anemometer.

A Model 900-1 constant temperature hot-wire anemometer (Flow Corp.) was used to measure the instantaneous velocities in the wake. The hot-

wire anemometer has a frequency response of 2500 Hz. The hot-wire probe (along with the 900-1 anemometer system) was calibrated in the Georgia Tech low turbulence wind tunnel in order to generate a curve of voltage output versus flow velocity.

After calibration the hot-wire probe was mounted in the rotor wake at several locations. The hot-wire anemometer output is always proportional to the velocity component perpendicular to the hot-wire filament. Thus, when the probe was mounted such that the hot-wire filament was parallel to the radial directions, the output of the hot-wire was proportional to the vector sum of the velocities in the axial and tangential directions.

At an axial distance of 3 inches from the rotor plane, the hot-wire probe was positioned at different radial locations. At each location of the probe, the hot-wire filament was oriented in both radial and axial directions and, at 1000 RPM, the voltage output of the hot-wire anemometer was recorded at every 6° interval in blade azimuth angle over two revolutions of the rotor. Then, using the calibration curve for the hot-wire anemometer, the fluctuations in velocity over the two revolutions were plotted. These velocity fluctuations were studied and compared with velocity fluctuations obtained using the vector anemometer system at the same locations in the rotor wake. It was observed that the hot-wire anemometer data showed velocity fluctuations of the same order and type as seen in the velocity data measured using the total vector anemometer system.

Thus, it was concluded that the frequency response of the total vector anemometer system was adequate for measurement of velocity fluctuations, like discontinuities across the vortex sheet and tip

vortex region.

(B) Blade Pitch Angle and RPM

Using the total vector anemometer, the instantaneous velocity variations with respect to the blade azimuth position were measured at selected locations in the rotor wake for blade pitch angles of 6.2° and 11.4° and at 1000, 1200, and 1350 RPM. After examining these velocity data carefully it was concluded that the peaks or the discontinuities in the instantaneous velocity variation with blade azimuth position, were almost the same magnitude for bothe blade pitch angles of 6.2° and 11.4°. The presence of the vortex sheet or the tip vortex was not seen more consistantly or more clearly at one pitch angle than at the other. Since the flow-visualization studies in the test cell (Appendix A) had been carried out at the 6.2° blade pitch angle, and since it was known that the flow in the test cell was stable at that pitch angle, it was decided to make the detailed velocity measurements at the blade pitch angle of 6.2°.

Representative instantaneous velocity measurements made at 1000, 1200, and 1350 RPM showed that there was no significant increase in the magnitude of peaks or discontinuities in the instantaneous velocity distributions either across the vortex sheet or in the tip vortex region with increase in RPM. The general noise level (random fluctuations) in the velocity distributions was of the same order of magnitude for all three RPM values. Therefore, it was decided to make the detailed velocity measurements at 1000 RPM.

(C) Determination of Measurement Interval for Velocity Data.

Before making detailed velocity measurements, it was necessary to decide on the measurement interval (in degrees of blade rotation) to be used. The interval should be small enough so as not to miss any significant velocity changes which may be occuring in short time intervals. At the same time, the interval should not be unnecessarily small, because the smaller the interval the larger will be the amount of data to be handled.

With the above thoughts in mind, the instantaneous velocity variation with blade azimuth angle (ψ) was measured at intervals ($\Delta\psi$) of 1°, 2°, and 6° at representative locations in the rotor wake. After examining these velocity variations carefully, it was concluded that there were no significant differences in the velocity data obtained with these three measurement intervals. Thus, it was decided to make the detailed velocity measurements at intervals of 6° in blade rotation.

Test Program

The selected test conditions of 6.2° blade pitch angle and 1000 RPM corresponds to a thrust coefficient (C_T) of 0.0026 and a blade tip speed of 209.4 ft/sec.

The velocity measurements were made at five axial locations at z/R values of -0.078, 0.0625, 0.125, 0.250 and 0.375. All velocity measurements were made along one particular radius, which corresponds to the arbitrarily selected blade azimuth angle (ψ) of zero degrees. Since the flow is cyclic with blade position in the hover mode, it was not considered necessary to make velocity measurements along other radii.

Figure 37 shows the rotor coordinate system and also the location of the stations where the velocity measurements were made. The measurements were made at one inch intervals in the radial direction outboard of r=10 inches.

Data Acquisition

Preliminary check-out

Before taking data, the acquisition system used in recording the total vector anemometer output had to be checked to make sure that the data were recorded correctly even though they were generated at a very rapid rate. To accomplish this, a sinewave generator was used to input a known sinusoidal voltage to the A/D converters. The rotor then was brought up to operating RPM in order to provide the proper trigger, and the digital outputs from the A/D converters were recorded at every 6° interval in blade azimuth angle. These output voltages were plotted to make sure that they showed the same variation as the known sinusoidal input. This test was repeated each time the location of the probe was changed.

As a check on possible contamination or damage to the probe sensors, measurements of the zero-velocity output of each data channel were made for comparison with the values supplied by the manufacturer. In addition, a short calibration check was performed using the calibration equipment built into the anemometer system. This calibration was performed at the start of each day and the zero-velocity check was made before each data run.

Data Runs

The anemometer probe tip was manually set to the required spatial location using the remotely controlled actuator. Ambient pressure and temperature then were recorded. Finally, the rotor was brought up to the desired RPM and the voltage outputs of the total vector anemometer and the corresponding azimuthal location of the rotor blade were recorded using the H.P. 2114B computer. After each run, the data recorded in the H.P. 2114 B computer was transferred to the H.P. 2100 computer where it was stored on disc.

Data Acquisition Programs

At each location of the anemometer probe, three different velocity measurement approaches were employed, each having a separate data acquisition program. The three approaches were as follows:

(1) Measurement of the instantaneous velocity at a 6° measurement interval over 10 continuous revolutions of the rotor

(2) Measurement of the instantaneous velocity at a 6° interval over 4 revolutions of the rotor, with a 4 second time interval between the measurement revolutions.

(3) Measurement of a mean velocity by recording anemometer voltage outputs averaged over 40 revolutions of the rotor at each azimuthal location of the blade.

Data Reduction

The voltage data stored on disc were reduced to get the instan-

taneous velocity components in the axial, radial and tangential directions using the reduction methods and calibration constants supplied by Thermo Systems, Inc. Details regarding the data reduction procedure are given in Appendix C.

At each location of the probe, the instantaneous velocity components measured during each run were computer plotted against the corresponding blade azimuth location in order to determine the passage of either the vortex sheet or the tip vortex as evidenced by peaks or discontinuities in the velocity history.

For each run, the instantaneous velocity components at every azimuth position were averaged over the number of revolutions available in that run in order to minimize the effects of turbulence and other random disturbances. These averaged velocity components also were machine plotted against the blade azimuth location.

CHAPTER IX

RESULTS AND DISCUSSION

To facilitate the discussion of the velocity data, a brief summary of the fundamental characteristics of the hovering rotor wake is given first.

A schematic of the wake from a single-bladed rotor in hover (reproduced from Ref. 27) is shown in Figure 38. The wake contains two main features. The first is the strong tip vortex, which arises from the rapid rolling up of that portion of the vortex sheet shed from the tip region of the blade. The second feature is the vortex sheet which is shed from the inboard sections of the blade. The axial (i.e.vertical) transport velocity near the outer end of the vortex sheet is much greater that of the tip vortex. The axial velocity of the vortex sheet decreases with decreasing radial location of observation. These characteristics of the vortex sheet largely result from the velocities induced by the strong tip vortex.

In discussing the wake geometry, the radial and axial wake co-ordinates are expressed as functions of the wake azimuth angle ψ. In a fixed co-ordinate system, which is the co-ordinate system of the velocity measurement made here, the value of for any vortex point(i.e. a point either on the vortex sheet or on the tip vortex) in the wake is the azimuth angle through which the blade has rotated from the time the vortex point was generated at the blade to the time when the vortex point reaches the fixed measuring station in the wake. Figure 39 shows a sche-

matic of the cross section of the near wake vortex system.

When instantaneous velocities are measured in the wake at any location, the variation of these velocities with respect to the blade azimuth angle (ψ) will indicate the passing of the vortex sheet or the tip vortex across the probe sensors as evidenced by discontinuities or peaks in the velocity variations with ψ. From such velocity data, then, one can deduce the vortex sheet and tip vortex locations.

Vortex Sheet

From the instantaneous velocity measurements in the inner wake region ($r/R < 1$), the vortex sheet azimuth angle is obtained for each location of the probe.

Figure 40 through 43 show some sample results for the distribution of instantaneous velocity components across the vortex sheet at different axial distances from the rotor plane. In these velocity plots, the passing of the vortex sheet across the anemometer sensors is seen either as a peak (a steep increase in one direction which decreases immediately; can be either positive or negative) or a discontinuity (a rise in one direction immediately followed by a steep fall in the opposite direction).

Examining the tangential velocity data in the above-mentioned plots, it is noticed that the passing of the vortex sheet across the probe sensors is seen as a positive peak in the tangential velocity distribution. This positive peak implies that the fluid elements in the vortex sheet have a higher tangential velocity than the other fluid elements in the wake. This is expected, because the vortex sheet shed at the trailing edge of the rotor blade is primarily formed from the boundary layer on the blade surface. Because of viscous effects, the fluid elements

in the boundary layer and hence in the vortex sheet will have a high velocity in the direction of blade rotation. The blade azimuth angle (ψ) corresponding to the positive peak in tangential velocity distribution is taken as the azimuth angle of the vortex sheet at that particular measuring station.

Now consider the radial velocity component as seen from Figure 39. As the vortex sheet passes across the probe sensors the radial velocity component measured by the probe should increase and then decrease sharply, forming a discontinuity in the radial velocity distribution. In the near wake region (small z/R), the vortex sheet is almost parallel to the rotor plane and an appreciable discontinuity in the radial velocity distribution would be expected as the vortex sheet passes across the probe sensors. These discontinuities are clearly seen in the radial velocity distributions in Figure 40 thorugh 42. Another way of interpreting the radial velocity distributions in these figures is that the radial velocity component becomes larger inward and then suddenly larger outward (although not necessarily accomplished by a sign change) as the vortex sheet passes across the probe sensors. Thus, the azimuth angle of the vortex sheet at a particular location in the wake is obtained from the position of the discontinuity in the radial velocity distribution at that particular station.

Returning again to Figure 39, consider the axial velocity component. As the vortex sheet passes across the probe sensors the measured axial velocity should first decrease and then show a sharp increase. In the near wake region, where the vortex sheet is almost parallel to the rotor plane, the axial velocity discontinuity across the

vortex sheet is small. In addition since there is already a large axial component of velocity in the wake, the discontinuity in the axial velocity distribution due to the vortex sheet is not expected to be prominent, and the axial velocity discontinuity shown in Figures 40 through 42 is small compared to the radial velocity discontinuity. In some cases, the axial velocity discontinuity was so small that it was not observable in the axial velocity distribution plots. Thus, the azimuth angle of the vortex sheet at certain locations in the wake cannot be obtained from axial velocity distribution plots alone.

The azimuth angle, ψ of the vortex sheet at a particular measuring station as obtained from the tangential, radial, and axial velocity distributions are essentially the same; the differences between them are at most 5° in azimuth angle. The usual practice was to abtain from all the three velocity distributions and then take the average of these three values.

In Figures 40 through 42, the azimuth angle, ψ of the vortex sheet is clearly evident from either the peak in tangential velocity or the discontinuity in radial velocities. Beyond $z/R = 0.375$, there is no clear indication of a peak in tangential velocity distribution. This is thought to be due to viscous diffusion of the vortex sheet at larger z/R, and also instabilities in the far wake.

In Figure 40, the instantaneous velocity distributions across the vortex sheet at different radial stations for a fixed axial distance from the rotor are shown. These plots indicate that the azimuth angle of the vortex sheet is 100° at $x=0.542$, 80° at $x=0.667$ and 60° at $x=0.791$. Thus it is seen that the outboard end of the vortex sheet has a greater axial

transport velocity than has the inner end.

Figure 44 shows a sample plot of the velocity distributions across the vortex sheet when the instantaneous velocity components at each azimuth location have been averaged over 10 consecutive revolutions of the rotor. This averaging should cancel out most of the random fluctuations in the velocities due to turbulence and other disturbances. Thus, the discontinuities in velocity components due the passage of the vortex sheet, which repeats every revolution, whould be more pronounced when the averaged velocity components are plotted versus ψ. Comparing Figures 44 and 41, it is observed that the random velocity fluctuations are less in the case of averaged velocities but the discontinuities or peaks due to the passage of the sheet are smaller for the averaged case. This is to be expected because, when the velocity components are averaged, unless the vortex sheet passage exactly repeats in each revolution, averging the velocities will average out some of the effects of the vortex sheet on the velocity distributions. Although this comparison of two figures suggests that the vortex sheet passage is not repeating a detailed study of the instantaneous velocity distributions across the sheet for 10 consecutive revolutions , in many runs, indicated that the vortex sheet passage was repeating within $\pm 5°$ in ψ. Instantaneous velocity data taken over 4 revolutions of the rotor, with a 4 seconds time interval between them, also indicated that the vortex sheet passage was repeating within about $\pm 6°$.

It can be concluded that the averaged data give the azimuth angle of the vortex sheet with little better accuracy than the instantaneous

data. It can be thus said that the different dataacquisition procedureused in obtaining the data (done with the idea of getting different kinds of averaged velocities), do not provide any new or additional information concerning the vortex sheet.

At each spatial location of the anemometer probe, the vortex sheet azimuth angle, ψ, was measured from the instantaneous data for each of the blade revolutions in a particular run at that location. The value of was also also obtained from the velocity distribution across the vortex sheet averaged for each run. The mean of all the resulting values as calculated to get the mean ψ for the vortex sheet at that spatial location. In the near-wake region, the vortex sheet passage was not detected from the velocity data measured outboard of x=0.8 or inboard of x=0.4. This is to be expected because the airfoil section shape of the rotor blade starts only at x=0.25, and also because the blade counterweight extends up to x=0.36 and creates a flow disturbance up to around x=0.4. Outboard of x=0.8 the strength of the vorticity shed at the blade trailing edge is weak. The velocity data taken outboard of x=0.8 starts to show the effect of the strong tip vortex.

Comparison of the vortex geometry obtained from the experiments with theory [23] are shown in Figures 45 and 46. The agreement between the experimental results and the theory is good considering the fact that the repeatability of the vortex azimuth angle in the experiments is $\pm 6°$.

Figures 40 and 41 show that the discontinuity in the radial velocity distribution is well defined and it appears the strength of the vortex sheet could be measured as the discontinuity in the velocity component along the direction tangential to the vortex sheet. However, in

most of the cases the discontinuity associated with the vortex sheet in the radial and axial velocity component distributions was not well defined. In some cases, it was barely noticeable. Also in the cases where it was well defined, the magnitude of the discontinuities did not repeat with different runs at the same probe locations. The above noted results about the strength of the discontinuities is probably caused by errors in measurement of velocity magnitude and direction using the total vector probe. Also, the random fluctuations caused by turbulence and other disturbances in the flow in the test cell will also affect the magnitude of the discontinuities in velocity distributions.

It should be noted that although the total vector anemometer was not very precise, the vortex sheet geometry obtained from the experimental data is satisfactorily accurate, because the determination of the vortex sheet geometry does not depend on the exact magnitude of the velocity components but rather on changes in the velocity component magnitudes and directions.

Tip Vortex

The azimuth anglesof the tip vortex (ψ) at different downstream locations in the rotor wake, were obtained from the instantaneous velocity data.

As has been explained, instantaneous velocity components were measured at different axial locations in the wake, at 1 inch intervals along a radial direction. The instantaneous velocity variations with respect to blade azimuth angle in the tip vortex region ($0.7 < x < 1.0$) were examined carefully to see the influence of the passage of the tip vortex. These velocity variations did not show any strong peaks

or discontinuities when the tip vortex passed at a large radial distance from the probe sensors. However, the velocity variations at the radial locations closest to the tip vortex passage, were characterized by either very strong velocity peaks or by very strong velocity discontinuities.

The behaviour of the axial velocity component was sometimes useful in determining the radial position of the tip vortex. There was a large change in the axial velocity with the passage of the tip vortex, depending upon whether the tip vortex passed inboard or outboard of the probe location. Thus, the radial location of the tip vortex at each axial distance from rotor blade was determined within a distance of 0.50."

The distribution of the instantaneous velocity components across the tip vortex region are plotted in Figures 47 through 50 for different axial docations. It is noted that peaks or discontinuities in these distributions are very large, of the order of 10 v_o (i.e. 75 ft/sec) compared to the discontinuities across the vortex sheets (of the order of v_o). It is seen that the passage of the tip vortex near the probe sensors is characterized by a positive peak in the tangential velocity component and a strong discontinuity in the radial and axial velocity components. The positive peak in the tangential velocity component is attributed to the fact that the tip vortex is primarily formed from the boundry layer near the tip surface of the rotor blade and hence, the fluid particles in it have a higher tangential velocity in the direction of blade rotation.

From Figures 48 and 49 it is seen that the azimuth angle of the tip vortex is around 290° for x=0.875 and z/R=0.125 where as at further

downstream position of $z/R = 0.250$ and $x = 0.83$ it is around 500°. This is because the rotor blade which generated the tip vortex at $\psi=0°$ has completed one full revolution before reaching the anemometer probe.

Figure 51 is a plot of the distribution of the averaged velocity components across the tip vortex region at $x=0.875$ and $z/R=0.125$. Comparing Figures 51 and 48, it is seen that the distribution of the averaged velocity components across the tip vortex region is characterized either by peak or by discontinuities of a smaller magnitude than those in the instantaneous velocity distributions, but random fluctuations have been suppressed. As explained earlier in connection with this vortex sheet, this behavior is attributed to the fact that averaging the velocity components tend to cancel out random fluctuations but smears out the discontinuities because the tip vortex passage is precisely repeatable.

The azimuth angle of the tip vortex at each axial position of the probe was obtained for each revolution in all the runs, and also from the averaged velocity plots for each run. The average of all of these values was obtained. A comparison of the tip vortex geometry obtained from these average values of ψ with an emperical geometry (based on smoke studies, Ref. 27) is shown in Figure 52. The agreement in the axial location of the tip vortex is very good. The radial location of the tip vortex from the present experiments does not agree well with the emperical values. It is thought that the differences in radial location are due to relatively large dimensions of the probe sensor (0.3" sphere), which could be modifying the flow locally, and changing the radial location of the tip vortex. Also, since this velocity

measurement was made at an interval of one inch (0.04R), the best accuracy expected in this radial location of the tip vortex is ±0.02 x.

Because of the relatively large dimensions of the probe sensors and this large uncertainties in the velocity measurements at the higher flow inclination angles with respect to the probe, no attempt was made to measure the velocity distribution inside of the tip vortex nor to obtain the strength of the tip vortex.

A sample plot of the variations of the instantaneous velocity components with respect to blade azimuth angle, for a point outside of the wake, in the backflow region, is shown in Figure 53. No well-defined peaks or discontinuities are observed in this velocity variations region. The velocity variations abserved are characterized by a negative mean axial velocity (averaged over all the measured angles in one revolution) and small mean radial and tangential velocities.

Figure 54 shows a sample plot of the variations of the instantaneous velocity components in the inflow region. These velocity variations are characterized by a large mean positive radial velocity denoting inflow.

Mean Velocity in the Wake

At each location of the anemometer probe in the wake and inflow region, all of the instantaneous velocity components available from all the different runs were averaged to get the mean velocity components at that location. The radial distribution of the measured mean velocity components are compared, in Figures 55 thorugh 65, with the mean velocity components abtained from a theoretical analysis [23] for the hovering rotor.

The radial distribution of the mean axial velocity of several

values of z/R is plotted in Figures 55 through 59. Figure 55 shows the radial distribution of the mean axial velocity in the inflow region (z/R=-0.0702), which is characterized by a flat distribution of the in the inboard areas with a sharp decrease as x approaches unity. This distribution is in good agreement with theoretical results. The radial distribution of the mean axial velocity at different downstream locations in the wake are plotted in Figures 57 through 60. All of those distributions are characterized by a triangular shape with a sharp gradient near the wake boundary ($x \approx 0.9$). The radial distribution at z/R=0.0625 (Figure 56) does not show good agreement with the theoretical prediction for $x \geq 0.7$. The differences with this experimental axial velocity being considerably larger than the theortical values, cannot be presently explained. At other axial locations, the agreement between the measured and theoretical values is good except for larger values of z/R, where the peak theoretical values are higher than those obtained from measurements. This difference is thought to be due to the fact that the theortical calculations do not take into account viscous effects, which tend to reduce the gradients in the axial velocity particularly near the wake boundary.

The radial distributions of the mean radial velocity component at different axial locations are plotted in Figure 60 through 62. All of the mean radial velocity distributions are characterized by a positive peak near the wake boundary, which corresponds to an inflow into the wake. The maximum value of the mean radial velocity decreases with increasing axial distance down the wake from the rotor, the highest value occuring at z/R=0.0625, which is near the maximum contraction of

the wake. Agreement of the measured mean radial velocities with theoretical results is satisfactory except in the inflow region. In this region, the measured mean radial velocities are considerably larger than the theortical values for $x > 0.8$. It should be noted that the magnitude of this mean radial and tangential velocities is small, sometimes in the range of 3-4 ft/sec. Random velocity fluctuations due to turbulence and other disturbances in the flow may be affecting the radial and tangential velocity components to a significant extent. This is thought to account for the scatter in this mean radial velocity distribution (Figures 61 and 62).

Figures 63 through 65 show the radial distribution of the mean tangential velocity component at different axial locations. The tangential velocity components are very small compared to the other velocity components. Near the rotor, on the downstream side (small positive z/R), the tangential velocity magnitude for small x is very large compared to the tangential velocities at the other locations. It is probable that this high tangential velocity is imparted to the fluid by the counterweight and rotor hub through the action of viscosity. The agreement of the experimental radial distribution of tangential velocity with the theory is satisfactory except for small values of x near the rotor, as noted above.

The overall agreement between the measured mean velocity components and the theoretical predictions is satisfactory. Some of the differences are probably caused by viscous effects which are not considered in this theory. Errors in measurement of the velocities, primarily

due to the total vector anemometer probe, also could be a reason for some of the differences. Random fluctuation due to turbulence and other flow disturbances in the test cell may also contribute to the differences.

There are very few cases in the literature where a comparison is made between theoretical results and experimental wake data for the rotor hover condition. There was no other suitable experimental or theoretical data available to compare with the velocities measured in this study. The agreement between the experimental data and theoretical results presented here is comparable with the agreement shown in Ref. 28, where mean axial velocities measured using pressure probes is compared with theory.

CHAPTER X

CONCLUSIONS AND RECOMMENDATIONS

On the basis of instantaneous velocity measurements made in the near wake of a single-bladed rotor in hover, the following conclusions are drawn:

(1) The vortex sheet at the outboard end has greater axial transport velocity than at the inner end. The measured vortex sheet geometry shows good agreement with theoretical predictions.

(2) Beyond an axial distance of $z/R = 0.250$ the instantaneous velocity data did not indicate the passage of a vortex sheet.

(3) The axial transport velocity of the tip vortex is much lower than that of the outer end of the vortex sheet.

(4) The measured tip vortex geometry shows good agreement with the available emperical geometry for the tip vortex as far as the axial coordinates are considered. However, the agreement of the radial locations is not as good. This lack of agreement is thought to be due to the comparatively large dimensions of the probe sensors, which may be changing the flow locally.

(5) The instantaneous velocity components at each azimuth location were averaged over number of blade-revolutions. However the averaged data did not improve the results.

(6) The radial distribution of the mean axial, radial and tangential components shows satisfactory agreement with theory.

(7) The total vector anemometer system used for measuring instantaneous velocities is adequate to obtain the vortex sheet and tip vortex geometry. However, the anemometer system is not adequate to obtain the strength of either the tip vortex or the vortex sheet because of large inherent errors in velocity measurements when the flow is inclined to the probe axis by more than 30 degrees.

Based upon the knowledge gained in the present study the following recommendations are made:

(1) Detailed velocity measurements should be made in the near-wake region using a laser velocimeter.

(2) Velocity measurements should be made in the far-wake of the rotor to study the instability of the wake, and to find where the tip vortex dissipates or breaks down.

Table 1. Sensitivity of Pressure Transducers

TRANSDUCER SERIAL NO.	CAVITY NO.	SENSITIVITY m. volts/psi/1 volt excitation (Measured values repeat within 1.5%)
8263	1	0.748
8266	2	0.8125
8267	3	0.9723
8264	4	0.8563
7063	5	0.831
5641	6	0.3457
1991-5-6x	-	0.485

Table 2. Pressure Coefficients on Rotor Tip; $\theta=0°$, 1350 RPM, Upper Surface and Flat Tip.

% CHORD	RADIAL POSITIONS						FLAT TIP		
	0.940	0.966	0.980	0.987	0.991	0.995	ROW1	ROW2	ROW3
.0	.897	.891	.875	.861	.867	.849			
1.0	.157	.079	.097	.072	.080	.051			
2.0	-.104	-.098	-.153	-.179	-.151	-.193		-.461	
5.0	-.295	-.299	-.288	-.292	-.291	-.292			
7.5	-.368	-.351	-.340		-.305	-.305		-.158	
10.5				-.327	-.298	-.292			
11.5	-.390	-.365	-.347				-.329		-.338
18.5	-.362	-.344	-.293				-.194		-.150
21.5				-.278	-.244	-.219			
22.5	-.358	-.336	-.306	-.261	-.236	-.220		-.075	
27.5	-.313	-.296	-.240	-.217	-.205	-.186	-.110		-.085
32.5	-.309	-.261	-.230	-.207	-.197	-.175	-.072		-.068
37.5	-.287	-.250	-.218	-.214	-.194	-.170		-.044	
42.5	-.256	-.235	-.210	-.192	-.193	-.165	-.062		-.066
47.5	-.256	-.236	-.219	-.193	-.176	-.178	-.076		-.082
52.5	-.233	-.220	-.178	-.176	-.173	-.163		-.089	
56.5	-.200	-.193	-.153	-.161	-.154	-.178	-.080		-.088
60.5	-.196	-.172	-.152	-.149	-.157	-.167	-.108		-.112
65.0	-.172	-.155	-.145	-.144	-.160	-.170		-.095	
69.0	-.143	-.121	-.135	-.131	-.150	-.190			
77.0	-.150	-.151	-.162	-.145	-.187	-.197		-.140	
84.4	-.113	-.130	-.129	-.145	-.160	-.182		-.115	
91.0	-.069	-.116	-.100	-.130	-.163	-.197		-.089	
93.0								.113	

Table 3. Pressure Coefficients on Rotor Tip; θ=6.2°, 1350 RPM, Upper Surface and Flat Tip.

% CHORD	RADIAL POSITIONS						FLAT TIP		
	0.940	0.966	0.980	0.987	0.991	0.995	ROW1	ROW2	ROW3
.0	.807	.812	.836	.835	.868	.849			
1.0	-.665	-.650	-.596	-.475	-.438	-.460			
2.0	-.812	-.734	-.722	-.652	-.593	-.561		-.621	
5.0	-.806	-.715	-.639	-.607	-.559	-.517			
7.5	-.752	-.680	-.613	-.560	-.513	-.460		-.178	
10.5				-.504	-.459	-.408			
11.5	-.685	-.615	-.539				-.188		-.442
18.5	-.535	-.468	-.415				-.126		-.280
21.5				-.359	-.330	-.284			
22.5	-.472	-.444	-.396	-.364	-.315	-.276		-.088	
27.5	-.412	-.380	-.320	-.300	-.266	-.247	-.134		-.227
32.5	-.385	-.310	-.269	-.264	-.247	-.249	-.114		-.198
37.5	-.334	-.267	-.262	-.254	-.241	-.250		-.064	
42.5	-.293	-.271	-.250	-.245	-.245	-.266	-.145		-.133
47.5	-.276	-.262	-.246	-.248	-.251	-.375	-.145		-.134
52.5	-.249	-.231	-.239	-.239	-.263	-.502		-.167	
56.5	-.233	-.220	-.218	-.225	-.287	-.532	-.180		-.120
60.5	-.226	-.216	-.203	-.218	-.331	-.548	-.201		-.131
65.0	-.211	-.202,	-.200	-.205	-.382	-.516		-.190	
69.0	-.193	-.178	-.203	-.222	-.444	-.479			
77.0	-.183	-.162	-.182	-.280	-.461	-.448		-.185	
84.4	-.121	-.133	-.176	-.379	-.455	-.416		-.174	
91.0	-.109	-.119	-.149	-.395	-.421	-.365		-.157	
93.0								.123	

Table 4. Pressure Coefficients on Rotor Tip; θ=6.2°, 1350 RPM, Lower Surface.

% CHORD	RADIAL POSITIONS					
	0.940	0.966	0.980	0.987	0.991	0.995
.0	.887	.862	.847	.861	.867	.845
1.0	.630	.626	.549	.543	.502	.426
2.0	.398	.380	.314	.287	.216	.165
5.0	.132	.029	-.014	-.010	-.038	-.079
7.5	-.064	-.088	-.097	-.098	-.104	-.133
10.5				-.153	-.144	-.175
11.5	-.158	-.154	-.162			
18.5	-.170	-.173	-.172			
21.5				-.162	-.149	-.152
22.5	-.173	-.181	-.181	-.150	-.159	-.149
27.5	-.180	-.180	-.179	-.162	-.151	-.138
32.5	-.200	-.191	-.178	-.162	-.154	-.147
37.5	-.202	-.185	-.171	-.154	-.145	-.139
42.5	-.191	-.169	-.162	-.140	-.140	-.127
47.5	-.191	-.179	-.162	-.154	-.147	-.138
52.5		-.169	-.158	-.132	-.134	-.136
56.5	-.174	-.159	-.153	-.134	-.139	-.126
60.5	-.168	-.164	-.121	-.139	-.135	-.129
65.0	-.167	-.154	-.145	-.123	-.134	-.125
69.0	-.159	-.145	-.139	-.124	-.126	-.117
77.0	-.145	-.148	-.145	-.132	-.122	-.117
84.4	-.134	-.133	-.129	-.109	-.104	-.104
91.0	-.088	-.106	-.122	-.109	-.109	-.084

Table 5. Pressure Coefficients on Rotor Tip; θ =11.4°, 1350 RPM, Upper and Lower Surfaces.

% CHORD	RADIAL POSITIONS						
	0.995		0.991	0.987	0.980	0.966	0.940
	UPPER SURFACE	LOWER SURFACE	UPPER SURFACE	UPPER SURFACE	UPPER SURFACE	UPPER SURFACE	UPPER SURFACE
0	0.641		0.619	0.514	0.108		
1.0	-0.864	0.567	-0.937	-1.023	-1.180		
2.0	-0.917	0.356	-1.001	-1.126	-0.979	-1.329	-1.013
5.0	-0.694	-0.050	-0.804				-1.228
7.5	-0.634		-0.720	-0.796	-0.758	-0.796	
10.5	-0.505		-0.590	-0.657			
11.5						-0.794	-0.879
18.5					-0.458	-0.516	-0.618
21.5	-0.404	-0.096	-0.400	-0.439			
22.5	-0.411	-0.107	-0.390	-0.424	-0.390	-0.514	-0.484
27.5	-0.377	-0.125	-0.357	-0.360	-0.365	-0.407	-0.480
32.5	-0.465	-0.120	-0.338	-0.340	-0.340	-0.337	-0.435
37.5	-0.624	-0.119	-0.353	-0.345	-0.328	-0.340	
42.5	-0.735	-0.111	-0.379	-0.322	-0.323	-0.320	-0.333
47.5	-0.767	-0.169	-0.484	-0.362	-0.328	-0.351	-0.320
52.5	-0.648	-0.159	-0.608	-0.401	-0.308	-0.308	-0.332
56.5	-0.568	-0.180	-0.715	-0.446	-0.314	-0.293	-0.316
60.5	-0.590	-0.113	-0.701	-0.451	-0.277	-0.260	-0.243
65.0	-0.576	-0.116	-0.674	-0.506	-0.286	-0.242	-0.220
69.0	-0.606	-0.108	-0.695	-0.589	-0.275	-0.218	-0.197
77.0	-0.593	-0.099	-0.683	-0.691	-0.338	-0.185	-0.155
84.4	-0.581	-0.124	-0.648	-0.766	-0.413	-0.153	-0.139
91.0	-0.466	-0.069	-0.565	-0.704	-0.466	-0.132	-0.069

Table 6. Pressure Coefficients on Rotor Tip; θ=0°, 1000 RPM, upper Surface and Flat Tip.

% CHORD	RADIAL POSITIONS						FLAT TIP		
	0.940	0.966	0.980	0.987	0.991	0.995	ROW1	ROW2	ROW3
.0	.936	.921	.916	.898	.901	.845			
1.0	.212	.133	.135	.098	.114	.090			
2.0	-.063	-.051	-.103	-.128	-.112	-.152		-.457	
5.0	-.253	-.250	-.241	-.242	-.233	-.243			
7.5	-.296	-.304	-.292	-.267	-.263	-.267		-.166	
10.5				-.275	-.261	-.252			
11.5	-.336	-.311	-.299				-.293		-.308
18.5	-.320	-.301	-.262				-.177		-.140
21.5				-.241	-.224	-.198			
22.5	-.330	-.300	-.265	-.242	-.223	-.204		-.069	
27.5	-.289	-.259	-.221	-.198	-.172	-.183	-.092		-.058
32.5	-.276	-.235	-.207	-.181	-.174	-.159	-.054		-.051
37.5	-.256	-.223	-.194	-.184	-.172	-.154		-.023	
42.5	-.234	-.207	-.186	-.172	-.166	-.135	-.048		-.050
47.5	-.224	-.226	-.186	-.157	-.176	-.180	-.073		-.057
52.5	-.199	-.179	-.170	-.120	-.159	-.136		-.084	
56.5	-.184	-.172	-.170	-.130	-.138	-.155	-.062		-.092
60.5	-.169	-.159	-.155	-.113	-.127	-.134	-.080		-.081
65.0	-.154	-.138	-.111	-.119	-.134	-.138		-.070	
69.0	-.117	-.113	-.100	-.104	-.117	-.147			
77.0	-.107	-.092	-.105	-.085	-.105	-.173		-.094	
84.4	-.077	-.047	-.081	-.091	-.105	-.140		-.060	
91.0	-.061	-.060	-.069	-.105	-.113	-.145		-.115	
93.0								.057	

Table 7. Pressure Coefficients on Rotor Tip; θ=6.2°, 1000 RPM, Upper Surface and Flat Tip.

% CHORD	RADIAL POSITIONS						FLAT TIP		
	0.940	0.966	0.980	0.987	0.991	0.995	ROW1	ROW2	ROW3
.0	.842	.836	.872	.877	.908	.890			
1.0	-.621	-.609	-.561	-.424	-.405	-.421			
2.0	-.760	-.673	-.683	-.605	-.559	-.517		-.633	
5.0	-.763	-.681	-.597	-.552	-.520	-.457			
7.5	-.703	-.639	-.560	-.519	-.468	-.415		-.141	
10.5				-.453	-.410	-.368			
11.5	-.638	-.577	-.495				-.147		-.403
18.5	-.514	-.446	-.388				-.122		-.278
21.5				-.344	-.305	-.263			
22.5	-.475	-.412	-.362	-.336	-.292	-.262		-.077	
27.5	-.422	-.370	-.325	-.282	-.239	-.232	-.121		-.199
32.5	-.382	-.315	-.262	-.248	-.236	-.243	-.119		-.185
37.5	-.335	-.264	-.246	-.241	-.232	-.239		-.063	
42.5	-.272	-.248	-.230	-.226	-.243	-.264	-.141		-.119
47.5	-.258	-.239	-.219	-.213	-.274	-.344	-.183		-.117
52.5	-.228	-.231	-.203	-.231	-.254	-.463		-.145	
56.5	-.223	-.205	-.191	-.196	-.281	-.493	-.160		-.087
60.5	-.187	-.177	-.177	-.184	-.301	-.511	-.175		-.100
65.0	-.171	-.168	-.169	-.185	-.352	-.465		-.158	
69.0	-.154	-.152	-.158	-.194	-.417	-.436			
77.0	-.149	-.147	-.144	-.254	-.436	-.453		-.174	
84.4	-.100	-.114	-.157	-.354	-.430	-.423		-.174	
91.0	-.069	-.080	-.120	-.356	-.448	-.367		-.165	
93.0								.051	

Table 8. Pressure Coefficients on Rotor Tip; θ=6.2, 1000 RPM, Lower Surface.

% CHORD	RADIAL POSITIONS					
	0.940	0.966	0.980	0.987	0.991	0.995
.0	.920	.904	.887	.906	.909	.885
1.0	.677	.670	.592	.594	.547	.468
2.0	.443	.429	.372	.327	.264	.210
5.0	.173	.072	.032	.029	.007	-.030
7.5	-.017	-.036	-.048	-.043	-.052	-.089
10.5				-.105	-.098	-.127
11.5	-.105	-.112	-.110			
18.5	-.151	-.152	-.145			
21.5				-.139	-.116	-.126
22.5	-.155	-.152	-.145	-.113	-.134	-.132
27.5	-.159	-.158	-.149	-.120	-.129	-.124
32.5	-.181	-.169	-.162	-.145	-.134	-.134
37.5	-.173	-.161	-.147	-.134	-.134	-.119
42.5	-.167	-.149	-.135	-.140	-.129	-.109
47.5	-.180	-.160	-.121	-.118	-.124	-.117
52.5		-.137	-.139	-.098	-.096	-.088
56.5	-.149	-.148	-.119	-.093	-.094	-.080
60.5	-.135	-.119	-.108	-.100	-.093	-.098
65.0	-.121	-.119	-.101	-.089	-.105	-.079
69.0	-.115	-.100	-.094	-.094	-.082	-.072
77.0	-.116	-.107	-.122	-.108	-.109	-.098
84.4	-.072	-.087	-.090	-.075	-.105	-.075
91.0	-.072	-.081	-.072	-.121	-.087	-.069

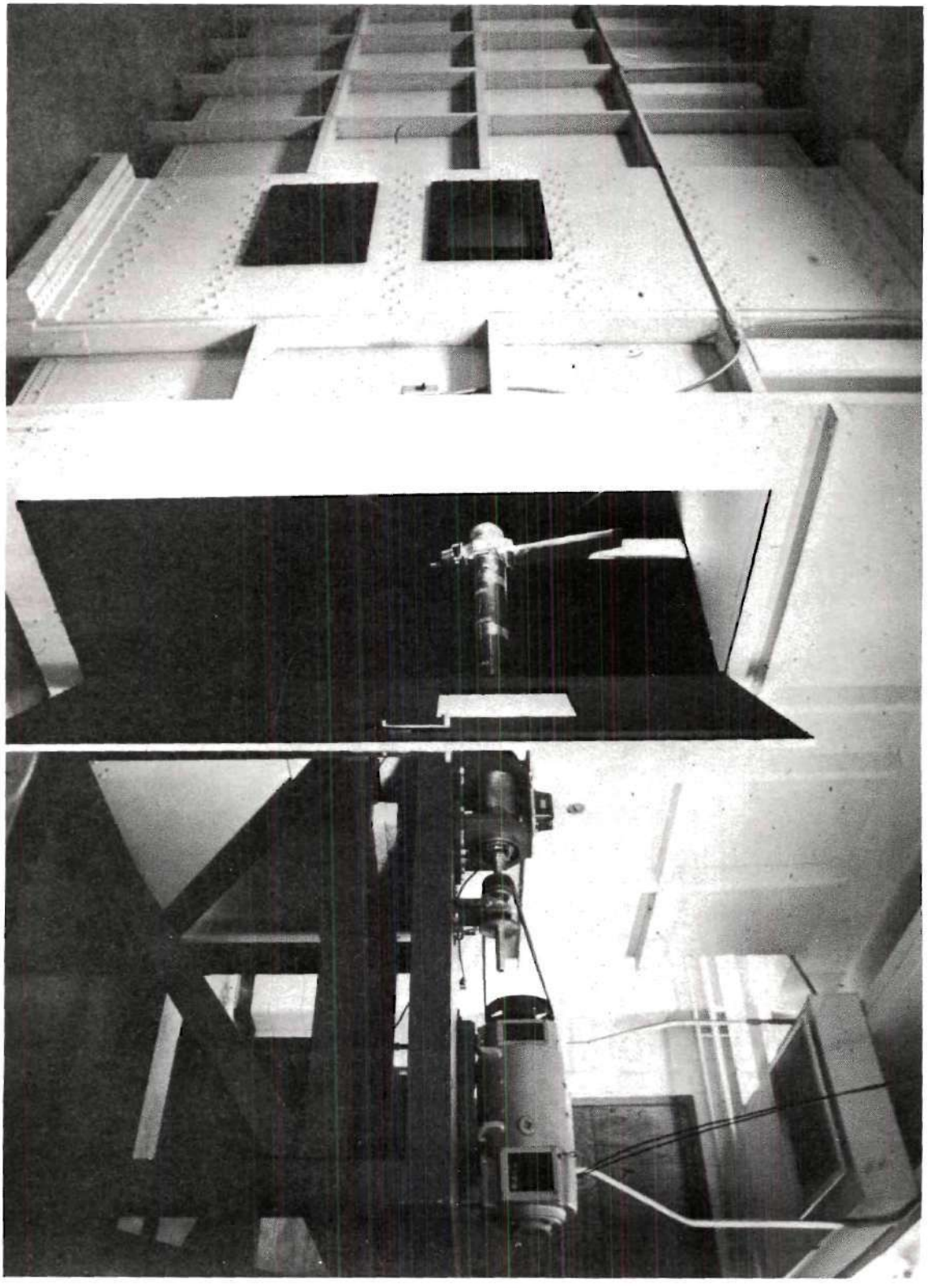

Figure 1. Rotor Test Cell

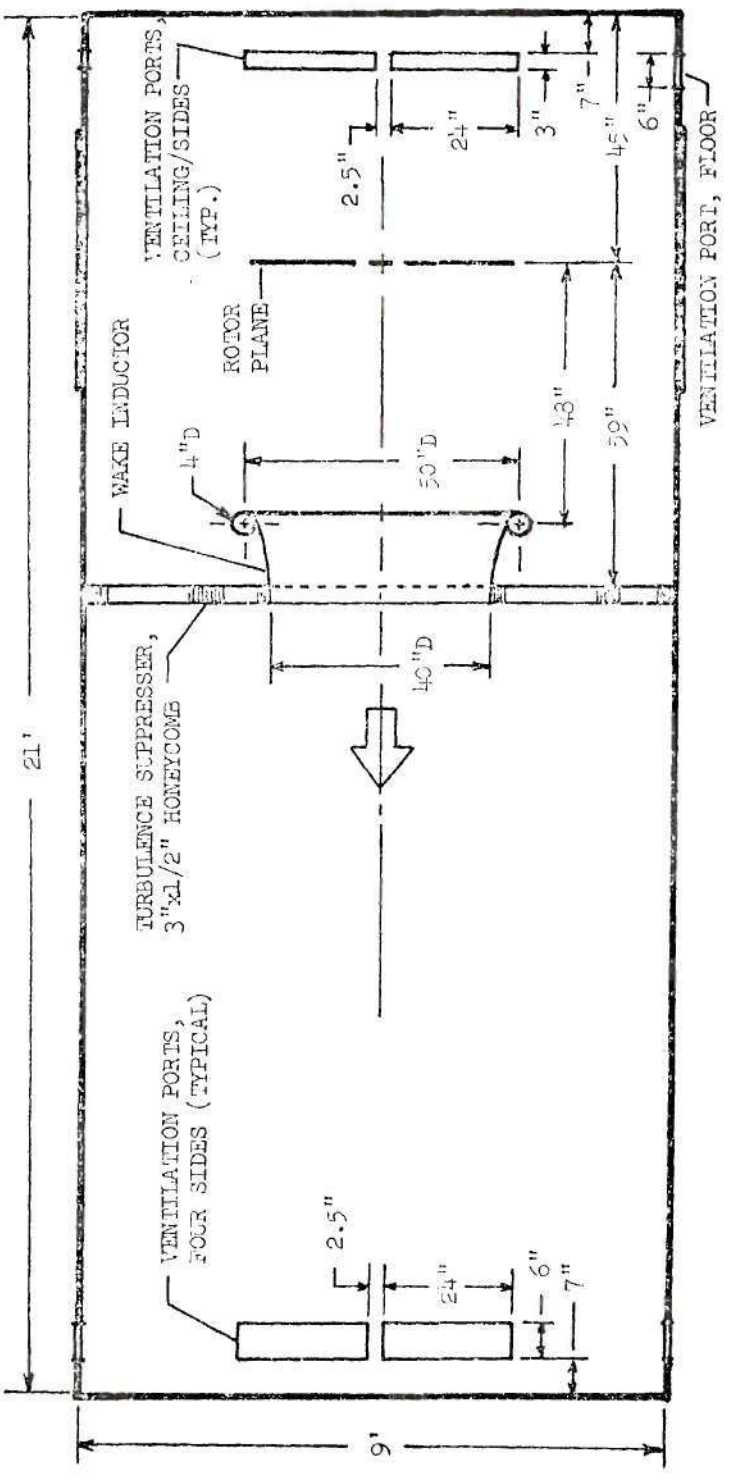

Figure 2. Longitudinal Cross-section of Hovering Test Facility for Model Rotors.

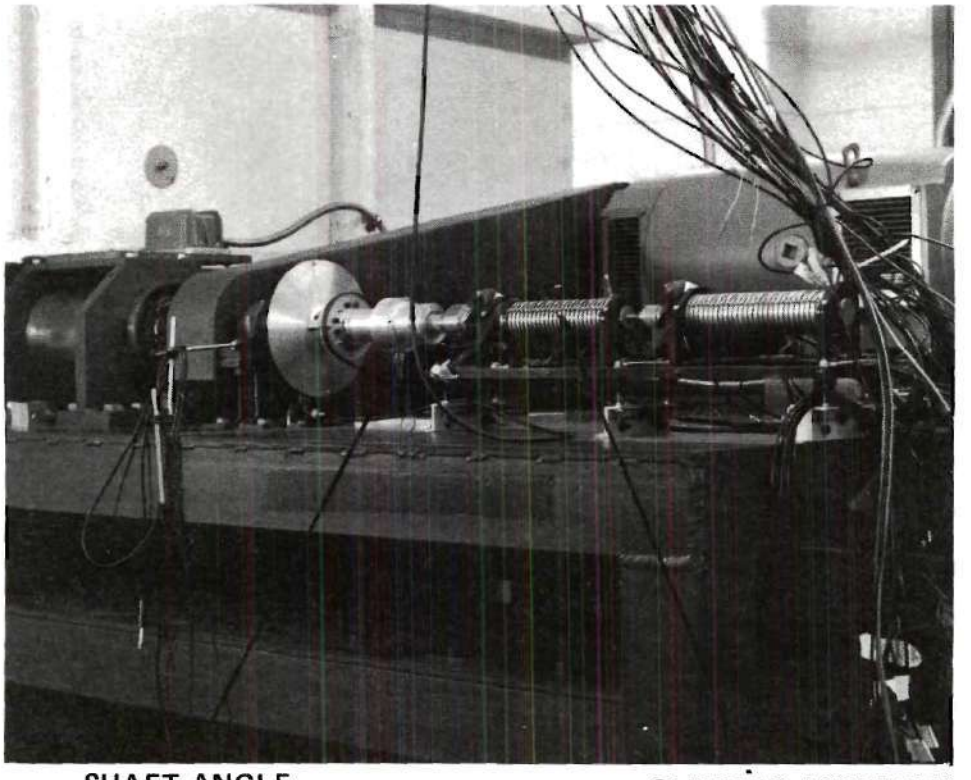

Figure 3. Slipring Assembly and Shaft Angle Encoder

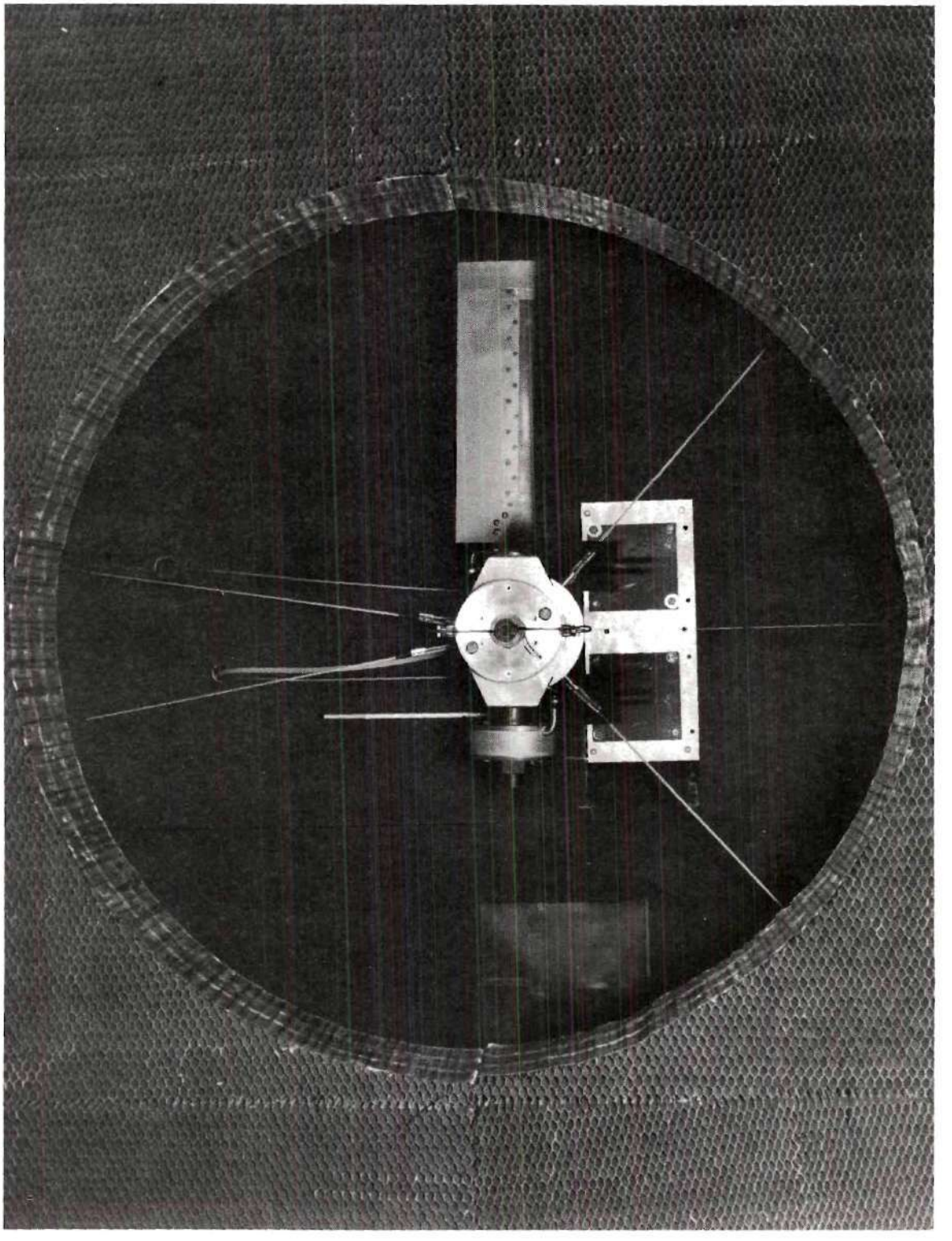

Figure 4. Model Helicopter Rotor

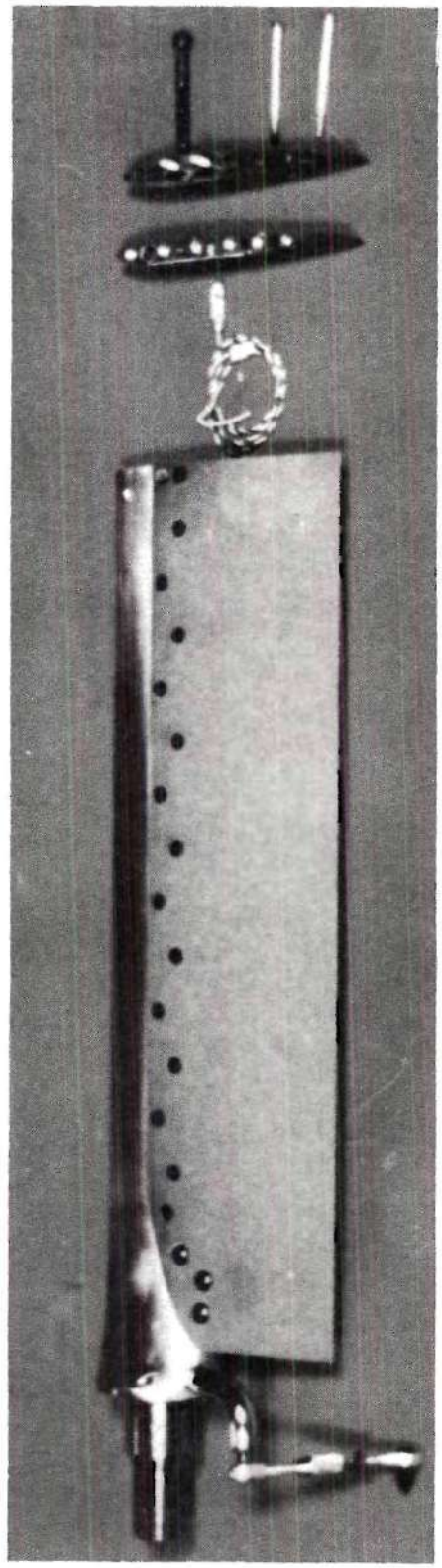

Figure 5. Exploded View of Model Blade and Tip Assembly

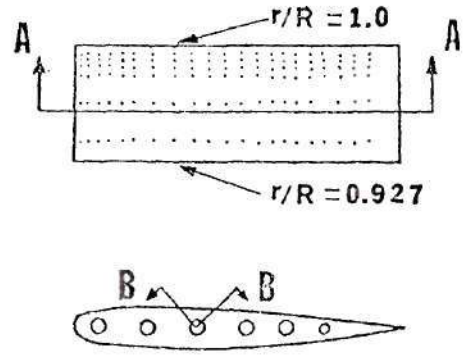

a) Removable blade tip

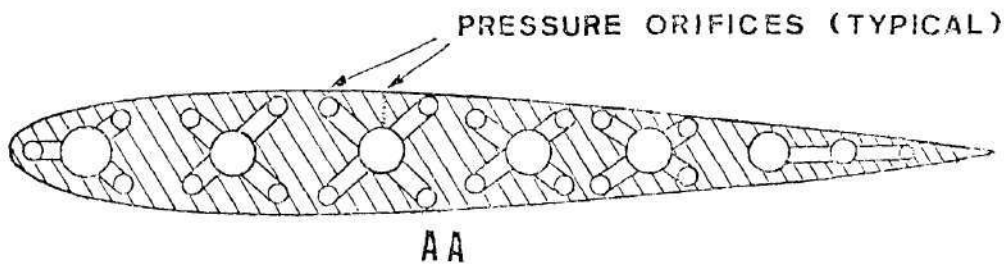

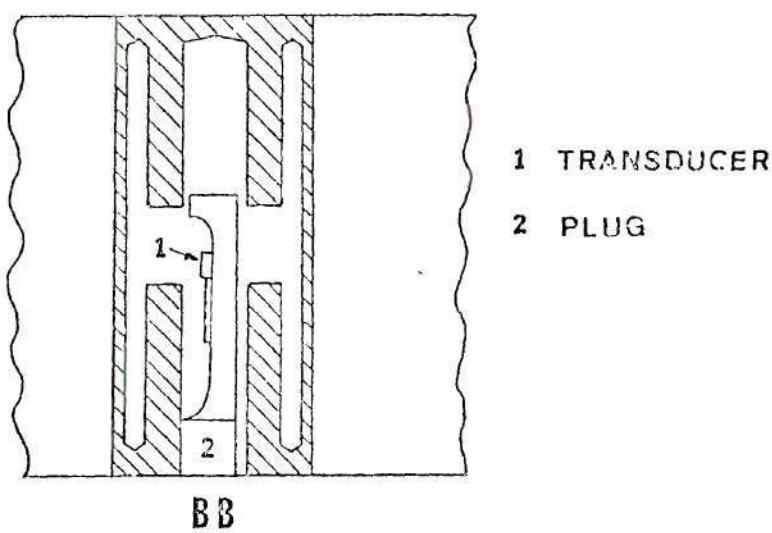

b) Cross-Sections

Figure 6. Details of Pressure Tip Design.

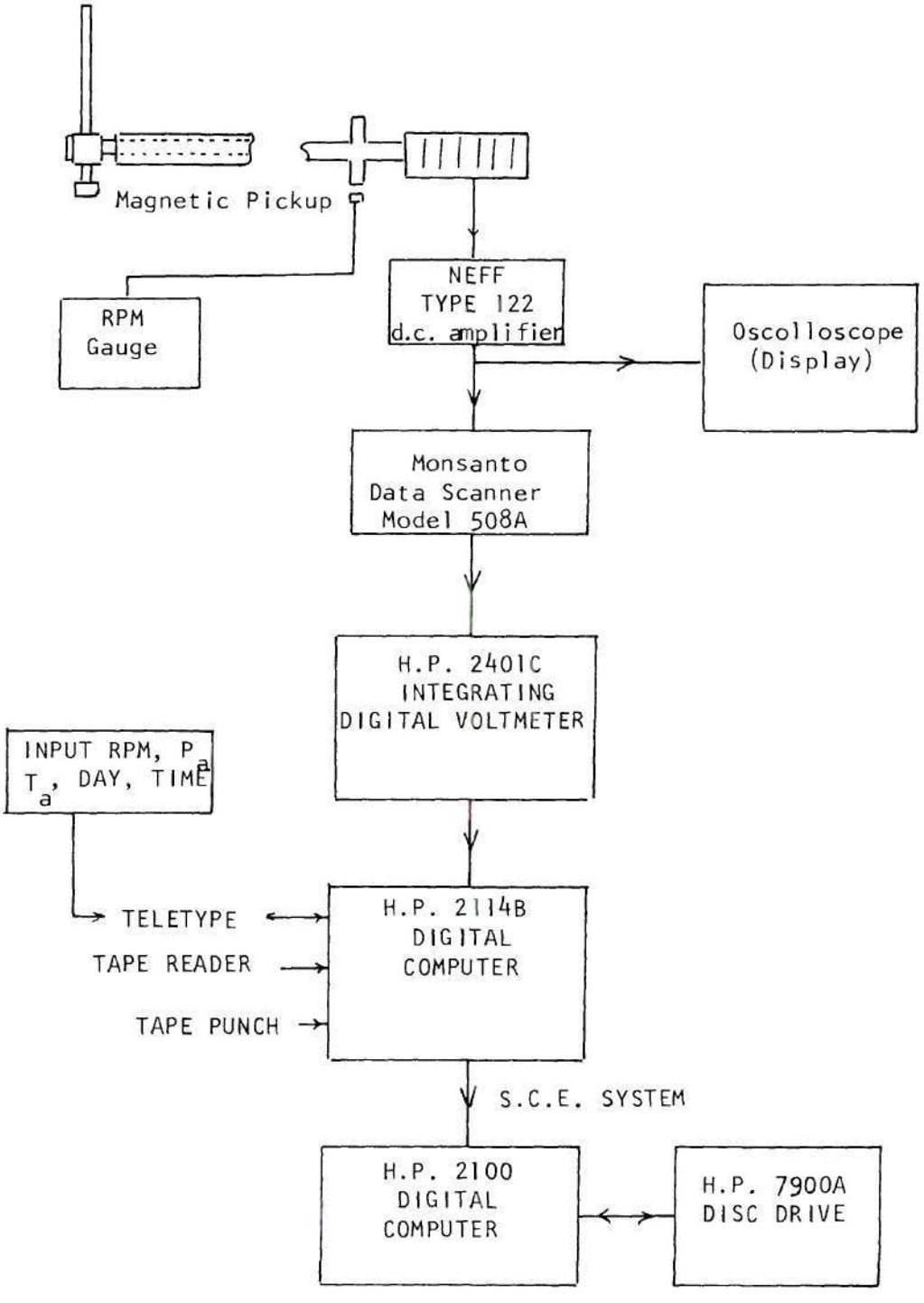

Figure 7. Block Diagram of Data Acquisition System.

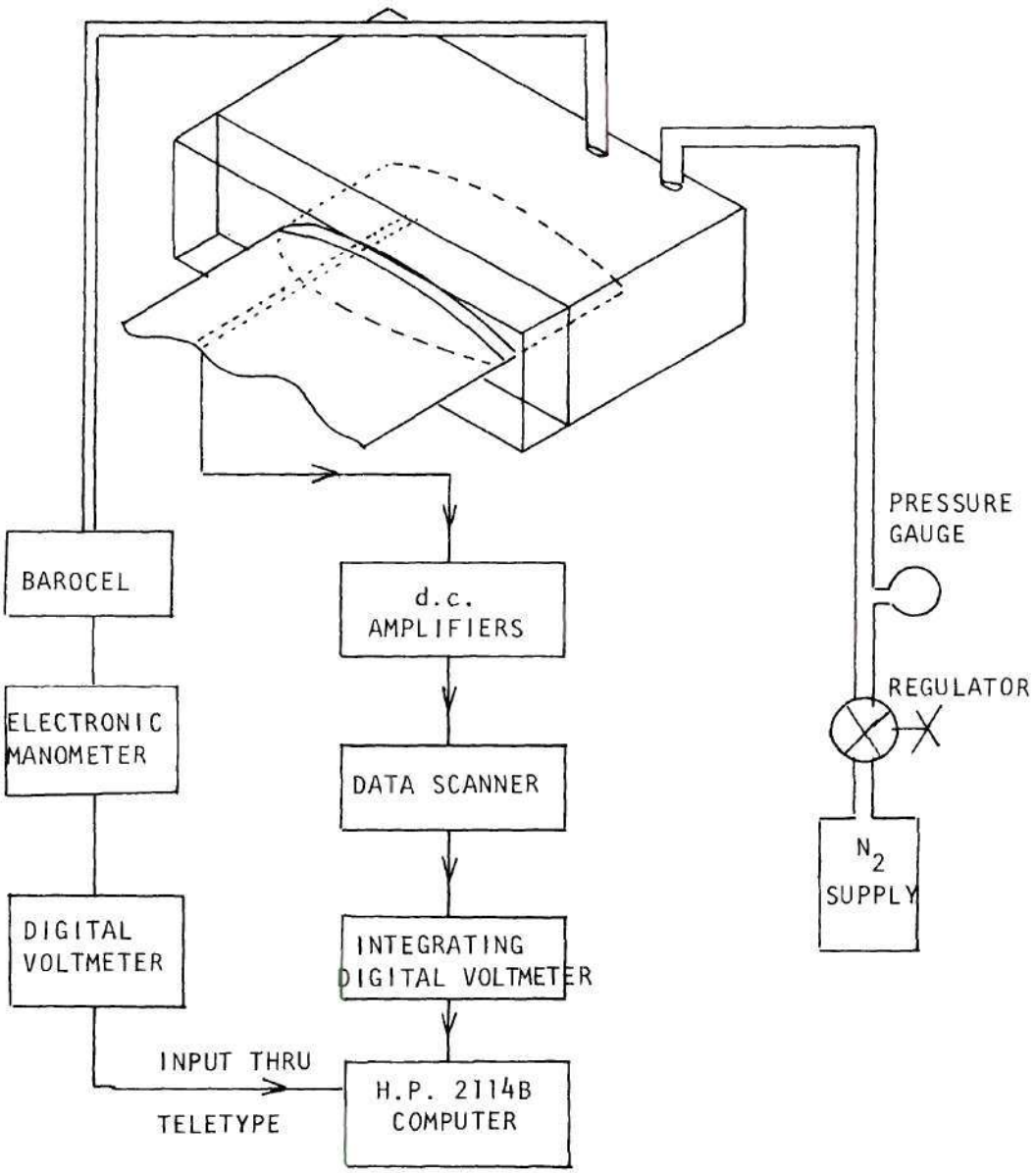

Figure 8. Schematic of the Equipment Setup for Static Calibration of Pressure Gauges.

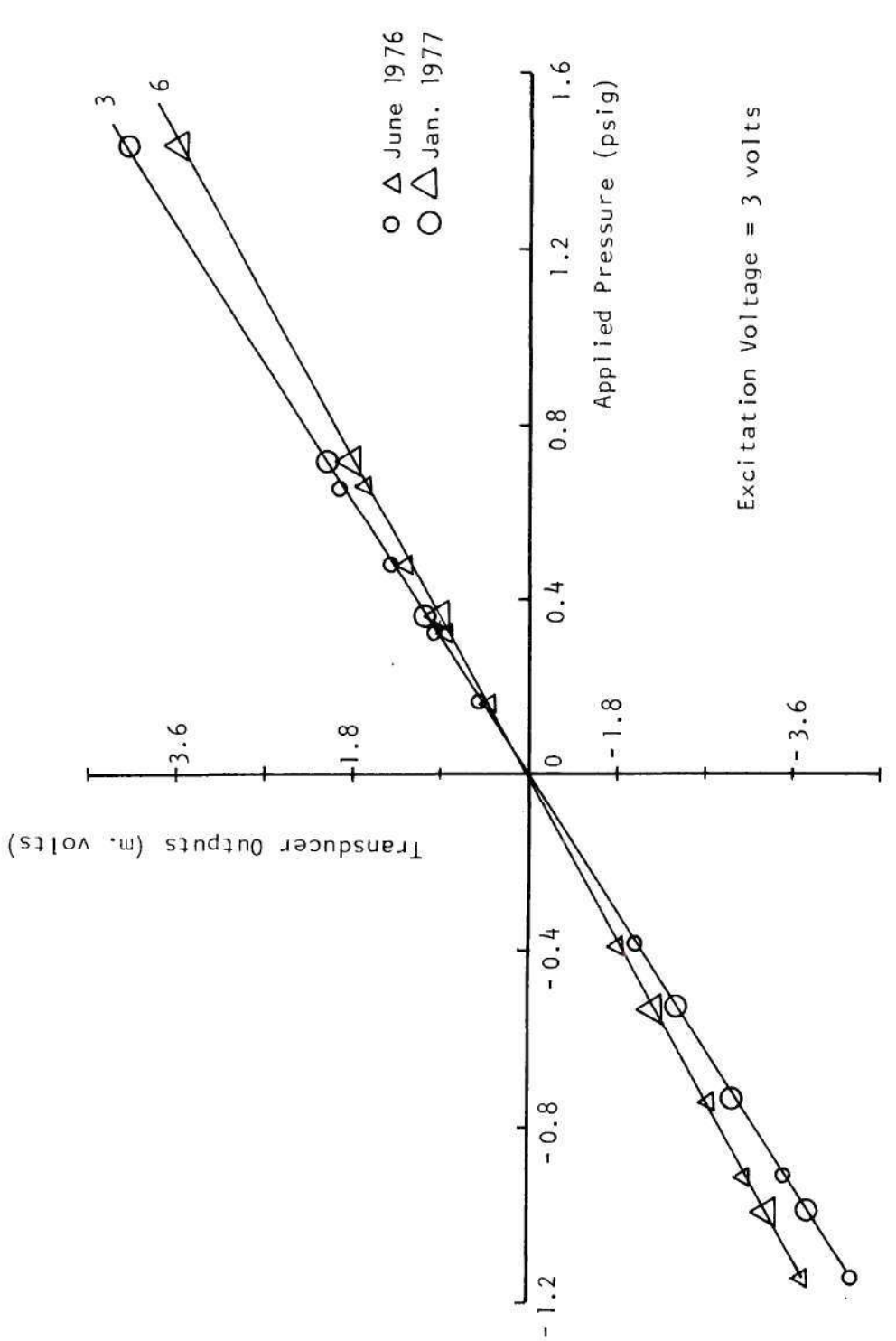

Figure 9a. Calibration Results for Transducers in Cavities 3 and 6.

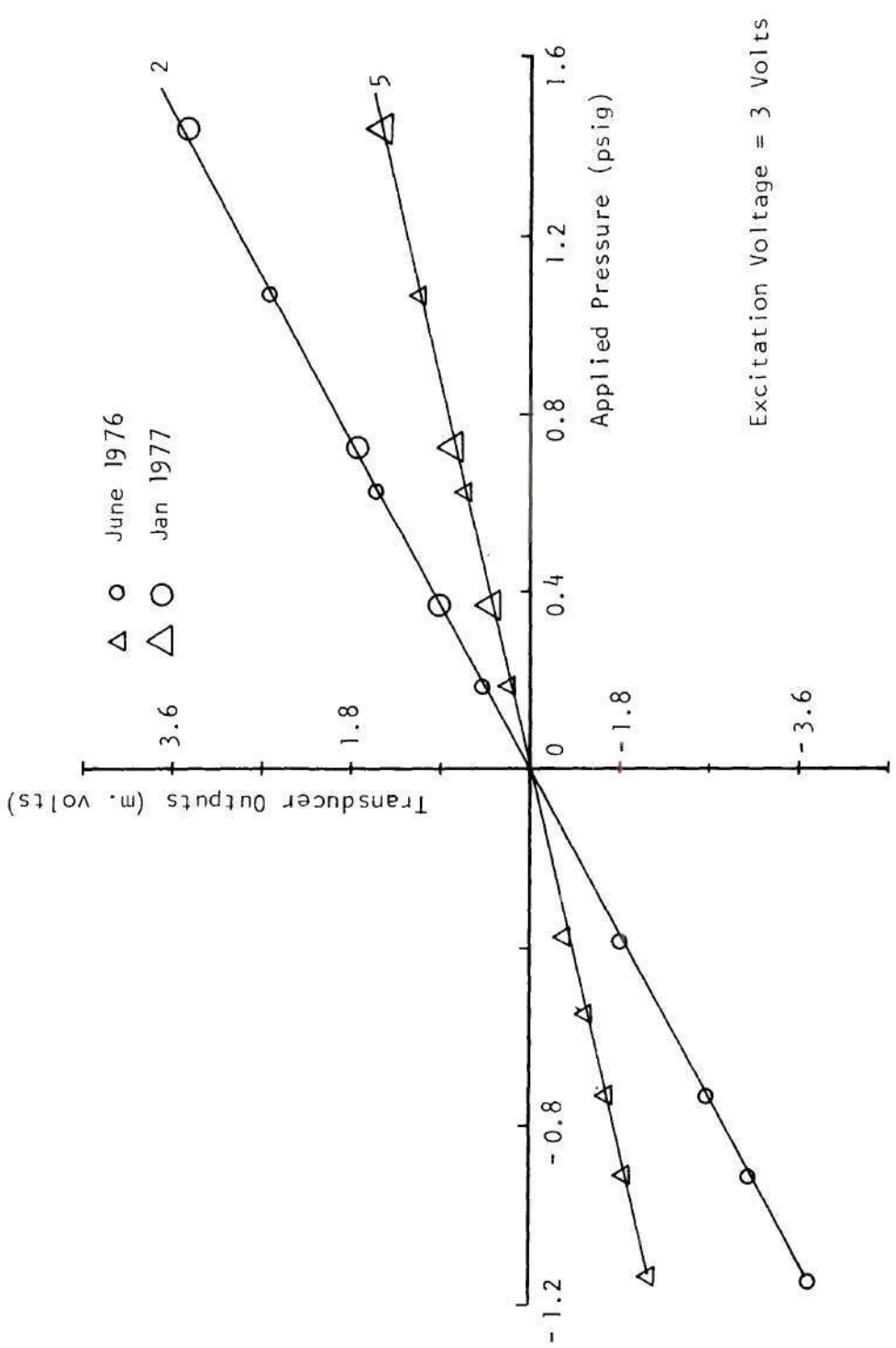

Figure 9b. Calibration Results for Transducers in Cavities 2 and 5.

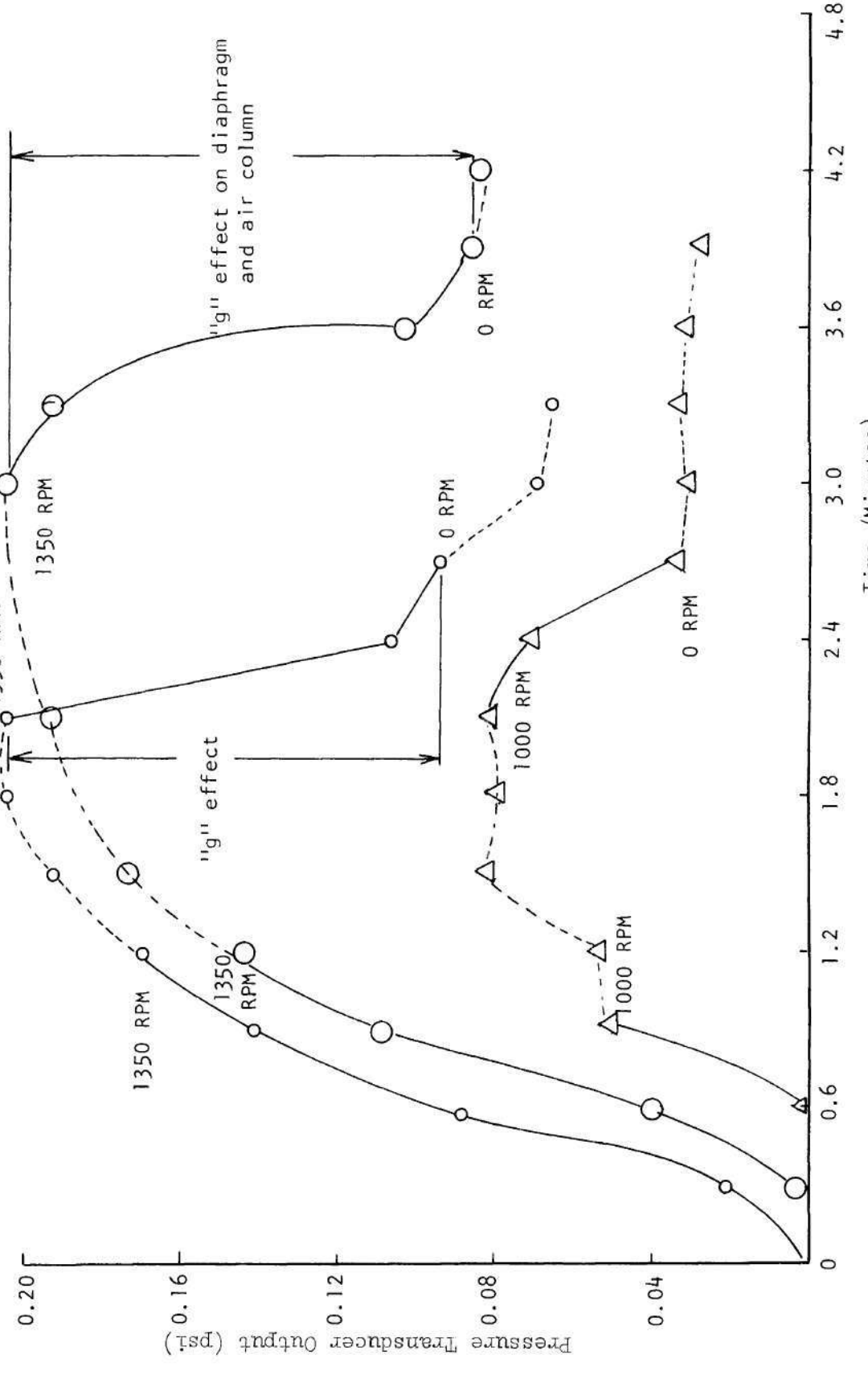

Figure 10. "g" Correction Evaluation Test Data, Cavity No. 4.

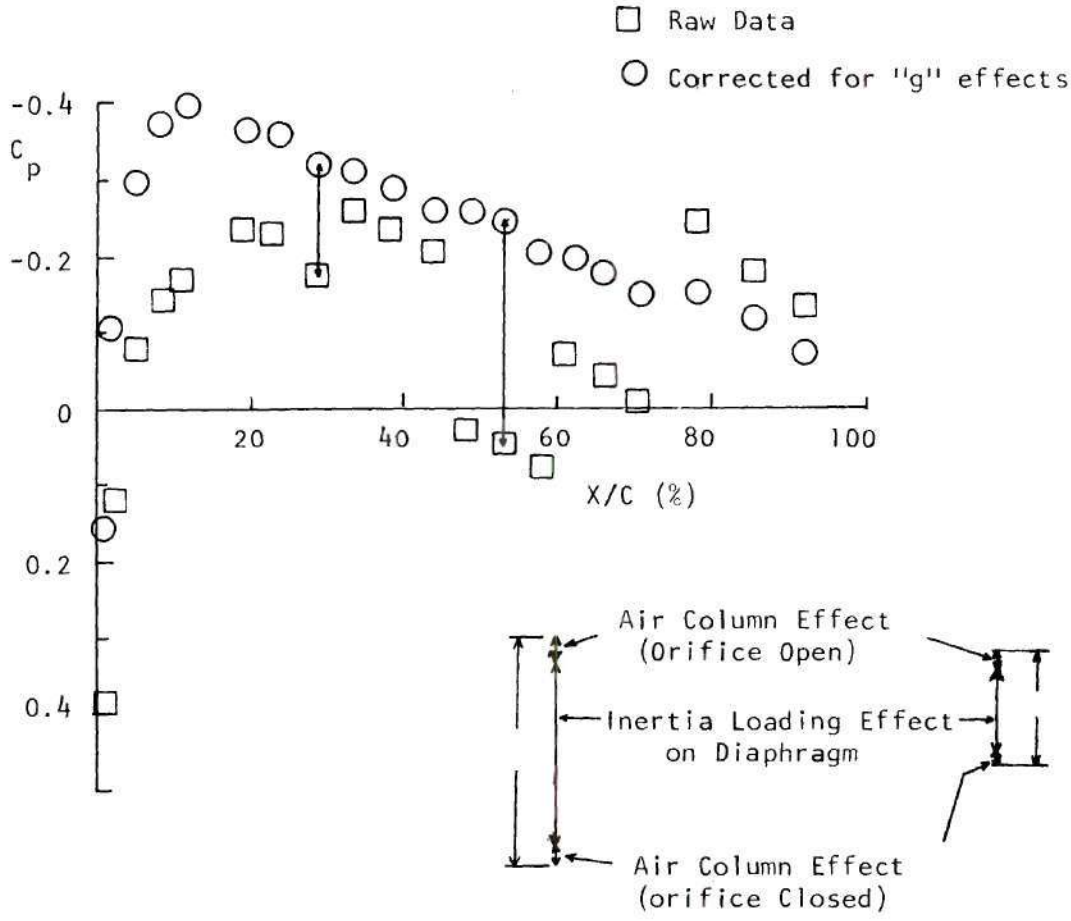

Figure 11. Typical Effect of Centripetal Acceleration Correction, $\theta = 0°$, RPM = 1350, r/R = 0.940.

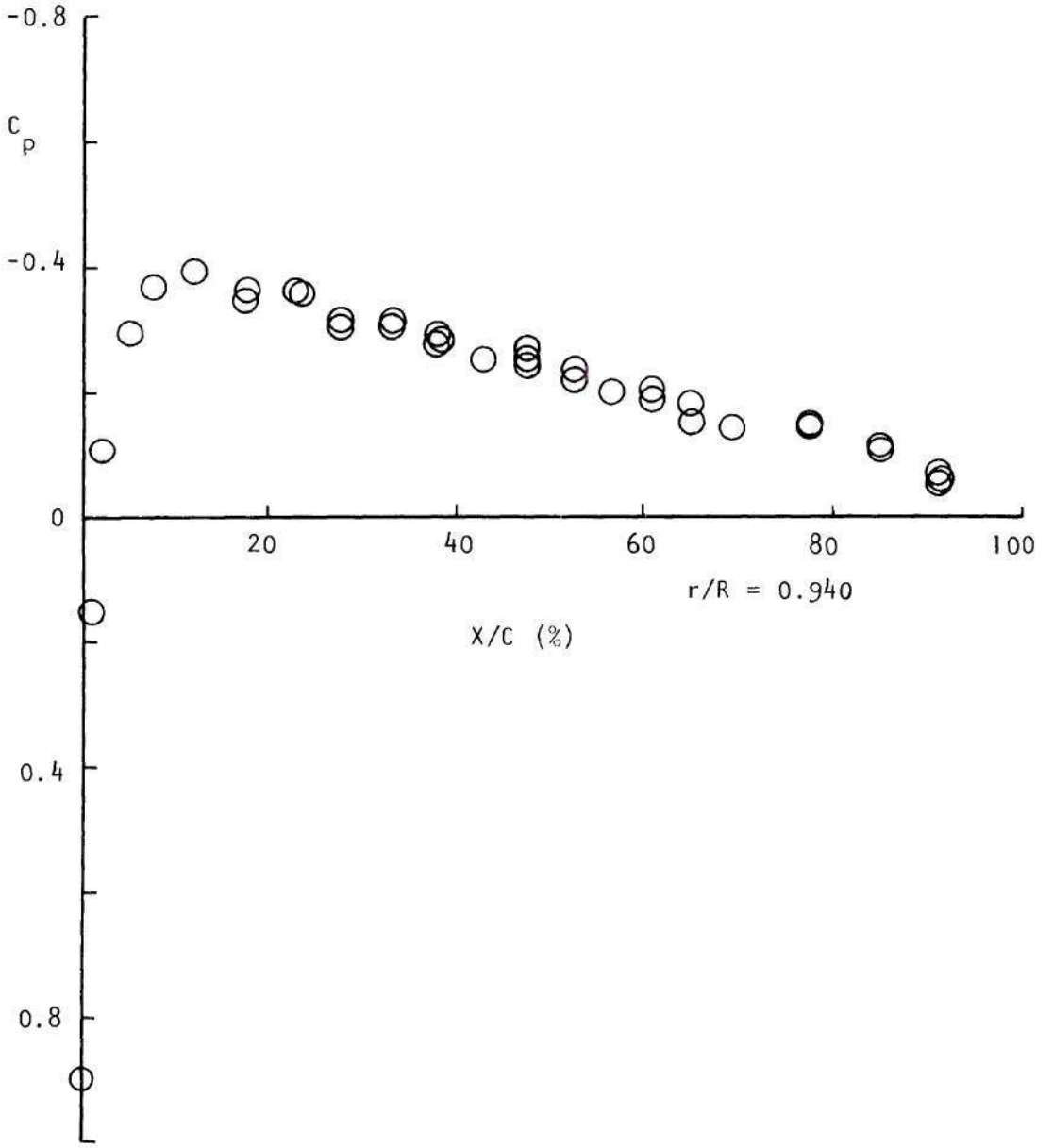

Figure 12a. Typical Repeatability, $\theta = 0°$.

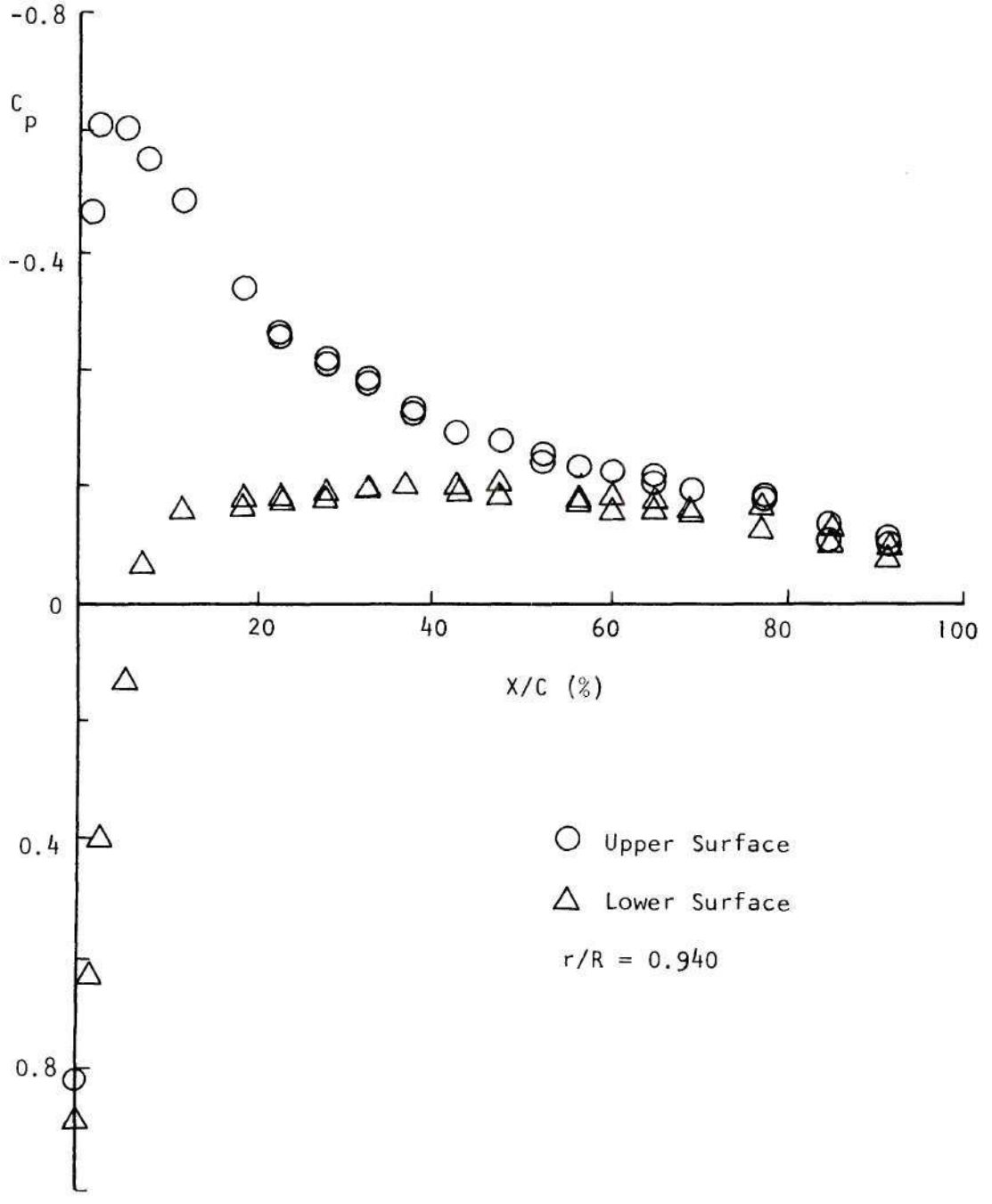

Figure 12b. Typical Repeatability, $\theta = 6.2°$.

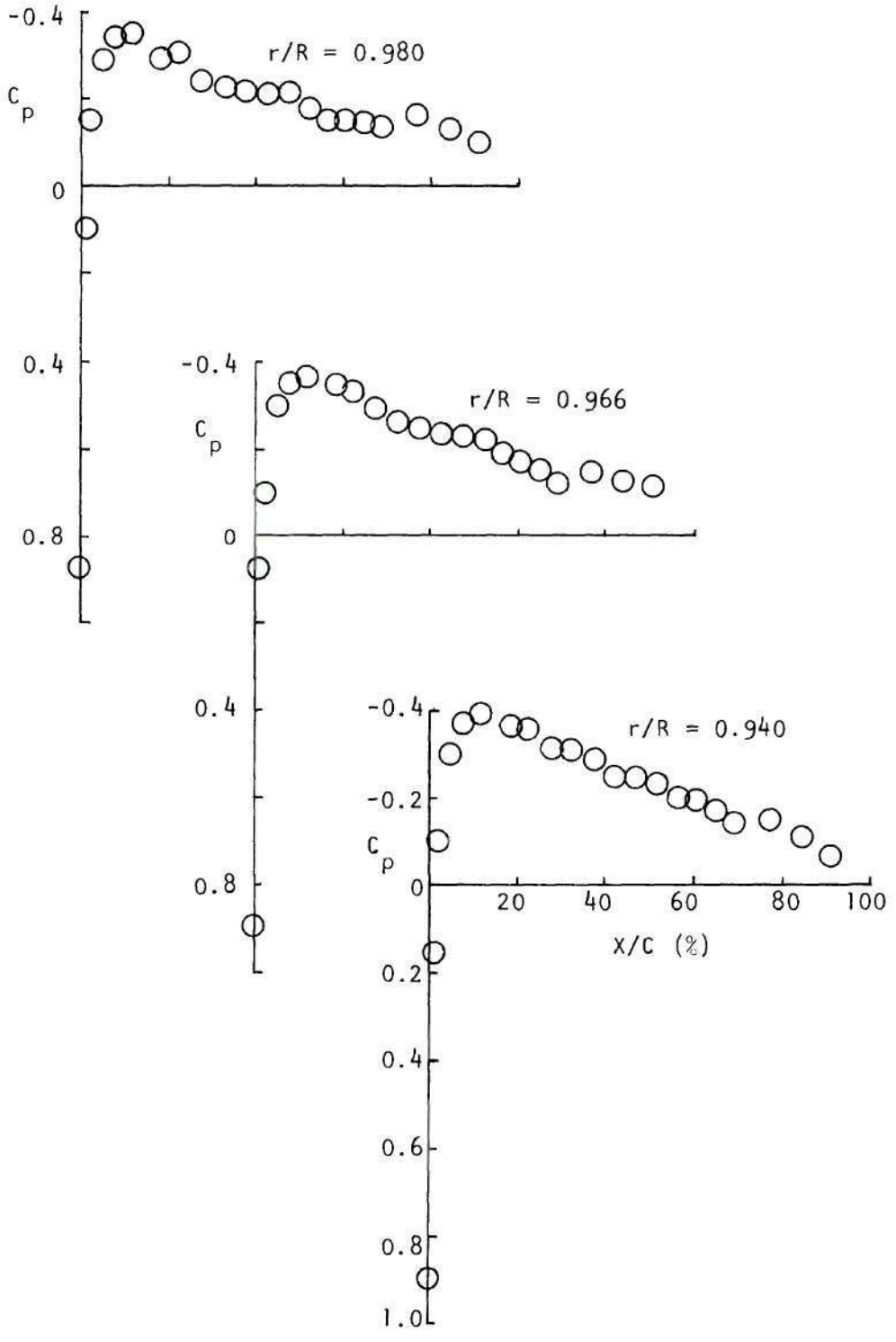

Figure 13. Pressure Distribution, $\theta = 0°$, RPM = 1350. (Continues)

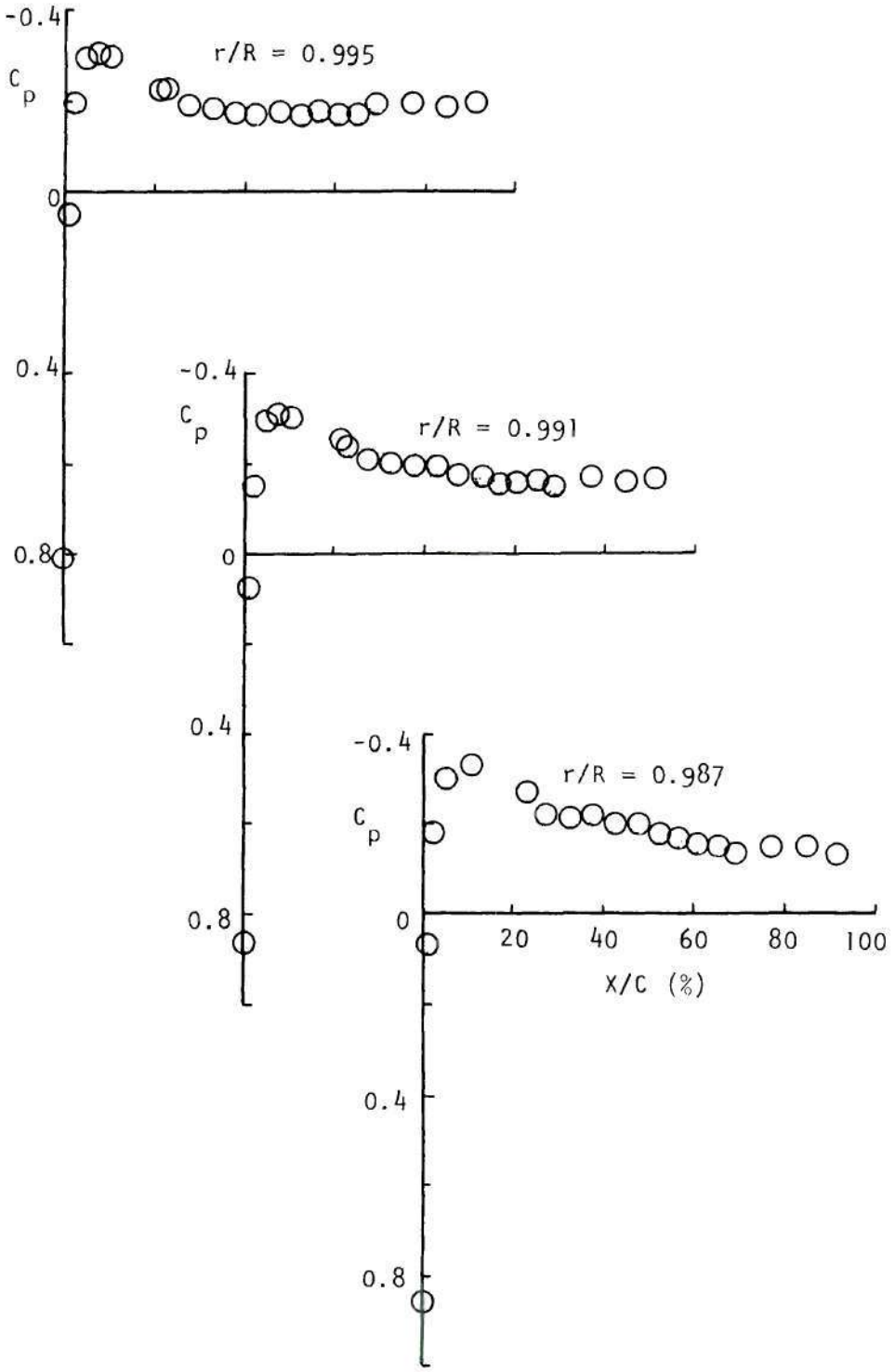

Figure 13. Pressure Distribution, $\theta = 0°$, RPM = 1350 (Continued).

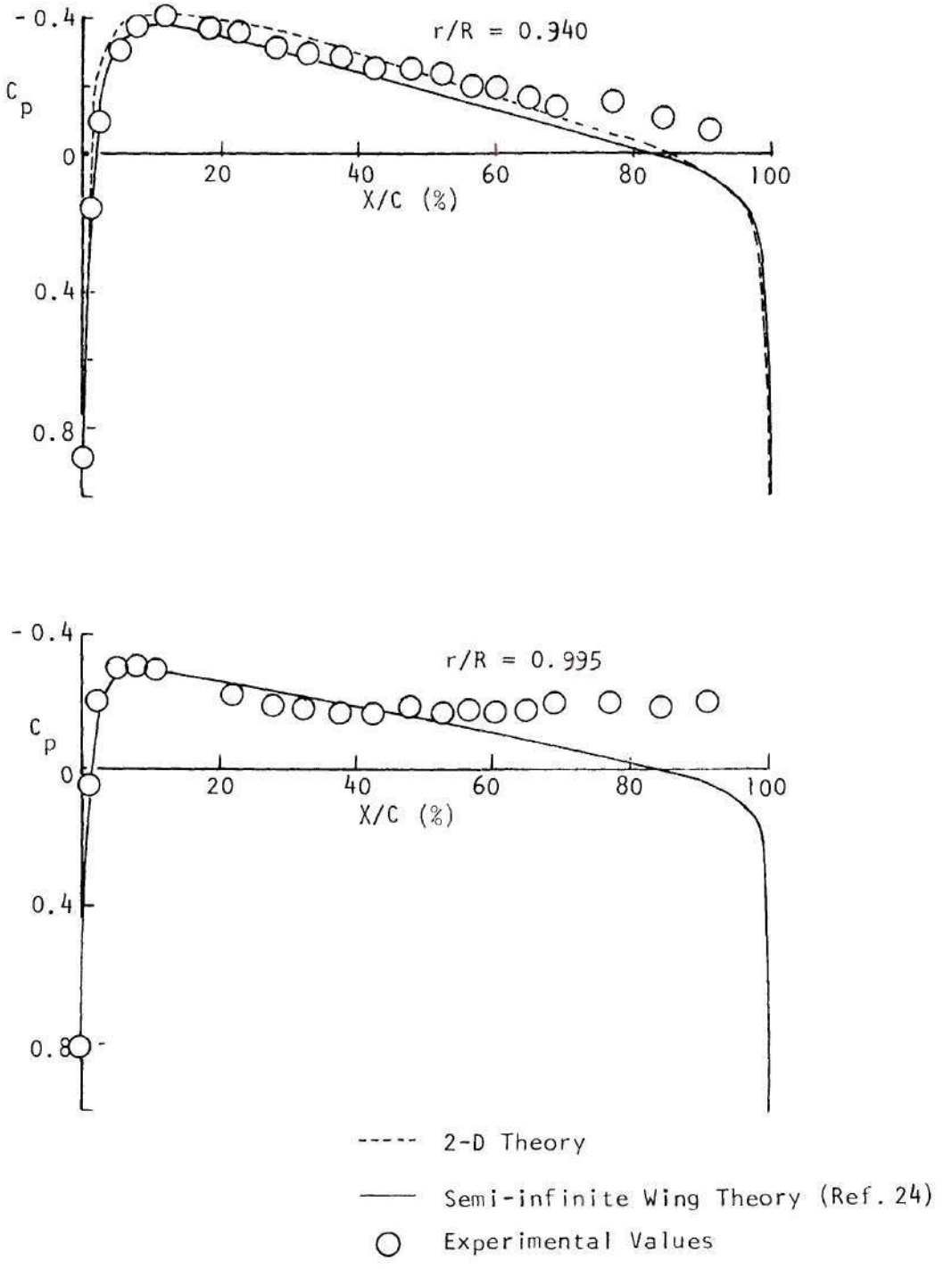

Figure 14. Comparison of the Experimental Values with Theoretical Solutions; $\theta = 0°$, RPM = 1350.

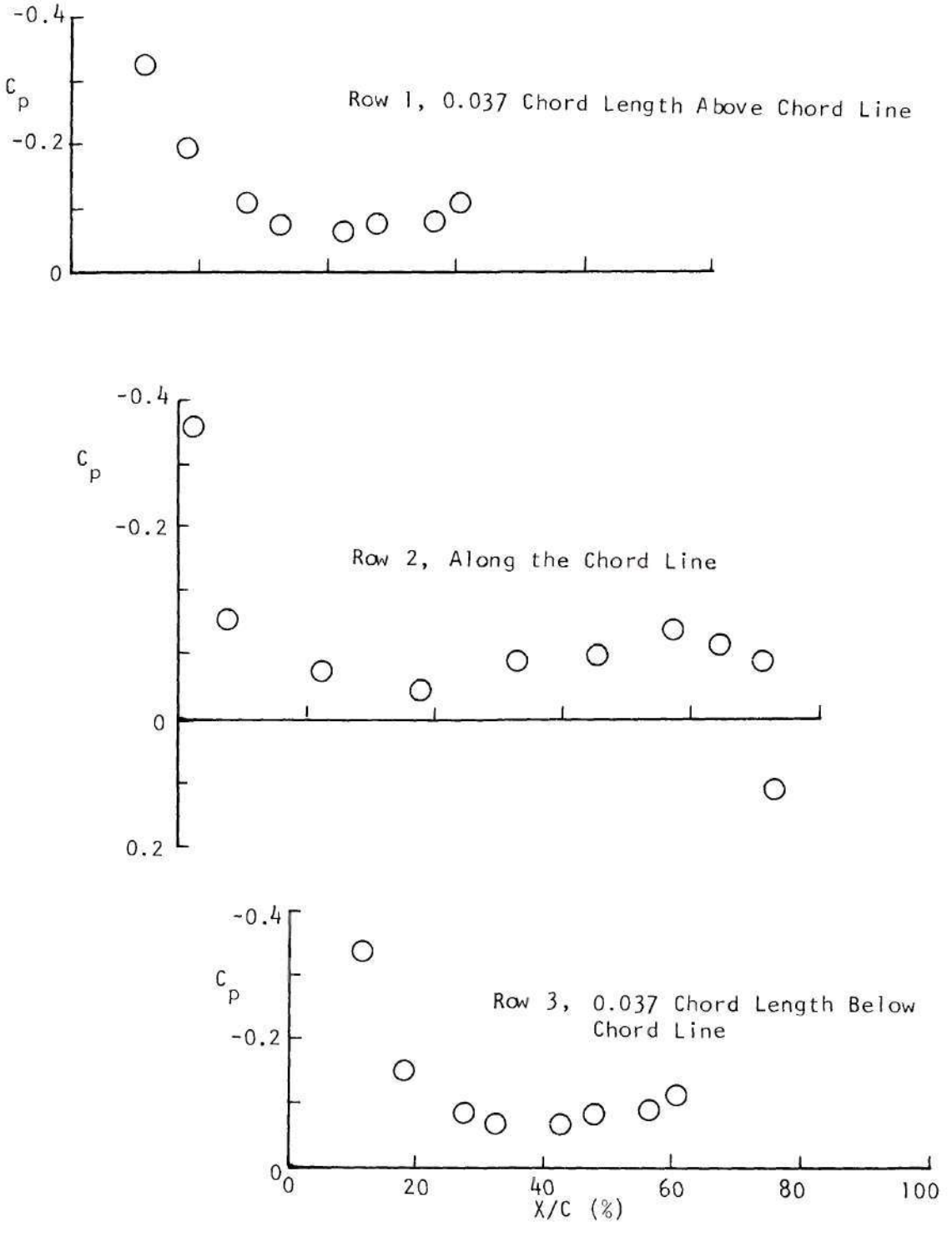

Figure 15. Pressure Distribution on Flat tip; $\theta = 0°$; RPM = 1350.

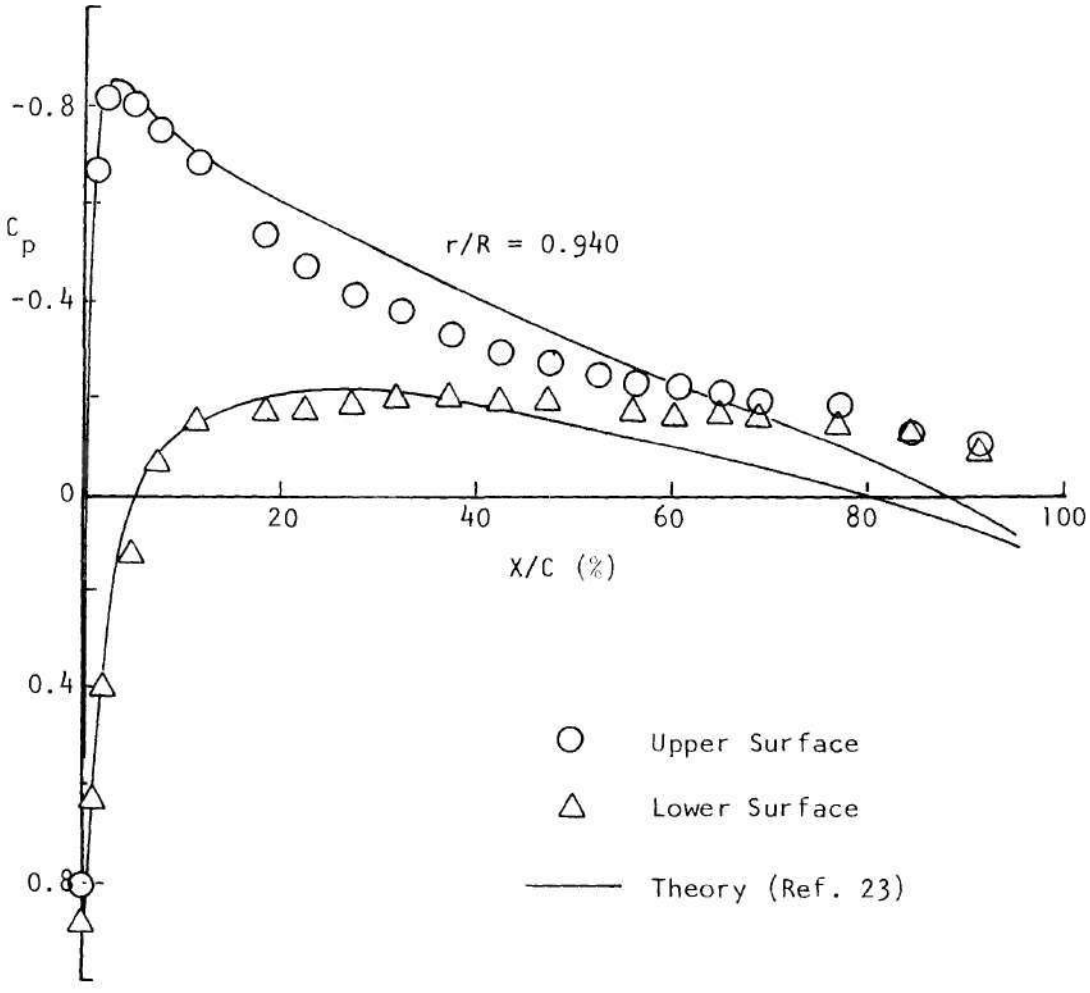

Figure 16. Comparison of the Experimental Values with Theoretical Solution, $\theta = 6.2°$, RPM = 1350.

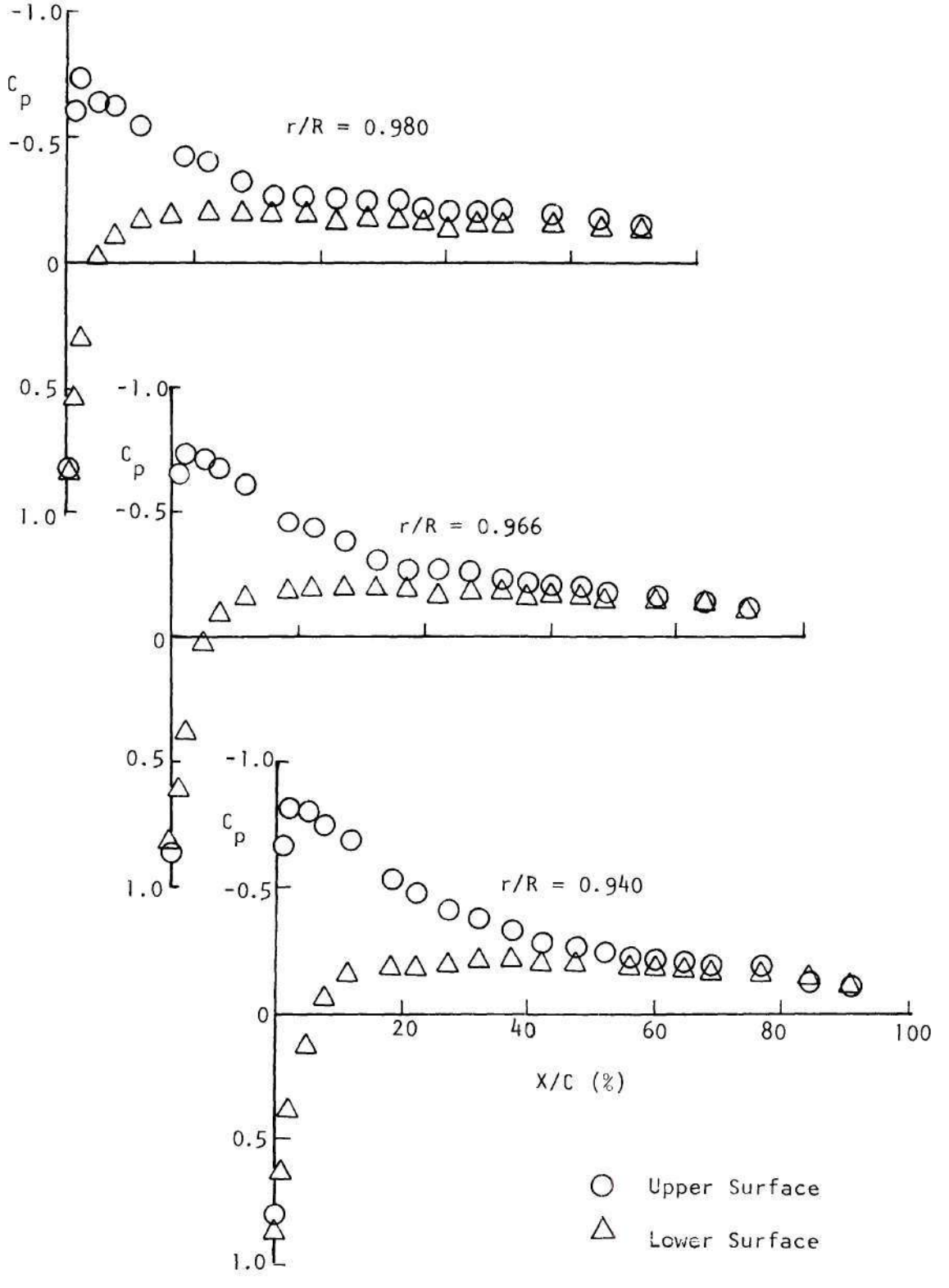

Figure 17. Pressure Distribution; θ = 6.2°, RPM = 1350. (Continues)

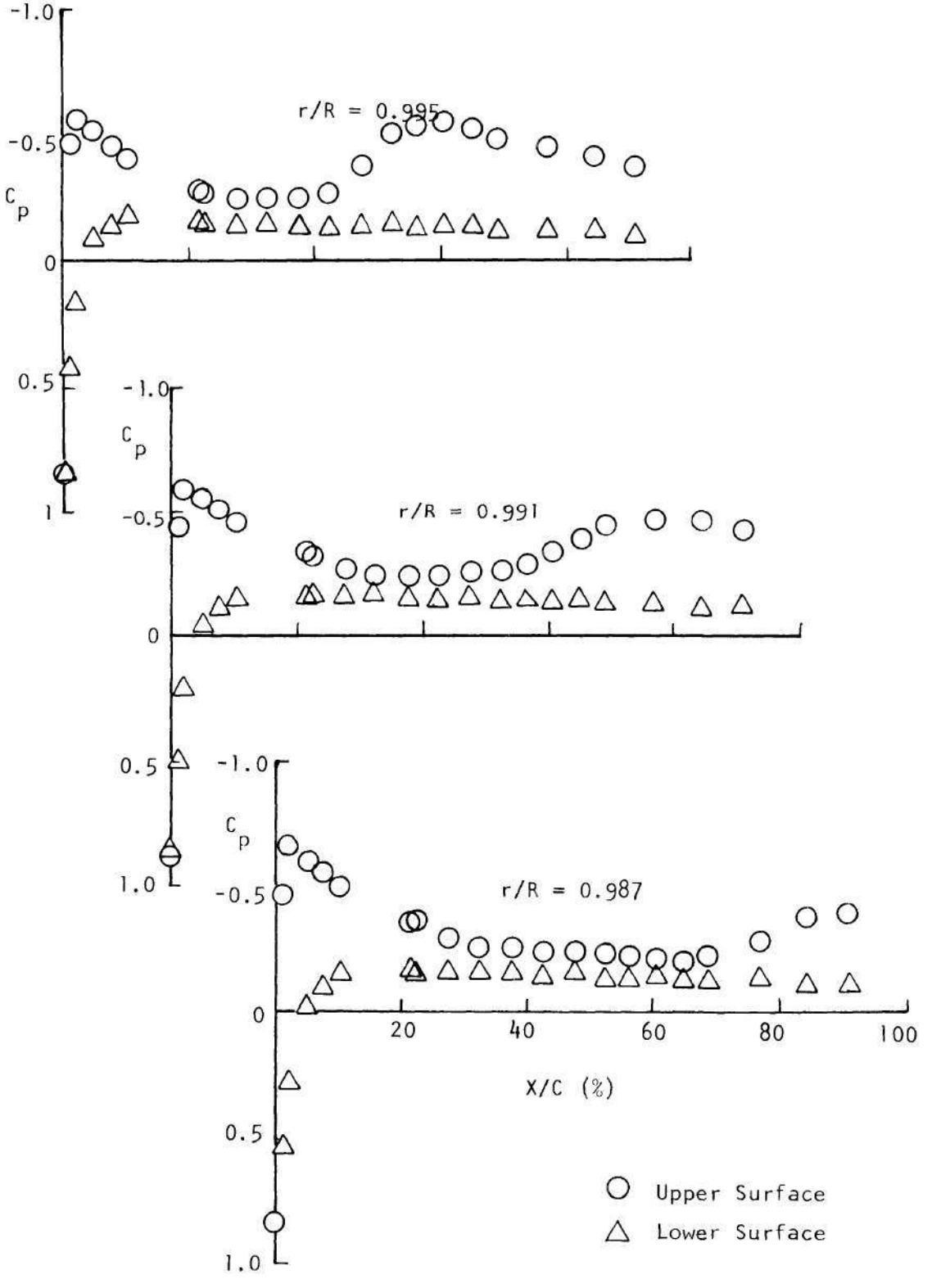

Figure 17. Pressure Distribution; $\theta = 6.2°$, RPM = 1350 (Continued)

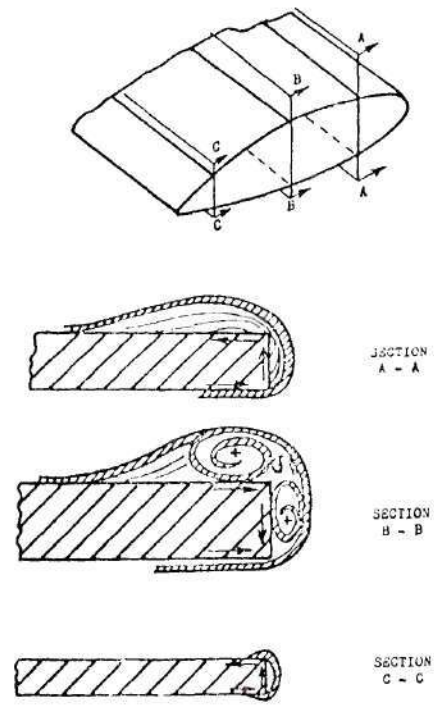

Figure 18. Sketch of Flow Patterns Around Square Tip (Ref. 2).

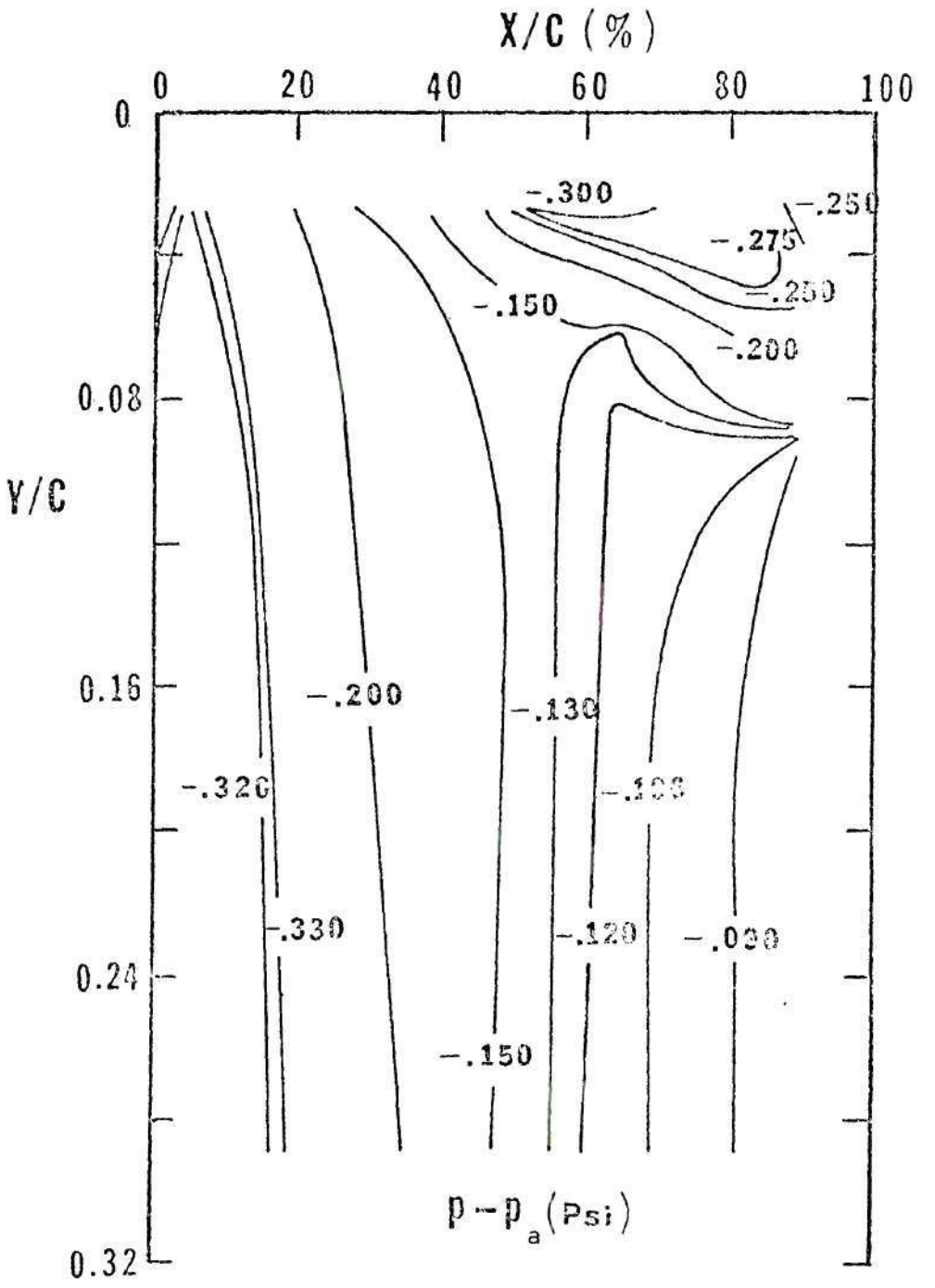

Figure 19. Constant Pressure Contours, Upper Surface, $\theta = 6.2°$, RPM = 1350.

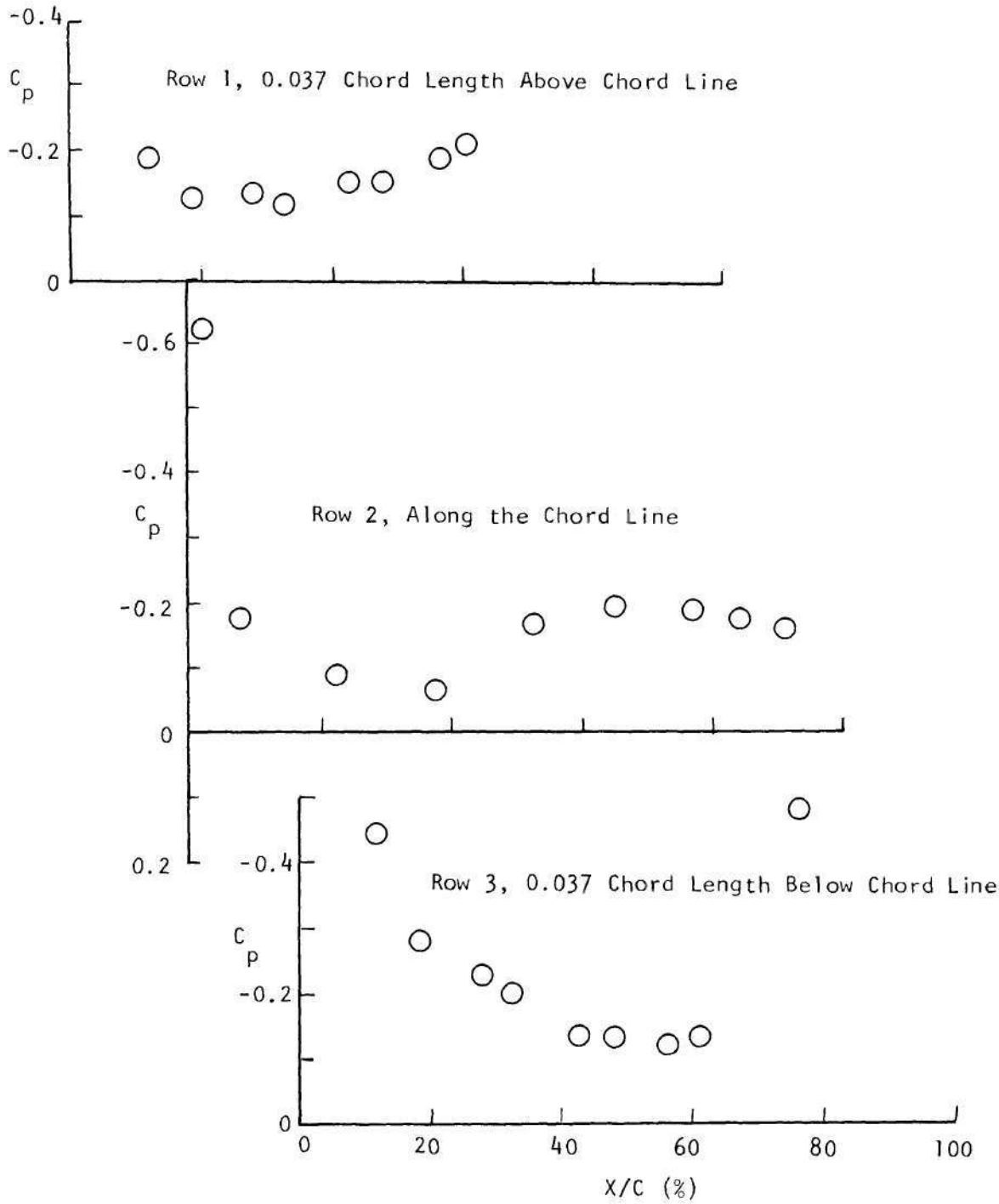

Figure 20. Pressure Distribution on Flat Tip; θ = 6.2°, RPM = 1350.

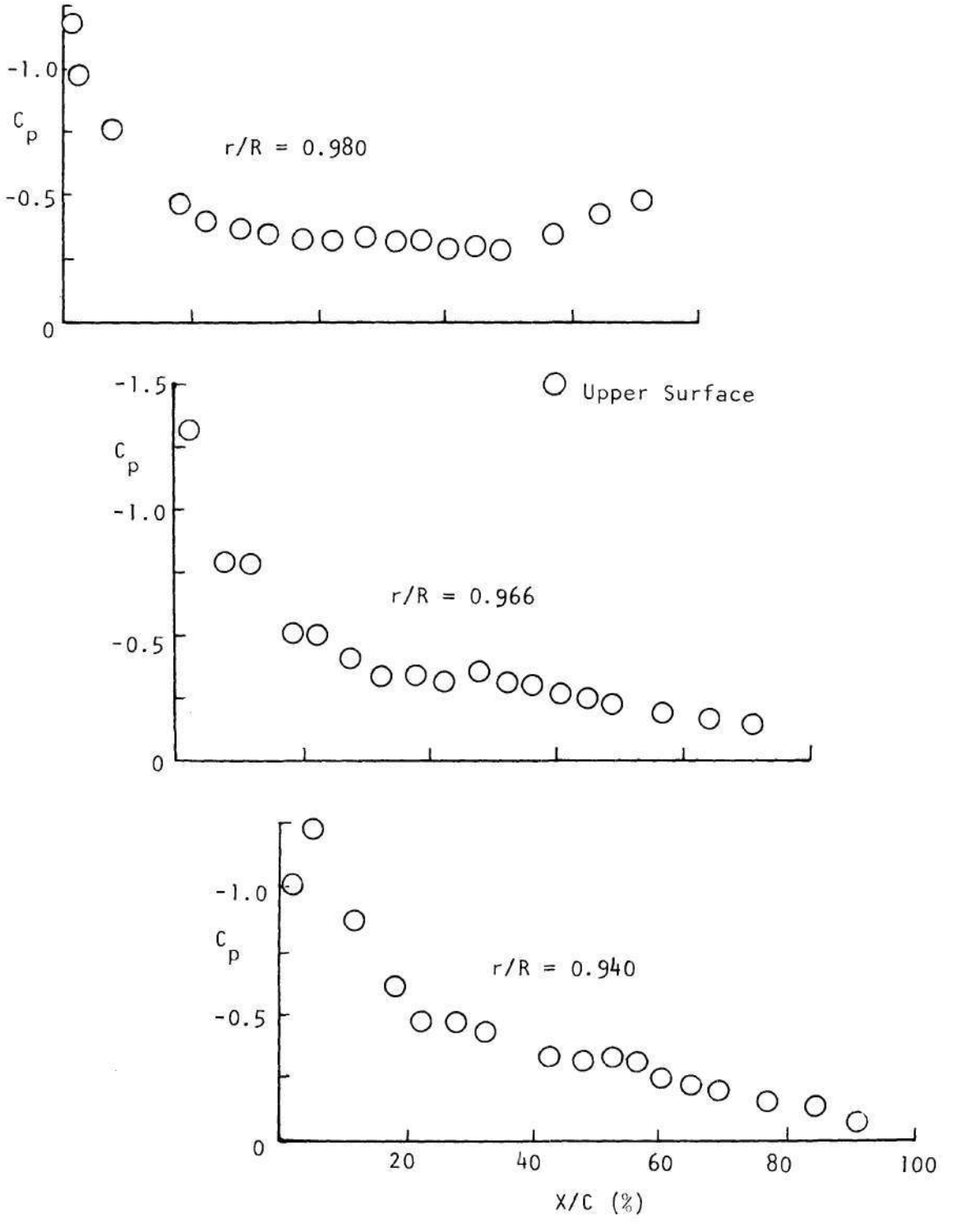

Figure 21. Pressure Distribution; θ = 11.4°, RPM = 1350. (Continues)

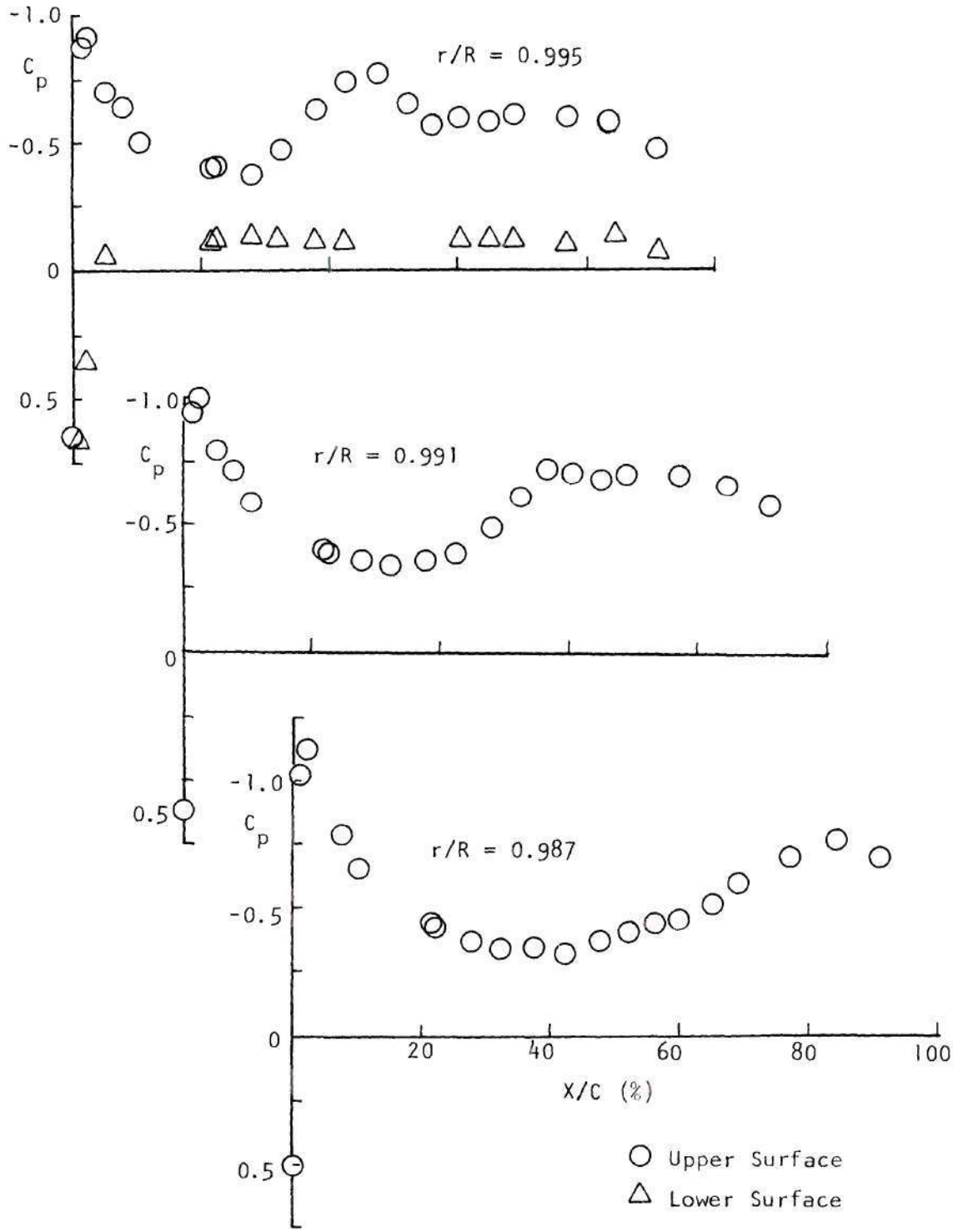

Figure 21. Pressure Distribution; θ = 11.4°; RPM = 1350. (Continued).

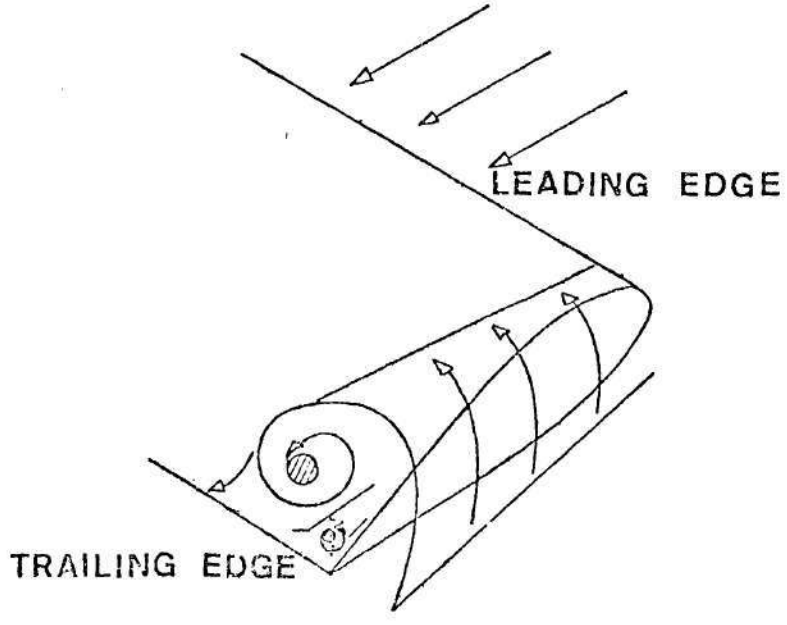

Figure 22. Vortex Formation Schematic, θ = 11.4° (Ref. 7).

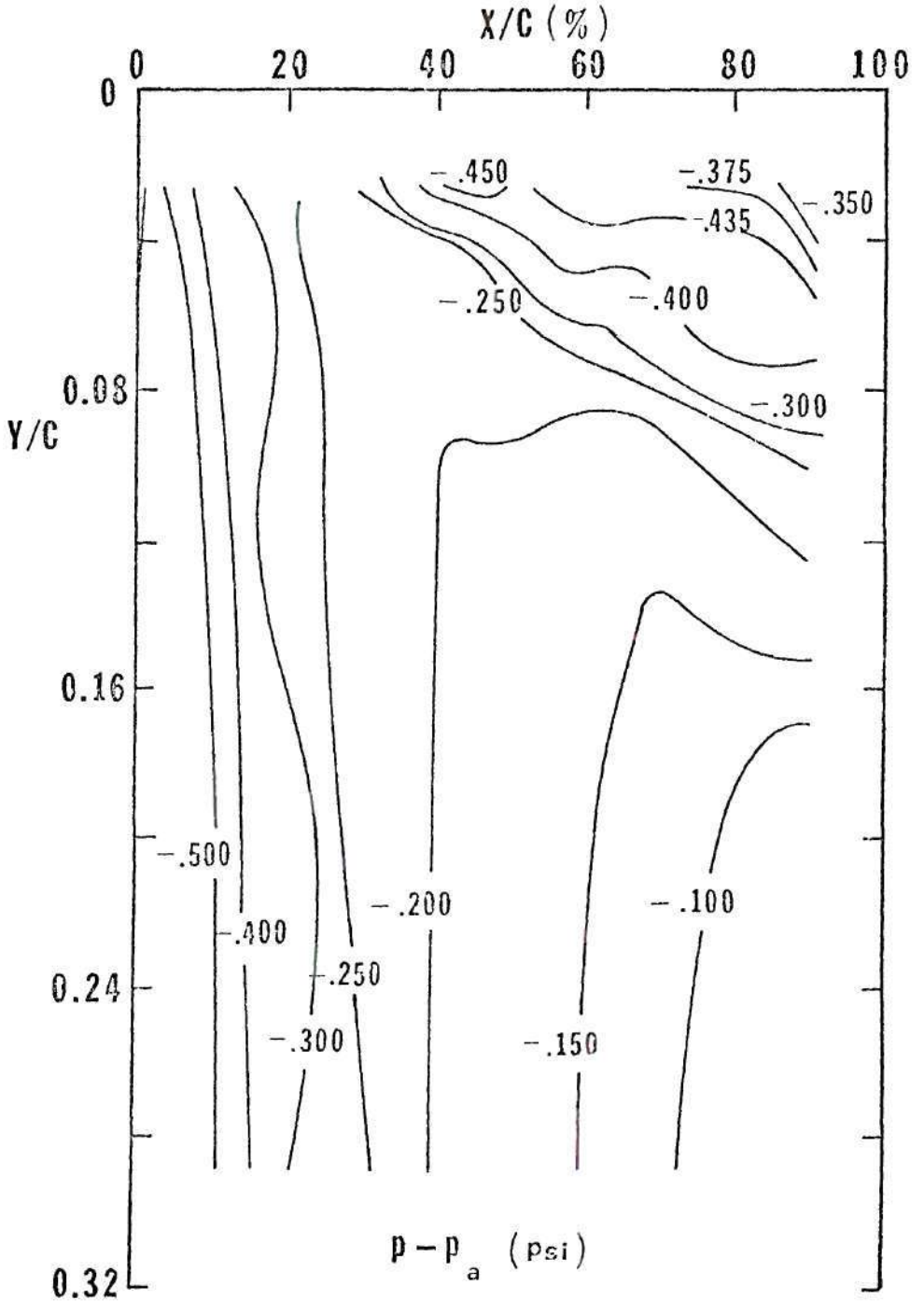

Figure 23. Constant Pressure Contours, Upper Surface, $\theta = 11.4°$, RPM = 1350.

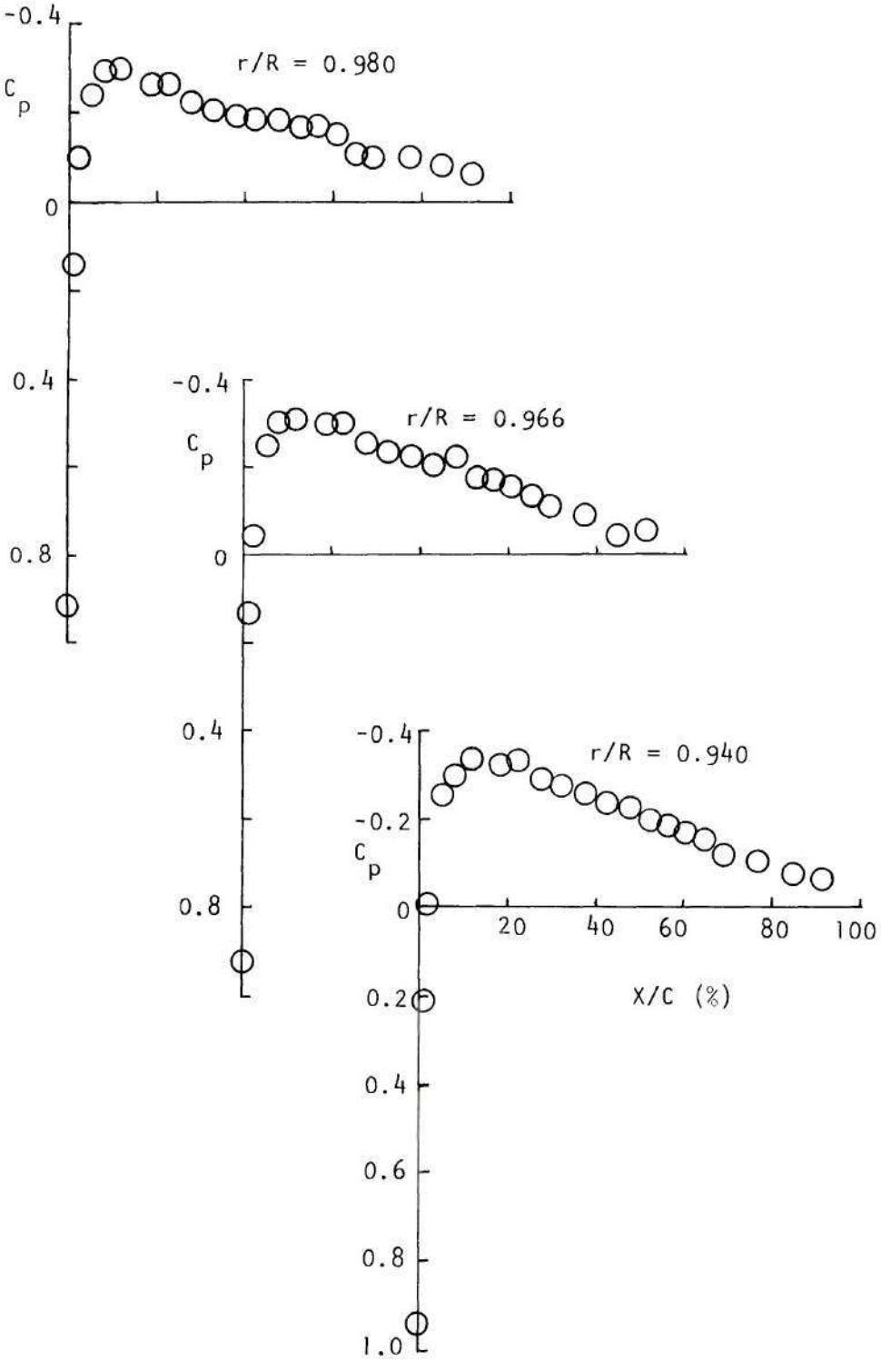

Figure 24. Pressure Distribution, θ = 0°, RPM = 1000. (Continues)

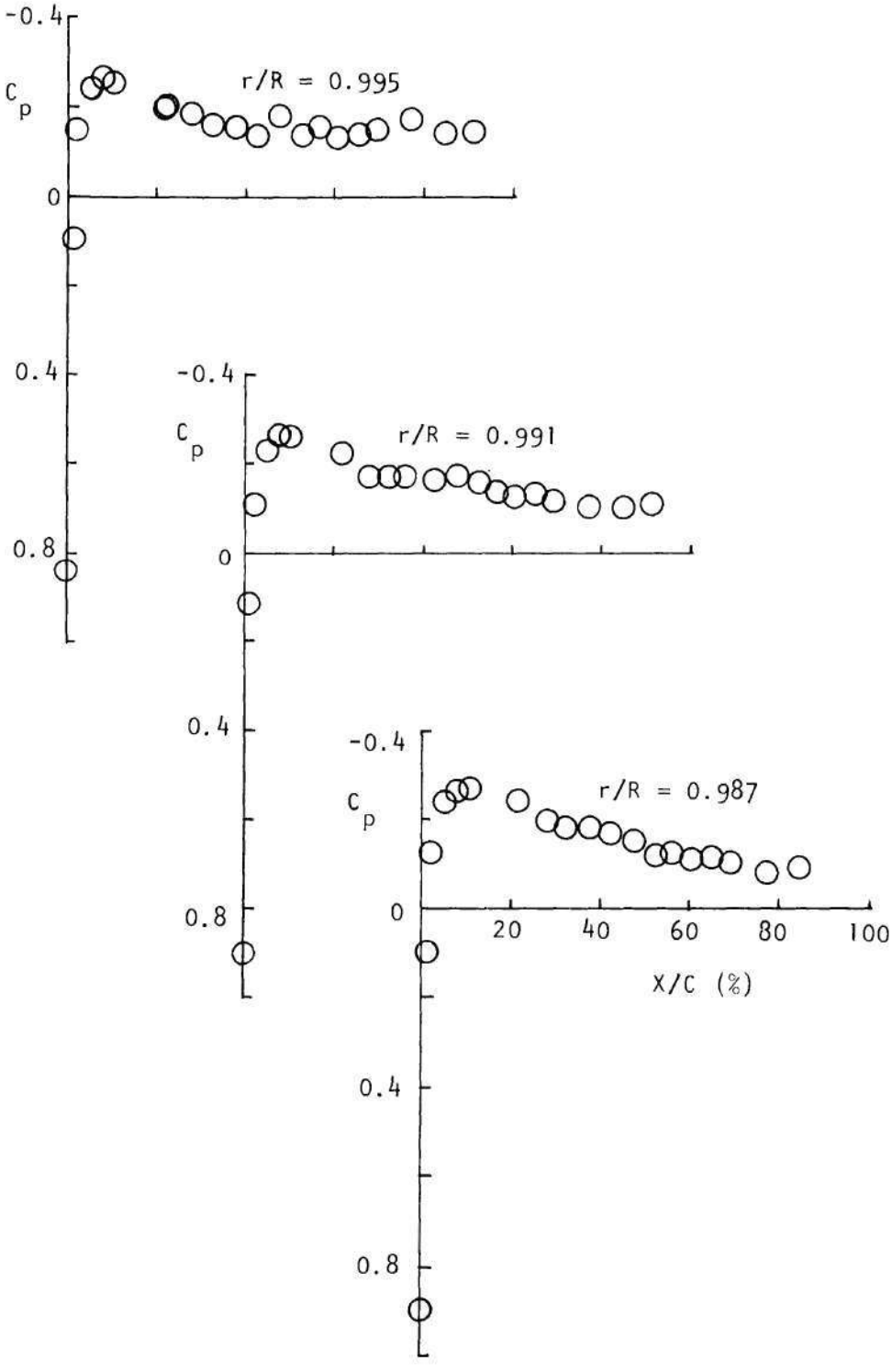

Figure 24. Pressure Distribution, $\theta = 0°$, RPM = 1000 (Continued).

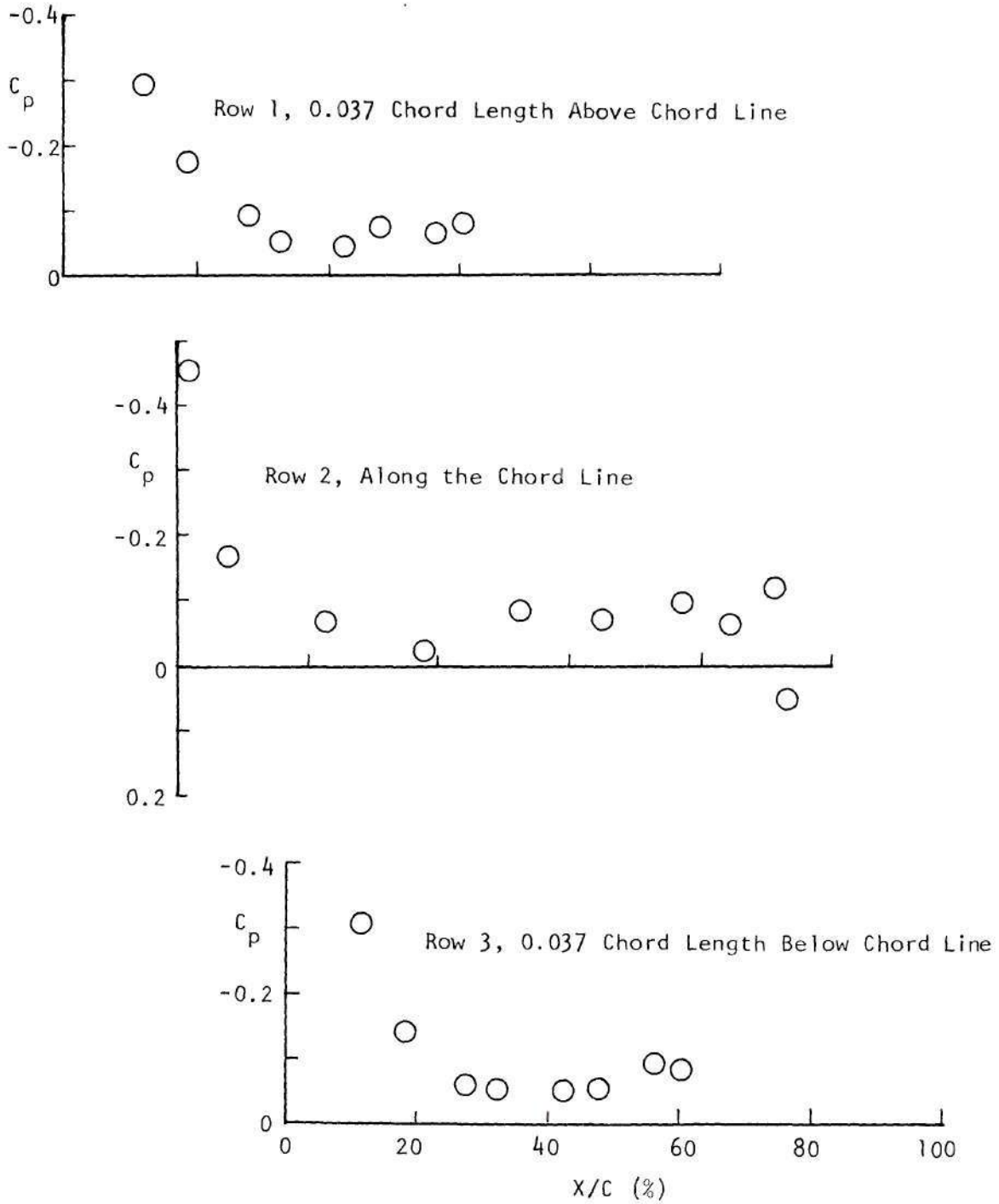

Figure 25. Pressure Distribution on Flat Tip; $\theta = 0°$, RPM = 1000.

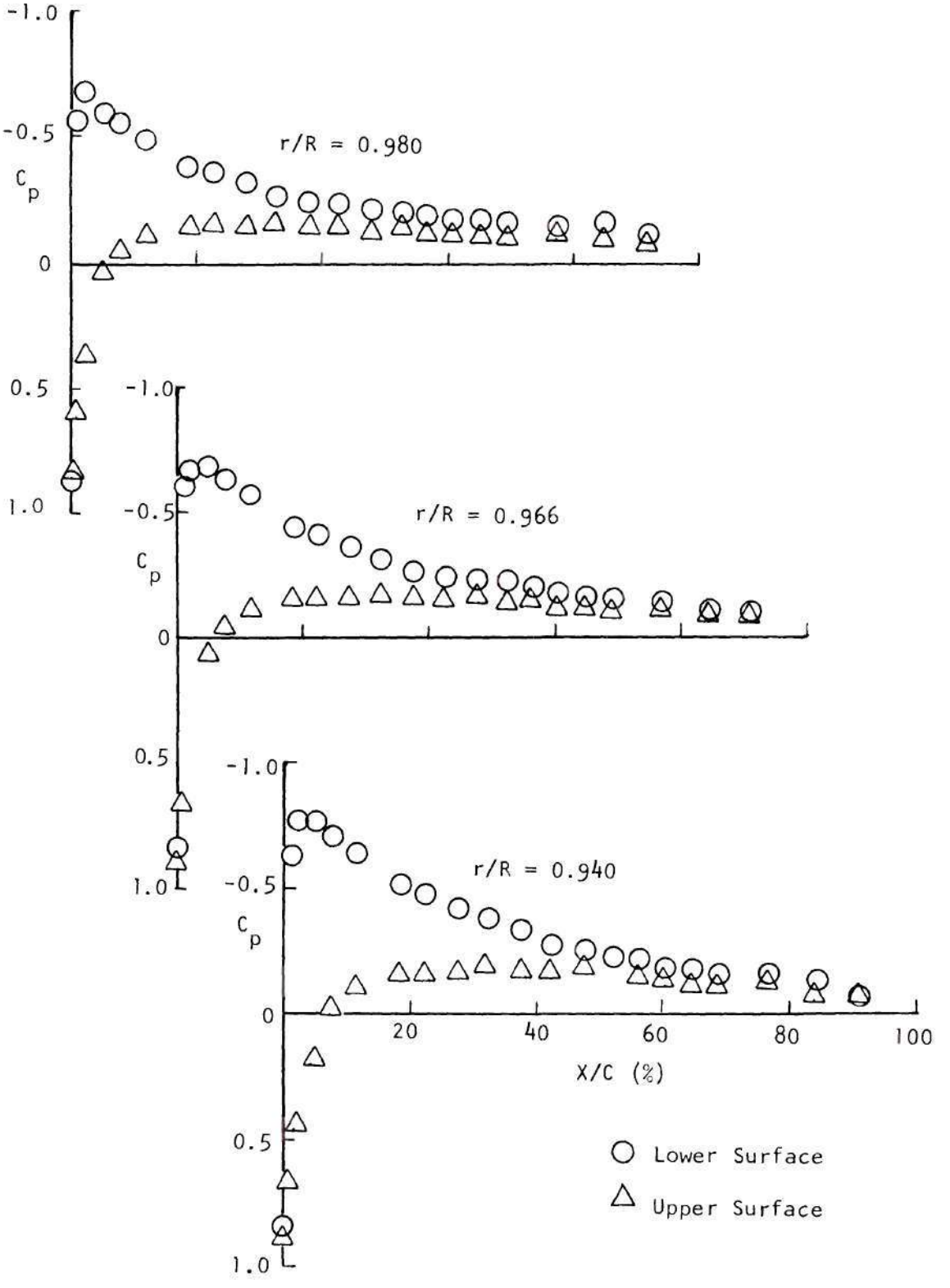

Figure 26. Pressure Distribution; $\theta = 6.2$, RPM = 1000. (Continues)

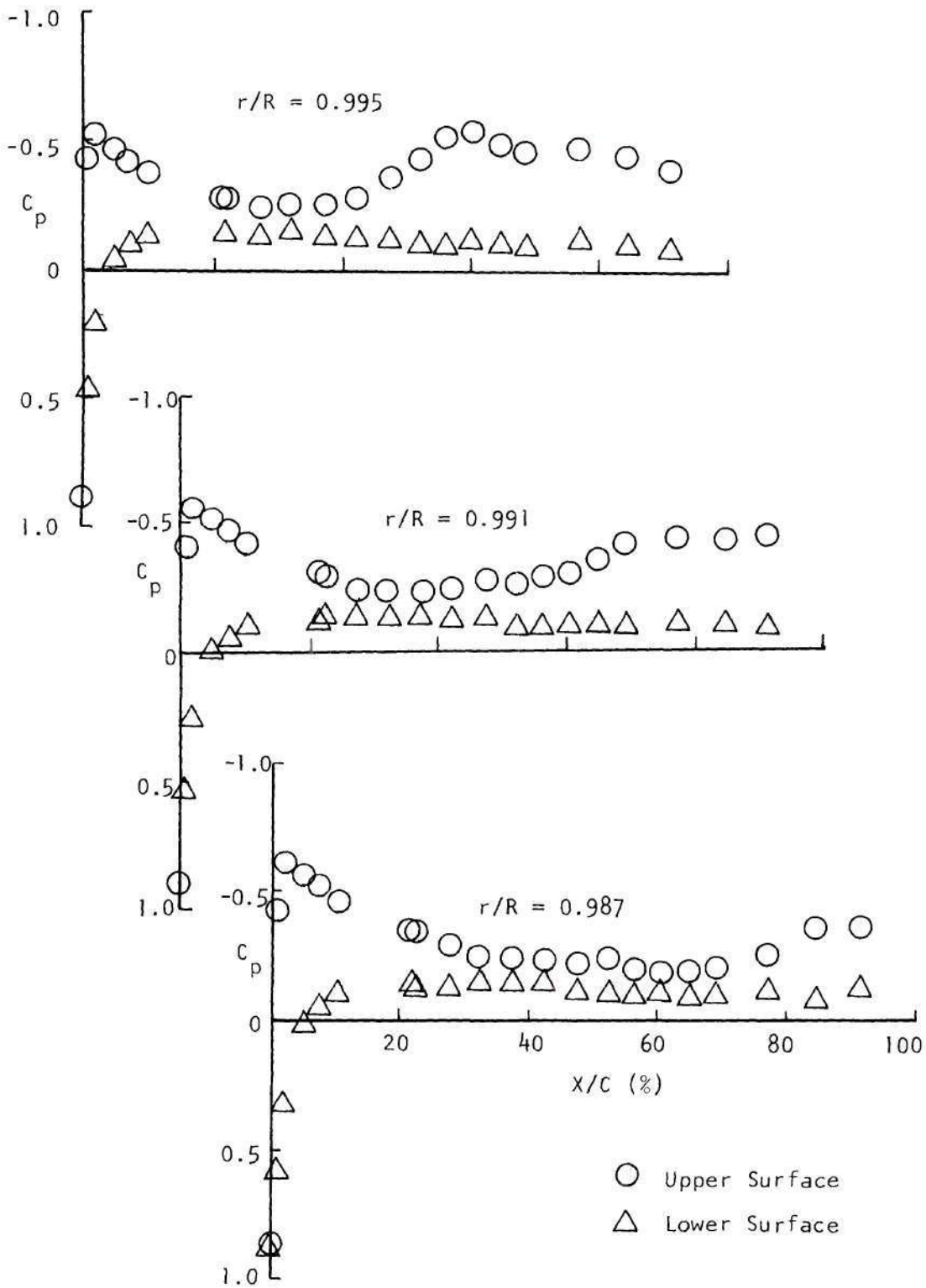

Figure 26. Pressure Distribution; $\theta = 6.2°$, RPM = 1000 (Continued).

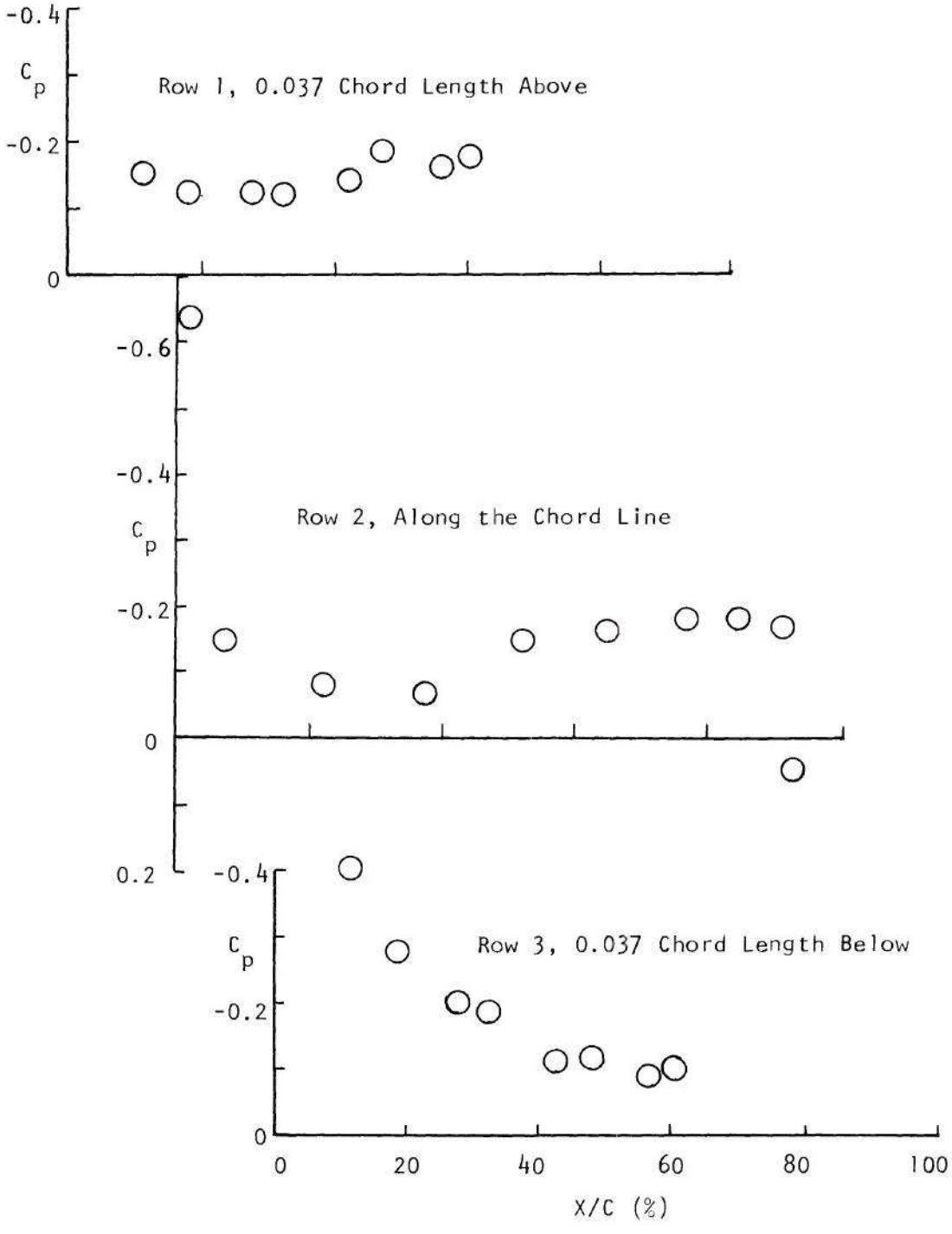

Figure 27. Pressure Distribution on Flat Tip; $\theta = 6.2°$, RPM = 1000.

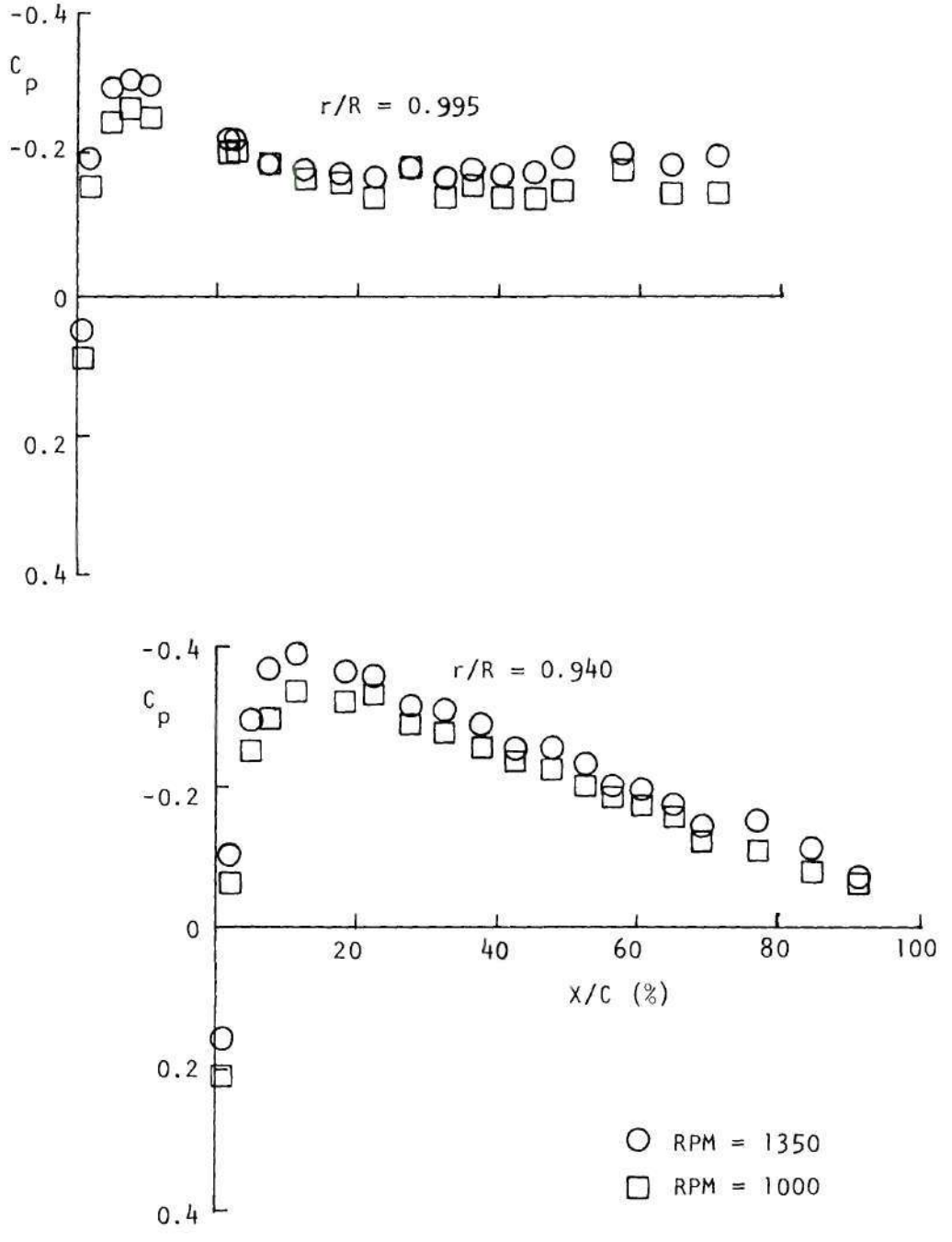

Figure 28. Comparison of Pressure Coefficient Distributions at RPMS 1350 and 1000, $\theta = 0°$.

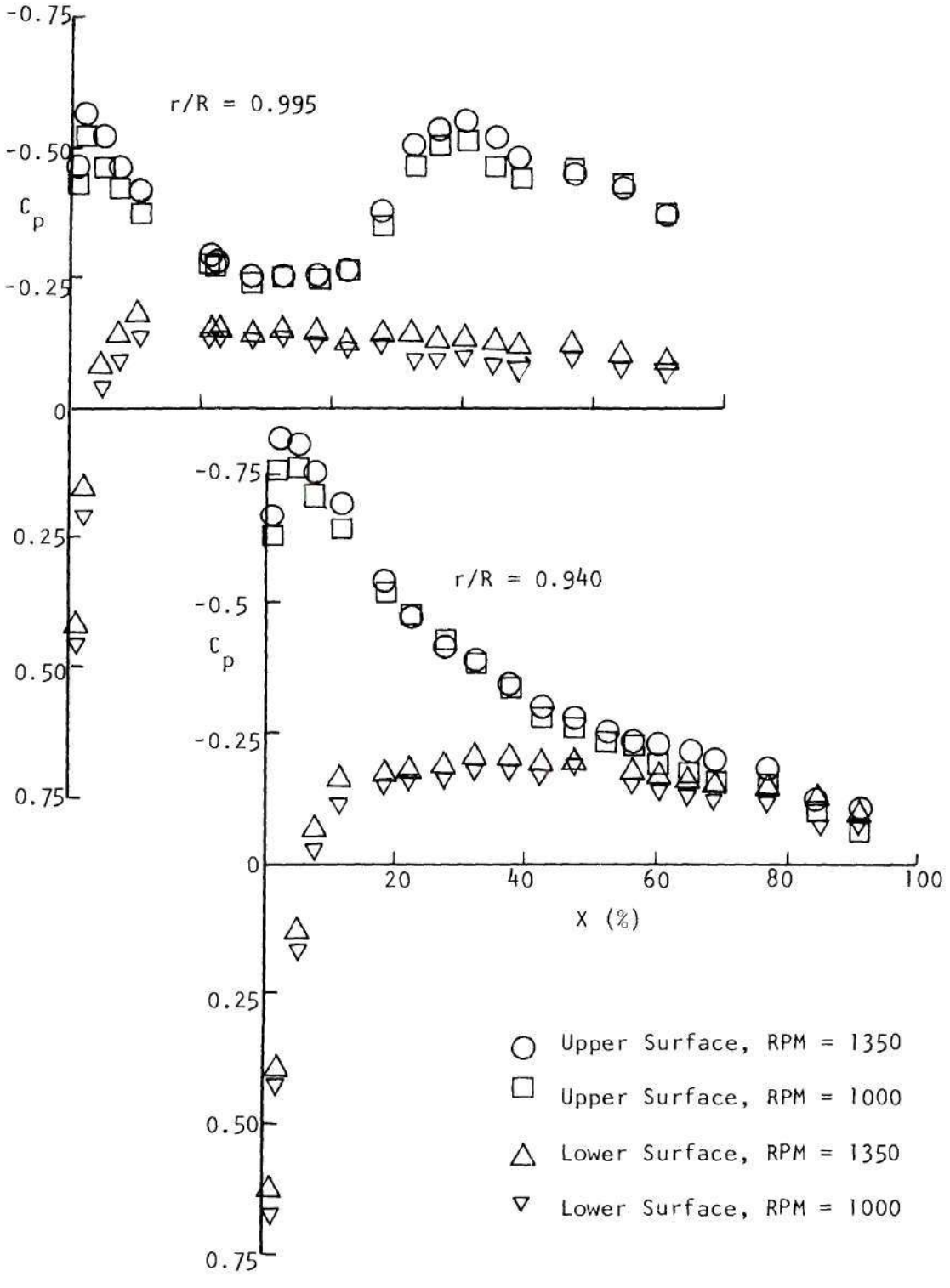

Figure 29. Comparison of Pressure Distributions at 1000 and 1350 RPM, $\theta = 6.2°$.

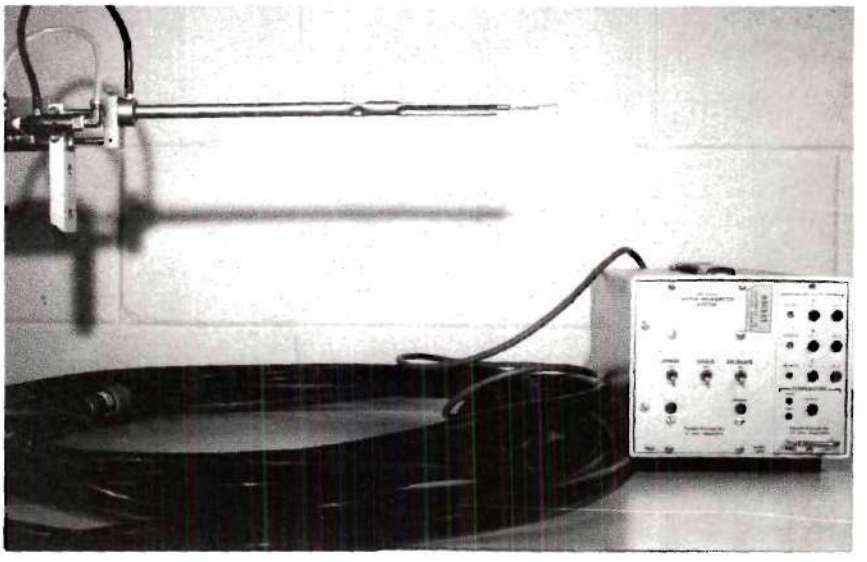

(a) Anemometer Probe and Control Circuit Box

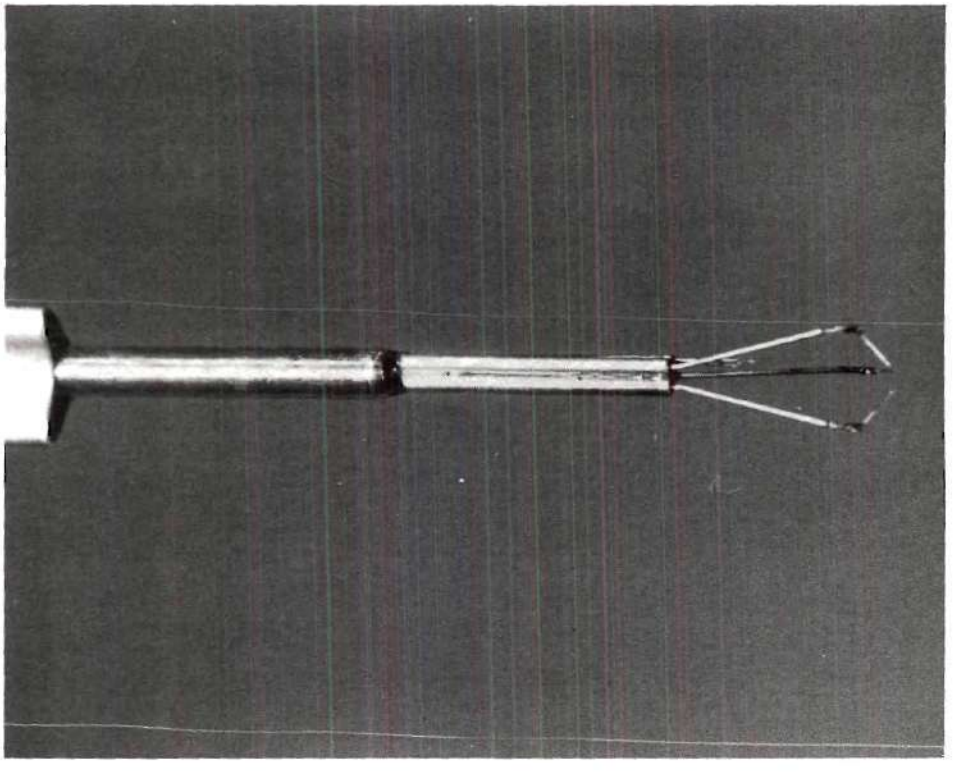

(b) Close-up of Sensors

Figure 30. Total Vector Anemometer System

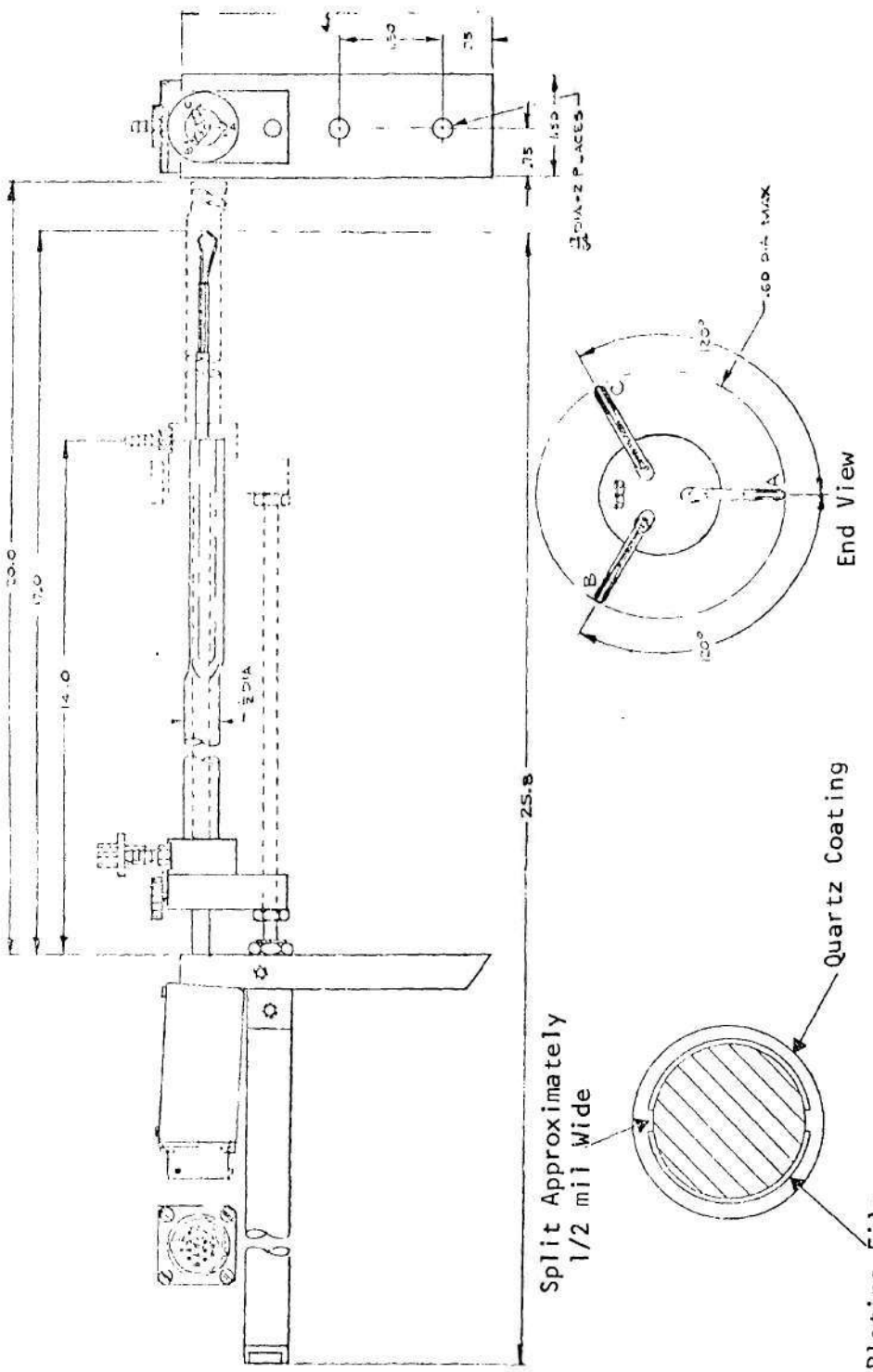

Figure 31. Schematic of Anemometer Probe.

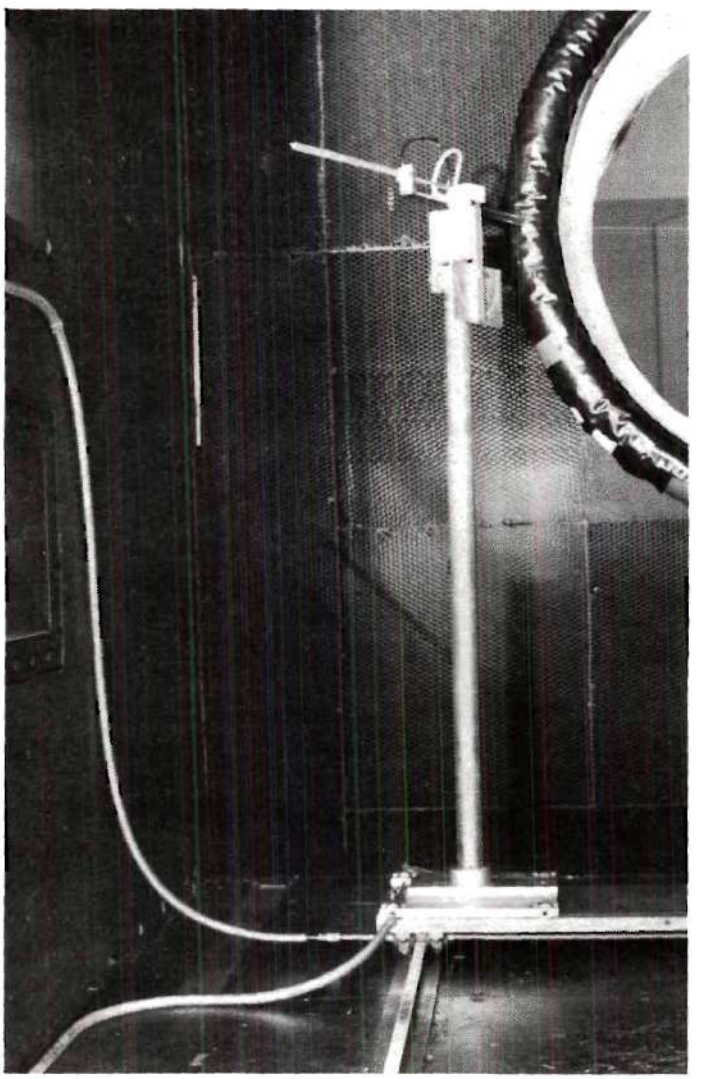

Figure 32. Actuator with Probe Installed

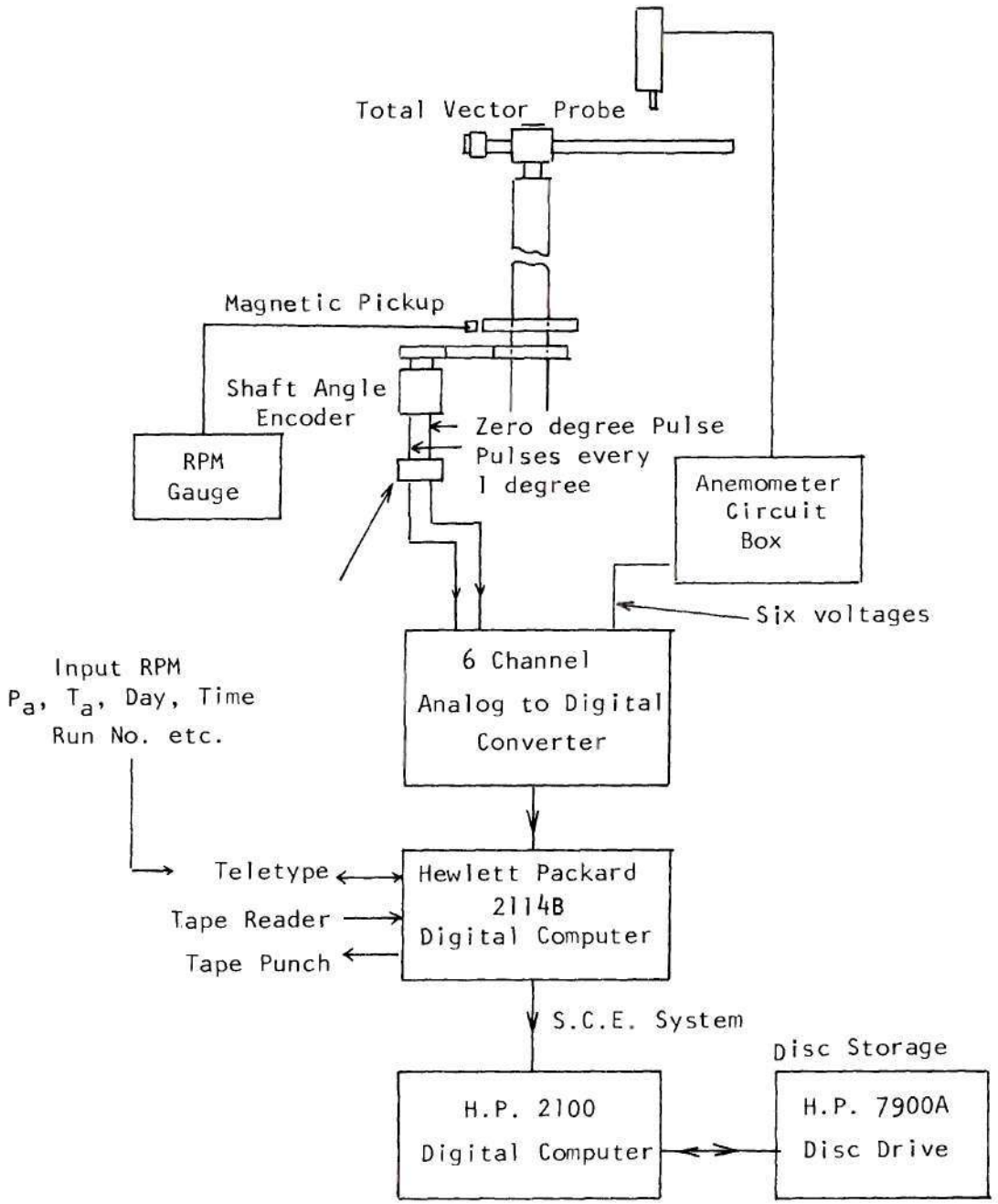

Figure 33. Block Diagram of Data Acquisition System for Velocity Measurements.

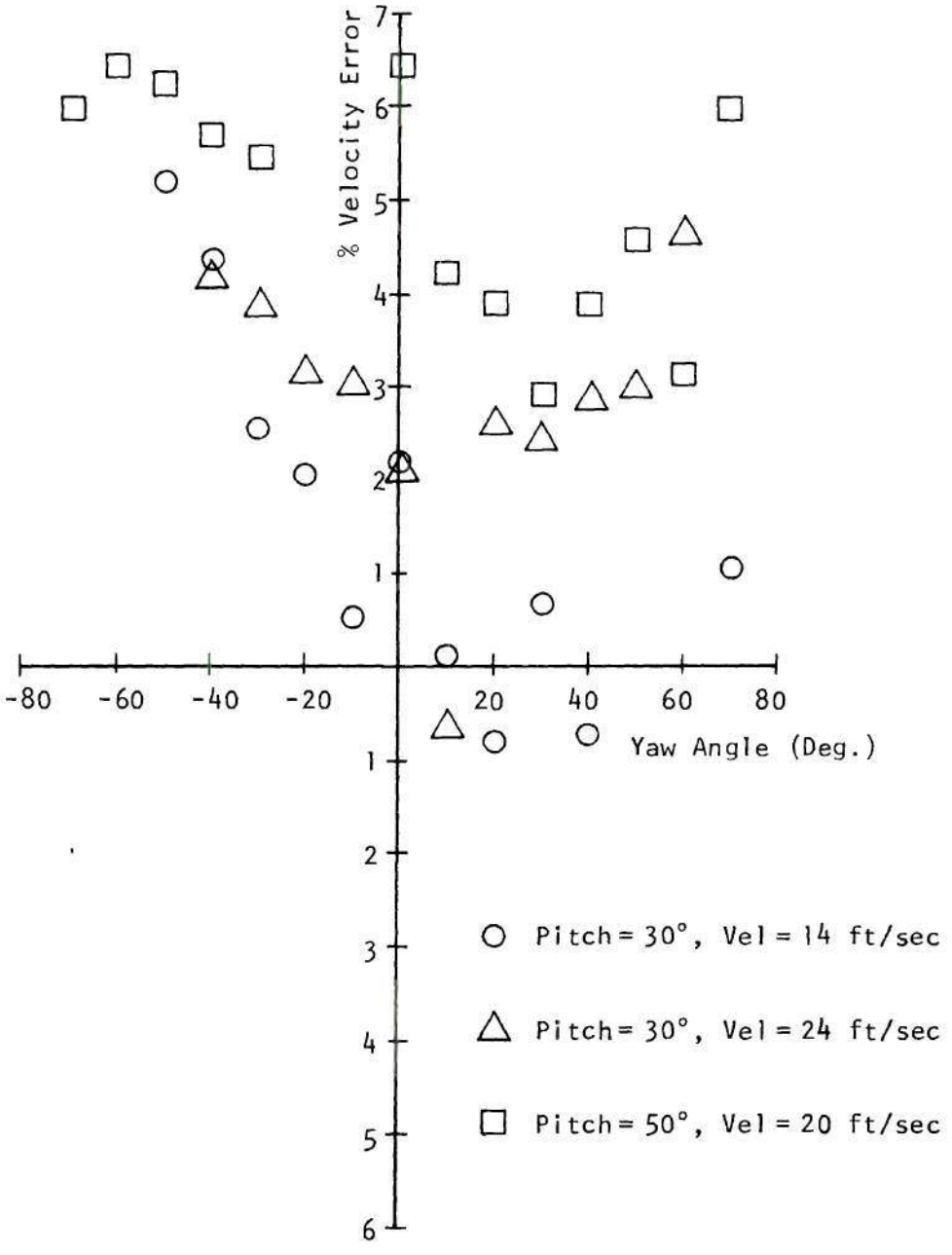

Figure 34. Percentage Error in Total Velocity, Pitch = 30°, 50°.

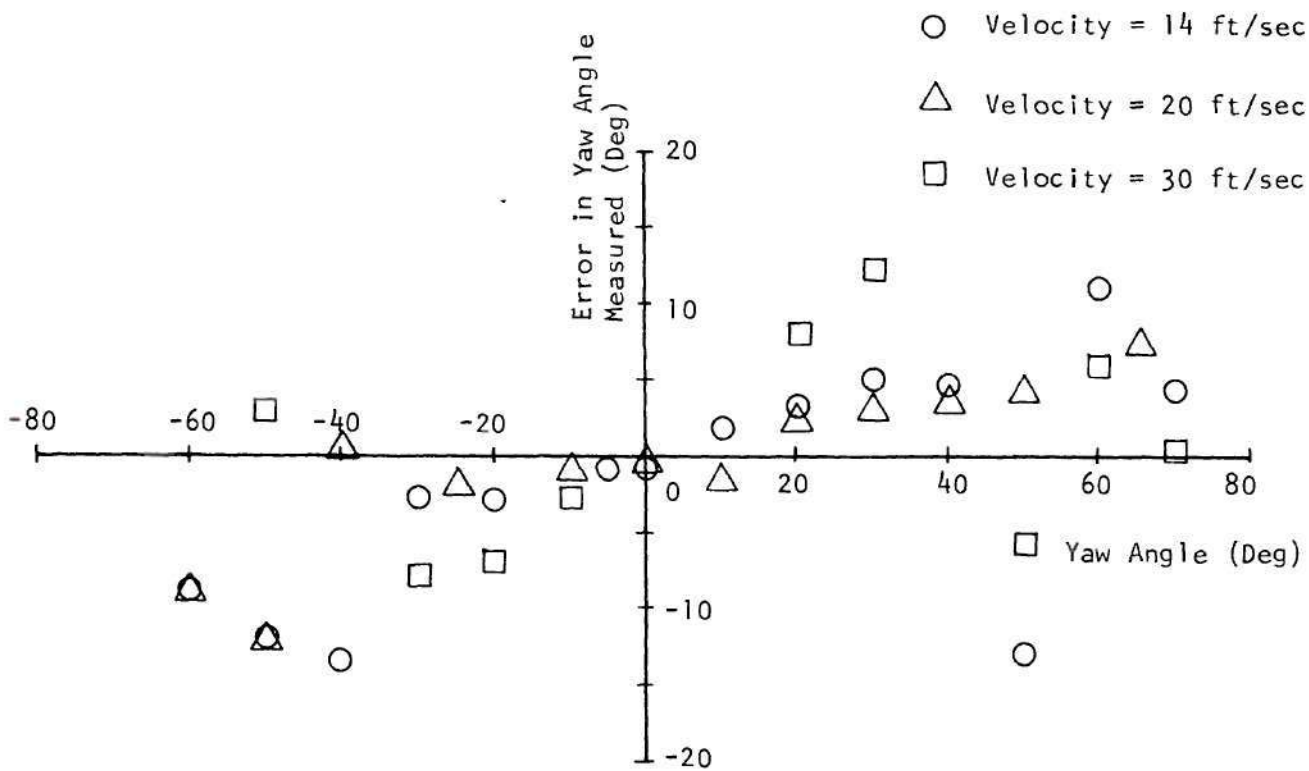

Figure 35. Angular Error in Yaw, Pitch Angle = 20°.

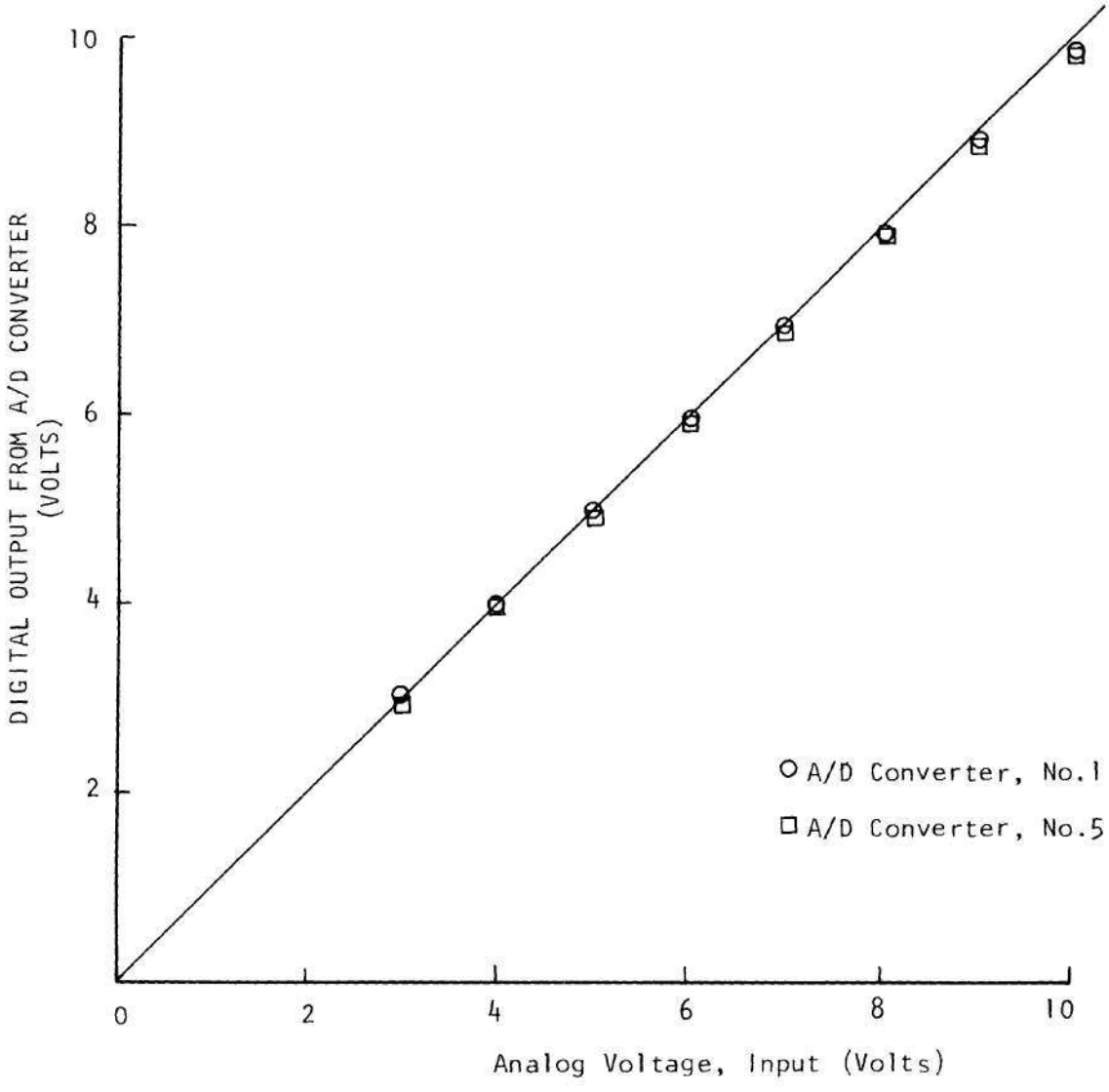

Figure 36. Non-Linearity of A/D Converters.

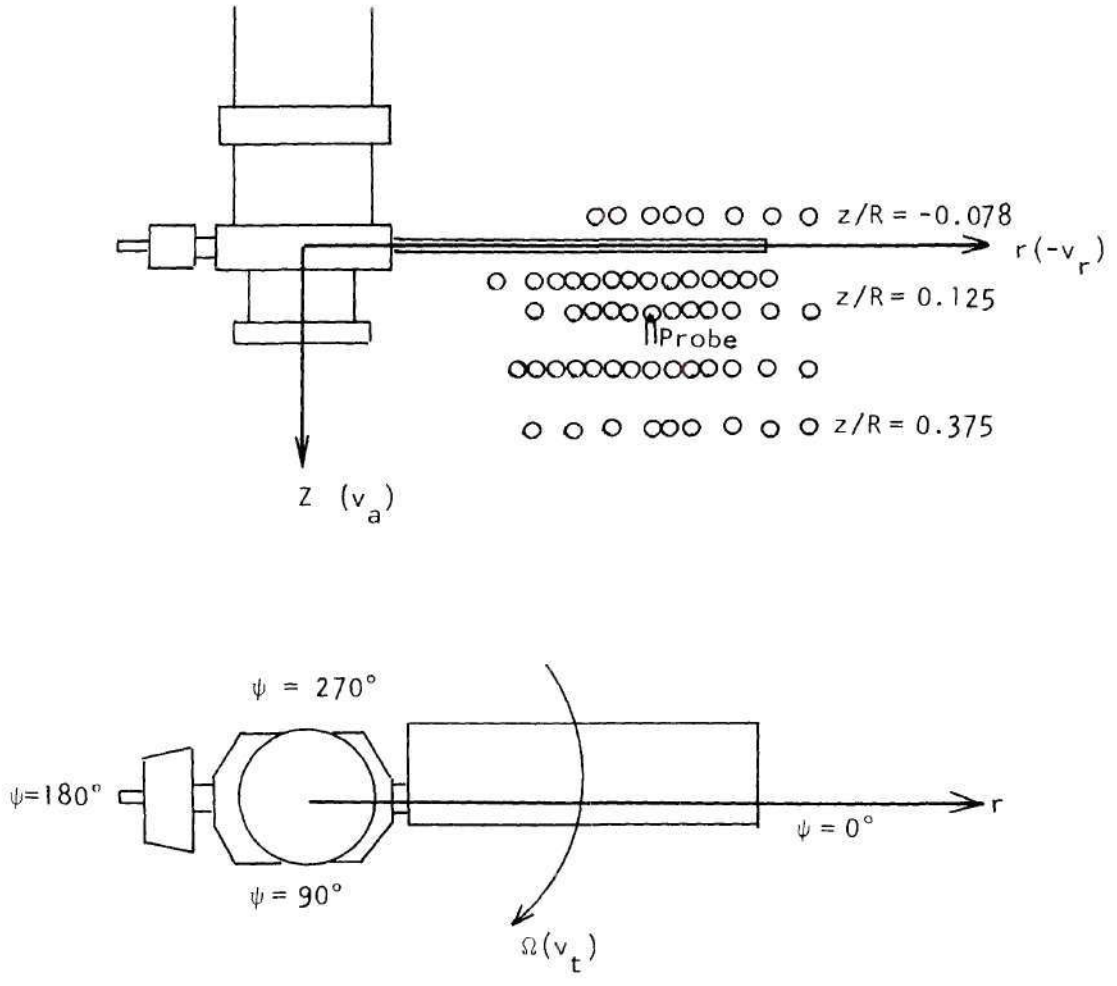

Figure 37. Schematic of Rotor Coordinate System and Measurement Locations.

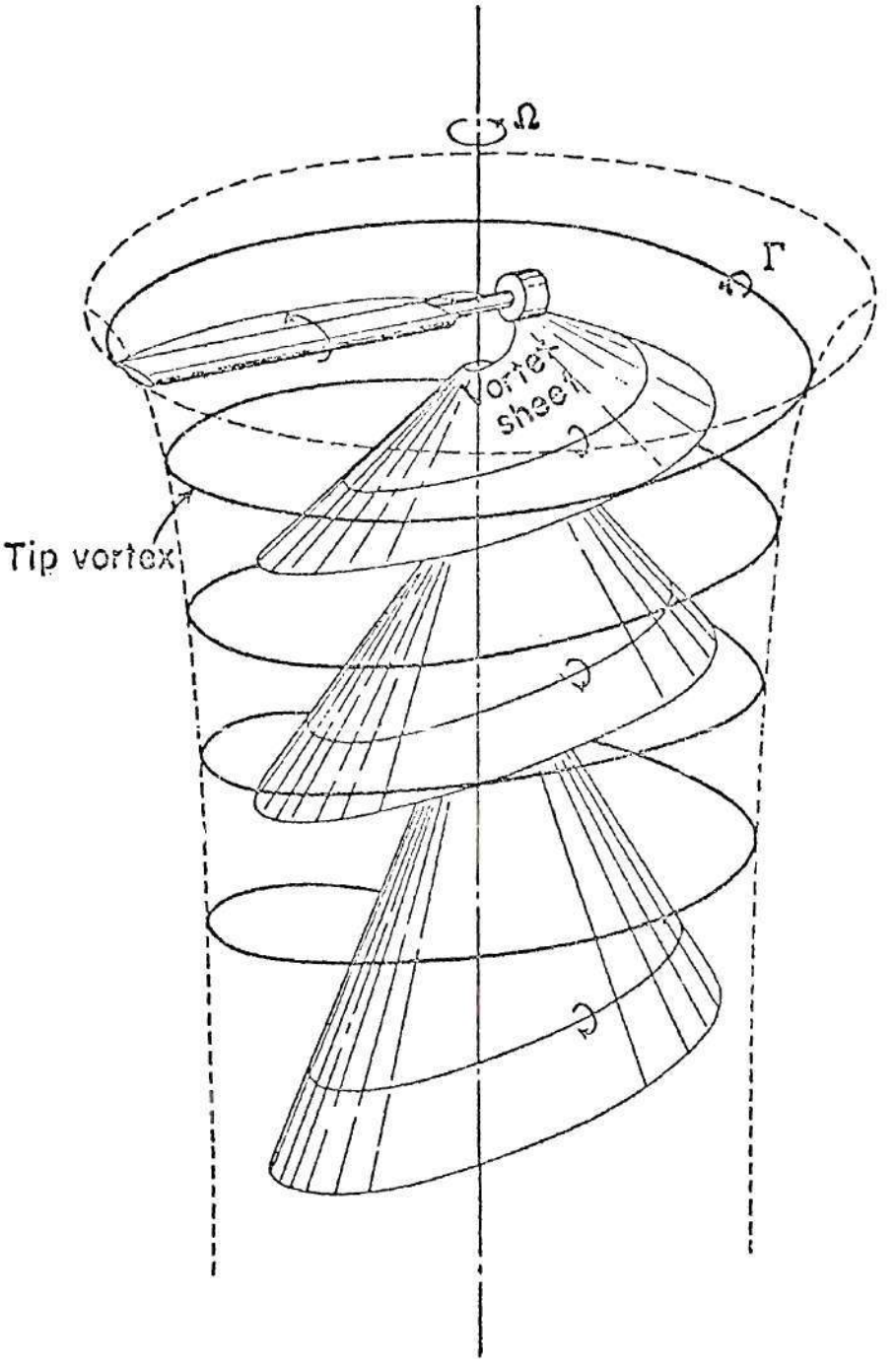

Figure 38. Schematic of Wake of a Single-Bladed Rotor in Hover.

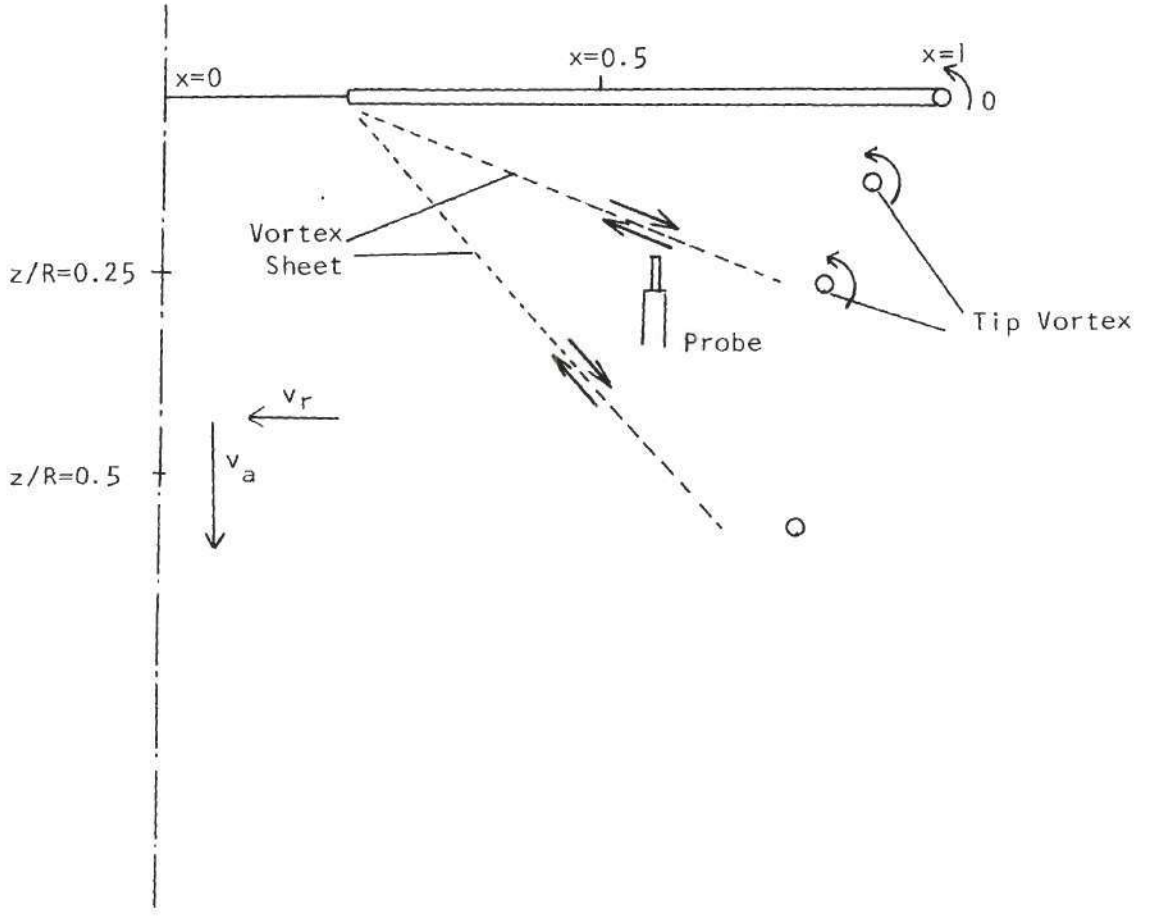

Figure 39. Schematic of Wake Cross Section.

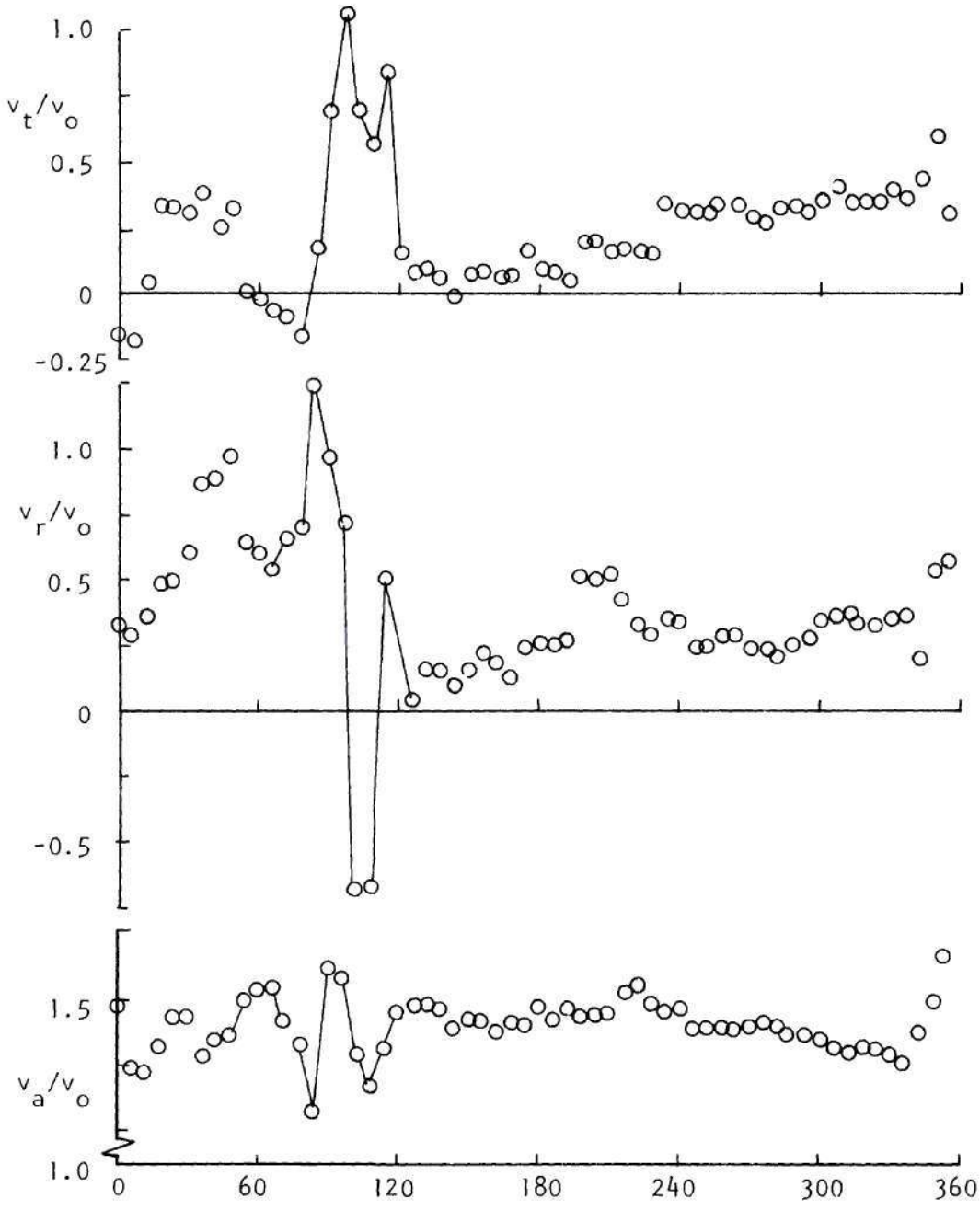

(a) x = 0.542

Figure 40. Distribution of Instantaneous Velocity Components Across the Vortex Sheet, z/R = 0.0625. (Continues)

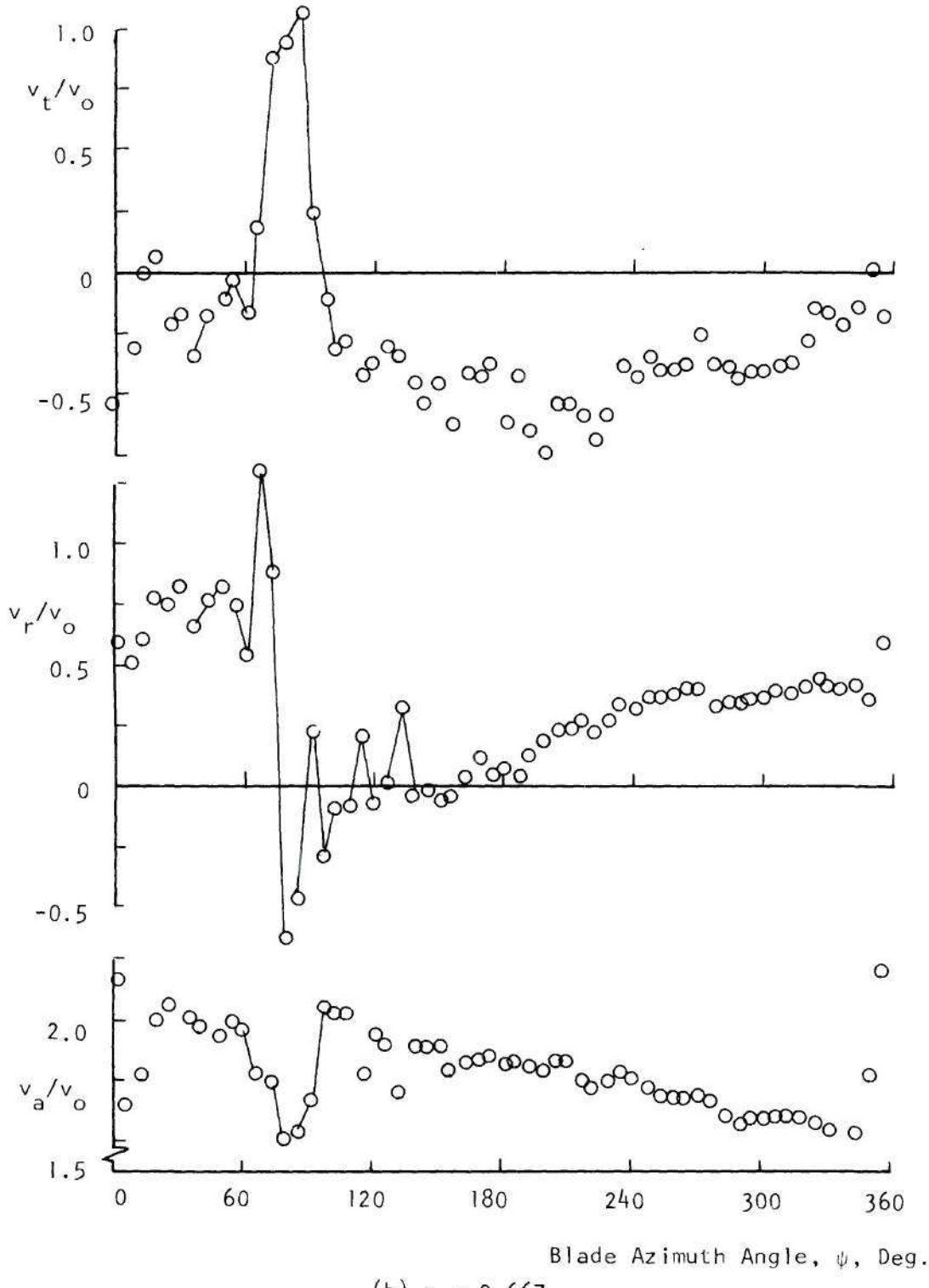

(b) x = 0.667

Figure 40. Distribution of Instantaneous Velocity Components Across the Vortex Sheet, z/R = 0.0625 (Continued).

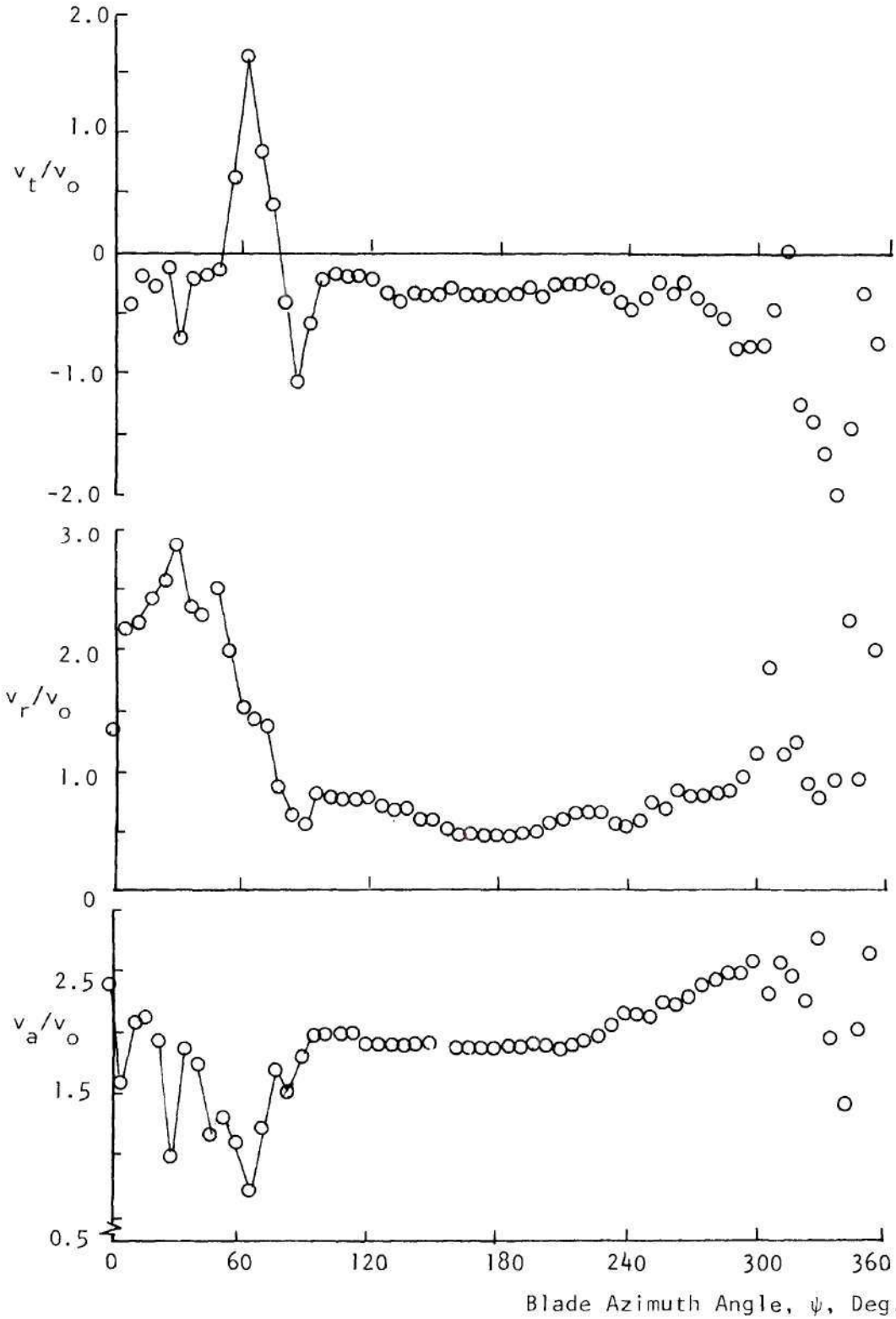

(c) x = 0.791

Figure 40. Distribution of Instantaneous Velocity Components Across the Vortex Sheet, z/R = 0.0625 (Continued).

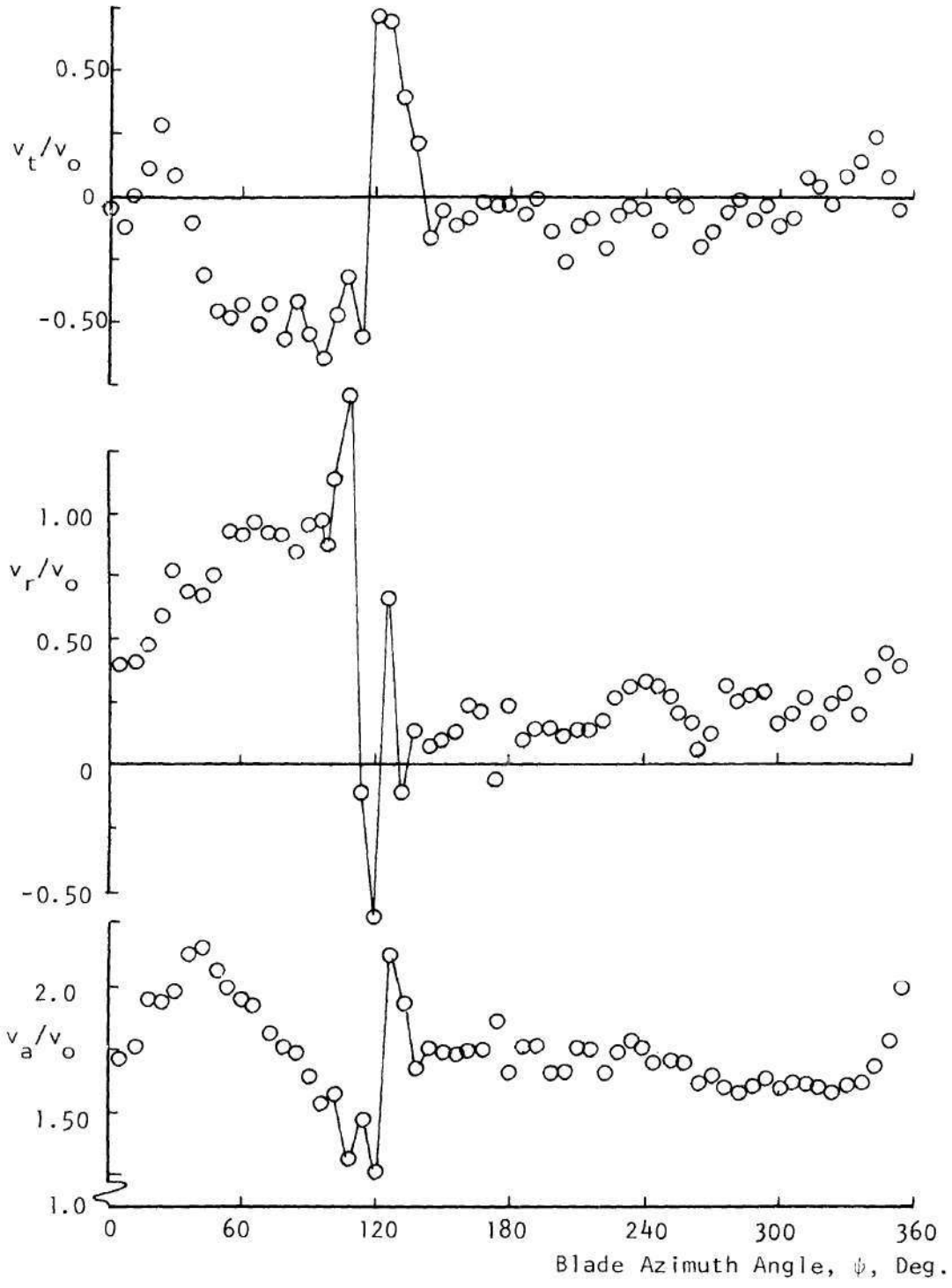

Figure 41. Distribution of Instantaneous Velocity Components Across a Vortex Sheet, x = 0.667, z/R = 0.125.

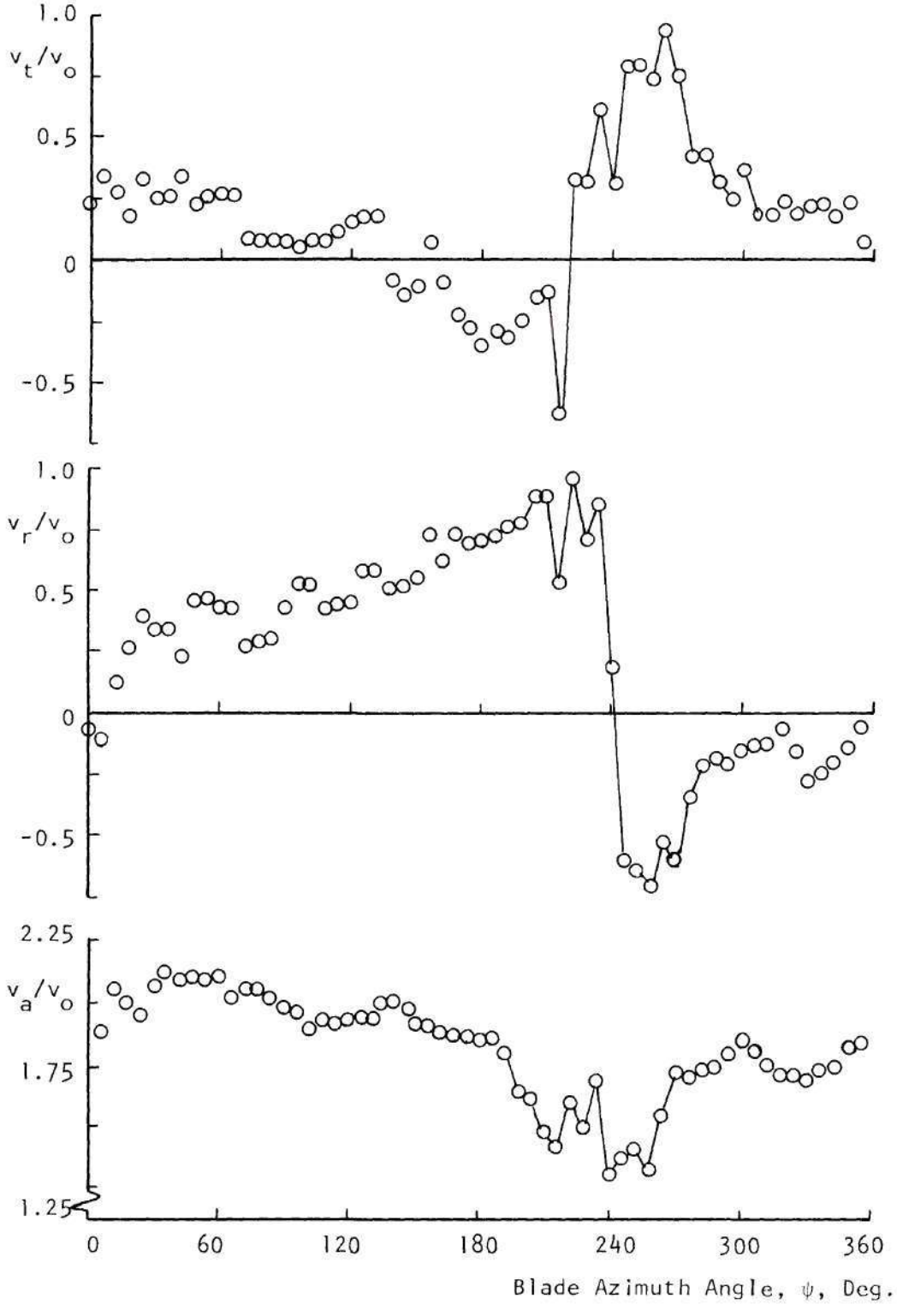

Figure 42. Distribution of Instantaneous Velocity Components Across the Vortex Sheet, x = 0.625, z/R = 0.25.

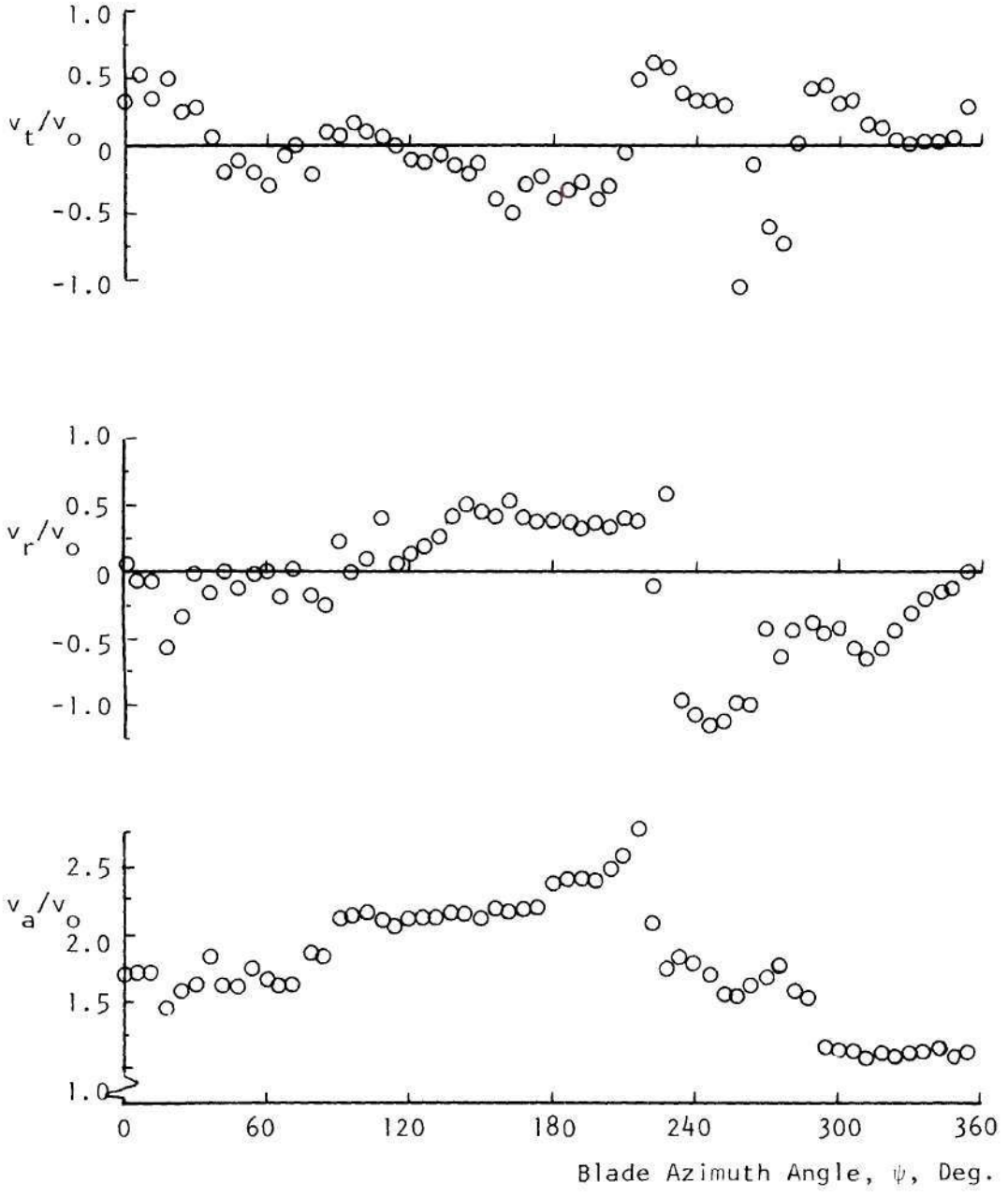

Figure 43. Distribution of Instantaneous Velocity Components Across the Vortex Sheet, z/R = 0.375, x = 0.583.

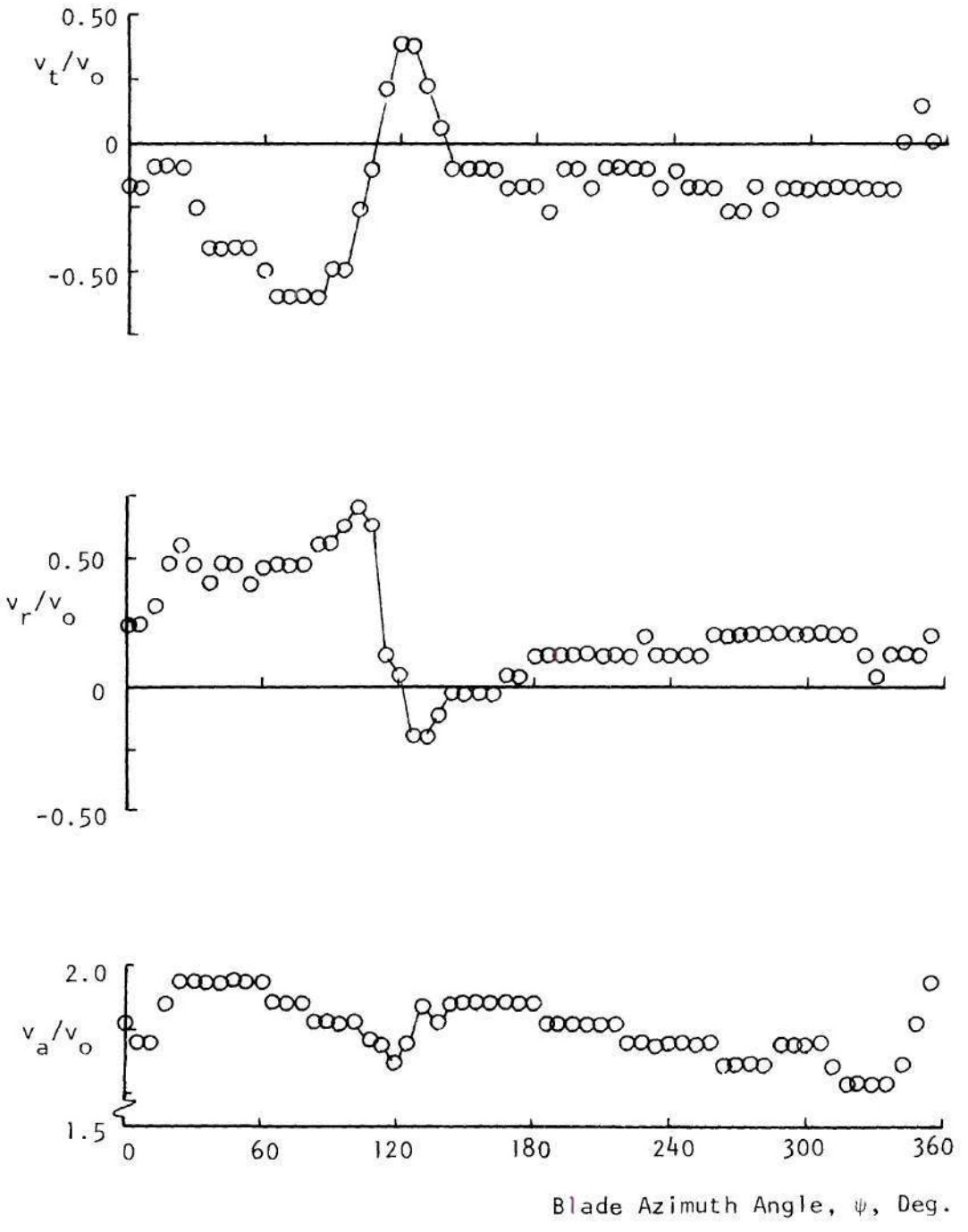

Figure 44. Distribution of Velocity Components Across the Vortex Sheet, Averaged over 10 Revolutions $x = 0.667$, $z/R = 0.125$.

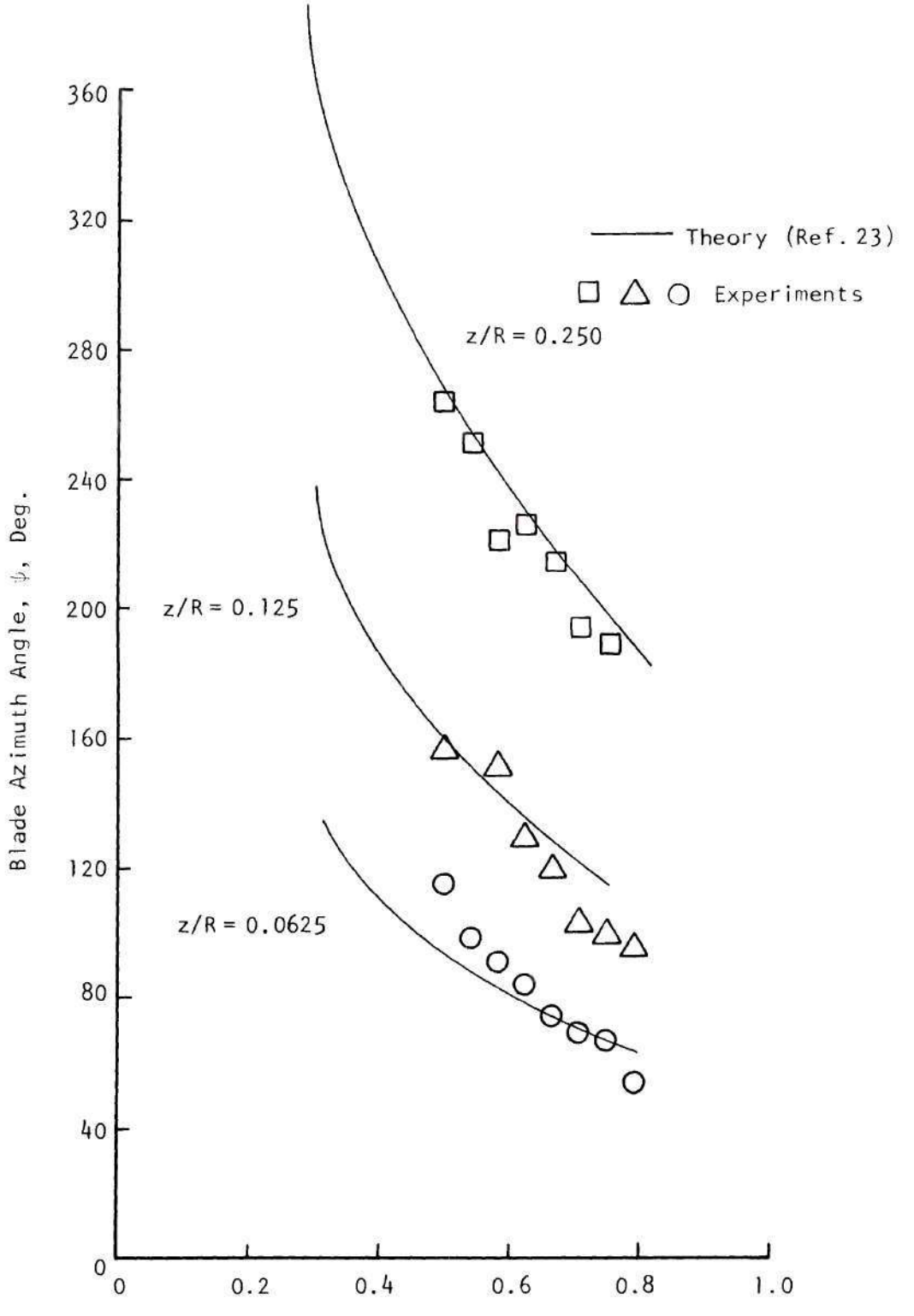

Figure 45. Comparison of Experimental and Theoretical Sheet Location.

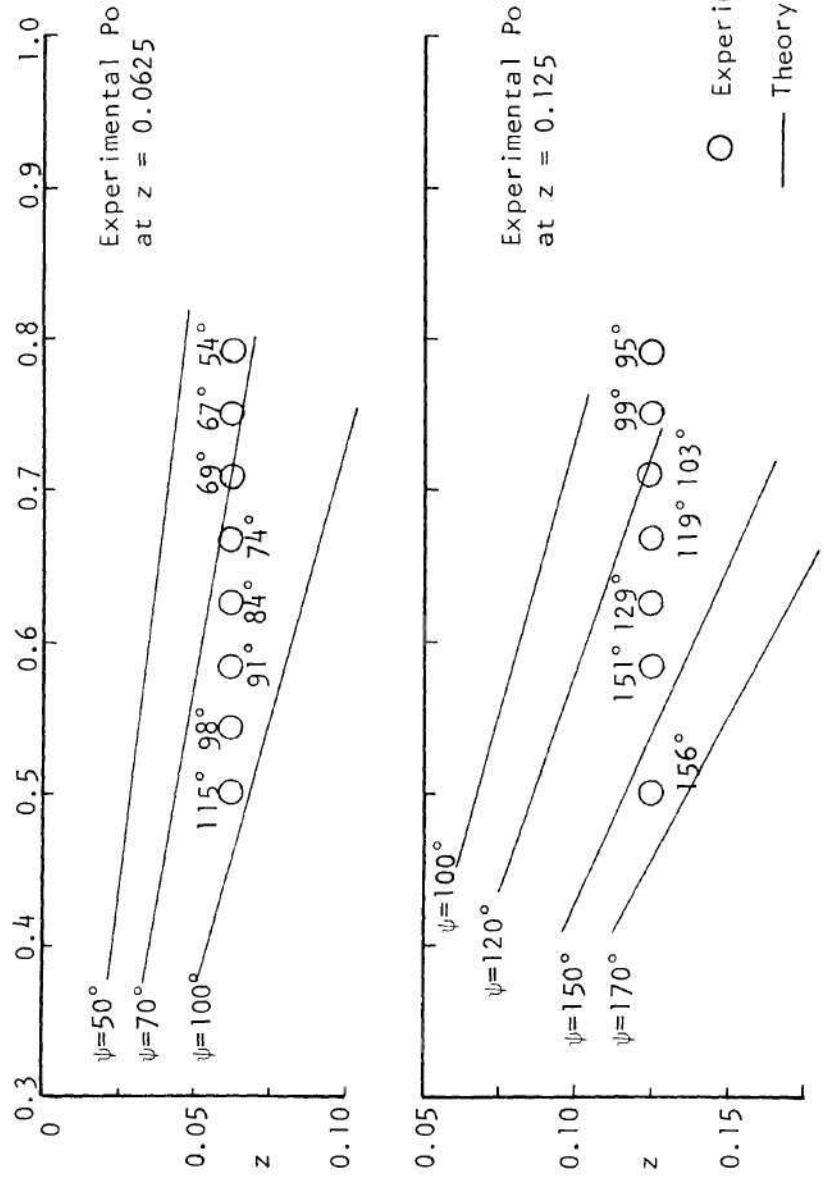

Figure 46. Comparison of Experimental and Theoretical Location of Vortex Sheet in Terms of Blade Azimuth Angle (ψ). (Continues)

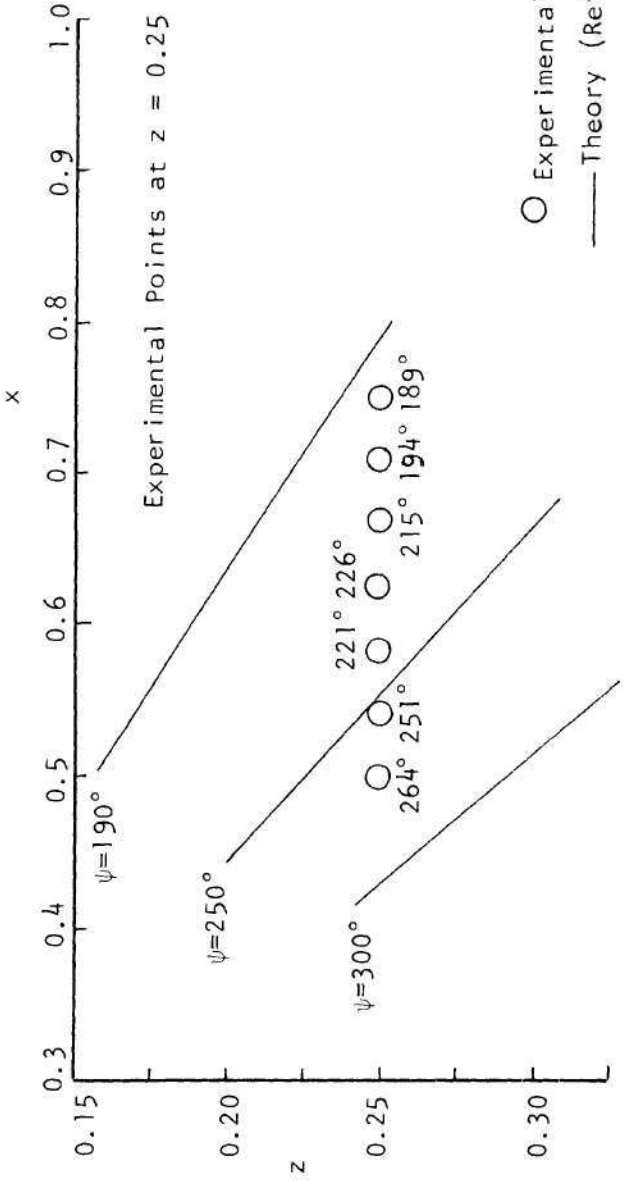

Figure 46. Comparison of Experimental and Theoretical Location of Vortex Sheet in Terms of Blade Azimuth Angle (ψ) (Continued).

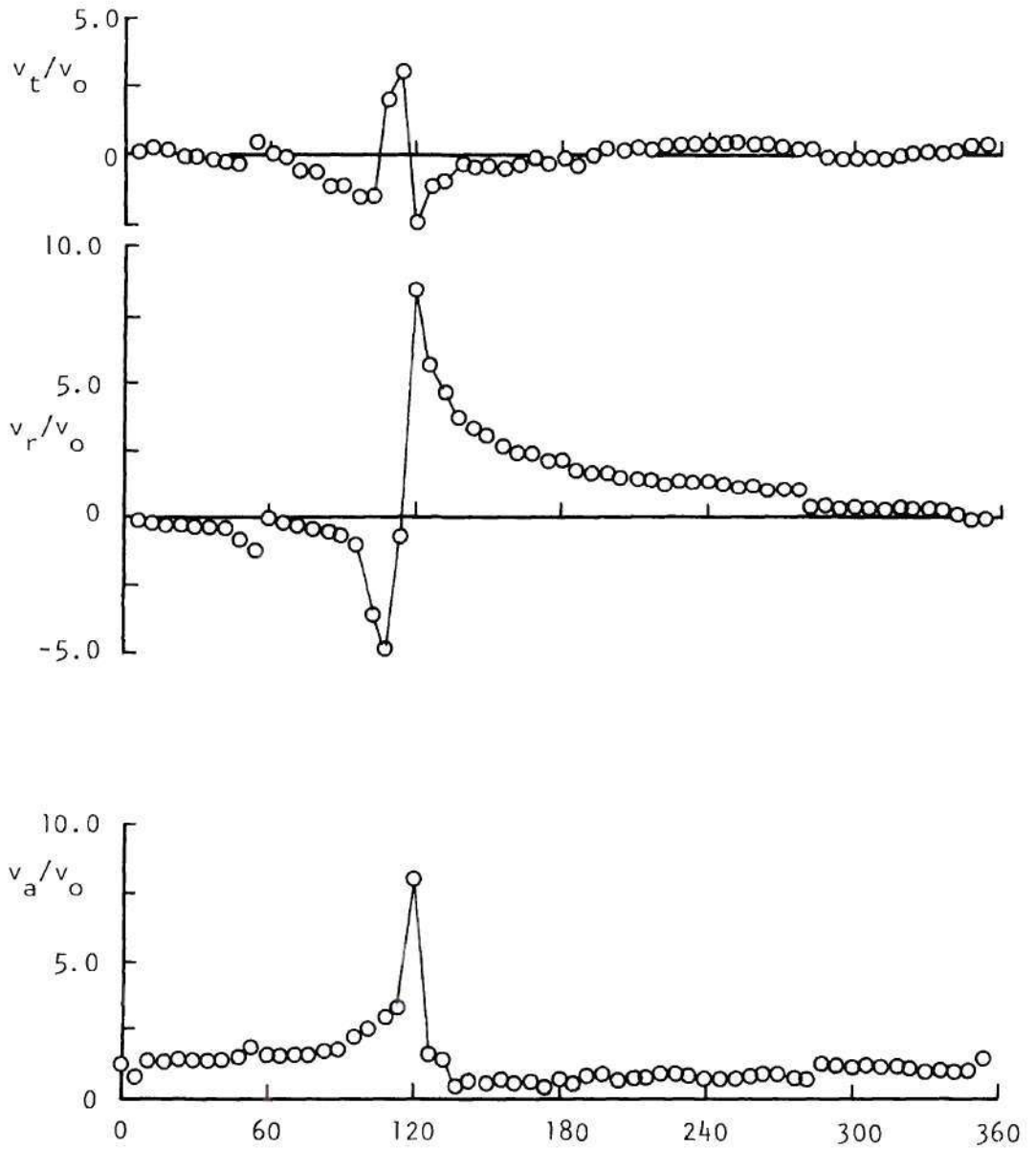

Figure 47. Distribution of Instantaneous Velocity Components Across Tip Vortex Region, x = 0.958 z/R = 0.0625.

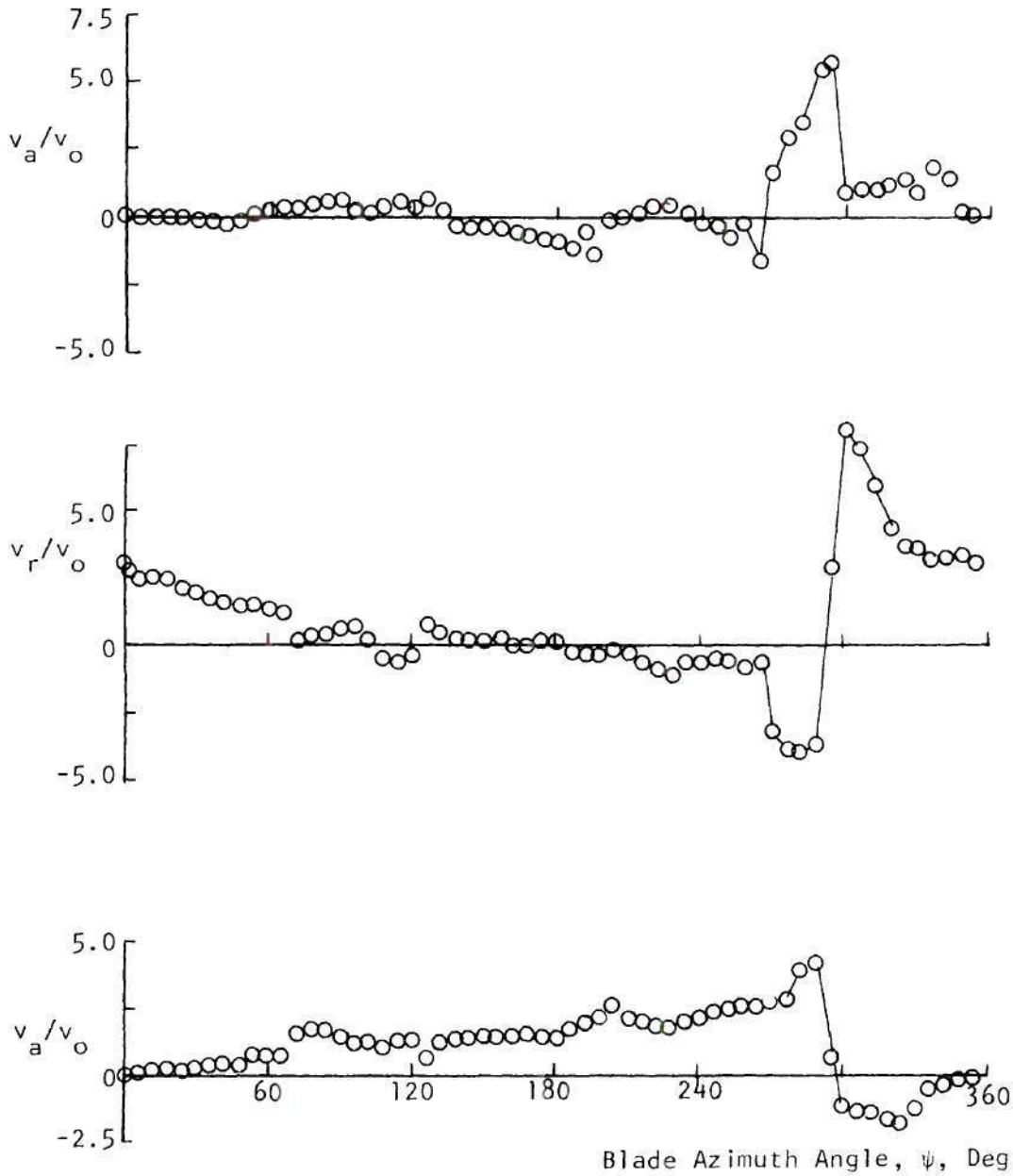

Figure 48. Distribution of Instantaneous Velocity Components Across Tip Vortex Region, x = 0.875, z/R = 0.125.

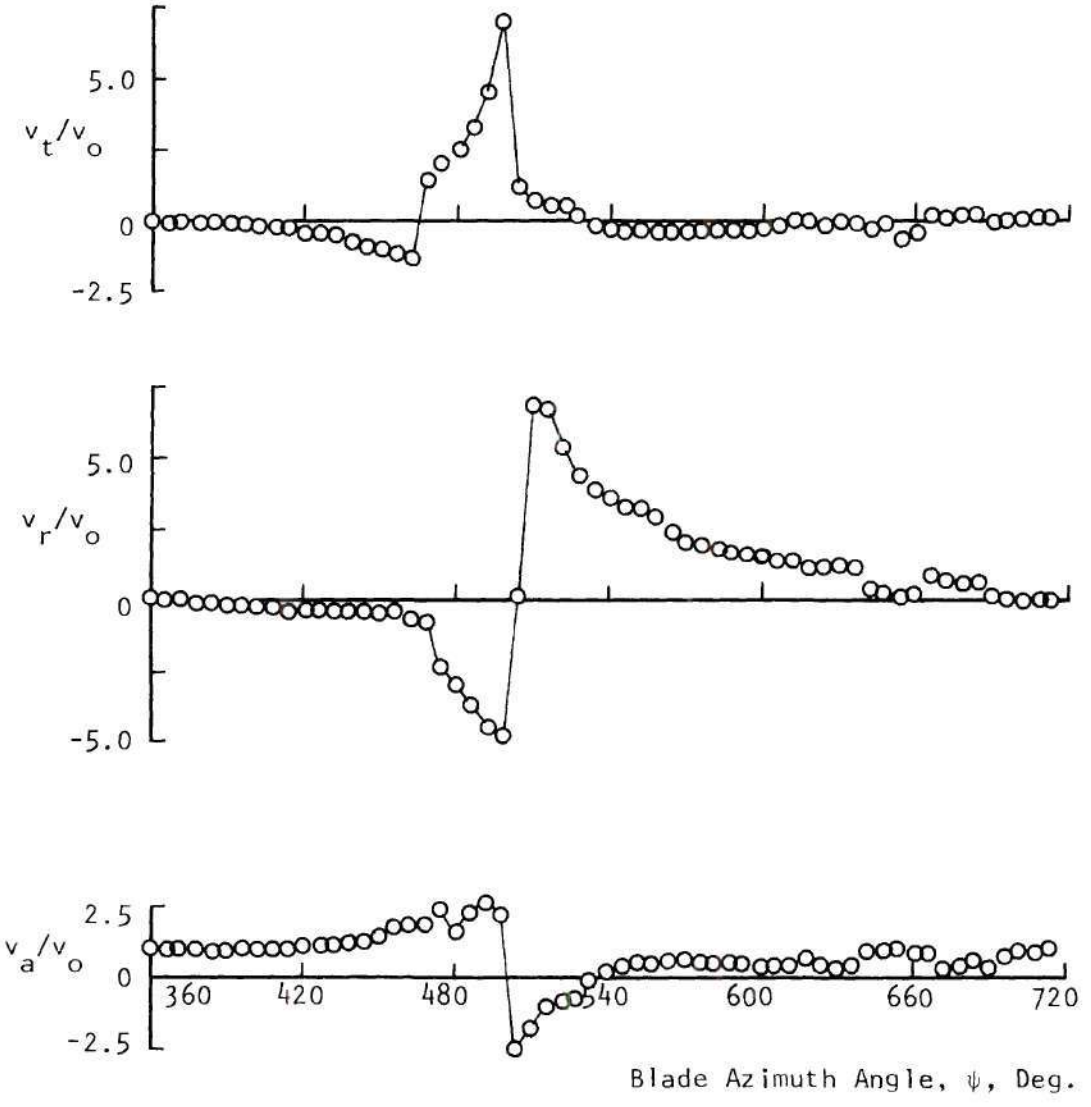

Figure 49. Distribution of Instantaneous Velocity Components Across Tip Vortex Region, x = 0.83, z/R = 0.25.

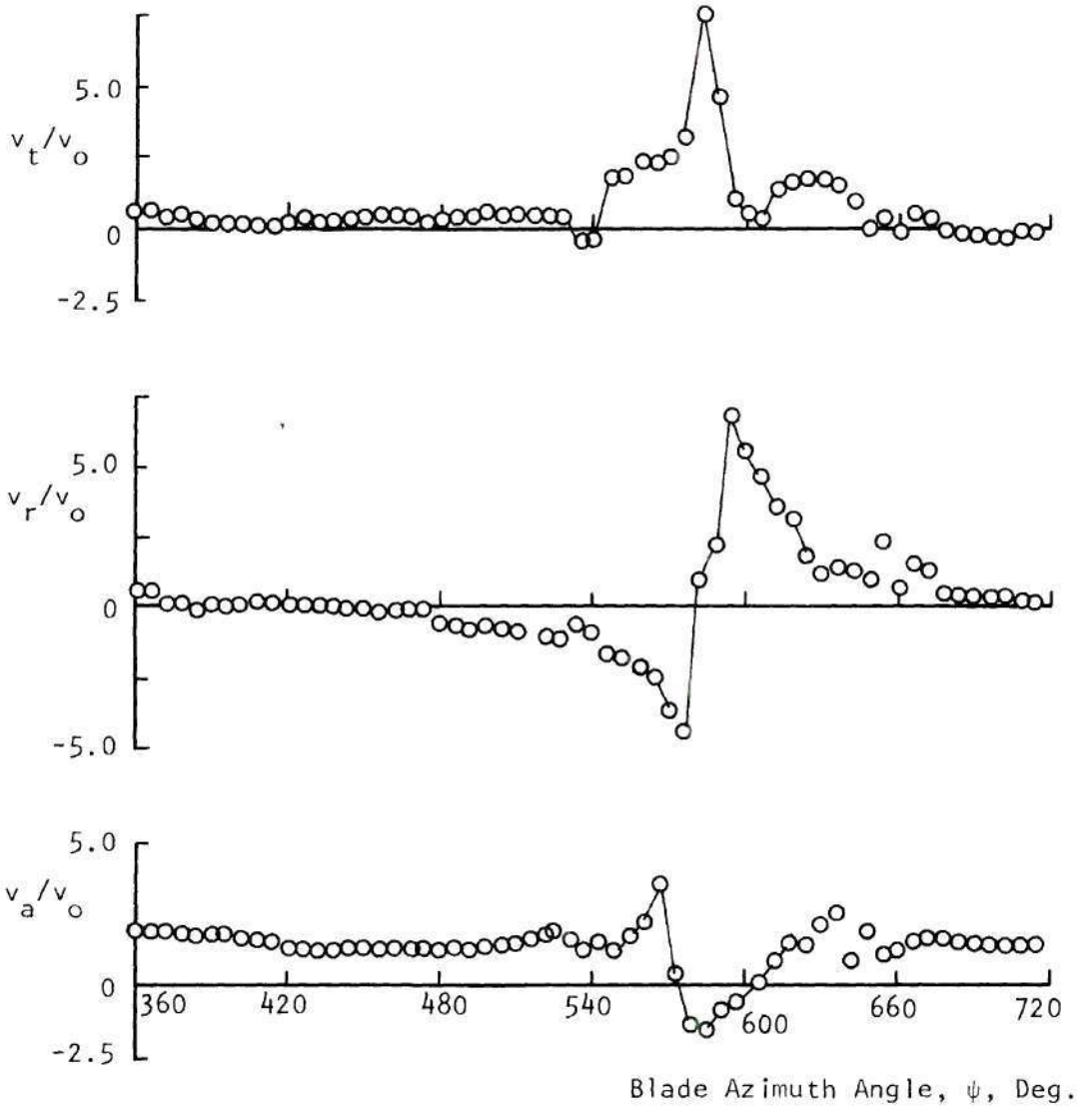

Figure 50. Distribution of Instantaneous Velocity Components Across Tip Vortex Region, $x = 0.79$, $z = 0.375$.

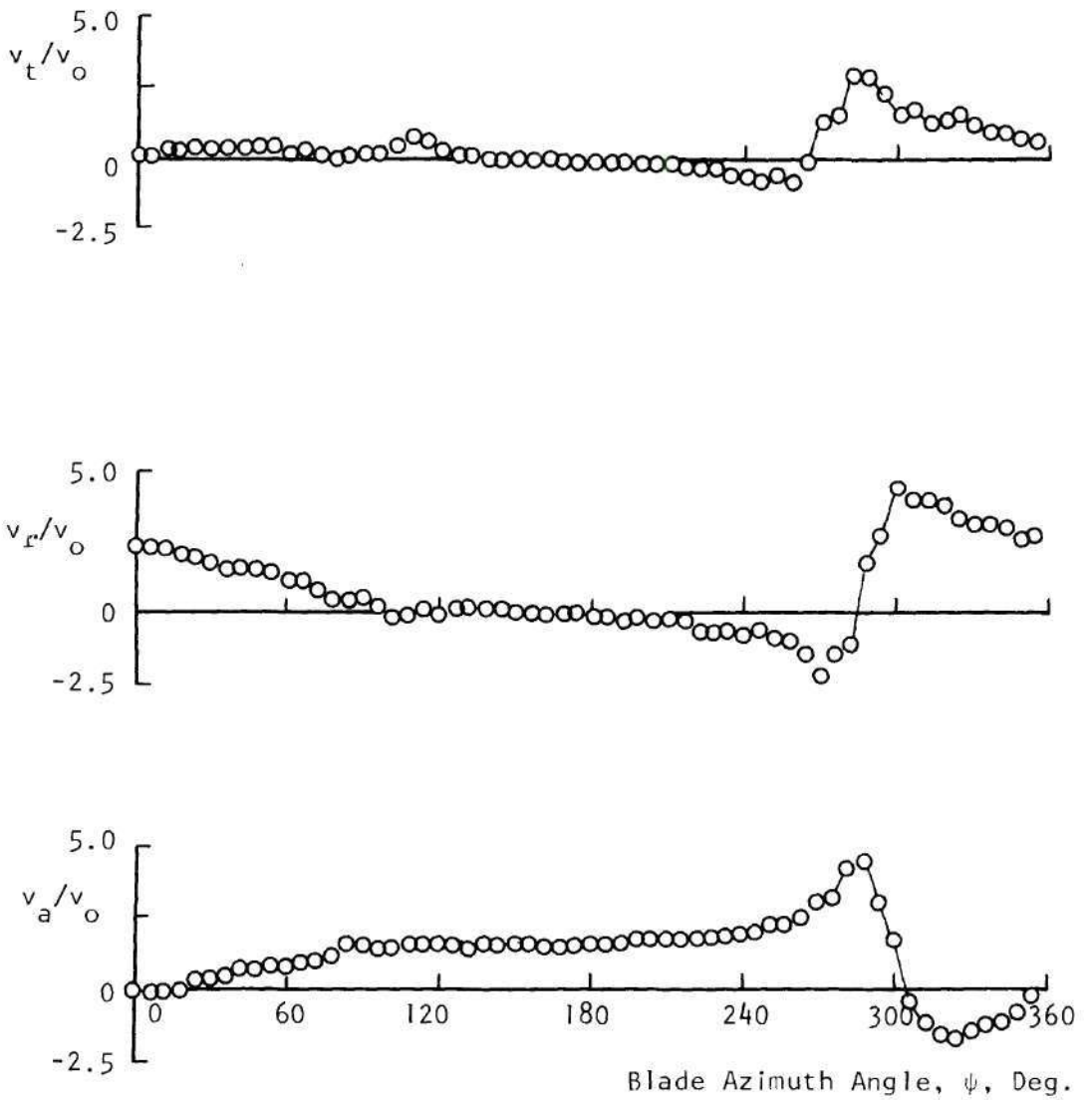

Figure 51. Distribution of Velocity Components Across Tip Vortex Region, Averaged over 10 Revolutions, x = 0.875, z/R = 0.125.

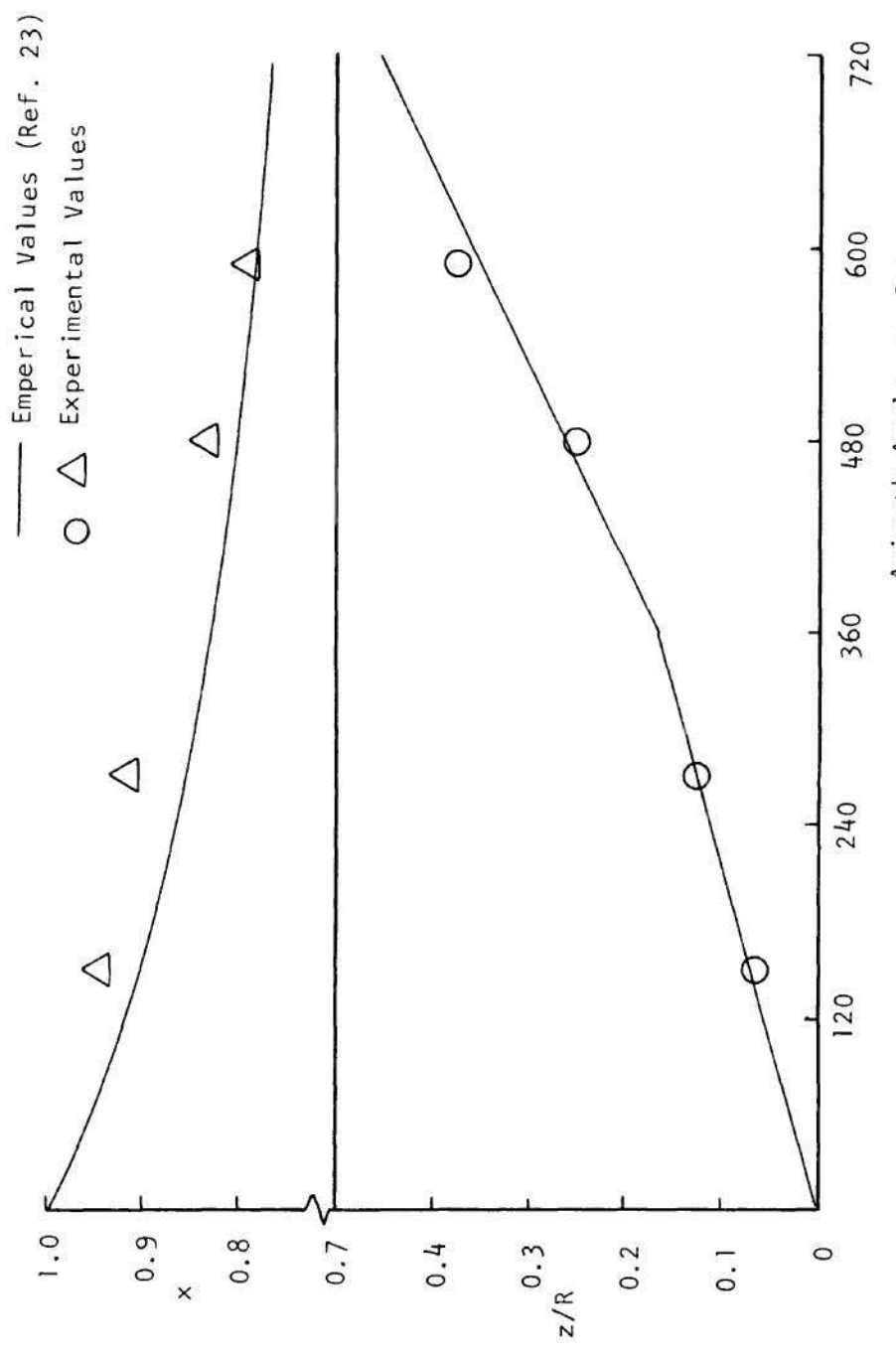

Figure 52. Comparison of Experimental Tip Vortex Geometry with Emperical Geometry.

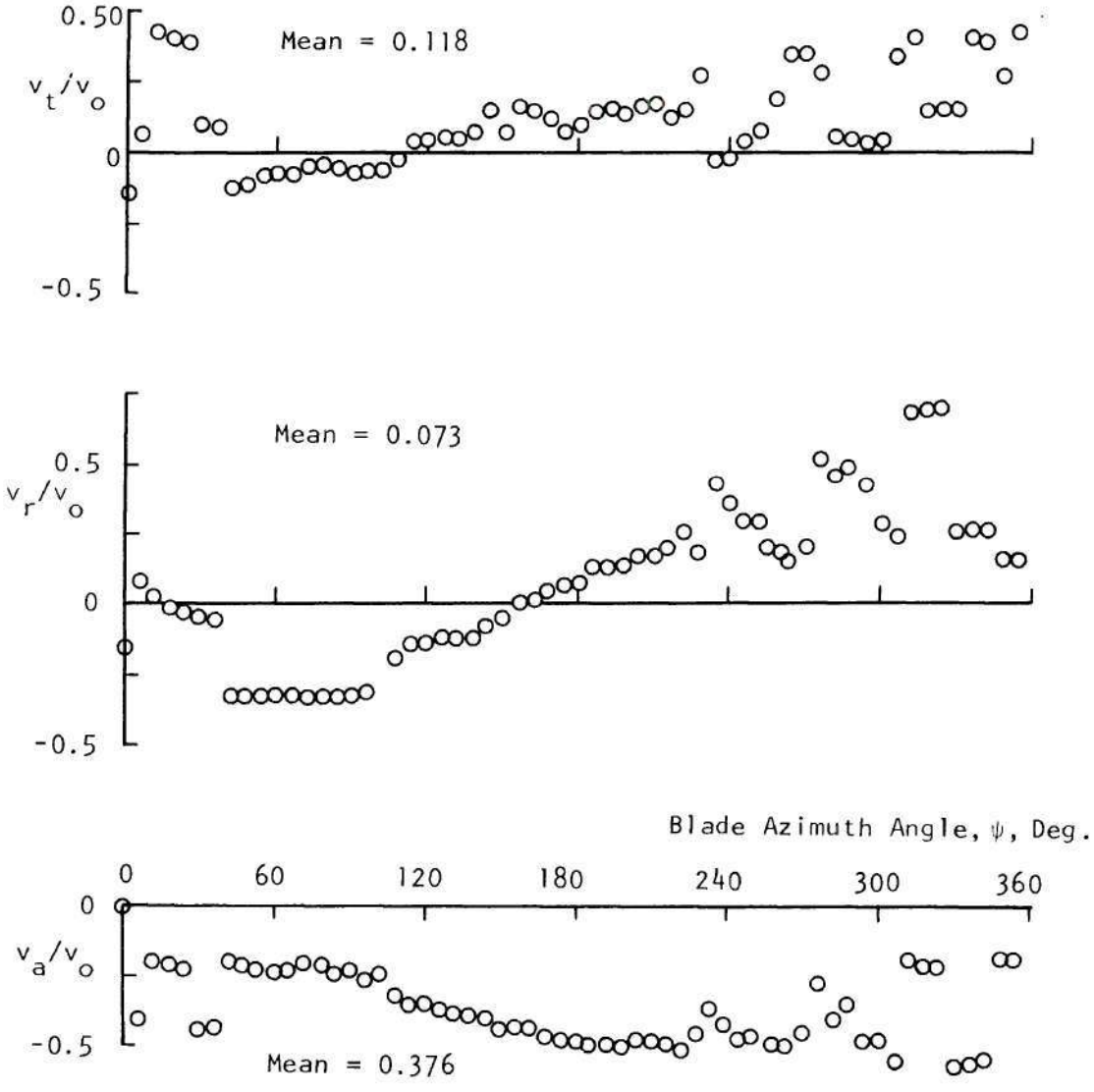

Figure 53. Distribution of Instantaneous Velocity Components Outside the Wake, x = 1.0, z/R = 0.125.

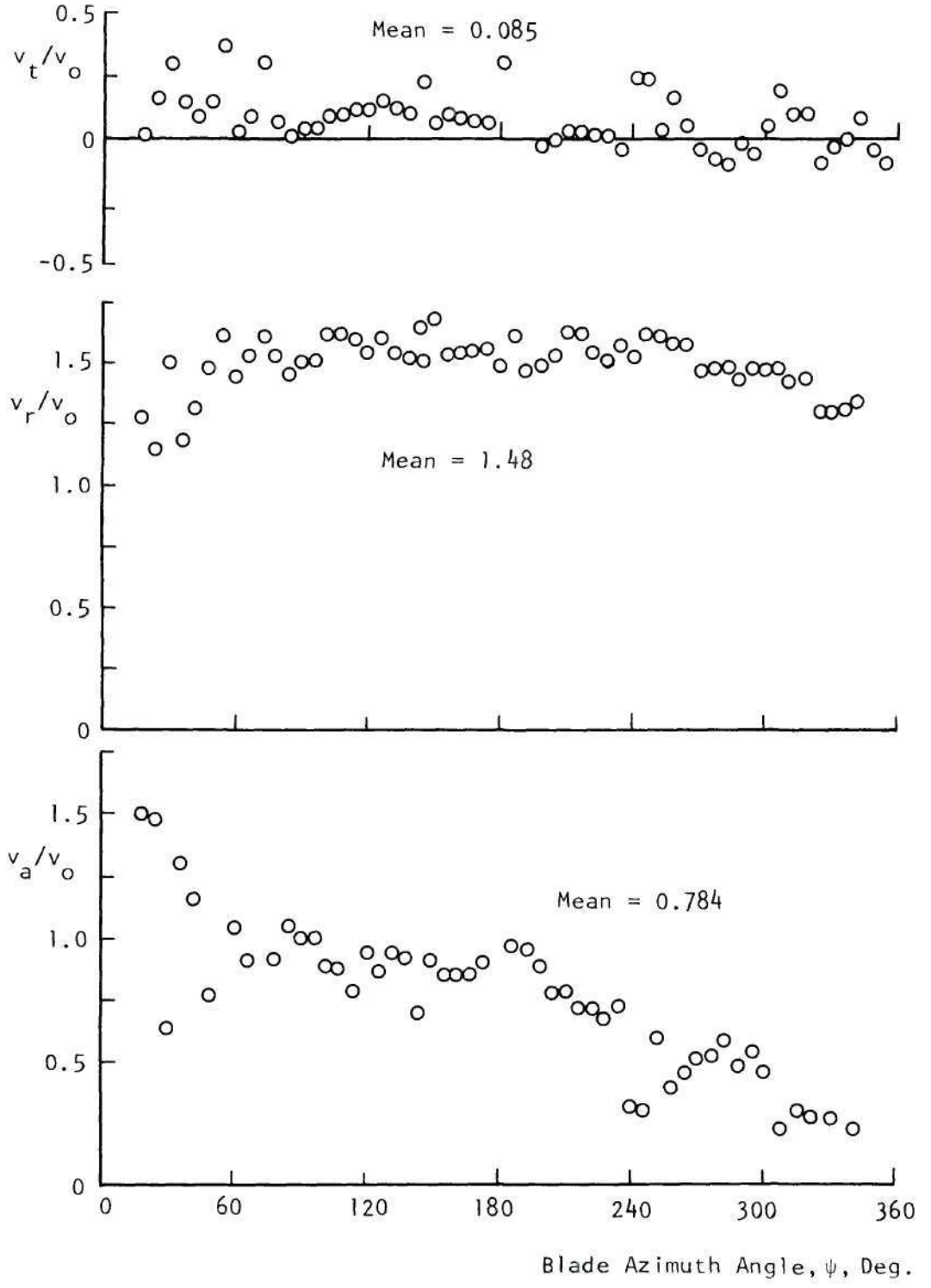

Figure 54. Distribution of Instantaneous Velocities in the Inflow Region, x = 0.841, z/R = -0.0708.

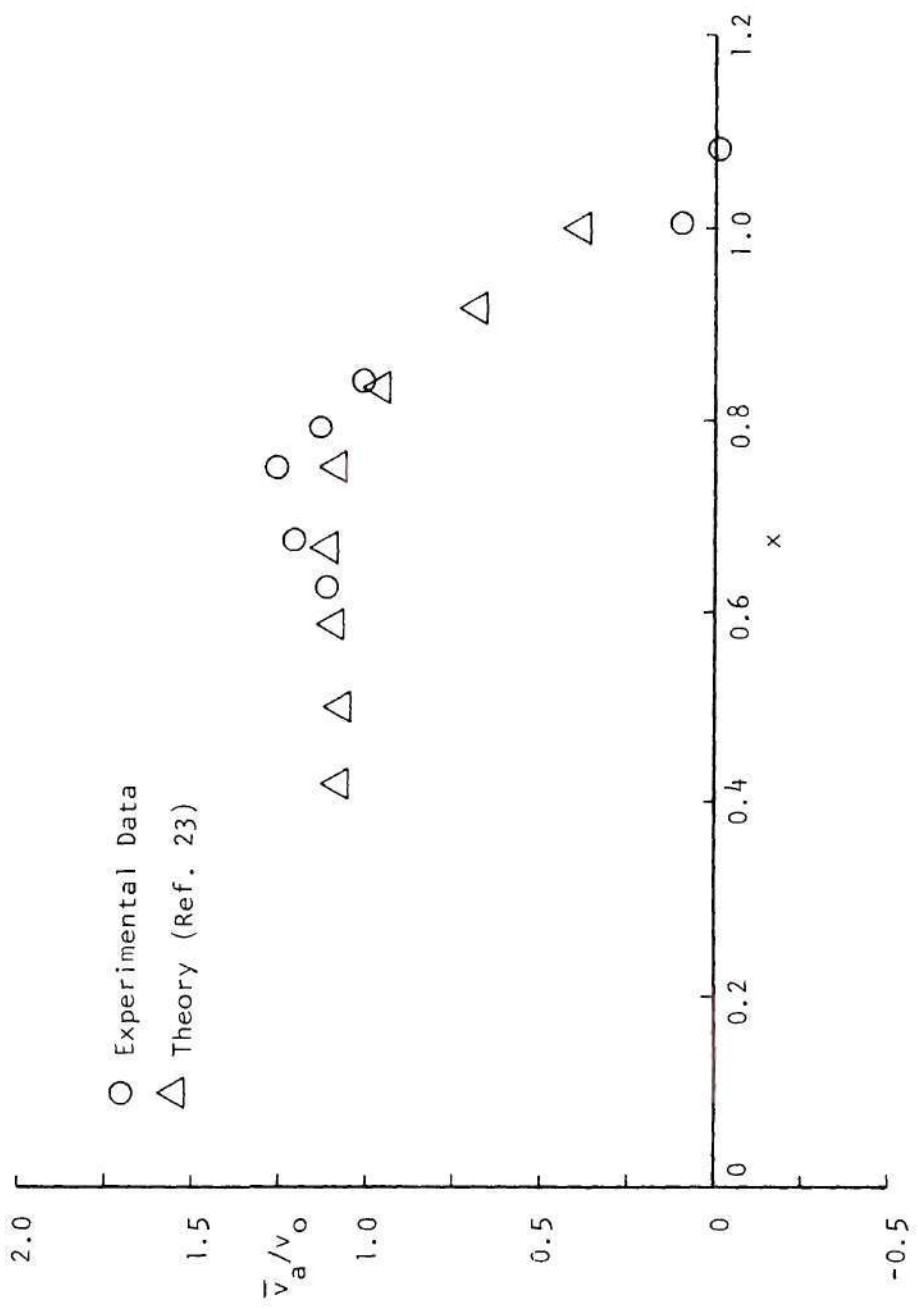

Figure 55. Radial Distribution of Mean Axial Velocity, z/R = -0.0702.

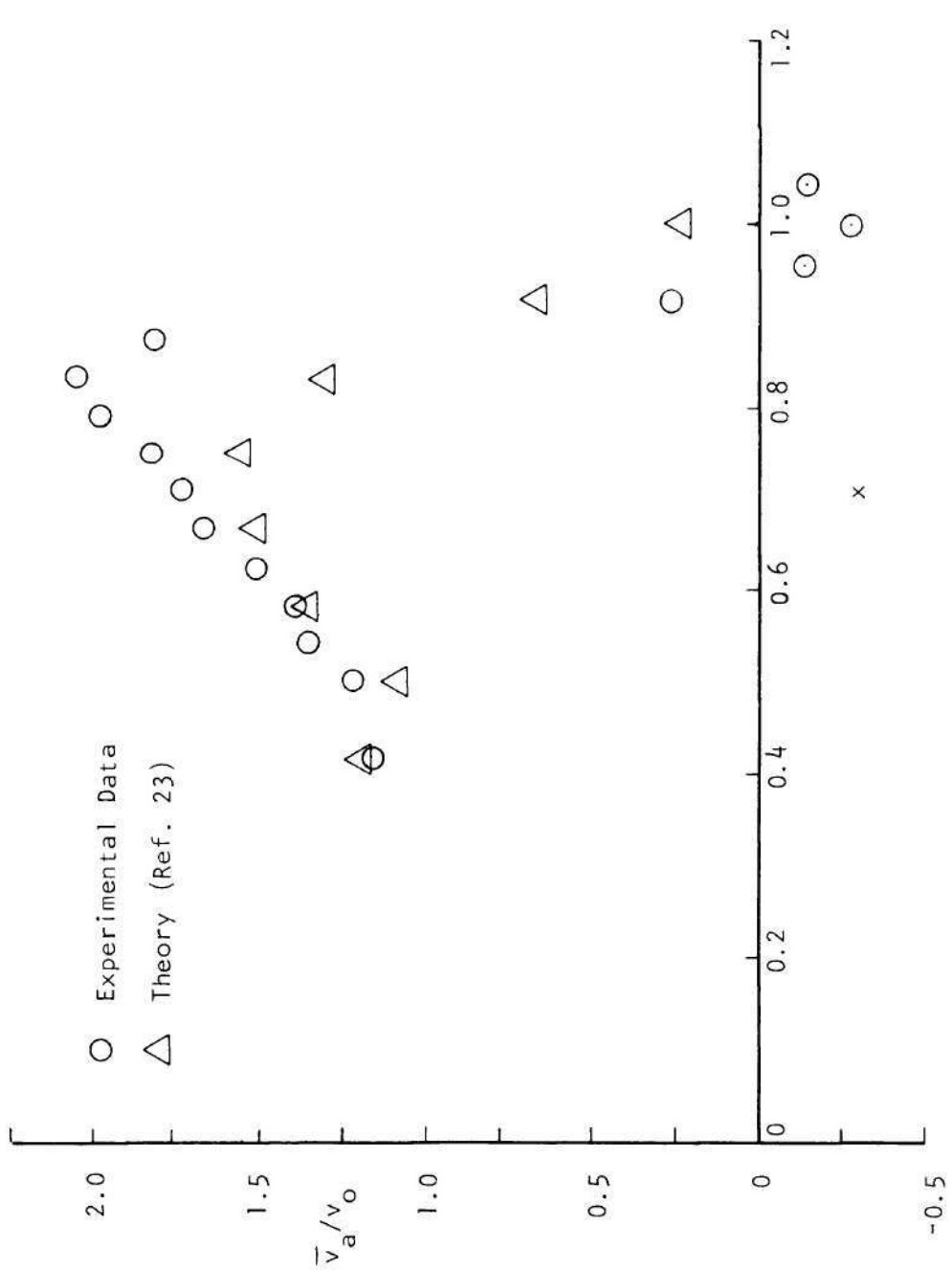

Figure 56. Radial Distribution of Mean Axial Velocity, z/R = 0.0625.

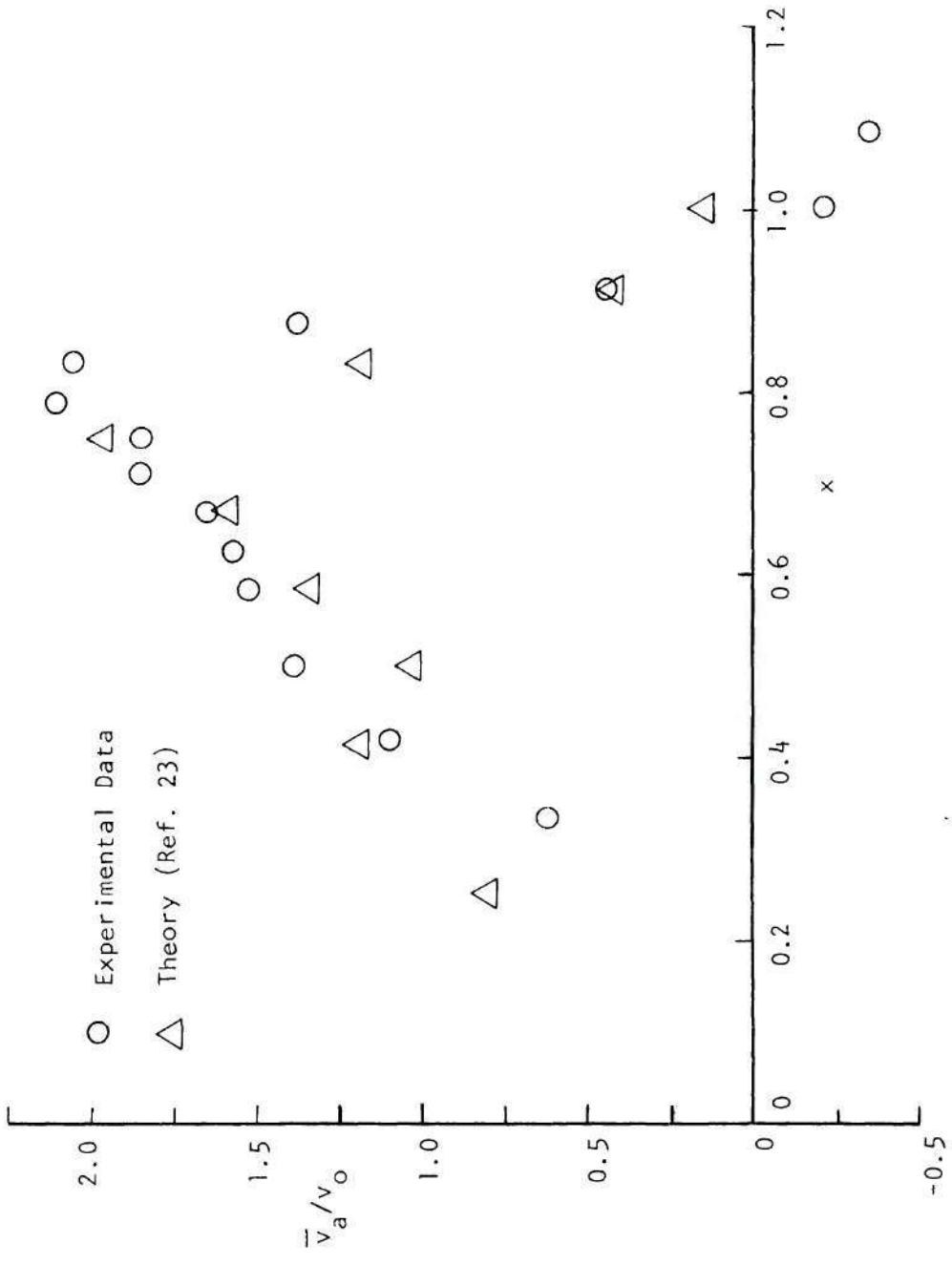

Figure 57. Radial Distribution of Mean Axial Velocity, z/R = 0.125.

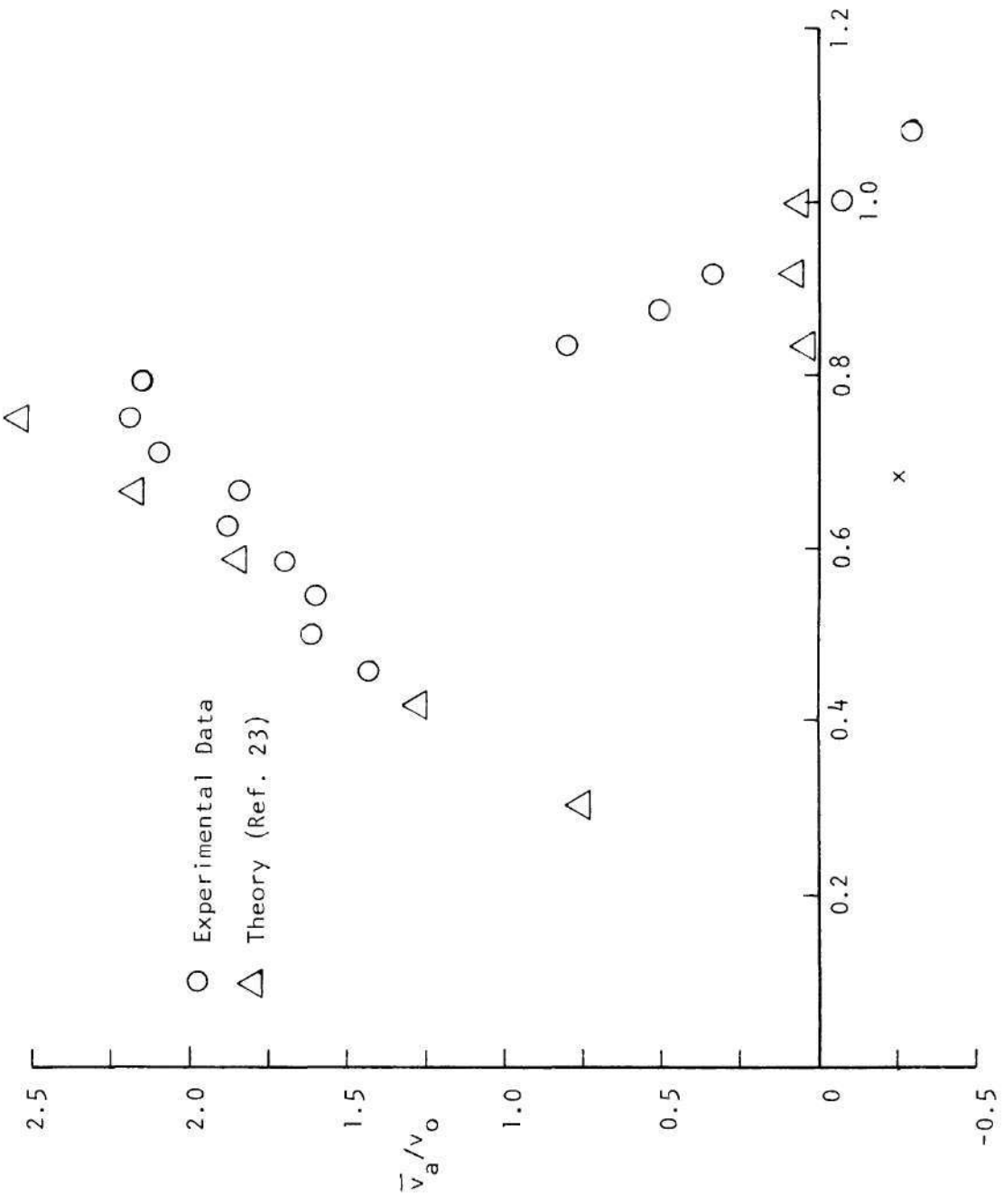

Figure 58. Radial Distribution of Mean Axial Velocity, z/R = 0.250.

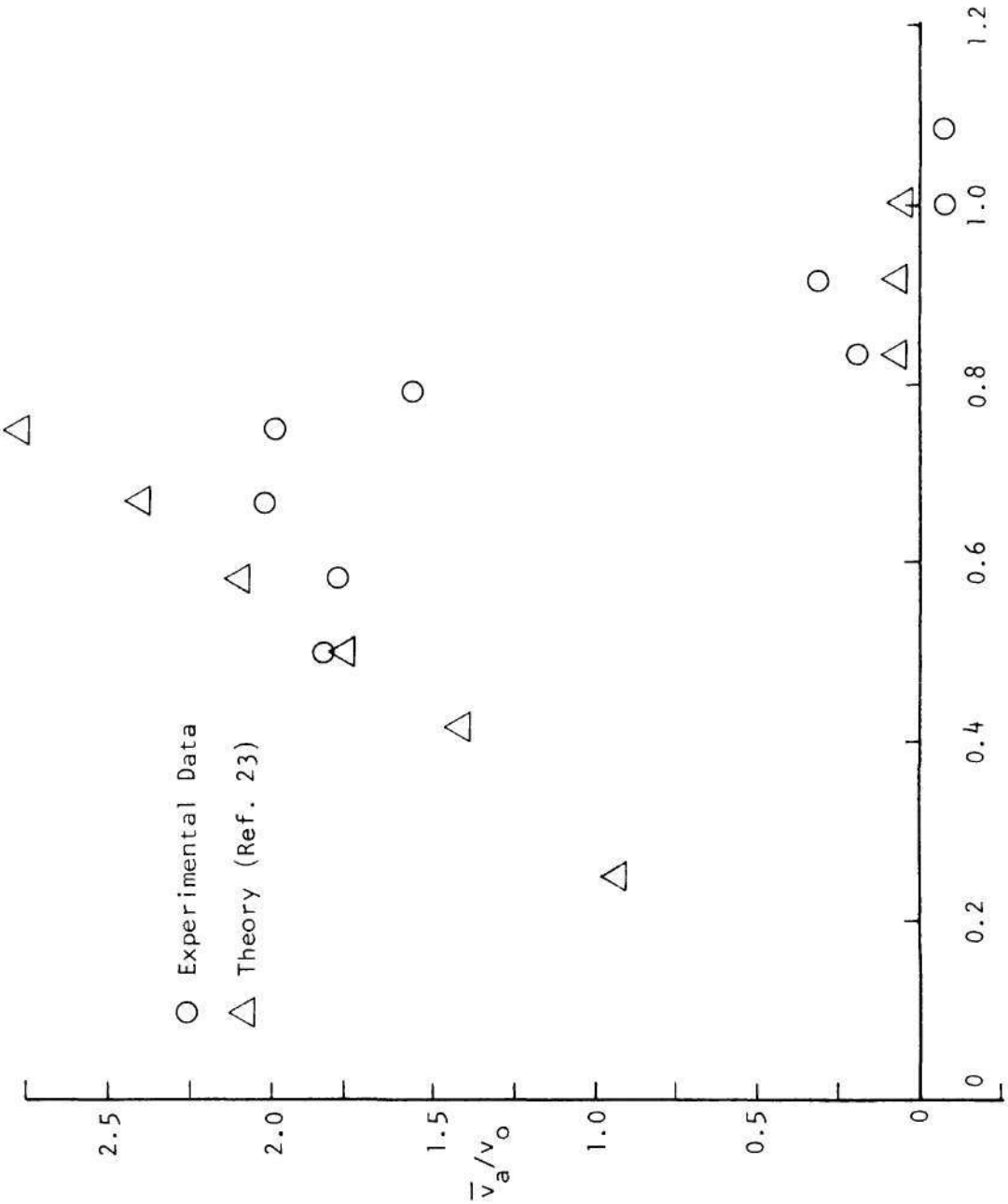

Figure 59. Radial Distribution of Mean Axial Velocity, z/R = 0.375.

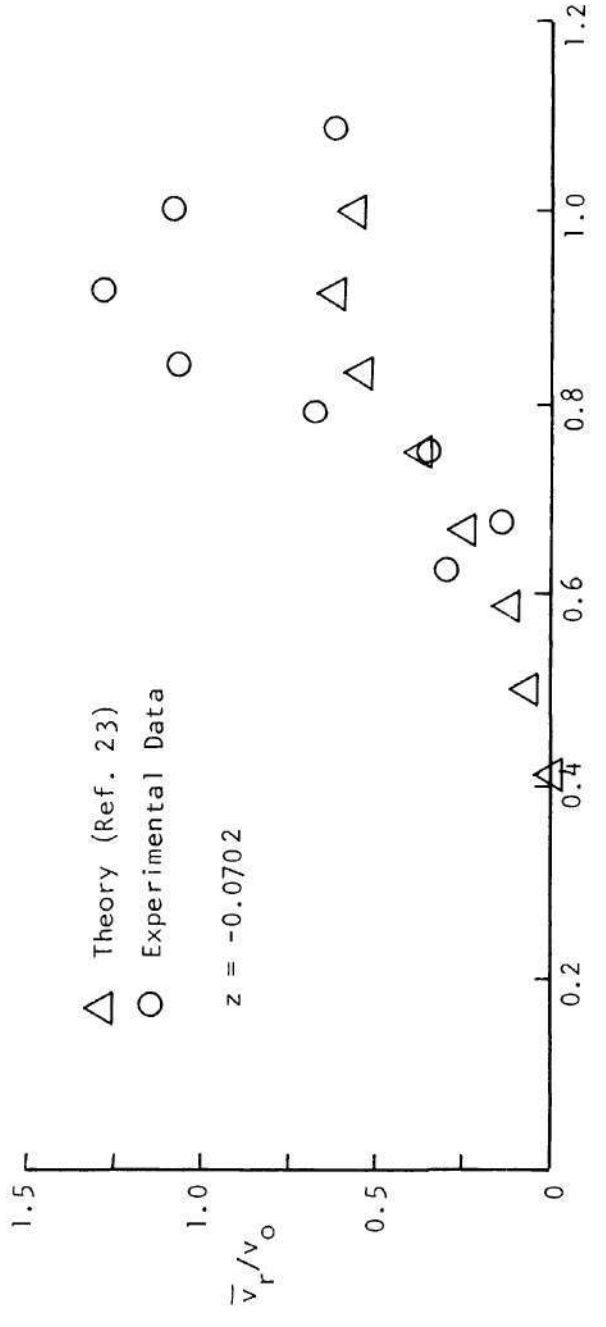

Figure 60. Radial Distribution of Mean Radial Velocity, z/R = -0.0702.

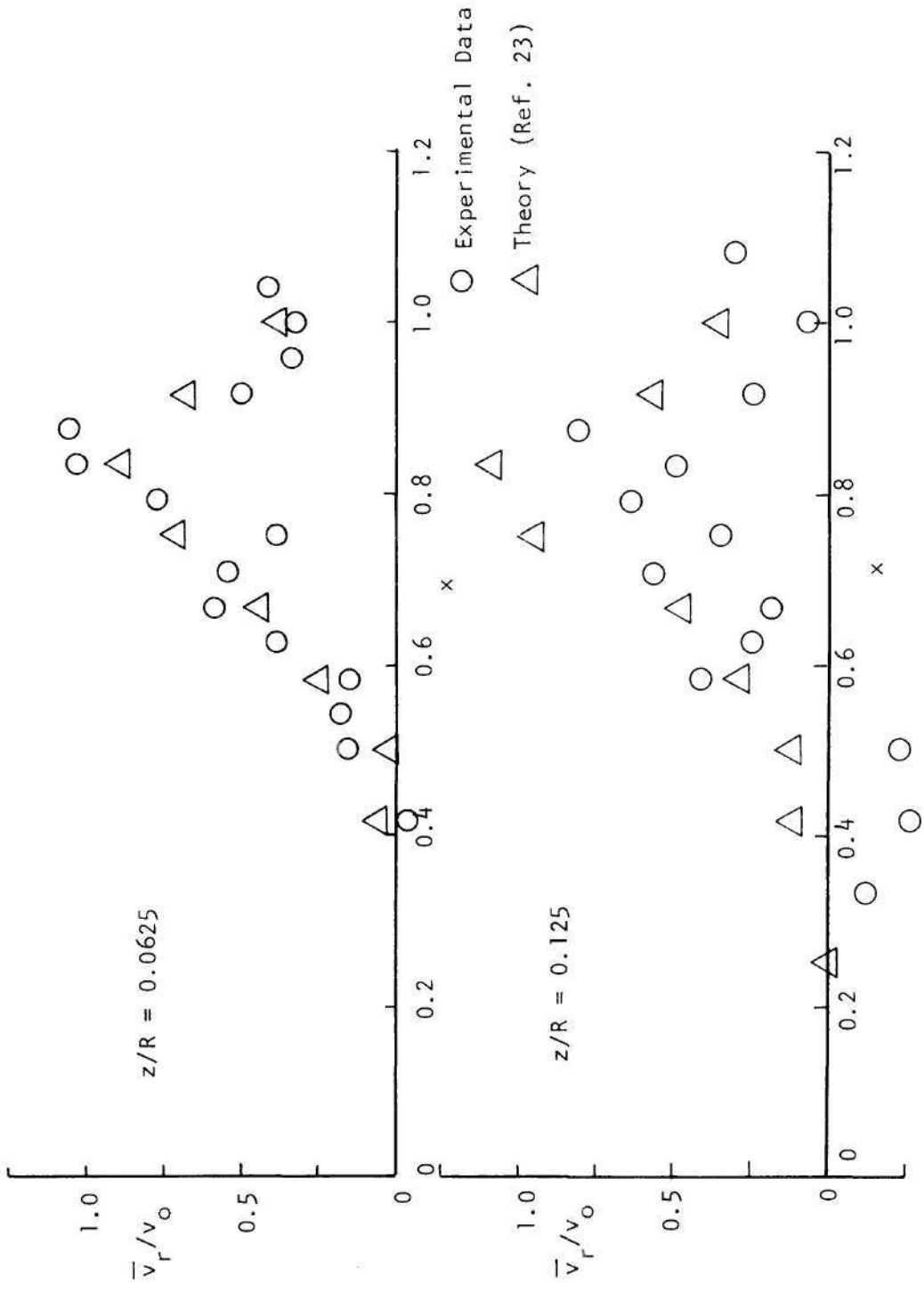

Figure 61. Radial Distribution of Mean Radial Velocity; z/R = 0.0625, 0.125.

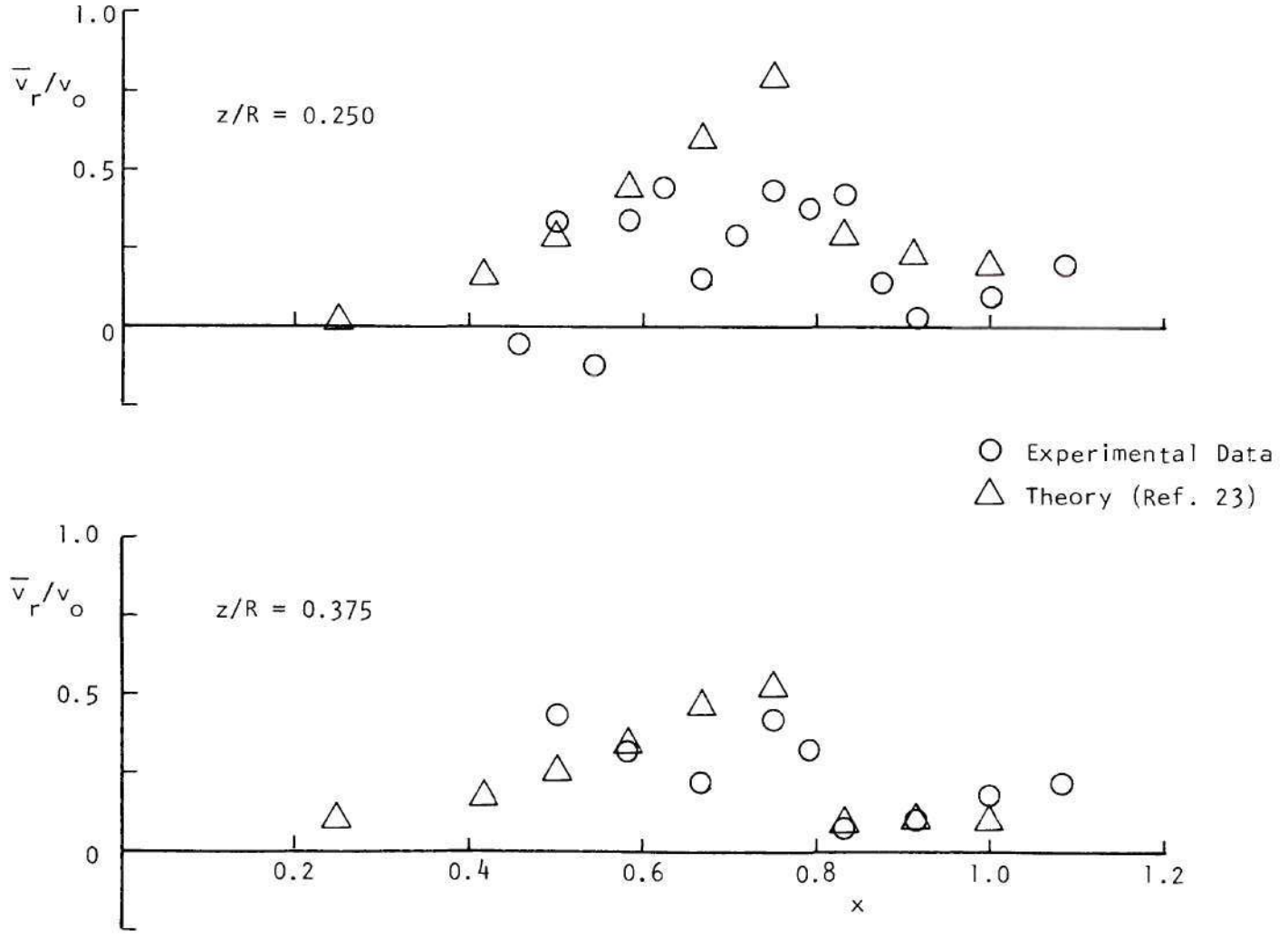

Figure 62. Radial Distribution of Mean Radial Velocity, z/R = 0.250, 0.375.

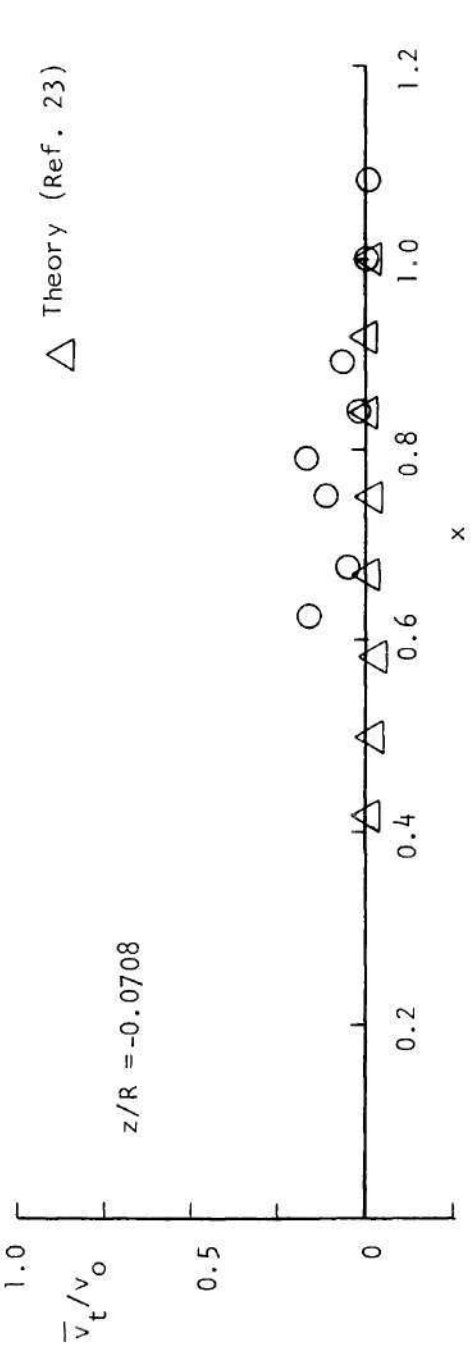

Figure 63. Radial Distribution of Mean Tangential Velocity, z/R = -0.0708.

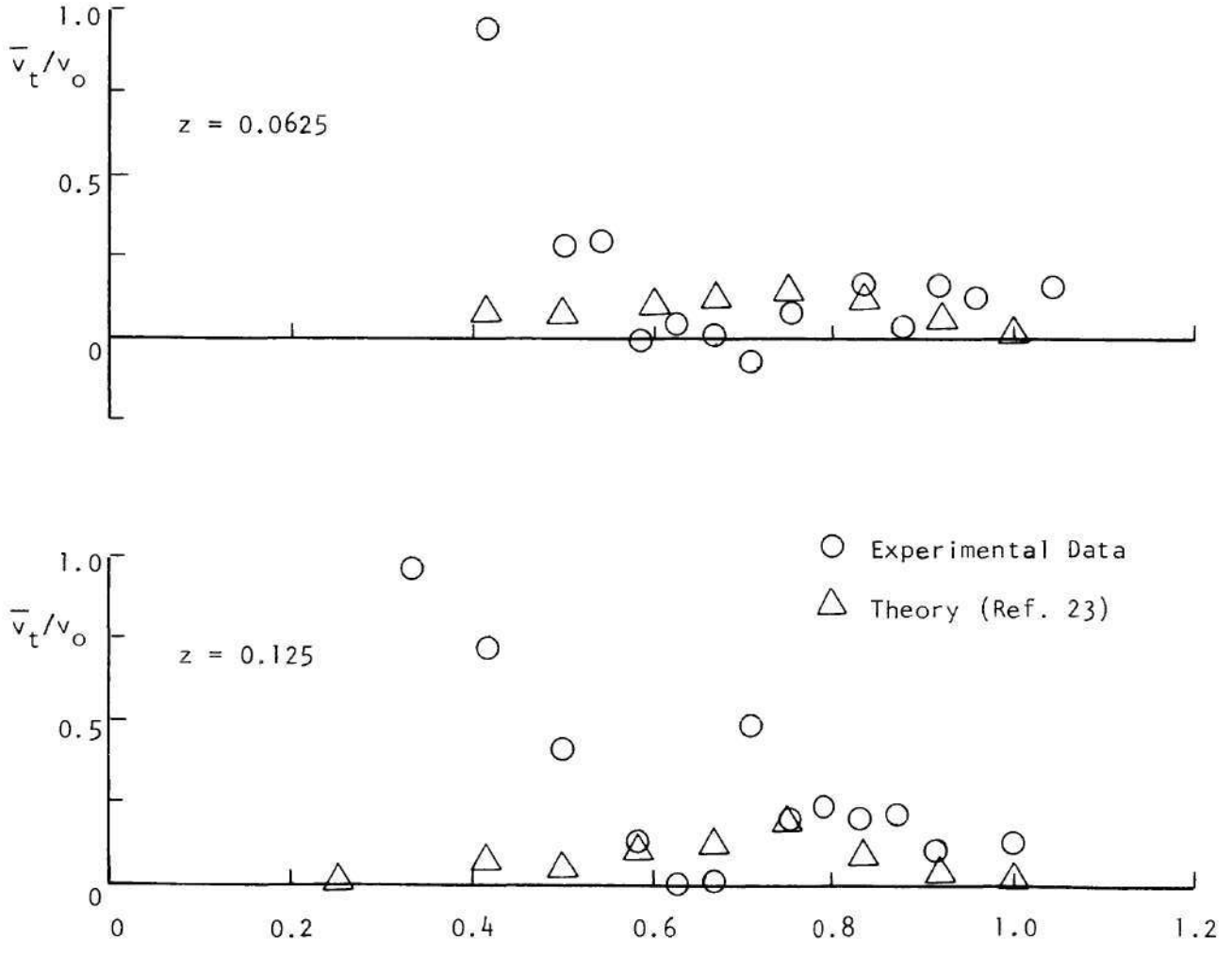

Figure 64. Radial Distribution of Mean Tangential Velocity; z/R = 0.0625, 0.125.

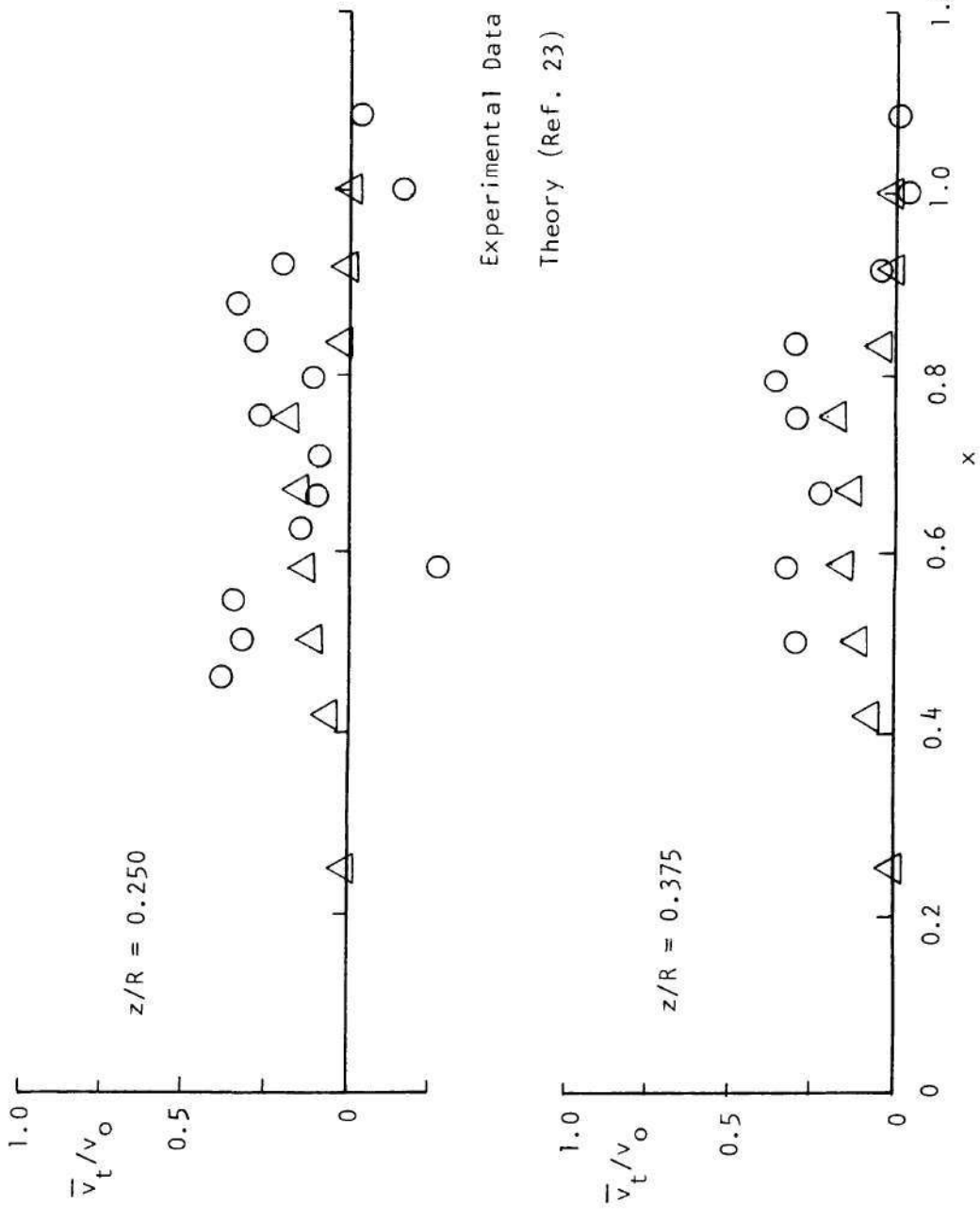

Figure 65. Radial Distribution of Mean Tangential Velocity, z/R = 0.25, 0.375.

APPENDIX A

TEST CELL CONFIGURATION AND FLOW VISUALIZATION STUDIES CONDUCTED TO EXAMINE THE FLOW IN THE TEST CELL

Historically, model helicopter rotors have been tested in large rooms in order to reduce the effects of this confinement to a reasonably small level. To allow clearances of several rotor diameters in all directions, the rotor blade dimensions had to be small which in effect made instrumentation of the rotor more difficult. In the testing of rotors in large rooms, there is no adequate protection for personnel or equipment. With these problems in mind, the test facility shown in Figures 1 and 2 were constructed.

The design of this test facility was based on results obtained from testing a series of model airplane propellers ranging in diameter from seven to fourteen inches in a large room and in a closed chamber 27" x 27" x 62". Sixteen different internal configurations of the test chamber were investigated including square and octagonal cross-sections and with various combinations of screens, honey comb, and flow dividers. Rotor thrust and pitching moment were measured. It was determined that the thrust was reduced by as much as 25% below the free air value, with a periodic variation of up to 8% of the mean value, depending upon the internal configuration of the chamber. The pitching moment variation was aperiodic about zero, with an amplitude of as much as 8% of the product of the corresponding thrust and blade raduis. It was

found that a honey comb placed about one diameter downstream of the rotor in a square chamber, and having a hole large enough to pass the contracted wake, resulted in a thrust measurement of about 99% of the freestream value and eliminated the pitching moment entirely.

Flow visualization studies[29] using small, neutrally buoyant, helium-filled soap bubbles were conducted to study the flow inside the test cell. The bubbles were produced with a commercial bubble generating system (Sage Action, Inc.) consisting of a control console and a 1/4 inch diameter bubble generating head. The bubbles produced were about 1/16 inch in diameter. They were observed with a continuous light and a strobe light.

Four different test cell configurations were investigated. These were

1. A closed cell with no internal flow guides;
2. A closed cell with a honeycomb insert at several axial positions
3. A closed cell with a honeycomb insert and a bell-mouth wake conductor;
4. A ventilated cell with a honeycomb insert and a bell-mouth wake conductor. (Final configuration)

For the flow visualization studies, the nozzle of the helium generator was placed at various locations in the test cell. The bubbles were observed passing directly into the rotor plane at various positions and being entrained by the wake and the tip vortex. Some of the bubbles were observed to make at least one complete circuit of the wake and the return flow. The flow in the test cell was found to be more or less

stable depending upon the internal configuration of the cell.

For configuration 1, the closed cell with no internal flow guides, the return flow near the rotor plane was very turbulent, with the flow directions changing almost continuously. A varying level of rotor noise was easily heard.

For configuration 2, the closed cell with a honeycomb insert, the return flow near the rotor plane was much smoother and there was a noticeable reduction in rotor noise. However, abrupt changes in the flow direction near the rotor plane were observed. The flow would be relatively steady for a period of ten to fifteen seconds, would then shift to a different direction for a period of several seconds, and then shift back to the initial direction. Although these changes were more or less periodic with time, it was not established that this phenomenon represented a flow field whose position was continually changing in the azimuth direction, since all the observations were performed in the same azimuth plane. A second problem was that the tip vortex did not always pass through the circular cut-out in the honeycomb. The position of the honeycomb was varied between three and five feet downstream of the rotor plane with no noticeable effect.

When the helium-filled bubbles were introduced into the wake and illuminated with a strobe light which was flashing at the rotor frequency, as many as eight half-turns of the tip vortex helix were observed over an axial distance beneath the rotor of about one rotor diameter. Thus, the tip vortex seemed to be stable for configuration 2, although the return flow was not.

Configuration 3 was generated by installing a bell-mouth inlet in the circular cut-out of the honeycomb insert. The passage of the wake through the bell mouth appeared to be freer but there was essentially no improvement in the return flow characteristics. Flow visualization studies were conducted in greater detail in the inflow region near the rotor. It was discovered that tornado-like vortices occassionally formed between the thrust side of the rotor and the walls of the test cell. These vortices would move around in a random manner for several seconds before dissipating, only to form again later at a different location.

To eliminate these vortices the test cell was ventilated to obtain configuration 4(the final configuration, Figure 2.) It was verified that the return flow was improved, that only minor fluctuations remained, and that the perceived rotor noise was reduced in level.

It has been shown by Gray (Ref.29) that the computed thrust and torque coefficients for the isolated rotor agree closely with the measured coefficients for the model rotor hovering in the test facility.

APPENDIX B

EVALUATION OF THE MODEL 1080 VECTOR ANEMOMETER SYSTEM IN A WIND TUNNEL

The published characteristics of the Model 1080 vector anemometer system indicate a velocity magnitude accuracy of 3% of reading over a range of 0-300 ft/sec. and a direction accuracy within 3 degrees over the complete solid angle. Other users of this vector anemometer system (Ref. 26) have stated that it is not as accurate as claimed by the manufacturer. Thus, it was decided to conduct several tests in the Georgia Tech nine-foot wind tunnel in order to determine the accuracy of the anemometer system.

The anemometer probe was mounted in the wind-tunnel test section at various known pitch and yaw angles of the probe shank relative to the freestream flow direction. The yaw angle was varied from -80° to +90° at each pitch angle and the pitch angle was varied from -60° to 50°. The wind tunnel was run at several known freestream velocities over the range from 10 to 30 ft/sec at each orientation of the probe. The six voltage outputs of the anemometer system were measured simultaneously and the corresponding velocities were calculated. The results were compared with the known velocity direction and magnitudes.

The variation in the percentage error $\left(\frac{V_\infty - V_m}{V_\infty} \cdot 100\right)$ in the velocity magnitude with yaw angle is shown in Figure B1 through B5. No general pattern is evident from the plots. In most cases, when the yaw

angles were in the range of -30° to 30° the velocity magnitude errors were less than 4% of the true velocity. That is, when the probe was inclined to the flow directions at small angles (<30°) the velocity magnitude errors were close to the values given by manufacturer. At higher angles of probe inclination, the velocity magnitude errors were in the range of 6% of the velocity reading.

Variations of error in measured yaw angle as a function of yaw angle are shown in Figures B6 and B14. Here again, no general pattern is evident from the plots. In most cases, when the yaw angle is in the range -25 to 25° and the pitch angle is in the range -30 to 30°, the yaw angle error is about ±7 degrees. At higher angles of yaw and pitch, the yaw angle error is in the range -15° to 10°. It was observed that, in most cases, the largest angular error occurs near a yaw angle of -40° or 40°. Close examination of the data reduction procedure shows that these large angular errors occur because, for those probe orientations small fluctuations in the flow can cause a change in sign of the angle between the total velocity vector and the sensor elements. This changes the direction of the total velocity vector and causes large errors in the calculated velocity components.

Variations of angular error in pitch with pitch angle are shown in Figure B15 through B17. When the yaw angles and pitch angles are in the range of ± 30 degrees, the angular error in the pitch measurements is in the range -7° to +5°. At higher angles of pitch and yaw, the error is in the range -12 to 10°. Figure B18 shows that in most cases when the yaw angle is high (70° to 80°), the measured pitch angle is at 35.26 degrees regardless of the value of the actual pitch angle. This occurs

because at high yaw angles, the angle between sensor A and velocity vector (ϕ_A) is often forced to zero in the data reduction. When ϕ_A=0, the data reduction program causes the pitch angle of the probe to be output as 35.26 degrees.(explained in detail in Appendix C).

The behaviour of the anemometer system as shown in Figures B1 through B18, was repeatable within 5 degrees in velocity direction and within about 2% in velocity magnitude. However, since there were no general patterns evident in the plots, corrections of the velocity magnitude and direction was not possible.

After examining the results of these evaluation tests on the total vector anemometer system, it is concluded that the accuracy of the velocity data is strongly dependent on the orientation of the anemometer probe with respect to the flow direction. When the probe is inclined to the flow at large angles (> 30°), the velocity magnitude errors are about 6% of reading and the angular errors are in the range of -15° to 10°. When the probe is inclined to the flow at smaller angles (less than 30°), the accuracy of the anemometer system was closer to the values specified by the manufacturer; the velocity magnitude accuracy is about 4.5% of reading and the angular error is in the range of -7° to 7°.

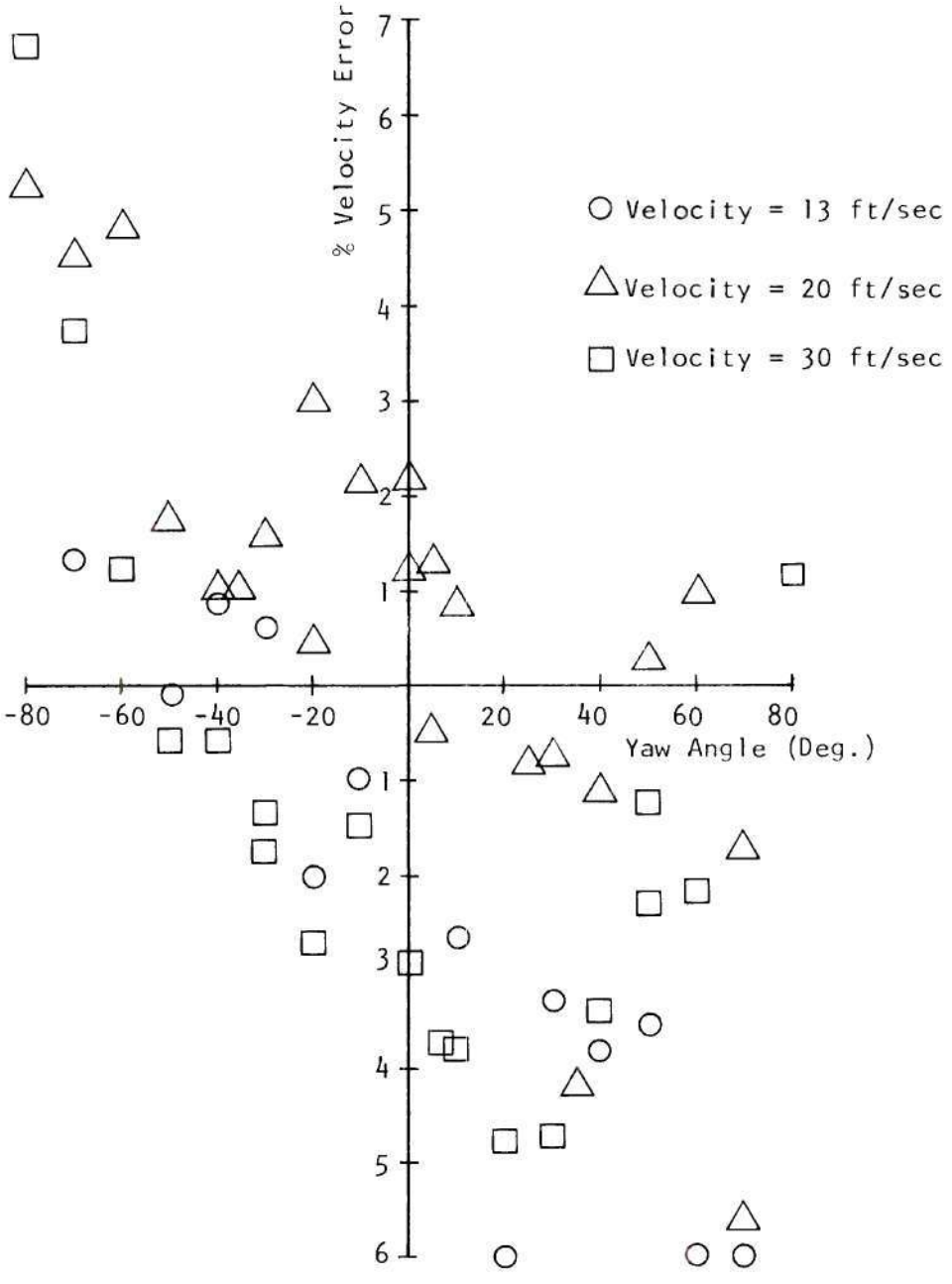

Figure B-1. Percentage Error in Total Velocity, Pitch = 0°.

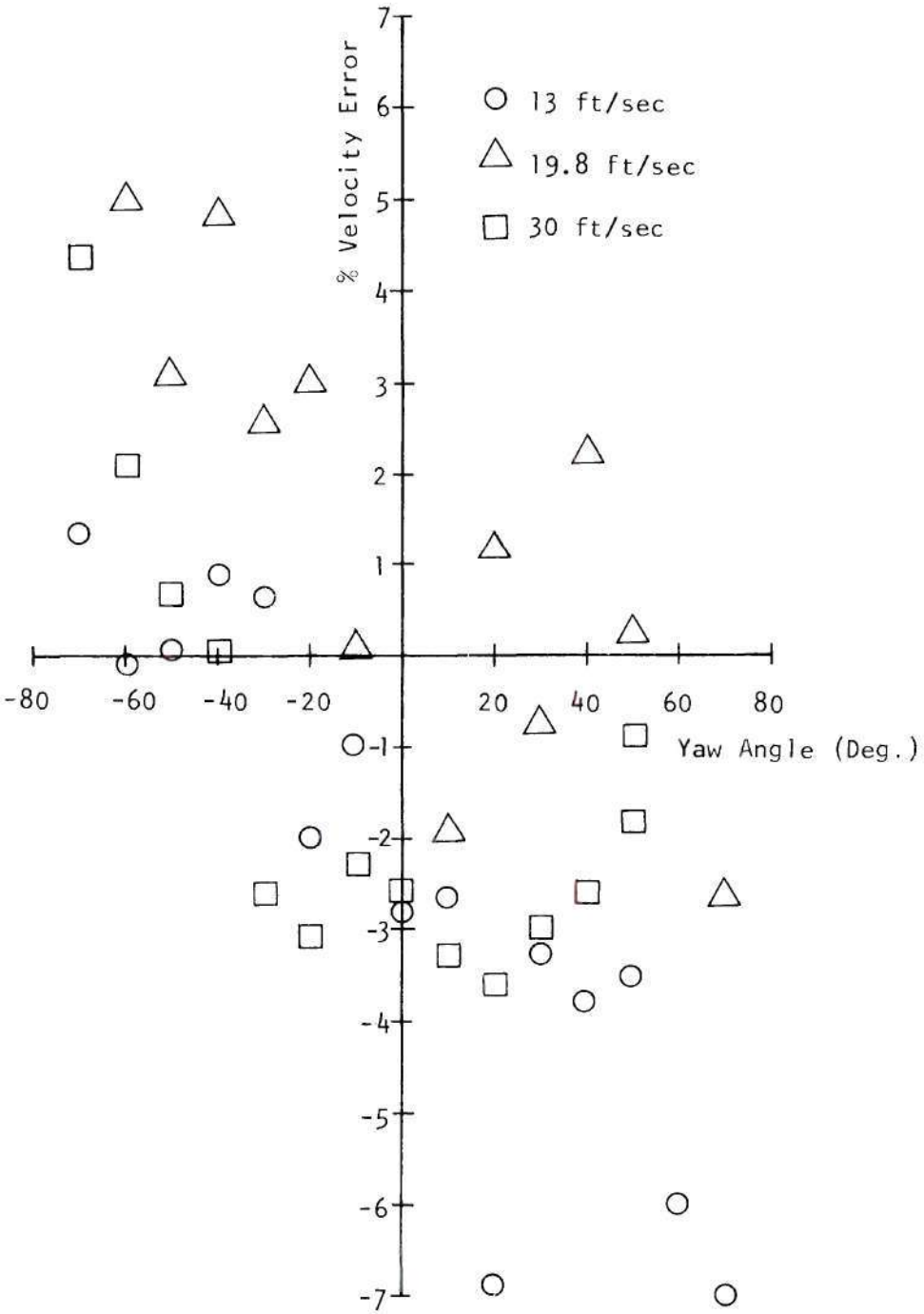

Figure B-2. Percentage Error in Total Velocity, Pitch = 10°.

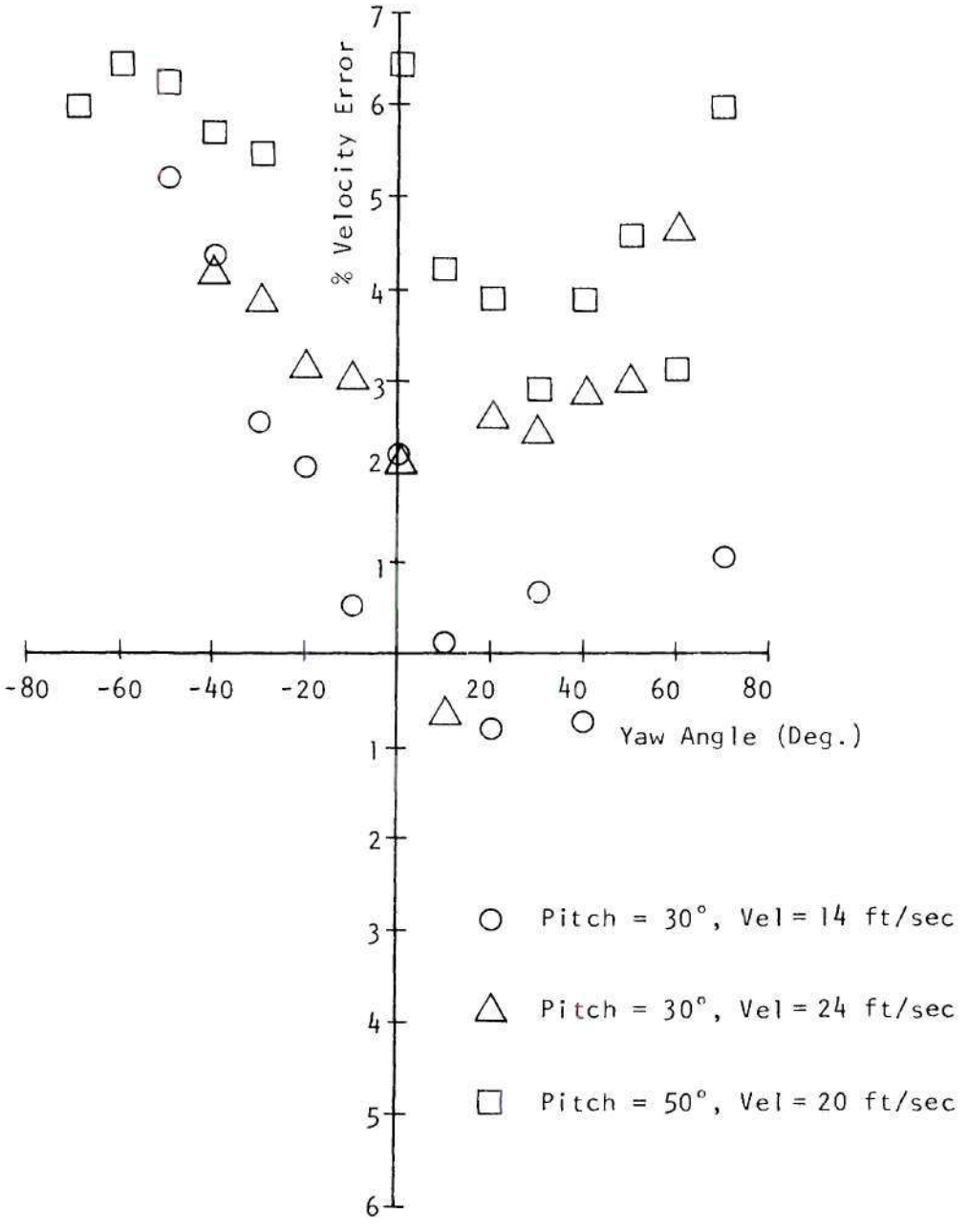

Figure B-3. Percentage Error in Total Velocity, Pitch = 30°, 50°.

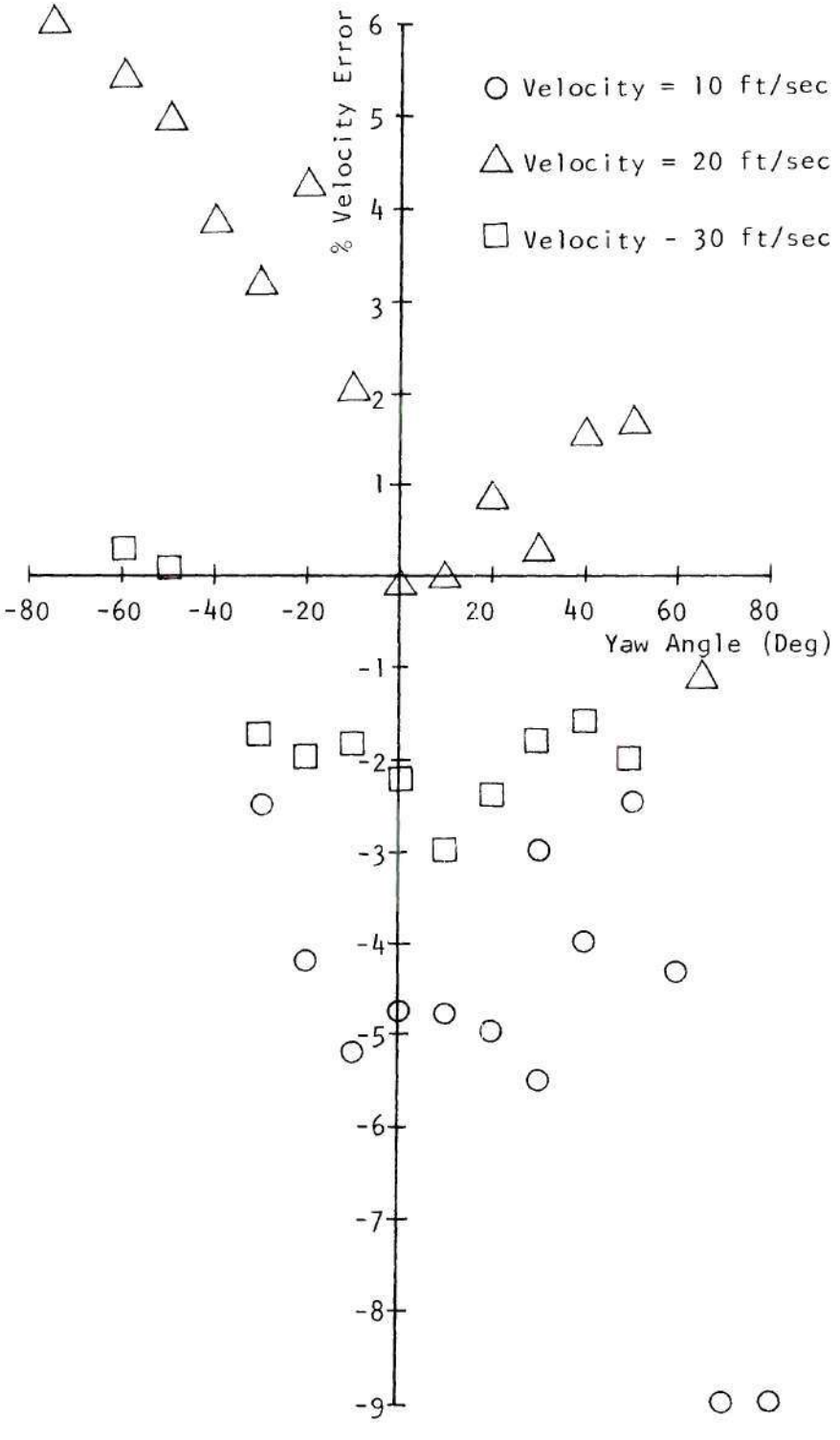

Figure B-4. Percentage Error in Total Velocity, Pitch = -10°.

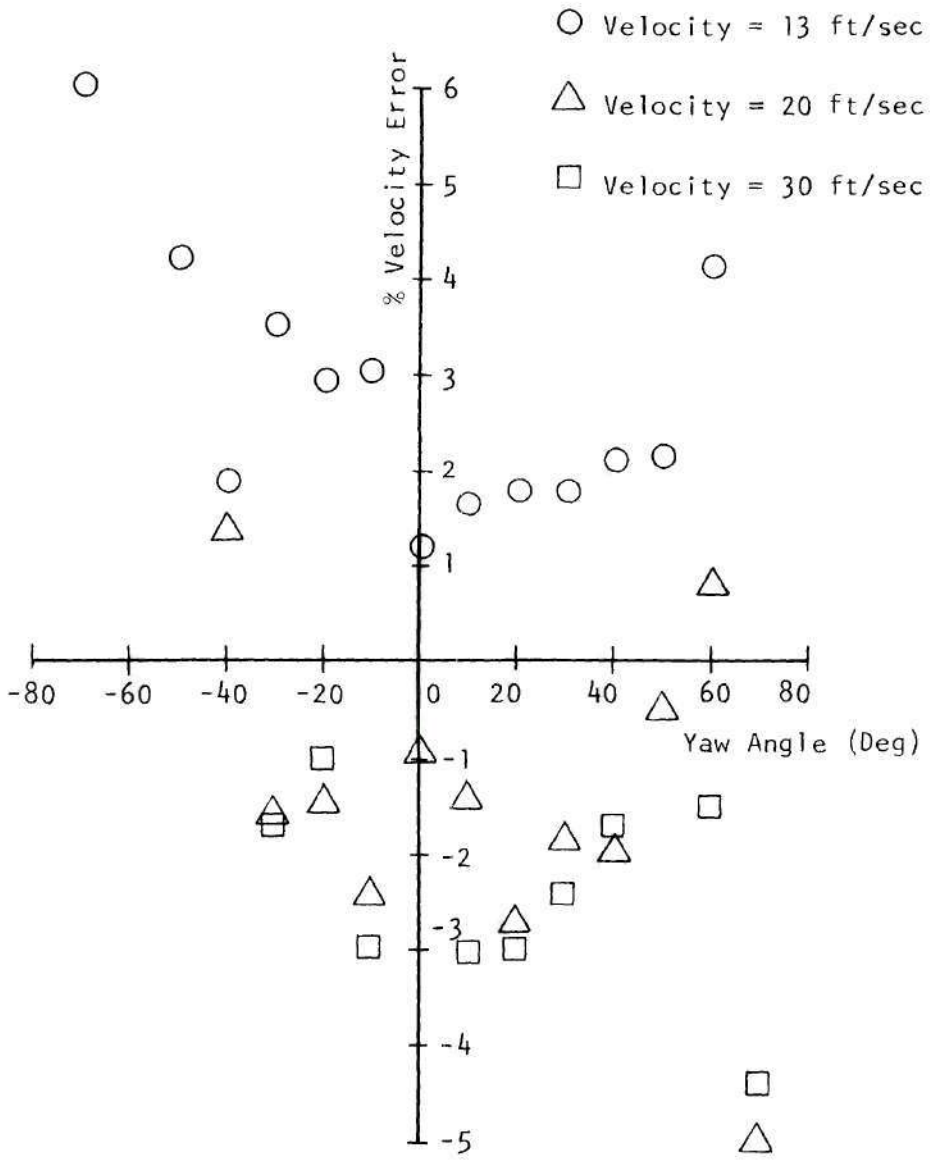

Figure B-5. Percentage Error in Total Velocity, Pitch = -20°.

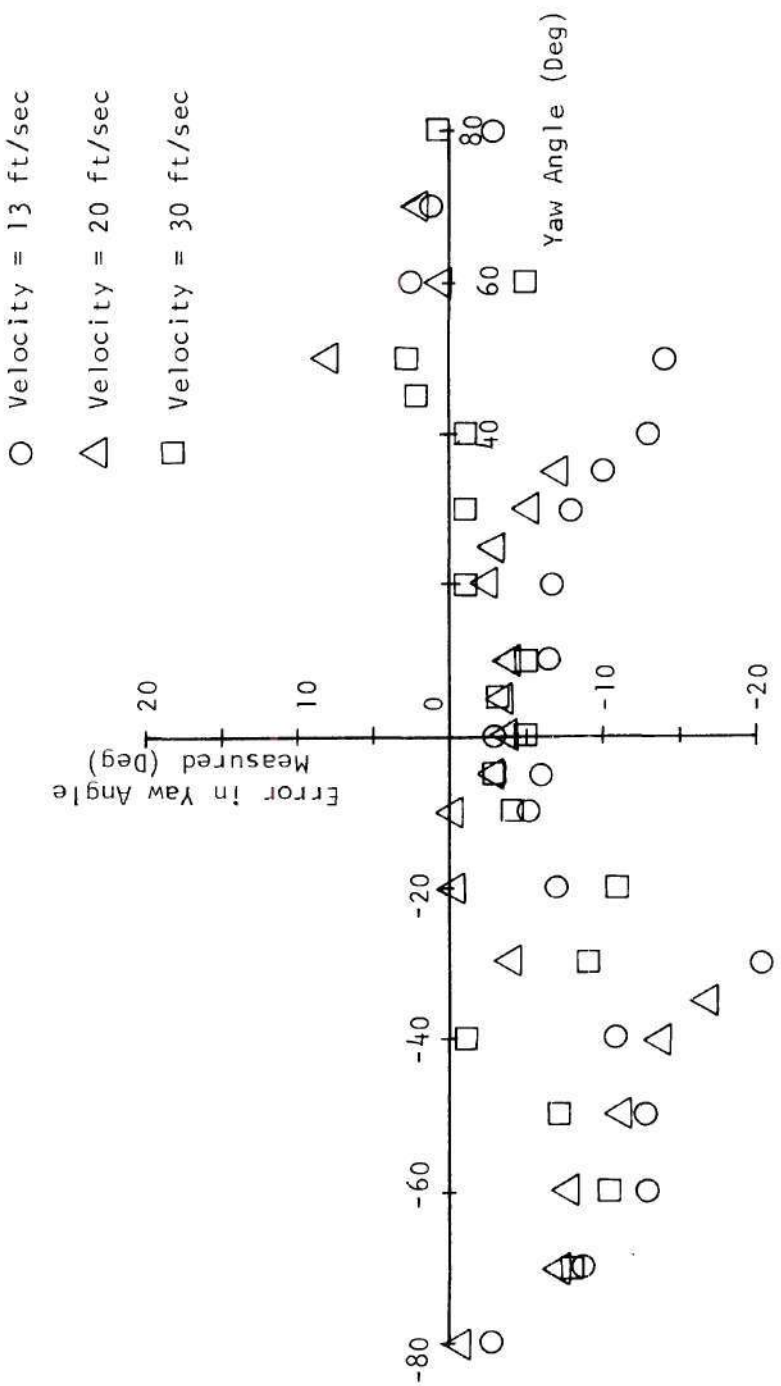

Figure B-6. Angular Error in Yaw, Pitch Angle = 0°.

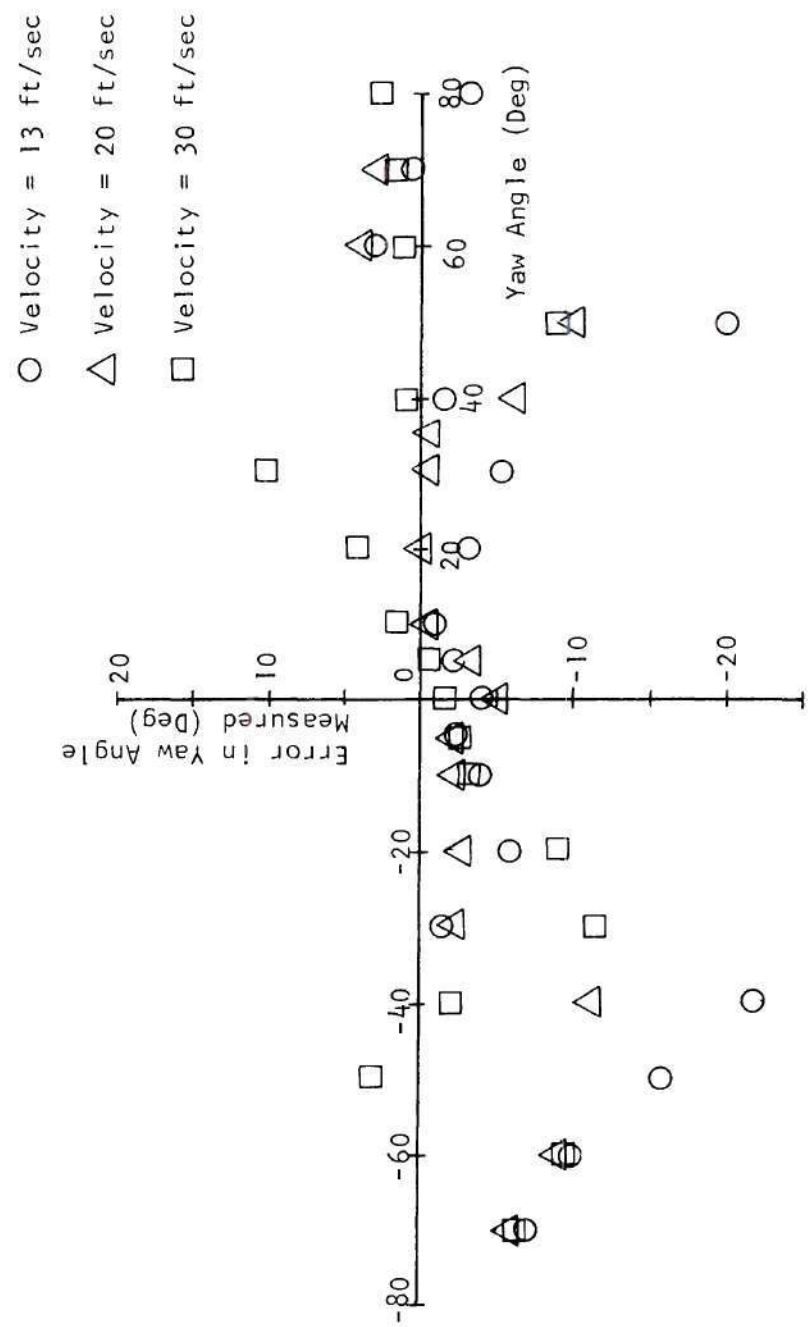

Figure B-7. Angular Error in Yaw, Pitch Angle = 10°.

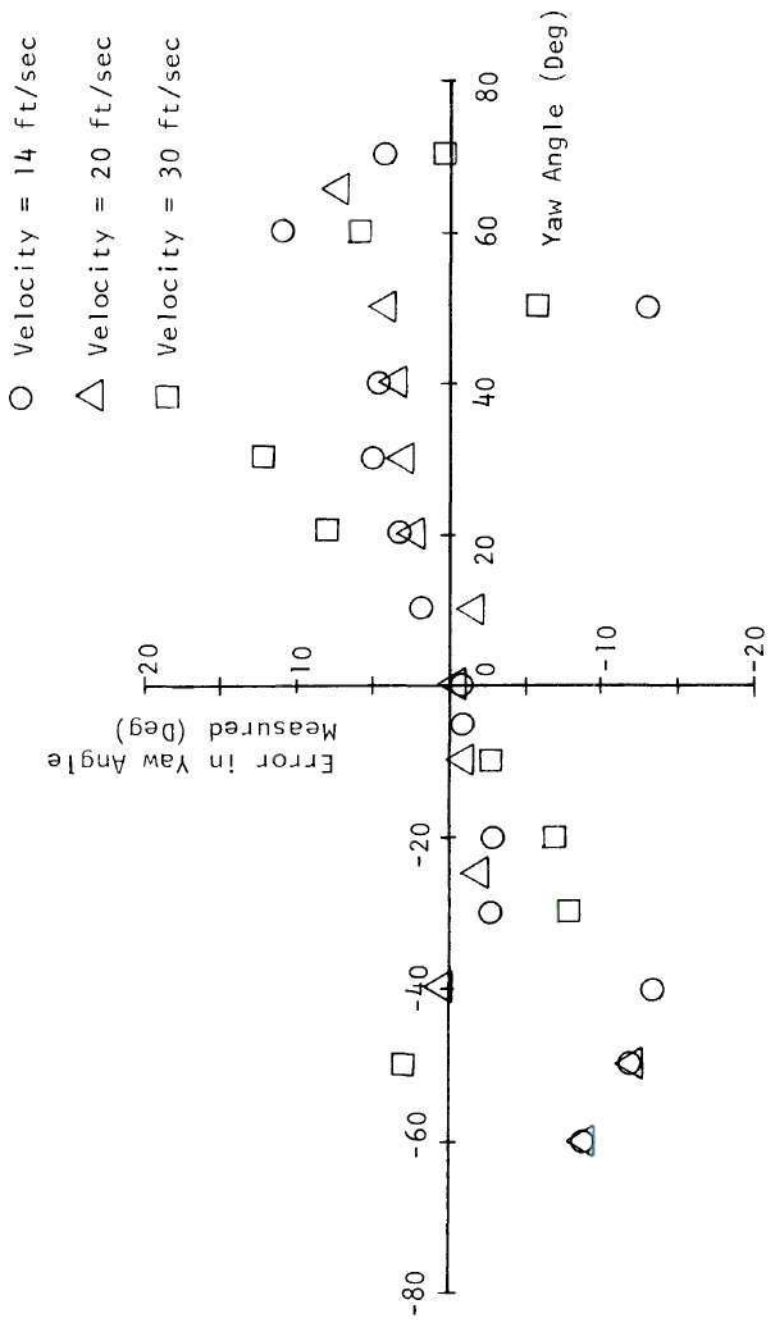

Figure B-8. Angular Error in Yaw, Pitch Angle = 20°.

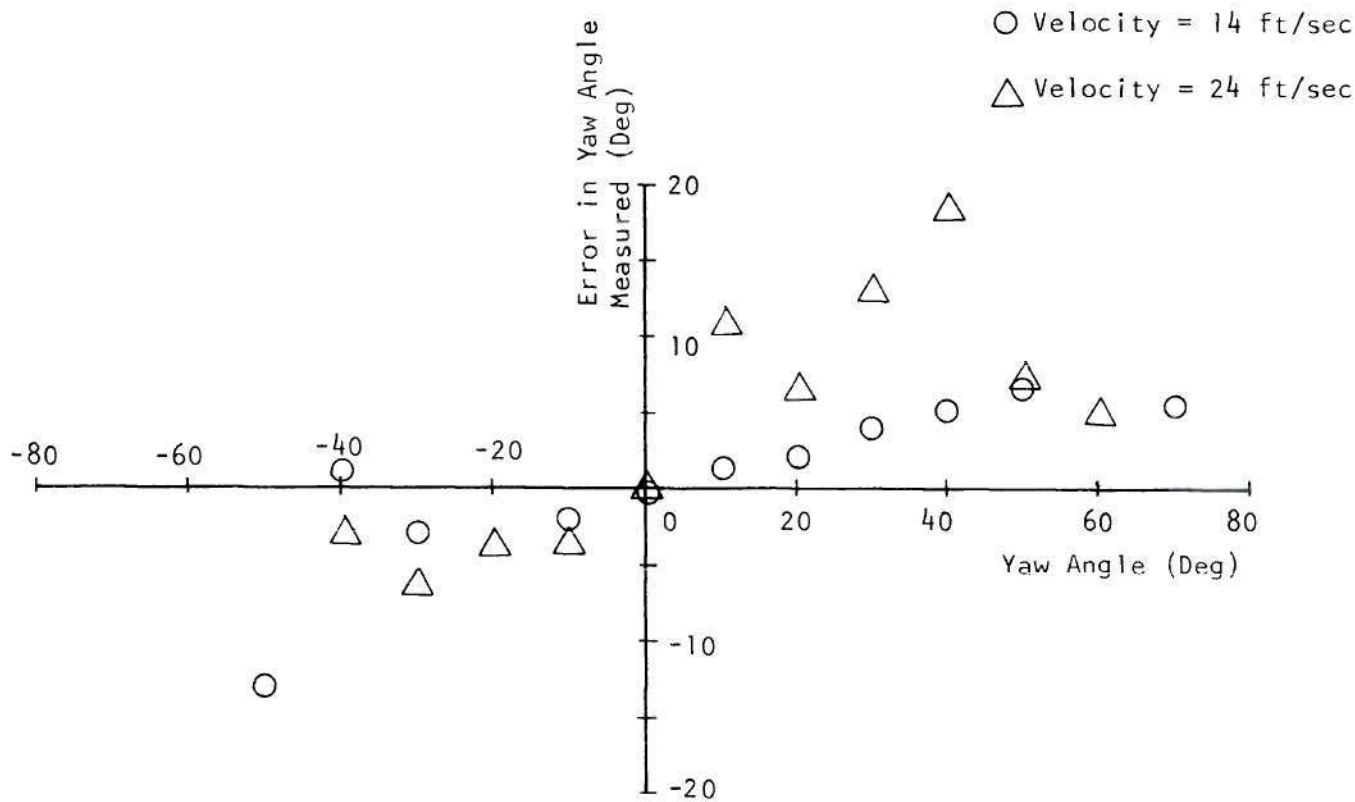

Figure B-9. Angular Error in Yaw, Pitch = 30°.

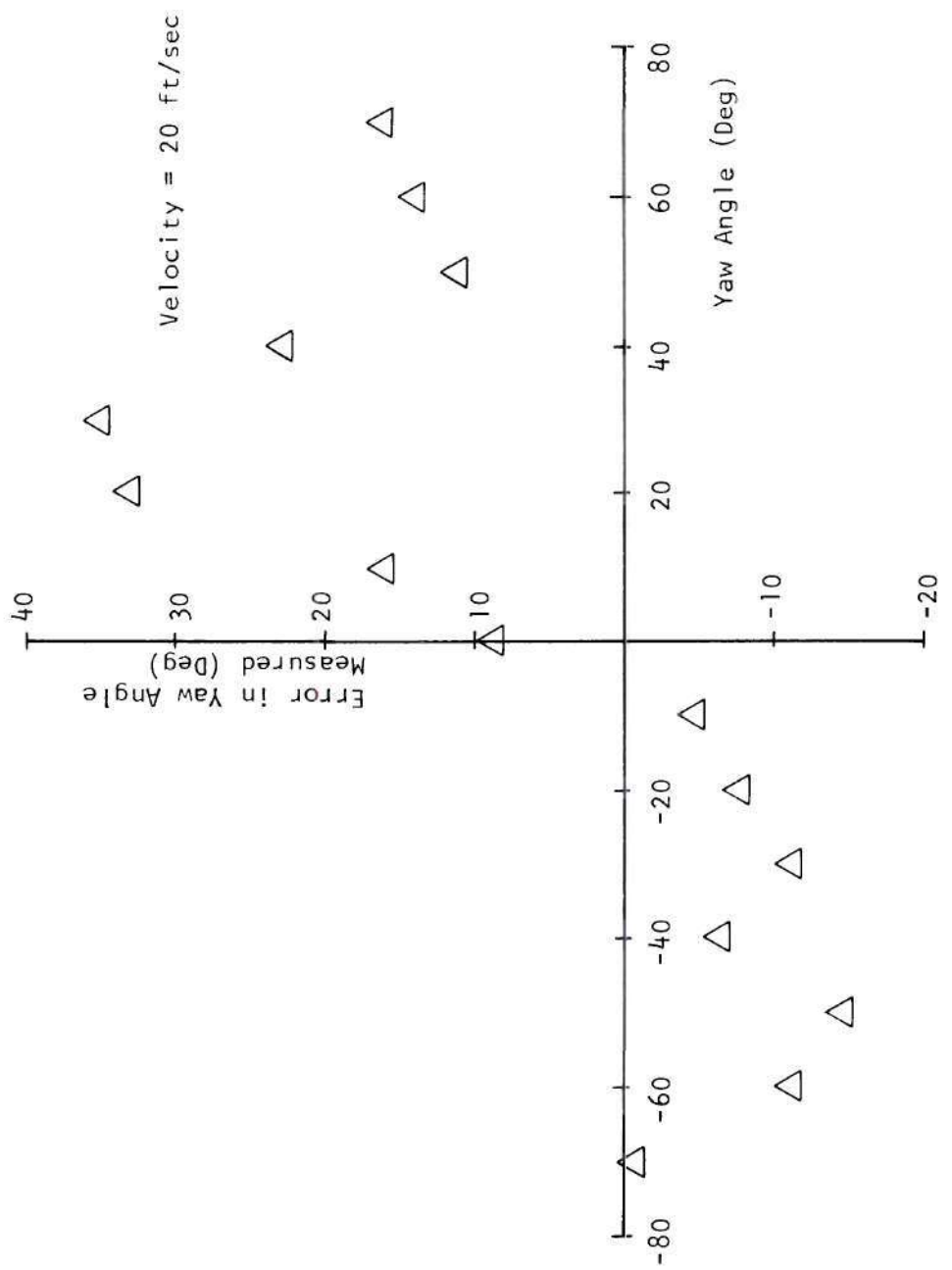

Figure B-10. Angular Error in Yaw, Pitch = 50°.

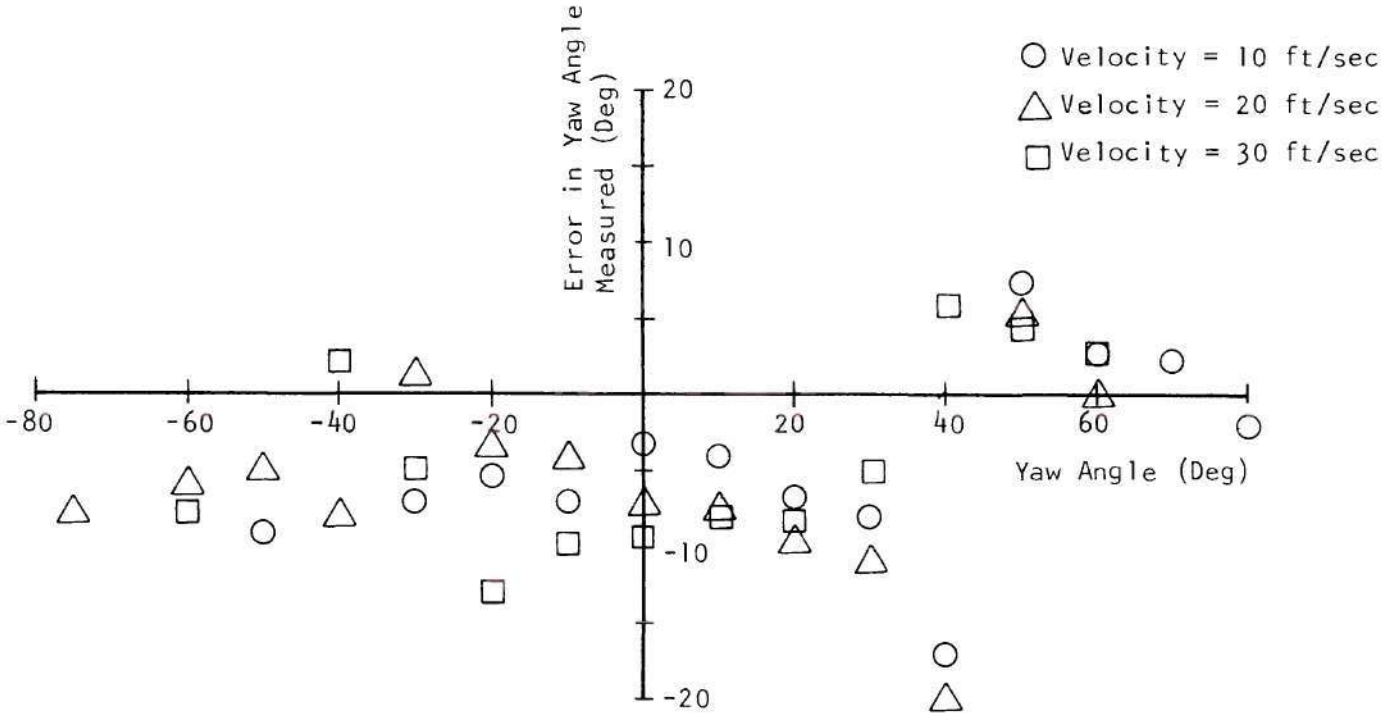

Figure B-11. Angular Error in Yaw, Pitch = -10°.

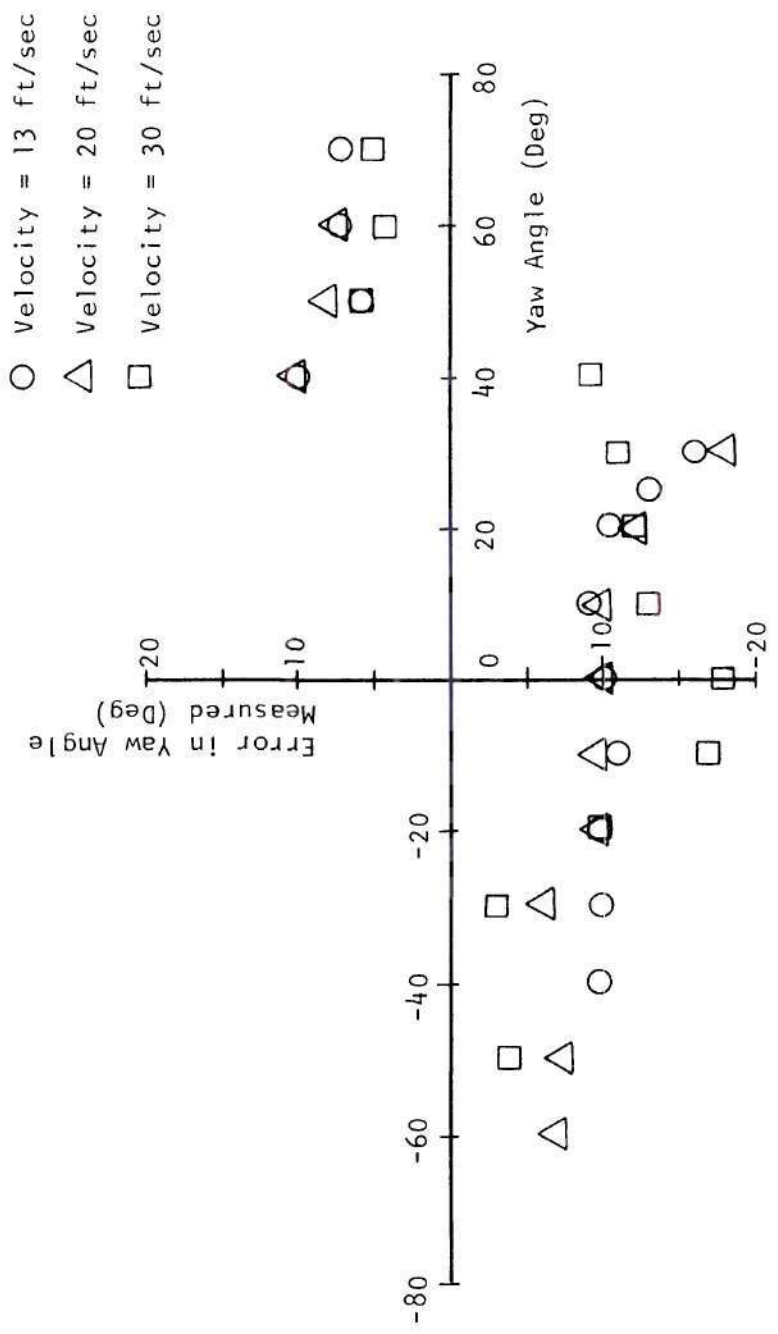

Figure B-12. Angular Error in Yaw, Pitch = -20°.

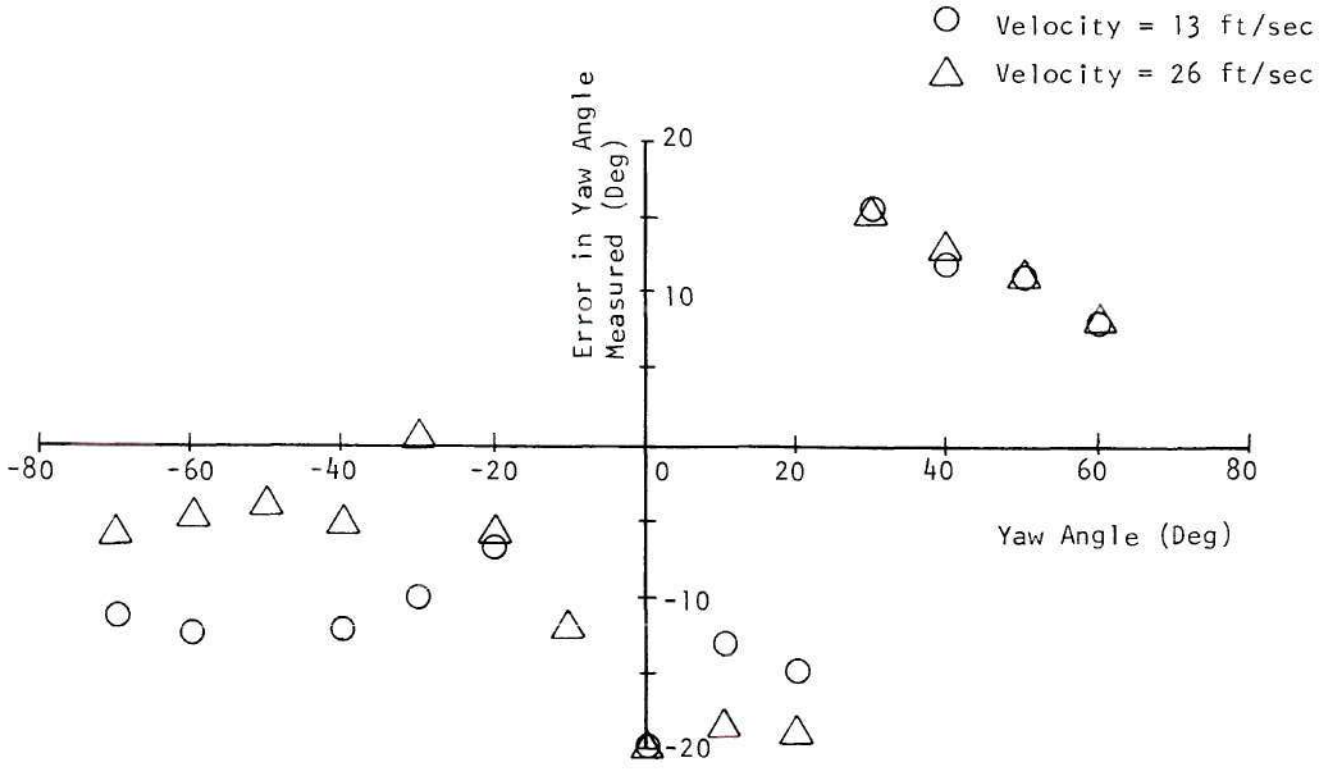

Figure B-13. Angular Error in Yaw, Pitch = -30°.

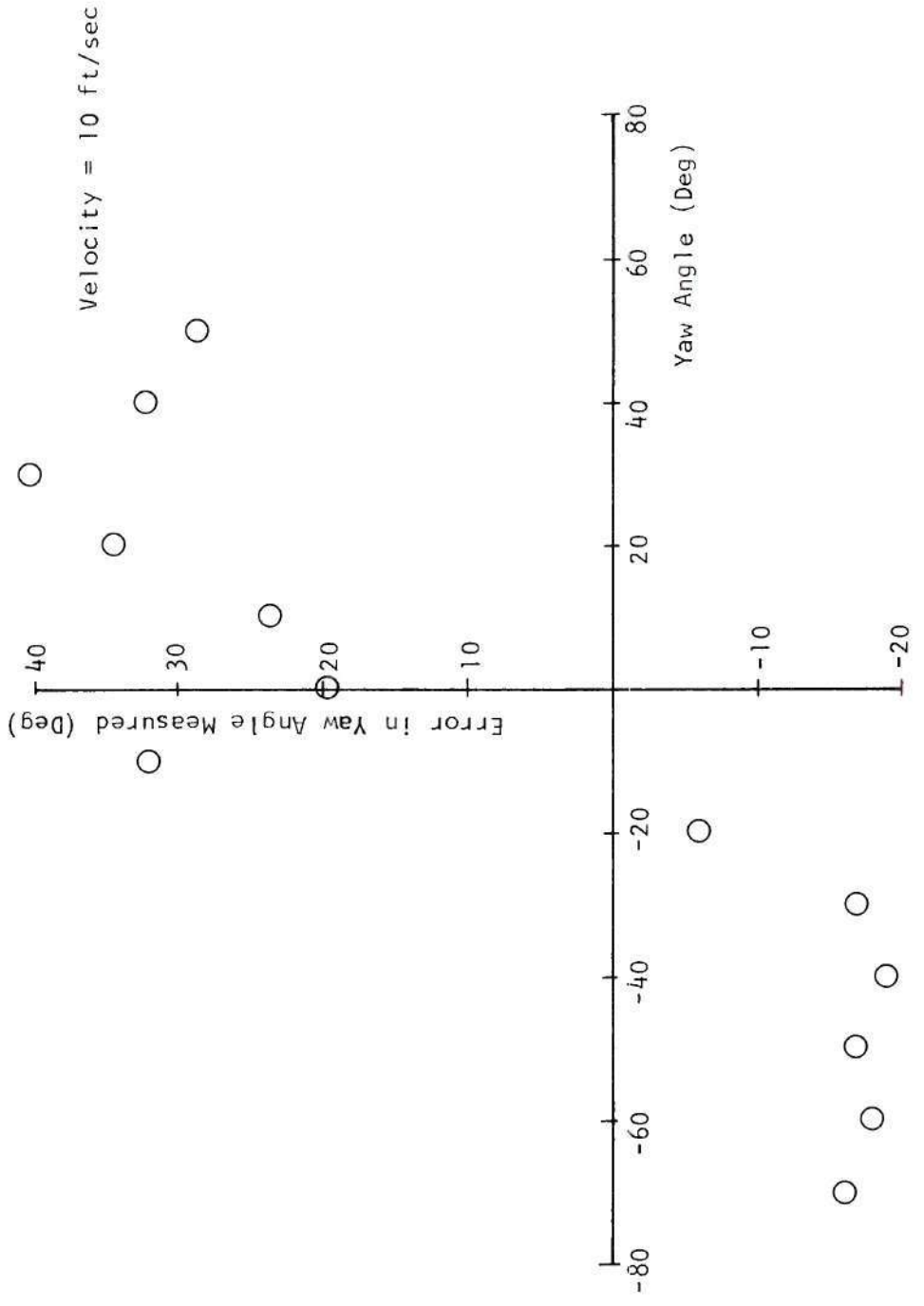

Figure B-14. Angular Error in Yaw, Pitch = -60°.

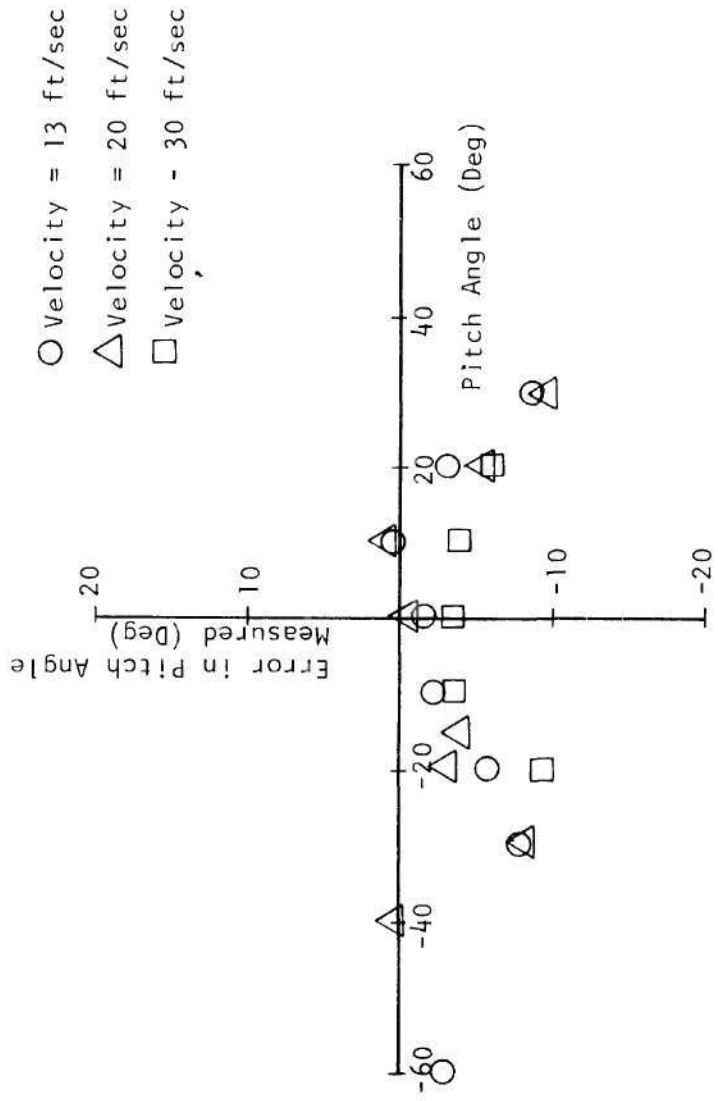

Figure B-15. Angular Error in Pitch, Yaw Angle = 0°.

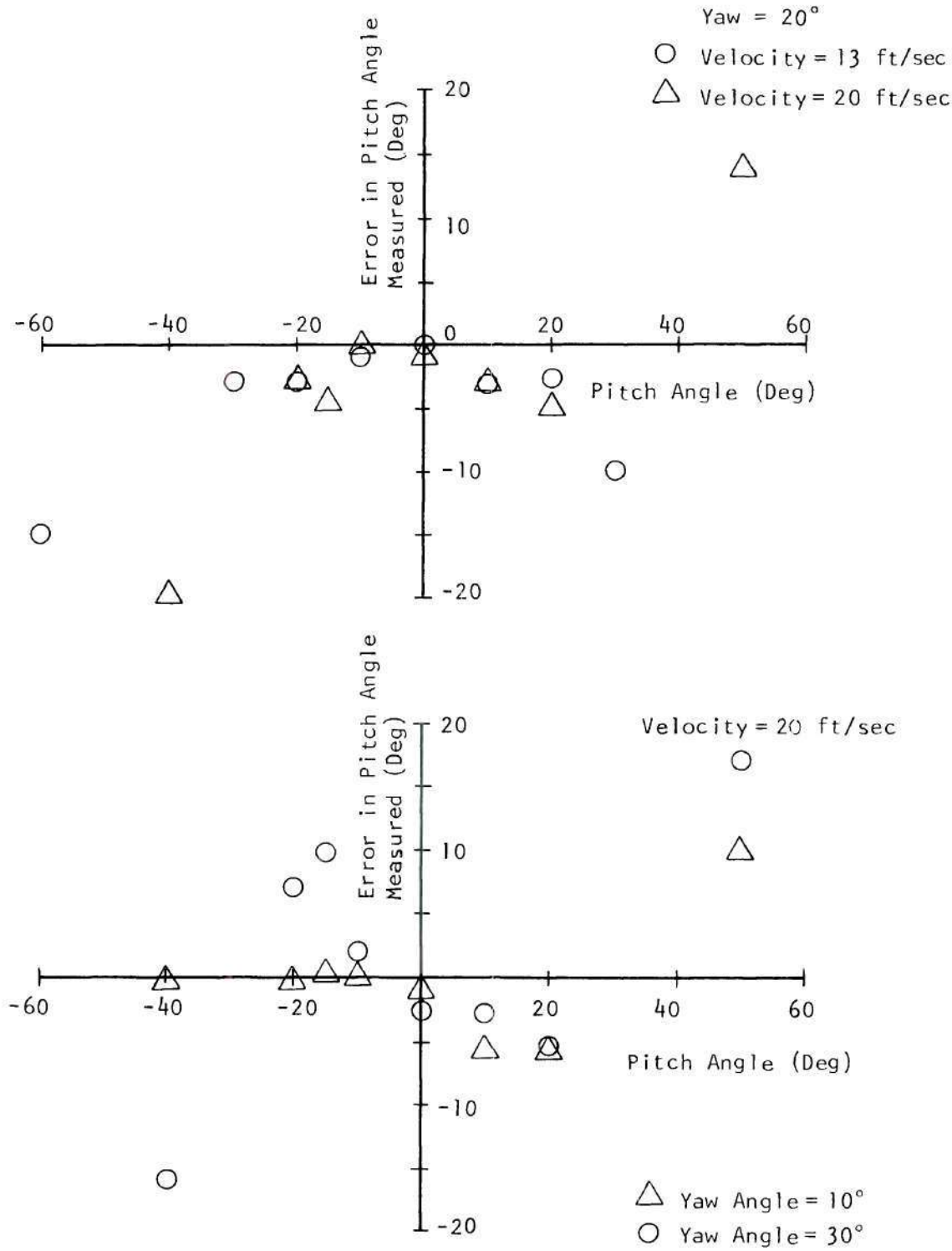

Figure B-16. Angular Error in Pitch ,Yaw = 20°, 10°, 30°.

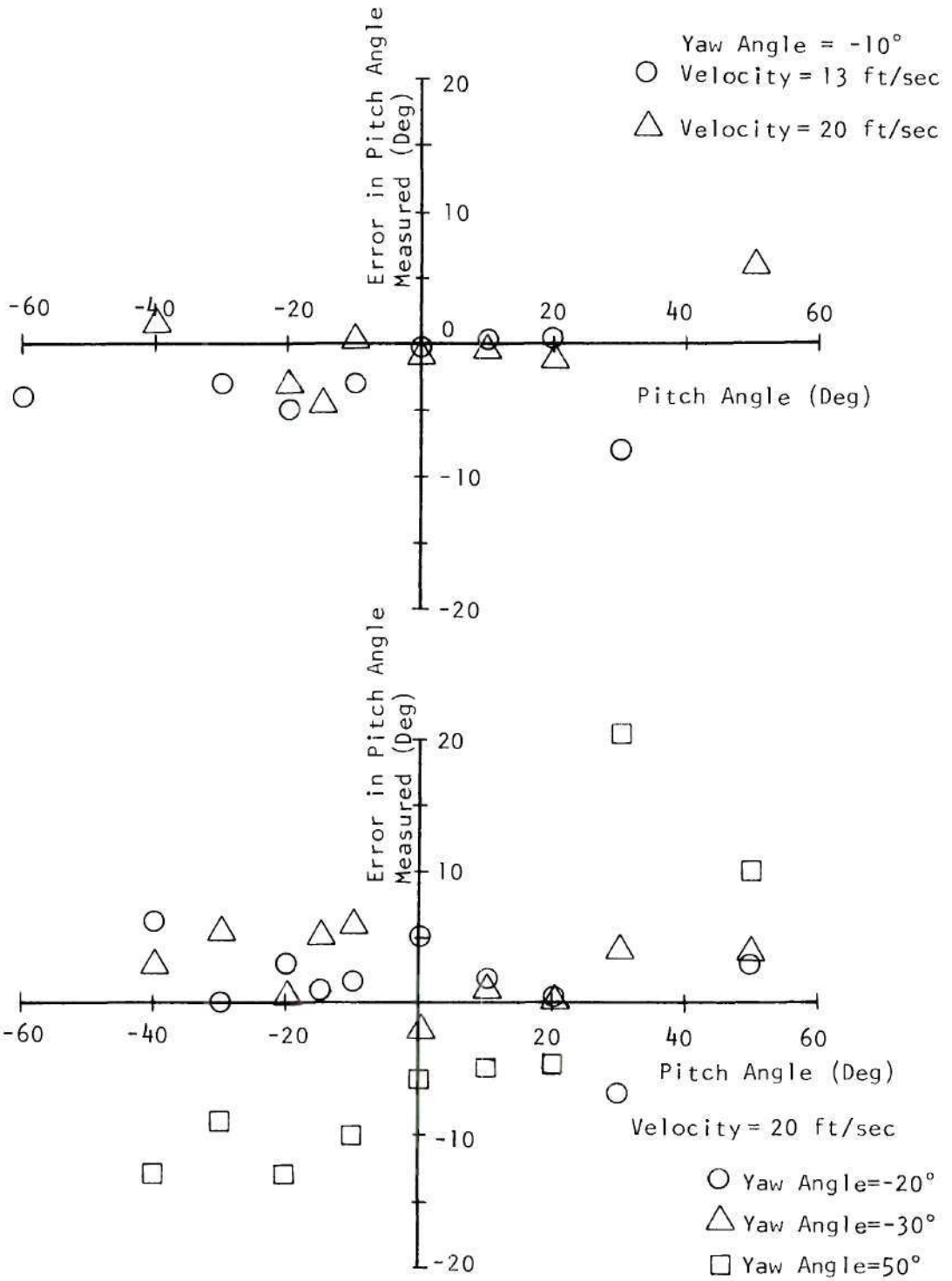

Figure B-17. Angular Error in Pitch, Yaw Angle = -10°, -20°, -30°, 50°.

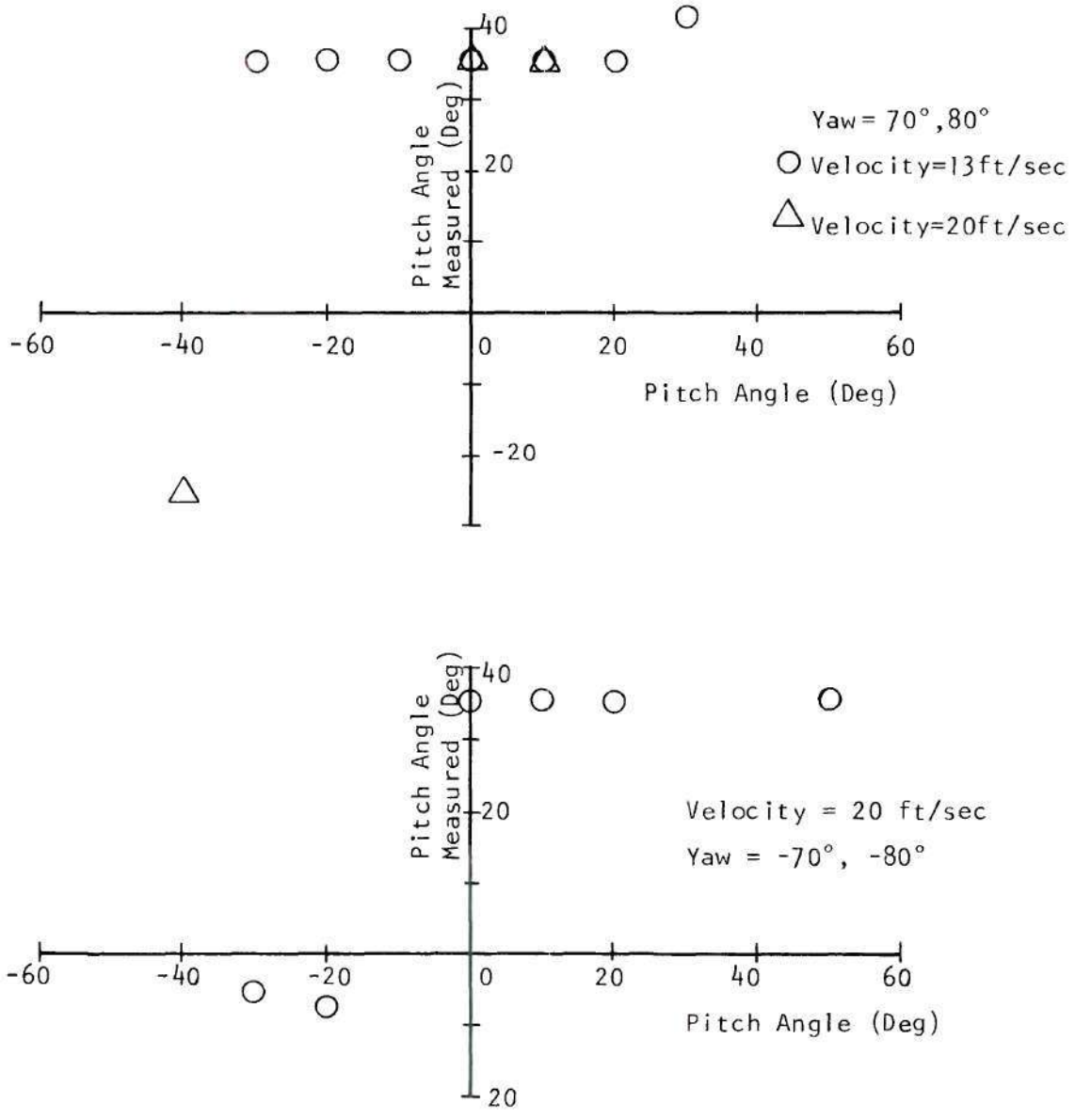

Figure B-18. Plot of Measured Pitch Angles, Yaw Angle = 70°,80°; -70°, -80°.

APPENDIX C

THEORETICAL BACKGROUND AND DATA REDUCTION SCHEME FOR THE MODEL 1080 TOTAL VECTOR ANEMOMETER

The data reduction scheme discussed here basically follows the data reduction procedure given by the manufacturer of the total vector anemometer system.[25] Some conclusions concerning the data reduction scheme are also mentioned here.

The first theoretical solution for heat transfer from a heated cylinder was developed by L. V. King[33] in 1914. Collins and Williams'[34] improvement to King's solution is given by

$$Nu = (A + B\, R_{e_d}^{n})\left(\frac{T_m}{T_a}\right)^{0.174} \qquad (1)$$

where T_m/T_a represents the temperature loading of the wire. A, B and n are constants which were determined by Collins and Williams. The heat transferred from a hot film per unit time is:

$$q = h_f\, a(T_f - T_a)$$

Introducing the Nusselt number, $(Nu = h_f d/K_m)$,

$$q = Nu\, k_m\, a(T_f - T_a)/d \text{ , where } a = \pi dL$$

Substituting (1) for Nu yields

$$q = k_m\, \pi L\, (T_f - T_a)\left\{\frac{T_m}{T_a}\right\}^{0.174} (A + B\, R_{e_d}^{n})$$

Neglecting conduction and radiation losses, $q = I^2R_f$ so that

$$I^2R_f = C\ k_m\ \pi L(T_f - T_a)\left\{\frac{T_m}{T_a}\right\}^{0.174}\ (A + B\ R_{e_d}^{n})$$

It follows that the relation between the velocity of the fluid and the power required to operate the sensor at a given temperature in a specific fluid may be given by

$$\frac{I^2R_f}{T_f - T_a} = C_1 + D_1(\rho U_e)^n$$

where U_e is the effective cooling velocity. It is the normal velocity that would produce the same amount of cooling of the sensor as is produced by the actual velocity at the same angle of attack.

Relating the effective cooling velocity to standard pressure and temperature (p_s = 14.7 psia, T_s = 530°R), it is recognized that $\rho U_e = \rho_s U_{es}$. Since ρ_s = constant, it may be incorporated in the constant. Then

$$\frac{I^2R_f}{T_f - T_a} = \frac{q}{\Delta T} = C + D\ U_{es}^{n} \qquad (2)$$

For a split-film sensor where both films are operating at the same temperature,

$$(Q/\Delta T) = \frac{I_I^2 R_I + I_{II}^2 R_{II}}{T_f - T_a} \qquad (3)$$

where R_I and R_{II} are the hot resistances of the two films.

For the Thermo-System, Inc. Model 1080 anemometer system, the

voltages across each of the six bridges are measured. For one sensor, say the B sensor, let R_{B_I} and $R_{B_{II}}$ be the two total bridge resistances. Then

$$R_{B_I} = R_I + R_{C_I} + R_{M_I}$$

$$R_{B_{II}} = R_{II} + R_{C_{II}} + R_{M_{II}}$$

where R_I and R_{II} are the film resistances for sensor B, R_{C_I} and $R_{C_{II}}$ are the cable resistances associated with sensor B, and R_{M_I} and $R_{M_{II}}$ are the fixed resistances in the arm of the bridge which is adjacent to the cable and film arm.

Defining $K_{B_I} = R_I/R^2_{B_I}$, $K_{B_{II}} = R_{II}/R^2_{B_{II}}$, and since $I_I R_{B_I} = E_{B_I}$ and $I_{II} R_{B_{II}} = E_{B_{II}}$, then from equation (3)

$$(Q/\Delta T)_B = \frac{\frac{R_I}{R^2_{B_I}} I^2_I R^2_{B_I} + \frac{R_{II}}{R^2_{B_{II}}} I^2_{II} R^2_{B_{II}}}{T_{f_B} - T_a} = \frac{K_{B_I} E^2_{B_I} + K_{B_{II}} E^2_{B_{II}}}{T_{f_B} - T_a}$$

and from equation (2)

$$(Q/\Delta T)_B = \frac{K_{B_I} E^2_{B_I} + K_{B_{II}} E^2_{B_{II}}}{T_{f_B} - T_a} = (C + D\, U^n_{es})_B$$

where E_{B_I} and $E_{B_{II}}$ are the bridge voltages for films I and II at sensor B. The constants K_{B_I} and $K_{B_{II}}$ also correct for surface area and

resistance differences in the two films and are determined experimentally. For all velocities of interest in this study, C may be eliminated by adjusting the constants K_{B_I} and $K_{B_{II}}$. This yields

$$(Q/\Delta T)_B = \frac{K_{B_I} E_{B_I}^2 + K_{B_{II}} E_{B_{II}}^2}{(\Delta T)_B} = D(U_{es}^n)_B \qquad (4)$$

The constants D and n are to be determined from the calibration data for the anemometer. According to the manufacturer, these values are to be chosen according to the criterion

	D	1/n
$Q/\Delta T < 0.503$	0.177	3
$Q/\Delta T > 0.503$	0.125	2.25

K_{B_I}, $K_{B_{II}}$ and T_{f_B} are furnished by Thermo Systems, Inc. from in-house calibration of each sensor. E_{B_I} and $E_{B_{II}}$ are the measured output of the anemometer.

Thus, $(U_{es})_B = [Q_B/(\Delta T)_B D]^{1/n}$ for sensor B.

Similarly,

$$(U_{es})_A = \left[\frac{Q_A}{(\Delta T)_A D}\right]^{1/n}$$

and

$$(U_{es})_C = \left[\frac{Q_C}{(\Delta T)_C D}\right]^{1/n}$$

for sensors A and C.

When a sensor is yawed with respect to the mean flow, according

to Hinze[35]

$$U_{es}^2 = U_s^2(\cos^2\phi + k^2 \sin^2\phi) \tag{5}$$

where U_s is the magnitude of the velocity under standard conditions (p_s, T_s) and ϕ is the angle of yaw, being defined as the angle between the normal to the sensor and the velocity vector. The factor k is used to indicate the contribution of the lateral velocity component to the total cooling velocity when the sensor is yawed with respect to the mean velocity vector.

Using equation (5), solving for U_s, and using the geometrical relations (sensors A, B and C are mutually perpendicular)

$$\sin^2 \phi_A + \sin^2 \phi_B + \sin^2 \phi_C = 1$$

$$\cos^2 \phi_A + \cos^2 \phi_B + \cos^2 \phi_C = 2$$

then,

$$U_s = \left[\frac{(U_{es})_A^2 + (U_{es})_B^2 + (U_{es})_C^2}{(2 + k^2)} \right]^{1/2} \tag{6}$$

where U_s is the magnitude of the velocity vector, ft/sec, at standard conditions (p_s, T_s).

Now, the k values as supplied with the anemometer are

$k = 0.2$ for $U_s > 20$ ft/sec

$k = 0.9/U_s^{1/2}$ for $U_s < 20$ ft/sec.

The magnitude of the velocity vector, at local conditions (p,T) may be expressed as, $U = U_s(P_s T/p T_s)$.

The equation (5) for a particular sensor, say B, yields

$$U^2_{es_B} = U^2_s(\cos^2 \phi_B + k^2 \sin^2 \phi_B)$$

Solving for ϕ_B

$$|\phi_B| = \arcsin \left[\frac{1 - \frac{U^2_{es_B}}{U^2_s}}{1 - k^2} \right]^{1/2} \qquad (7)$$

Similarly for sensors A and C,

$$|\phi_A| = \arcsin \left[\frac{1 - \frac{U^2_{es_A}}{U^2_s}}{1 - k^2} \right]^{1/2}$$

$$|\phi_C| = \arcsin \left[\frac{1 - \frac{U^2_{es_C}}{U^2_s}}{1 - k^2} \right]^{1/2}$$

The above equations give the magnitude of the angle of yaw of the velocity vector with respect to sensors A, B and C.

It should be noted that, in an actual measurement, the quantity $[1 - U^2_{es}/U^2_s]$ may from time to time become negative resulting in imaginary values for ϕ. This happens because of some errors in the voltage outputs of the anemometer system due to mutual interference

of sensors in the flow. To avoid this problem, Tielman[26] suggests setting $(1 - U_{es}^2/U_s^2) = 0$ in such cases.

The sign of the angle is determined from the following rule:

$$
\begin{aligned}
\phi_A: \quad & + \quad \text{if} \quad E_{IC} > R_c E_{IIC} \\
& - \quad \text{if} \quad E_{IC} < R_c E_{IIC} \\
\phi_B: \quad & + \quad \text{if} \quad E_{IA} > R_A E_{IIA} \\
& - \quad \text{if} \quad E_{IA} < R_A E_{IIA} \\
\phi_C: \quad & + \quad \text{if} \quad E_{IB} > R_B E_{IIB} \\
& - \quad \text{if} \quad E_{IB} < R_B E_{IIB}
\end{aligned}
\tag{8}
$$

where R_A, R_B and R_C are furnished with the anemometer system as part of the factory calibration data. At this point, three angles and the velocity vector magnitude have been determined. Only two angles are really required, so that the third is redundant.

Equations for Improved Accuracy

The above procedure gives good results up to a velocity of about 20 ft/sec. Above this velocity Olin and Kiland[36] found that k is not only a function of the magnitude of the velocity but is also a function of the sensor yaw angle, ϕ. Therefore, they suggested that the following correction be introduced into the data reduction procedure when the computed magnitude of the total standard velocity (U_s) from the first approximation is greater than 20 ft/sec.

For $i = A, B$ or C sensors

$$\alpha_i = 1 + \beta_i \cos^2 \phi_i$$

$$\beta_i = -12 + 0.6\, U_s \quad \text{if} \quad \phi_i \leq 0 \quad \text{and} \quad 20 < U_s < 30$$

$$= -22 + 1.1\, U_s \quad \text{if} \quad \phi_i > 0 \quad \text{and} \quad 20 < U_s < 30$$

$$\beta_i = 5 + 0.033\, U_s \quad \text{if} \quad \phi_i \leq 0 \quad \text{and} \quad U_s > 30$$

$$= 9 + 0.067\, U_s \quad \text{if} \quad \phi_i > 0 \quad \text{and} \quad U_s > 30$$

Then for this second approximation, equation (6) becomes

$$U_s' = \left[\frac{U_{es_A}^2 + U_{es_B}^2 + U_{es_C}^2}{2 + k^2(\alpha_A \sin^2\phi_A + \alpha_B \sin^2 \phi_B + \alpha_C \sin^2\phi_C)} \right]^{1/2}$$

and the corrected equations for ϕ are

$$|\phi_A'| = \arcsin \left[\frac{1 - U_{es_A}^2 / U_s'^2}{1 - \alpha_A k^2} \right]^{1/2}$$

$$|\phi_B'| = \arcsin \left[\frac{1 - U_{es_B}^2 / U_s'^2}{1 - \alpha_B k^2} \right]^{1/2}$$

$$|\phi_C'| = \arcsin \left[\frac{1 - U_{es_C}^2 / U_s'^2}{1 - \alpha_C k^2} \right]^{1/2}$$

and finally, U_T = total velocity magnitude

$$= U_s' (p/T)_s \; (T/p)_{ambient}$$

The components of the velocity vector along the sensors A, B and C are given by

$$V_A = U_T \sin \phi'_A$$
$$V_B = U_T \sin \phi'_B$$
$$V_C = U_T \sin \phi'_C$$

While measuring the velocities in the rotor wake the anemometer probe was mounted such that the probe shank was aligned with the axis of the rotor. The sensor rods, which are mutually perpendicular are inclined at 54.73 degrees to the probe shank.

Thus, the axial component is given by

$$V_{axial} = \cos 54.73 \ (V_A + V_B + V_C)$$
$$V_{axial} = 0.5774 \ (V_A + V_B + V_C)$$

In the wake, V_{axial} is positive when it is away from rotor plane. The radial component is given by

$$V_{radial} = \sin 54.73 \cdot \cos \ (V_C - V_B)$$
$$V_{radial} = 0.70711 \ (V_C - V_B)$$

In the wake, V_{radial} is positive when it is radially inward. The tangential component is given by

$$V_{tangential} = \sin 54.73[V_A - \sin 30(V_B + V_C)]$$
$$V_{tangential} = 0.8165[V_A - 0.5(V_B + V_C)]$$

In the wake, $V_{tangential}$ is positive when it is in the direction of rotation of the rotor.

Rough Check on Data Accuracy

After calculating the ϕ values from the 6 voltage outputs of the anemometer system, if the sum $\sin^2\phi_A + \sin^2\phi_B + \sin^2\phi_C$ is calculated and all measurements are accurate then the sum must be equal to 1. However, small errors in the voltage outputs will alter this quantity by small amounts. The variations of $(\sin^2\phi_A + \sin^2\phi_B + \sin^2\phi_C)$ from 1.000 is a rough indication of the errors in the voltage outputs.

Some Deficiencies in the Data Reduction Procedure

While using the total vector anemometer system and reducing the velocity data, some deficiencies in the data reduction procedure were noticed. Two of the deficiencies which have a bearing on the accuracy of the calculated velocities are discussed here.

(1) A problem associated with the vector anemometer system which from time to time may affect the results in the use of equations (8) to determine the sign of the sensor yaw angles. When, in equations (8), the ratio of E_{1i}/E_{2i} for any sensor i approaches the value of R_i, then, with even small fluctuations in the flow, the ratio E_{1i}/E_{2i} also fluctuates about R_i making the ϕ_i sign decision vague and questionable. Sometimes this effect may cause large errors in determining velocity components.

(2) When ϕ_A is set to 0 to avoid imaginary values for ϕ_A, the axial component of the velocity becomes

$$V_{axial} = 0.5774\ (V_B + V_C)$$

and the tangential component of the velocity becomes

$$V_{tangential} = -0.40825\ (V_B + V_C)$$

Hence, the pitch angle of the probe with respect to the velocity is given by

$$\theta = \arctan \frac{V_{tangential}}{V_{axial}}$$

$$\theta = \arctan\ (0.707) = 35.26 \text{ degree}$$

This shows that when $\phi_A = 0$, the reduced data indicates the pitch of the probe to be 35.26 degrees regardless of the actual pitch. This can cause large errors in determining the velocity components. While reducing the measured data it was noticed that ϕ_A was set to zero on isolated occasions.

REFERENCES

1. Ham, N.D., "Technical Evaluation Report on Fluid Dynamics Specialists' Meeting on the Aeordynamics of Rotary Wings," AGARD-61, March 1973.

2. Hoffman, J.D. and Velkoff, H.R., "Vortex Flow Over Helicopter Rotor Tips," Journal of Aircraft, Vol. 8, No. 9, Sept. 1971.

3. White, R.P. and Balcerk, J.C., "The Nemesis of the Trailed Tip Vortex-Is It Now Conquered?" 28th Annual National Forum of the American Helicopter Society, Preprint No. 624, Washington, D.C., May 1972.

4. Scheimann, J. and Ludi, "Qualitative Evulation of the Effect of Helicopter Rotor Blade Tip Vortex on Blade Airloads," NASA TN D-1637, May 1963.

5. McCormick, B.W. and Surendraiah, M., "A study of Rotor Blade-Vortex Interaction," 26th Annual National Forum of the American Helicopter Society, Preprint No. 421, Washington, D.C., June 1970.

6. Spivey, W.A. and Morehouse, G.A., "New Insights into Design of Swept $_{tip}$ Rotors," 26th Annual National Forum of the American Helicopter Society, Preprint No. 420, Washington, D.C., June 1970.

7. Spivey, R.F., "Blade Tip Aerodynamics-Profile and Planform Effects," 24th Annual National Forum of the American Helicopter Society, Preprint No. 205, Washington, D.C., May 1968.

8. Chigier, N. A., "Experimental Studies of Turbulent Aircraft Wakes," Israel Journal of Technology, Vol. 11, No. 6, 1973, pp. 367-372.

9. Chigier, N. A. and Corriglia, V.R., "Tip Vortices-Velocity Distributions," 27th Annual National Forum of the American Helicopter Society, Preprint No. 522, Washington, D.C., May 1971.

10. Landgrebe, A.J. "The Wake Geometry of a Hovering Helicopter Rotor and Its Influence on Rotor Performance." Journal of the American Helicopter Society,17, No. 4 (Oct. 1972), p. 3

11. Samant, S. and Gray, Robin B., "A Semi-emperical Correction for the vortex core effect on hovering rotor wake geometries." 33rd Annual National Forum of the American Helicopter Society, Preprint No. 77. 33-02. Washington, D.C., May 1977.

12. Langrebe, Anton J., "An Analytical And Experimental Investigation of Helicopter Rotor Hover Performance and Wake Geometry Characteristics, USAAMRDL Technical Report 71-24, Eustis Directorate, U.S. Army Air Mobility Research and Development Laboratory, Fort Eustis, Virginia, June 1971.

13. Jenney, David S., Olson, John R., and Landgrebe, Anton J.,"A Reassessment of Rotor Hovering Performance Prediction Methods, Journal of the American Helicopter Society, Vol. 13, No. 2.

14. Gray, R.B., "On the Motion of the Helical Vortex Shed from a Single-Bladed Hovering Helicopter Rotor and Its Application to the Calculation of the Spanwise Aerodynamic Loading, Princeton University Aeronautical Engineering Department, Report No. 313, Sept. 1955.

15. Erickson, J.C., Jr. "A Continuous Vortex Sheet Representation of Deformed Wakes of Hovering Propellers", Cornell Aeronautical Lab., USAAML, 3rd Symposium, Buffalo, N.Y. 1969.

16. Boatwright, Donald W., "Measurements of Velocity Components In The Wake of a Full-scale Helicopter Rotor in Hover," USAAMRDL Technical Report 72-33, Eustis Directorate, U.S. Army Air Mobility Research and Development Laboratory, Fort Eustis, Virginia, August 1972, AD 754644.

17. Boatwright, Donald W., :Three-Dimensional Measurements of the Velocity in the Near Flow Field of a Full-scale Hovering Rotor, ARO-D Interim Report EIRS-ASE-74-4, U.S. Army Research Office-Durham Durham, North Carolina.

18. Christian Maresca, Daniel Favier, and Jean Rebont "Instantaneous Velocity Measurements in the Near Wake of a Helicopter Rotor," Institute de Mecanique des Fluides de Marseille,Marseille, France. Feb. 1974.

19. James C. Biggers and Kenneth L. Orloff, " Laser Velocimeter Measurements of the Helicopter Rotor-Induced Flow Field." 30th Annual National Forum of the American Helicopter Society, Washington, D.C., May 1974.

20. James C. Biggers, Sing Chu and Kenneth L. Orloff "Laser Velocimeter Measurements of Rotor Blade Loads and Tip Vortex Rollup." 31st Annual National Forum of the American Helicopter Society, Preprint No. 900. Washington , D.C., May 1975.

21. Landgrebe, A.J. and Johnson, B.V., "Measurements of Model Helicopter Rotor Flow Velocities With a Laser Doppler Velocimeter," Journal of the American Helicopter Society, Vol. 19, No. 3, July 1974.

22. Sullivan, J. P., "An Experimental Investigation of Vortex Rings and Helicopter Rotor Wakes Using a Laser Doppler Velocimeter," Massachusetts Institute of Technology Report 183, June 1973.

23. Samant. Satish, "An Improved Method for Calculating the Tip Vortex Geometry for Hovering Rotors," Ph.D. Dissertation. Georgia Institute of Technology, Atlanta, Georgia: School of Aerospace Engineering, November 1976.

24. Raj, P., "A Method of Computing the Potential Flow on Thick Wing Tips," Ph.D. Dissertation, School of Aerospace Engineering, Georgia Institute of Technology, Oct. 1976.

25. Thermo-Systems, Inc., "Operating and Service Manual for Model 1080 and Model 1080 D Total Vector Anemometer," Saint Paul, Minnesota, 1972.

26. H. W. Tieleman, K. P. Fewell and H. L. Wood "An Evaluation of the Three-dimensional Split-film Anemometer for Measurements of Atmospheric Turbulence," College of Engineering, Virginia Polytechnic Institute and State University, March 1973.

27. Gray, R. B., "An Aerodynamic Analysis of a Single-Bladed Rotor in Hovering and Low-Speed Forward Flight as Determined from Smoke Studies of the Vorticity Distribution in the Wake," Princeton University Aeronautical Engineering Department, Report No. 356, Sept. 1956.

28. Landgrebe, A. J. and Egolf, T. A., "Rotorcraft Wake Analysis for the Prediction of Induced Velocities," USAAMRDL Tech. Rept. 75-45, Eustis Directorate, USAAMRDL Fort Eustis, Va., Jan. 1976.

29. Gray, R. B., McMahon, H. M., Bird, G. T. Palfery, J. G., Samant, S. S., and Shivananda, T. P. "Helicopter Hovering Performance Studies: I. Vortex Wake Analysis; II. Test Facility; III. Blade Tip Pressure Distributions," Final Report for U.S. Army Research Office Grant No. DAAG29-76-G-0007. Georgia Institute of Technology, Atlanta, Georgia: School of Aerospace Engineering, October 1976.

30. J. J. Shrager, "A Summary of Helicopter Vorticity and Wake Turbulence Publications," National Aviational Facilities Experimental Centre, May 1974.

31. Landgrebe, A. J. and Cheney, M. C., Jr., "Rotor Wakes - Key to Performance Prediction, Symposium on Status of Testing and Modeling Techniques for V/STOL Aircraft," Mideast Region of the American Helicopter Society, Essington, Pa., Oct. 26-28, 1972. (Also, AGARD-CP-111, AGARD Conference Proceedings on Aerodynamics of Rotary Wings, Fluid Dynamics Specialists Meeting, Marseilles, France, Sept. 13-15, 1972.

32. Gray, R. B. and Brown, G. W. "A Vortex Wake Analysis of a Single-Bladed Hovering Rotor and a Comparison with Experimental Data," AGARD-CP-111. AGARD Conference Proceedings on Aerodynamics of Rotary Wings, Fluid Dynamics Panel Specialists Meeting, Marseilles, France, September 13-15, 1972, p. 4-1.

33. King, L. V., "On the Convection of Heat from Small Cylinders in a Stream of Fluid." Phil Trans. Royal Society A214: 373, 1914.

34. Collins, D. C. and Williams, M. J., "Two-Dimensional Convection from Heated Wires at Low Reynolds Numbers." Journal of Fluid-mechanics, 6:357-358, 1959.

35. Hinze, J. O., "Turbulence: An Introduction to its Mechanism and Theory." McGraw-Hill Book Company, Inc., New York, 1959.

36. Olin, J. G. and Kiland, R. B., "Split-film Anemometer Sensors for Three-Dimensional Velocity Vector Measurement," Symposium on Aircraft Wake Turbulence, Seattle, Washington, September 1970.

VITA

Tumkur Parameswaraiah Shivananda was born on June 7, 1950 in Tumkur, India. He attended high school in Davanagere, Karnataka (India), graduating in June 1965. In July, 1961 he entered the National College, Bangalore University for one year pre-university course.

In August 1966, he entered Indian Institute of Technology, Madras, India. He earned his Bachelor of Technology degree in 1971 in Aeronautical Engineering.

In the fall of 1972 he entered the Georgia Institute of Technology as a graduate student and research assistant in the School of Aerospace Engineering. He received his M.S. degree from the Georgia Institute of Technology in December 1973.